

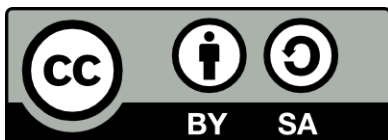
Some refinements in the phase-field and sharp interface treatments of eutectic growth

Zur Erlangung des akademischen Grades eines
Doktors der Ingenieurwissenschaften
(Dr.-Ing.)
von der KIT-Fakultät für Maschinenbau des
Karlsruher Instituts für Technologie (KIT)

genehmigte
Dissertation
von

M.Tech. Sumanth Nani Enugala

Tag der mündlichen Prüfung :	21 st May, 2021
Hauptreferent :	Prof. Dr. rer. nat. Britta Nestler
Korreferent :	Prof. Dr. habil. Mathis Plapp



This work is licensed under the Creative Commons Attribution-ShareAlike 4.0 International License. To view a copy of this license, visit <http://creativecommons.org/licenses/by-sa/4.0/>.

Abstract

The diffuse and sharp interface approaches to the problem of binary eutectic growth are refined and advanced further to some extent. The scope and need for the improvements are pointed out at each stage before working out the details. First, the phase-field modeling equations are re-obtained in a derivation whose starting point and the subsequent progression are majorly prompted and guided by the thermodynamical first principle requirements. Next, the obtained multi-phase equations are analyzed for their vanishing interface width limiting behavior. The treatment is refined as opposed to most of the previous attempts in the sense that the entire vector valued phase-indicator is handled instead of its two-component reduction. Moreover, the local (inner) and matching analysis of the junction regions is also carried out in a full-fledged manner. Each and every prediction of the perturbative analysis is numerically verified, for which, the heretofore adopted prescription for carrying out the interface width reduction studies had to be replaced by an efficacious one. Various options for multi-well forms and bulk energy as well as interfacial mobility interpolating forms are examined to determine the most computationally economic combination. In the case of multi-obstacle implementations which do not lend themselves to an equally complete mathematical analysis, the performance is tested by comparing with the the sharp-interface solutions of those problems which capture the individual physics (the result of whose interplay is the actual co-operative growth phenomenon). Towards the other end, the long-standing approximation of planar solidification front invoked in the sharp-interface formulation of the steady-state eutectic growth problem, namely the Jackson-Hunt analysis, is relaxed both for lamellar and rod-growth cases. In the latter, the hexagonal symmetry of the distribution of rods within the matrix is accurately accommodated. The pitfalls to be avoided when using software packages for extracting free-energy versus composition data from CALPHAD databases is discussed, and, precautions to be taken for ensuring a complete overlap between the Jackson-Hunt problem and the limiting case of the phase-field model are explicitized. Finally, the predictions of the diffuse and the sharp interface treatments are compared revealing a better agreement post the refinements.

Kurzfassung

Die zum Problem des binären eutektischen Wachstums gehörenden Ansätze der diffusen und scharfen Grenzfläche werden verfeinert und zum Teil weiterentwickelt. Dabei wird jeweils auf den Umfang und die Notwendigkeit der Verbesserungen hingewiesen, bevor die Details ausgearbeitet werden. Zunächst werden die Gleichungen zur Phasenfeldmodellierung in einer Herleitung neu gewonnen, deren Ausgangspunkt und weiterer Verlauf im Wesentlichen durch die Anforderungen des thermodynamischen ersten Prinzips veranlasst und geleitet wird. Anschließend werden die erhaltenen Mehrphasengleichungen auf ihr Grenzflächenverhalten untersucht. Im Gegensatz zu den meisten früheren Versuchen wird die Behandlung in dem Sinne verfeinert, dass der gesamte vektorwertige Phasenindikator anstelle seiner Zweikomponentenreduktion behandelt wird. Darüber hinaus wird auch die innere und übereinstimmende Analyse der Übergangsbereiche vollwertig durchgeführt. Jede einzelne Vorhersage der Störungsanalyse wird numerisch verifiziert, wofür die bisher gewählte Art zur Durchführung der Grenzflächenbreitenreduktionsstudien durch eine wirksame ersetzt werden musste. Es werden verschiedene Optionen für Multiwellformen sowie für Interpolationsformen der Volumenenergie und Grenzflächenmobilität untersucht, um die rechnerisch günstigste Kombination zu ermitteln. Im Falle von Implementierungen mit mehreren Hindernissen, die sich nicht für eine ebenso vollständige mathematische Analyse eignen, wird die Leistungsfähigkeit durch den Vergleich mit den Lösungen für scharfe Grenzflächen der Probleme getestet, die die individuelle Physik erfassen (deren Zusammenspiel das eigentliche kooperative Wachstumsphänomen darstellt). Auf der anderen Seite wird die langjährige Approximation planaren Erstarrungsfront, die in der scharfen Grenzflächenformulierung des stationären eutektischen Wachstumsproblems angewendet wird, d.h. die Jackson-Hunt-Analyse, ist sowohl für lamellares als auch für stabförmiges Wachstum entspannt. Im letzteren Fall wird die hexagonale Symmetrie der Verteilung der Stäbe innerhalb der Matrix genau berücksichtigt. Die Probleme, die bei der Verwendung von Softwarepaketen zur Gewinnung von Daten aus freier Energie und der Zusammensetzung aus CALPHAD-Datenbanken vermieden werden müssen, werden erörtert. Schließlich werden die Vorhersagen der diffusen und scharfen Grenzflächenbehandlung verglichen, die nach den Verfeinerungen eine bessere Übereinstimmung zeigen.

Once...

A man was extremely dissatisfied with the content he managed to generate for his thesis. He prayed to the universal Mother, the bestower of all prosperities, శ్రీమహాలక్ష్మి. A year later, the man was happy with the content he now had for his thesis.

Contents

I Introduction	1
1 Introduction and motivation	2
II Refinements in the phase-field theory of eutectic growth	6
2 Phase-field modeling of co-operative growth	7
2.1 Introduction	7
2.2 phase-field modeling of solidification in compressible pure systems	10
2.3 Generic formulation	15
2.3.1 Isothermal solidification in incompressible binary alloys	16
2.3.2 Comparative discussion with other models	19
2.3.3 Isothermal evolution of multi-phase, multi-component, rigid alloy system	20
2.3.3.1 Summation constraint	24
2.4 Binary eutectic growth model	25
3 Asymptotic analysis	28
3.1 Introduction	28
3.2 Asymptotic analysis of scalar phase-field model	31
3.2.1 Timescale $\tau = t/\epsilon^2$	32
3.2.2 Timescale $\tau = t/\epsilon$	32
3.2.3 Timescale $\tau = t$	34
3.3 Multi-phase-field asymptotic analysis of grain growth	36

3.3.1	Timescale $\tau = t/\epsilon^2$	37
3.3.2	Timescale $\tau = t/\epsilon$	40
3.3.3	Timescale $\tau = t$	43
3.3.3.1	Leading order local analysis of binary interfaces	44
3.3.3.2	Next-to-leading order local analysis of binary interfaces	48
3.3.3.3	Leading order local analysis of junctions	50
3.3.3.4	Next-to-leading order local analysis of junctions	56
4	Approaching the asymptotic limits in numerics	65
4.1	Introduction	65
4.2	Efficacious ϵ v.s. Δx relations for the numerical realization of the asymptotic limits	70
4.3	Numerical realization of the asymptotic behavior of the multi-phase-field model	76
4.3.1	Binary interface behavior in numerical simulations	77
4.3.1.1	Thin interface analysis of binary interfaces	82
4.3.2	Triple junction behavior in numerical simulations	88
5	Final considerations and eutectic growth simulations	102
5.1	Introduction	102
5.2	Multi-obstacle potential phase-field models	103
5.3	Three grain evolution	106
5.4	Isothermal, directional eutectic growth	111
5.4.1	Lamellar growth	113
5.4.1.1	Simulation setup	113
5.4.1.2	Simulation results	113
5.4.2	Rod growth	117
5.4.2.1	Simulation setup	117
5.4.2.2	Simulation results	118
5.4.3	Discussion of results	120

5.4.3.1	Accounting the huge deviation observed between the simulations and the classical JH	120
5.4.3.2	Evaluating the credibility of the modeled system properties	123
5.4.3.3	Rationalizing the residual errors	125
III Refinements in the sharp interface analysis of eutectic growth		128
6	Jackson-Hunt analysis of lamellar growth	129
6.1	Introduction	129
6.2	Sharp interface governing equations of lamellar eutectic growth	130
6.3	ZOLPA problem in stoichiometric systems	134
6.3.1	Computation of the steady state concentration field	136
6.3.2	Calculation of the steady state growth speed	138
6.3.3	Construction of the self-consistent interface shape	139
6.4	Complete solution in stoichiometric systems and applications	141
6.4.1	Relaxing the zeroth order and low Péclet number approximations	141
6.4.2	Application to NiZr-NiZr ₂ system	142
6.4.2.1	Isothermal eutectic solidification	142
6.4.2.2	Isothermal off-eutectic solidification	146
6.5	Other extensions	149
6.5.1	Modifications for directional solidification led by imposed moving temperature gradient	149
6.5.2	Non-stoichiometric systems	149
7	Jackson-Hunt analysis of rod growth	151
7.1	Introduction	151
7.2	Extension of the classical JH theory of rod growth	152
7.2.1	Incorporation of hexagonal symmetry	153
7.2.2	Incorporation of surface curvatures	156
7.2.3	Improved kinetics relation	159

IV Post-refinement comparisons	162
8 Final comparisons and discussion	163
8.1 Lamellar growth	163
8.2 Rod growth	170
V Summary and conclusion	174
9 Summary and conclusion	175
VI Appendices	179
Appendix A Appendices to chapter 2	180
A.1 Clarifications on the terminology	180
A.2 Thermodynamic consistency and generality of the framework of Ref. [18] (and [23])	181
A.2.1 Thermodynamic consistency of the grand-potential model	181
A.2.2 Thermodynamic consistency of the pure substance model	182
A.2.3 Generality of the framework	184
A.3 Generality of the framework of Ref [28] (and [27])	185
A.3.1 Adapting Wang <i>et al.</i> 's derivation: Method 1	185
A.3.2 Adapting Wang <i>et al.</i> 's derivation: Method 2	187
A.4 Further applications of the generic formulation	190
A.4.1 Non-isothermal solidification in rigid alloy systems	190
A.4.2 Solidification in incompressible pure systems	191
Appendix B Appendices to chapter 3	192
B.1 Existence, uniqueness and long time behavior	192
B.1.1 Analysis of Eq. (3.8)	192
B.1.2 Analysis of Eq. (3.12)	194
B.1.3 Analysis of Eqs. (3.26) and (3.27)	197
B.2 Derivations of the matching conditions	198

B.2.1	Single boundary layer variable	198
B.2.2	Two boundary layer variables	200
B.2.2.1	Some specific examples	200
B.2.2.2	Matching relations for the generic case	204
B.3	Analysis of the explicit solution of Eq. (3.32) for W^{FP} multi-well	209
B.3.1	Verification of the exactness	209
B.3.2	Exponential “decay”	211
B.3.3	Behavior of integrals of the kind given in Eqs. (3.44) and (3.45)	212
B.3.3.1	Bounds for the integral containing only ξ derivatives	212
B.3.3.2	Bounds for the integral containing only ζ derivatives	213
B.3.3.3	Analysis of the integral containing both ζ and ξ derivatives	216
Appendix C	Analysis of some relevant sharp interface problems	218
C.1	Sharp interface treatment of three grain evolution within the setup of Fig. 4.1	218
C.2	Sharp interface treatment of isothermal planar alloy solidification	220
Appendix D	Asymptotic analysis of multiphase binary alloy solidification model	223
D.1	Asymptotic analysis of Eqs. (2.43) and (2.44)	223
D.1.1	Outer analysis	223
D.1.2	Local analysis of binary interfaces	224
D.1.2.1	Leading order local analysis of binary interfaces	224
D.1.2.2	Next-to-leading order local analysis of binary interfaces	224
D.1.2.3	Next order local analysis of binary interfaces	225
Appendix E	Appendices to chapter 5	231
E.1	Three grain evolution	231
E.2	Single phase planar solidification	237
E.3	Cooperative growth	238
Appendix F	Appendices to chapter 6	240

F.1	Order and error estimates for the solutions of the ZOLPA problem in stoichiometric systems	240
F.1.1	Error in estimating the concentration field	240
F.1.2	Error in the estimation of the growth speed	243
F.2	Some relevant inequalities	244
F.2.1	Poincare inequality for functions in $H_*^1(\Omega_\infty)$	244
F.2.2	Trace theorem for $H_*^1(\Omega_\infty)$	245
List of Figures		xii
List of Tables		xx
Bibliography		xxiv

Part I
Introduction

Chapter 1

Introduction and motivation

These days, the principal philosophy of the phase-field methodology and the unique benefits it has to offer needs no separate introduction in materials science community. So does the success it enjoys and its current popularity. Suffice it to say that tremendous efforts by various researchers [1–26], especially over the past three-and-a-half decades, have established it as one of the most indispensable and cherished tools in the investigation of evolution dynamics of heterogeneous media. However, not all the time do the preliminary tests recommended to be performed before its deployment are steadfastly carried out.

Ideally, a thorough modeling of a given evolution process within the phase-field approach should involve the following three tasks: a) Derivation of the diffuse-interface governing equations, b) Demonstration that the sharp-interface version of the process description is indeed recovered in the vanishing limit of the diffuseness, and c) Validation of the numerical implementation by demonstrating that the employed parameter set is representative of the said limit to a decent degree.

Two quite distinct pathways are typically followed to accomplish the first of the above steps. One is regularizing the free boundaries and the associated boundary conditions in the sharp-interface formulation of the process. Of course, this readily implies that as soon as a) is carried out, b) already presents itself completed, and hence nothing more remains to be done in terms of it. However, this approach is not so popular in the materials community as compared to the second one, namely, the functional route. Where, a complete variational principle [9, 27, 28] or a partial one complemented with some additional arguments [3–5, 18] is invoked for deriving the governing equations. If this is adopted, then task b) translates to carrying out a matched asymptotic analysis on the derived modeling equations to recover the sharp-interface description, usually in parts over the course of first few orders of the perturbative analysis. Oftentimes, the governing equations are not derived from the scratch, i.e. directly from the functional,

but by intelligently modifying or expanding the ones so obtained for a different (often simpler) problem and preferably which are ensured to have passed the criterion of b). This is not to mean that the so constructed equations will readily recover the sharp-interface description of the dynamical process that they are intended to model. The manipulation of the modeling equations, however intelligent it may be, must always be substantiated by re-performing the asymptotic analysis, or justifying that the older one carries over, when it actually does so. Finally, sometimes the manipulation is done during the stage of the perturbative analysis itself, for example, precisely for the sake of retrieving the exact sharp-interface problem demanded in b) [13, 14] or to make the rate of its recovery faster [14, 15]. No matter at what step they are proposed, post such modifications, it might or might not be possible to place back the resultant equations in a variational scheme, i.e., derive from a monotonicity demand (partial or complete) on a functional; sometimes, even the fundamental meaning assigned to the phase-indicator might not continue to hold [17, 24, 25]. Hence, the term functional approach is only loosely used here, but the important message is that, if all one is interested in is to produce a diffuse counterpart for a given sharp-interface problem, then the details of step a) can altogether be ignored whereas step b) is indispensable. However, in the current thesis, thermodynamic consistency and generality of the model development is also of interest. Hence, due efforts will also be directed towards task a).

Coming to step c), it is usually shown by solving a benchmark problem and comparing the results. Typically, a benchmark case corresponds to the same evolution process but considered for simpler geometries or for specific temporal ranges for instance corresponding to the long time behavior, or, when it applies, the steady state behavior. The reason for studying a simpler case has nothing to do with the developed phase-field model but entirely with either the incapability of the sharp-interface equations to handle a more complicated situation or our inability to solve them when they can. Owing to the latter, sometimes, the best possible benchmarking may still fall short by an appreciable amount in establishing the validity of the implementation. To give an example, a process may exist which is an outcome of an interplay of various component physics which, at best, can only be studied in isolation from their sharp-interface formulation. More concretely, if the actual dynamical process were to be dictated by the combined effects of mass redistribution and heat flow whereas the sharp-interface governing equations capturing it cannot be solved at such generality, then two separate problems, each involving only one of the transport mechanisms freely operating and the other one overridden by an imposed condition, are only solved for benchmarking. Quite evidently, this is not a full-fledged validation, as a parameter set that can satisfactorily capture the individual components' physics need not necessarily do so for the combined effect. Strictly speaking, even when the exact case of interest in all its detail can be analyzed in the sharp-interface treat-

ment and the phase-field results are also seen to compare well, it still does not imply the accomplishment of c). This is because, the ‘passing to the limit’ detail still remains unaddressed. The solution to all this is to perform multiple simulations connected to each other by a decrease in the diffuseness of the interfacial region and compare the results for their convergence*.

In fact, there is a nice dichotomy here involving b): If b) were to be ensured, then the interface width reduction studies alone will suffice to establish c) even in the absence of any kind of benchmark solution, of course, with the term convergence understood in the Cauchy-sense. On the other hand, when a rich-enough benchmark solution is present, then showing that the interface width reduction results converge to it obviates the necessity of task b). Note that performing the required matched asymptotic analysis or obtaining a rich enough or representative benchmark solution could both be highly formidable tasks. Hence, it is a very welcome situation if one of them can be avoided by a mere flip of the type of the convergence inspected. On the whole, the gist of the argument is that the details of step a) can very well be ignored, it might even be possible to skip step b) sometimes, but to claim that a thorough (quantitative) diffuse-interface modeling has been carried out, performing task c) is unavoidable.

In the case of multi-component multi-phase diffuse interface models of solidification and microstructure evolution, the simplest yet representative enough benchmark case is directional co-operative growth of binary alloys forming regular morphologies—lamellar eutectic growth, for example. Anything simpler can very well be modeled using less sophisticated models and hence will not serve as a rich enough benchmark problem. For example, if junctions (common meeting points of three or more bulks) are absent, then single phase-field-variable models, in principle, can handle the situation, and, if mass transport were to be absent, simple multi-phase models will suffice. On the other hand, increasing the order of the junction or the number of evolving chemical species will still be representative but becomes redundantly complicated. Also, binary eutectic growth facilitates a wide choice of sub-cases starting from symmetry among all the three involved phases to complete dissimilarity while all along the way supporting a steady state behavior. This tremendously reduces the effort involved in collecting and comparing the results as the time variable is effectively eliminated from the later stages of the dynamics. The sharp-interface treatment of this steady-state problem is well studied and popular called the Jackson-Hunt (JH) analysis, first advanced in 1966 [29]. However, in this pioneering work, a lot of approximations are invoked to simplify the mathematical treatment. Though most of them are rectified over the intervening years, some still persisted; an example would be the assumption that the solidification front can be considered to be

*Of course, after ensuring that the mathematical and the numerical errors arising from the discretization choices are inconsequential.

planar in shape while estimating the solute distribution within the melt.

That means, here is a diffuse-interface idea adoption, namely the multi-component multi-phase-field models, which are extensively deployed to study a wide range of phenomena but without a proper sharp-interface solution to validate them. Of course, as mentioned above, this route of validation is not necessary as long as it is shown that the interface width reduction studies (Cauchy) converge and also that the governing laws making up the sharp-interface problem can all be recovered in the asymptotic limit of the models. However, research works presenting the former are very rare, if not non-existent, and, except for two treatments [30, 31], the latter is never performed in a full-fledged manner. Typically, only a single instance of interface width is simulated and the deviations found when comparing with the JH theory results are ascribed to the approximations invoked in the latter. To justify that the employed thickness is close enough to the limiting value, most of the works rely on previous demonstrations involving scalar phase-field variable models. However, this clearly is not sufficient, as the demands on the diffuseness by the junction neighborhoods can be more stringent. A similar state of affairs exists in regard to the step of the matched asymptotic analysis. Commonly, the analysis pertaining to the junction localities is not performed and the binary interfaces are studied only in isolation after reducing the multi-phase-field modeling equations to two-phase ones (which essentially are the same as scalar ones, as summation property is typically ensured). Moreover, even before getting into any of these concerns, the derivation of the governing equations itself feels more contrived than natural, most of the times.

In short, though a number of multi-component multi-phase-field models already exist, all of them lack in some or the other detail involved in the tasks a), b) and c), and leave a lot of scope for refinement or improvement. The subject matter of the dissertation is to perform afresh the quantitative modeling of eutectic growth by pointing out the shortcomings of the earlier treatments at each step and making sure that they are avoided to the extent possible. The exact details of the shortcomings in the contemporary models, the limitations caused by them, and the need or urgency for their rectification are provided in the introductions of the individual chapters where the refinements are carried out. This forms the next part, i.e., part II of the thesis. For proper validation, an indisputable benchmark solution is mandatory especially in the absence of asymptotics, hence, the remaining approximations that are still lingering in the Jackson-Hunt analysis are also relaxed which constitutes part III. Comparison of the diffuse and sharp interface treatments' predictions, post their refinements, is carried out in part IV and Part V summarizes the thesis. The intermediate or side results and derivations, although sometimes very central for establishing the validity of the arguments pursued in the main chapters, are still relegated to part VI, the appendices, to avoid obstruction to the flow of the exposition.

Part II

Refinements in the phase-field analysis of eutectic growth

Chapter 2

Phase-field modeling of co-operative growth

2.1 Introduction

A number of phase-field models have been constructed over the years to capture the physics governing the phenomenon of cooperative growth. The wide range of morphologies this growth mechanism is famously known to give rise to are all satisfactorily reproduced by these models [32–46]. Even applications to real systems by coupling with CALPHAD databases etc. have been carried out [47–50], and, instances reporting a good comparison of the recovered quantitative results with the theoretical and experimental findings do exist [48]. At this juncture, it seems doubtful if a new model can make any appreciable improvements over what is already achieved and raises the question of if it is even necessary. Indeed, the refined formulation to be presented does not lead to modeling equations that are radically different from those of the most successful of the existing multi-phase, multi-component models, but only spruces up the way they are developed.

The initial eutectic growth models are all similar in that they are extensions of WBM's isothermal single phase alloy solidification formulation [9] to multi-phase and possibly multi-component and non-isothermal systems. The key aspect of this model which later turned out to be responsible for a very limiting drawback is the treatment of the extensive quantity as the independent variable followed by the interpolation of the bulk thermodynamic potentials expressed in terms of it. Though often it is claimed that the interfacial energy getting coupled to bulk energy term is the said drawback, in actuality, this isn't by itself a big concern as the targeted free boundary problem is anyway recovered with the right surface tension entering into the Gibbs-Thomson condition. What is actually a shortcoming of the WBM model is that its choice of the independent variable and the

interpolation which leads to such a coupling puts up severe hurdles in the performance of a thin interface analysis which would otherwise tremendously reduce the computational demands especially if the system of interest has vanishing kinetic co-efficient.

Two alternative formulations have been suggested to overcome this. One is what is later came to be known as Kim-Kim-Suzuki's two-phase model [17] which is not a variational approach and the other which is is the grand-potential formulation put forth by Plapp [18] and independently by Choudhury and Nestler [23]. In the current thesis, only the variational or, to borrow the terminology introduced in Ref. [18], the coarse-graining approach is of interest. In these latter formulations, the starting point is a grand-potential functional as opposed to free energy employed by WBM and the interpolation is performed by expressing volumetric grand potential densities in terms of chemical potential. That is, instead of composition, the intensive quantity conjugate to it is preferred. Although this new approach very well eliminates all the drawbacks of the WBM model, relevant or otherwise, it subtracts significantly from the latter's simplicity and thermodynamic appeal.

While the WBM derivation straightforwardly demands free energy reduction or negative local free energy production rate for setting up the governing equations, the grand-potential formulation takes a different route. Where, a similar stipulation is indeed invoked, albeit selectively with regard to the phase indicator and an entirely different argument is pursued for deriving the evolution equation of the chemical potential field. Now it is well known from the laws of thermodynamics that in rigid systems, an isothermal irreversible process has to be necessarily associated with a negative production rate of the Helmholtz free energy in each locality due to internal changes while such a behavior is not generically required on the part of the grand-potential. If anything, the counterpart statement for grand-potential calls for its dissipation in those spontaneous processes where the system is isothermal, non-reactive and has constant chemical potential. In contrast, in problems to which the grand potential model is typically applied to, the chemical potential is far from being constant and in fact, prescription for its evolution is itself one of the governing equations constituting the model. Therefore, it is clear that the grand-potential reduction should not be the motivating argument for deriving the modeling equations. Of course, neither did Ref. [18] suggest that it is in their derivation, nor did it claim that it is one of the consequences*. In fact, the governing equations do ensure a negative production rate of Helmholtz free energy which should indeed hold true for isothermal processes in rigid systems (appendix A.2.1). However, the complaint is that it is unknown what physical principle its argumentation does actually spring forth from. The origin of its two step algorithm of a) dissipation with regard to phase indicator

*Surprisingly, this is not the case with many of its later adaptations. It is common to find many works employing this formulation claim that the governing equations minimize the grand-potential functional.

field and b) Fick's law connection for deriving chemical potential field evolution seems not to be rooted in any of the thermodynamical first principles.

It is worth noting that in the initial days of phase-field modeling of solidification where pure substance case is mainly looked at, a similar derivation is popularized. However, in the years to follow, calling this algorithm ad-hoc, Penrose and Fife [27] and later Wang *et al.* [28] proposed an alternate development which is completely consistent with and motivated from the thermodynamical stipulations. An alloy solidification model along the lines of this derivation, although contemplated briefly in Ref. [18], has never been explicitly attempted. When done, it will not be long before one comes to the realization that there are multiple ways of interpreting the method presented by Wang *et al.* and hence two different extensions are possible. However, only one of them recovers the advantageous bulk and interface decoupled governing equations, that too, in some special systems (appendix A.3); therefore, further clarifications about the methodology have to be supplied for generalizing the formulation. Such problems related to unifying the treatment also find place in the derivations of Refs. [18] and [23] as they cease to decouple bulk and interface properties when expanded to include non-isothermal processes (appendix A.2).

At this juncture, yet another model originally proposed for investigating eutectic growth by Folch and Plapp [22] is worth mentioning. It resembles WBM to the extent that the concentration is the independent variable and free energy minimization is demanded for obtaining the governing equations. In spite of this, surprisingly, the decoupling is recovered owing to an interesting way of interpolating the bulk free energies. In fact, the recovered equations merge with those of the grand-potential model. Unfortunately, only certain special kind of free energy versus concentration curves can be handled with this approach for example parabolae with same sharpnesses for both the solid and the liquid phases. That is, even this method falls short in the most generic case.

Overall, a formulation which facilitates a separate control of bulk and interfacial properties, and which is unified and thermodynamically motivated is so far unavailable. In view of this, a modified framework is presented which invokes simple initial hypotheses and the rest of the development is completely prompted by the thermodynamic requirements at each stage. It is sure to produce decoupled equations and can handle any number of phases and generalized thermodynamic force or flux fields. For the most part, the selection of the basic hypotheses itself has some thermodynamically motivated reasons behind it. Hence, a derivation demonstrating its parallel development alongside the eventual governing equations is first presented by choosing, for expository reasons, the case of solidification in pure, compressible systems. The main ideas that form the crux of the derivation are then collected together to set forth the generic formulation.

2.2 phase-field modeling of solidification in compressible pure systems

The primary hypothesis of the formulation is that the entropy density of the interfacial region is obtained by interpolating the bulk values corresponding to the same temperature T and chemical potential μ as that of the interface. That is, interpolating the bulk quantities when expressed as functions of “intensive” thermodynamic variables as opposed to “extensive” ones (please refer to appendix A.1 for a clarification about the special sense in which these terms are used). Hence, the entropy density is written as

$$s(T, \mu, \phi) = s_s(T, \mu) \mathbf{g}_s(\phi) + s_l(T, \mu) \mathbf{g}_l(\phi) \quad (2.1)$$

where ϕ is the phase-field variable denoting solid and liquid phases when $\phi = 1$ and $\phi = 0$, respectively; s_s and s_l are the volumetric entropy densities of the solid and liquid phases, respectively; $\mathbf{g}_s(\phi)$ and $\mathbf{g}_l(\phi)$ are the interpolating functions satisfying $\mathbf{g}_s(0) = 0$, $\mathbf{g}_s(1) = 1$ and $\mathbf{g}_l(\phi) = 1 - \mathbf{g}_s(\phi)$.

However, the above form lacks some of the information which is necessary for predicting state changes since only the fundamental relation, i.e., entropy expressed in terms of extensive variables carries all the necessary and sufficient content [51]. Hence, its dependence on internal energy density e and the number density ρ is needed. This can also be obtained if these latter quantities are themselves known in terms of the intensive variables, i.e., $e(T, \mu, \phi)$ and $\rho(T, \mu, \phi)$. However, at this point it is unknown how they are interpolated between the bulk values; there is no a priori reason to choose the same interpolation function as used for entropy density. Hence, we assume different ones as follows.

$$e(T, \mu, \phi) = e_s(T, \mu) \mathbf{f}_s(\phi) + e_l(T, \mu) \mathbf{f}_l(\phi), \quad (2.2)$$

$$\rho(T, \mu, \phi) = \rho_s(T, \mu) \mathbf{h}_s(\phi) + \rho_l(T, \mu) \mathbf{h}_l(\phi). \quad (2.3)$$

To establish the relationship between the functions \mathbf{f}_s , \mathbf{g}_s and \mathbf{h}_s , we demand that some of the relations satisfied by the bulk thermodynamic functions are also fulfilled irrespective of the value of ϕ . For instance, the partial derivative of entropy density with respect to energy density at constant number density is the inverse temperature. While this will necessarily be true individually for solid and liquid phases, it is unclear what happens when they are made ϕ dependent as in Eqs. (2.1), (2.2) and (2.3). This will be analyzed in the following.

From Eqs. (2.2) and (2.3), T and μ can be expressed in terms of e and ρ . i.e.,

$$T = T(e, \rho, \phi), \quad \mu = \mu(e, \rho, \phi). \quad (2.4)$$

Similarly, from $e_s(T, \mu)$ and $\rho_s(T, \mu)$, they can be written in terms of e_s and ρ_s as

$$T = T(e_s, \rho_s), \quad \mu = \mu(e_s, \rho_s). \quad (2.5)$$

Likewise,

$$T = T(e_l, \rho_l), \quad \mu = \mu(e_l, \rho_l) \quad (2.6)$$

can be constructed from $e_l(T, \mu)$ and $\rho_l(T, \mu)$. Substituting the T and μ of Eqs. (2.4), (2.5) and (2.6) in $s(T, \mu, \phi)$, $s_s(T, \mu)$ and $s_l(T, \mu)$ of Eq. (2.1), respectively, gives

$$s(T(e, \rho, \phi), \mu(e, \rho, \phi), \phi) = s_s(T(e_s, \rho_s), \mu(e_s, \rho_s)) \mathbf{g}_s(\phi) + s_l(T(e_l, \rho_l), \mu(e_l, \rho_l)) \mathbf{g}_l(\phi). \quad (2.7)$$

To keep the notation to a minimum, the same symbols are used for before and after the substitution. Hence, we have

$$s(e, \rho, \phi) = s_s(e_s, \rho_s) \mathbf{g}_s(\phi) + s_l(e_l, \rho_l) \mathbf{g}_l(\phi). \quad (2.8)$$

When $\phi = 1$, we will have $e = e_s$, $\rho = \rho_s$ and $s(e, \rho, \phi) = s_s(e_s, \rho_s)$; therefore, $\left. \frac{\partial s}{\partial e} \right|_{\rho, \phi=1} = \left. \frac{\partial s_s}{\partial e_s} \right|_{\rho_s} = \frac{1}{T_s}$ where T_s is the temperature of the solid phase as a function of energy and number densities. Similarly, $\left. \frac{\partial s}{\partial e} \right|_{\rho, \phi=0} = \left. \frac{\partial s_l}{\partial e_l} \right|_{\rho_l} = \frac{1}{T_l}$. However, for a general ϕ ,

$$\begin{aligned} \left. \frac{\partial s}{\partial e} \right|_{\rho, \phi} &= \left. \frac{\partial s_s}{\partial e_s} \frac{\partial e_s}{\partial e} \right|_{\rho, \phi} \mathbf{g}_s(\phi) + \left. \frac{\partial s_l}{\partial e_l} \frac{\partial e_l}{\partial e} \right|_{\rho, \phi} \mathbf{g}_l(\phi) \\ &\quad + \left. \frac{\partial s_s}{\partial \rho_s} \frac{\partial \rho_s}{\partial \rho} \right|_{\rho, \phi} \mathbf{g}_s(\phi) + \left. \frac{\partial s_l}{\partial \rho_l} \frac{\partial \rho_l}{\partial \rho} \right|_{\rho, \phi} \mathbf{g}_l(\phi) \\ &= \frac{1}{T_s(e_s, \rho_s)} \left. \frac{\partial e_s}{\partial e} \right|_{\rho, \phi} \mathbf{g}_s(\phi) + \frac{1}{T_l(e_l, \rho_l)} \left. \frac{\partial e_l}{\partial e} \right|_{\rho, \phi} \mathbf{g}_l(\phi) \\ &\quad + \frac{-\mu_s(e_s, \rho_s)}{T_s(e_s, \rho_s)} \left. \frac{\partial \rho_s}{\partial \rho} \right|_{\rho, \phi} \mathbf{g}_s(\phi) + \frac{-\mu_l(e_l, \rho_l)}{T_l(e_l, \rho_l)} \left. \frac{\partial \rho_l}{\partial \rho} \right|_{\rho, \phi} \mathbf{g}_l(\phi). \end{aligned} \quad (2.9)$$

A most important observation is now made which is single handedly responsible for the working of the derivation: in general, the functions $T_s : \mathbb{R}^2 \rightarrow \mathbb{R}$ and $T_l : \mathbb{R}^2 \rightarrow \mathbb{R}$ in Eq. (2.9) could be entirely different, however, since their arguments (e_s, ρ_s) and (e_l, ρ_l) correspond to the same T and μ as does the coordinate (e, ρ, ϕ) at which the above derivative is being evaluated, they take up identical numerical values. That is, $T_s(e_s, \rho_s)$ and $T_l(e_l, \rho_l)$ in Eq. (2.9) evaluate to T and similarly $\mu_s(e_s, \rho_s)$ and $\mu_l(e_l, \rho_l)$ have the same numerical value as that of μ . Hence Eq. (2.9) simplifies to

$$\left. \frac{\partial s}{\partial e} \right|_{\rho, \phi} = \frac{1}{T} \left(\left. \frac{\partial e_s}{\partial e} \right|_{\rho, \phi} \mathbf{g}_s(\phi) + \left. \frac{\partial e_l}{\partial e} \right|_{\rho, \phi} \mathbf{g}_l(\phi) \right) - \frac{\mu}{T} \left(\left. \frac{\partial \rho_s}{\partial e} \right|_{\rho, \phi} \mathbf{g}_s(\phi) + \left. \frac{\partial \rho_l}{\partial e} \right|_{\rho, \phi} \mathbf{g}_l(\phi) \right). \quad (2.10)$$

Now, if the first bracket turns out to be unity and the second one vanishes in the above equation, then we will have made an identity that is normally valid for the stable solid and liquid states to hold even for the intermediate ones, i.e., $0 < \phi < 1$. However, on substituting Eq. (2.4) in Eqs. (2.2) and (2.3), and partially differentiating the resultant equations with respect to e yields

$$\begin{aligned}\left.\frac{\partial e}{\partial e}\right|_{\rho,\phi} &= \frac{\partial}{\partial e} e_s(T(e, \rho, \phi), \mu(e, \rho, \phi)) \mathfrak{f}_s(\phi) + \frac{\partial}{\partial e} e_l(T(e, \rho, \phi), \mu(e, \rho, \phi)) \mathfrak{f}_l(\phi), \\ \left.\frac{\partial \rho}{\partial e}\right|_{\rho,\phi} &= \frac{\partial}{\partial e} \rho_s(T(e, \rho, \phi), \mu(e, \rho, \phi)) \mathfrak{h}_s(\phi) + \frac{\partial}{\partial e} \rho_l(T(e, \rho, \phi), \mu(e, \rho, \phi)) \mathfrak{h}_l(\phi).\end{aligned}$$

\Rightarrow

$$\begin{aligned}1 &= \left.\frac{\partial e_s}{\partial e}\right|_{\rho,\phi} \mathfrak{f}_s(\phi) + \left.\frac{\partial e_l}{\partial e}\right|_{\rho,\phi} \mathfrak{f}_l(\phi), \\ 0 &= \left.\frac{\partial \rho_s}{\partial e}\right|_{\rho,\phi} \mathfrak{h}_s(\phi) + \left.\frac{\partial \rho_l}{\partial e}\right|_{\rho,\phi} \mathfrak{h}_l(\phi).\end{aligned}$$

Thus, to have the desired relation, that is,

$$\left.\frac{\partial s}{\partial e}\right|_{\rho,\phi} = \frac{1}{T}, \quad (2.11)$$

\mathfrak{f}_s and \mathfrak{h}_s should both be identical to \mathfrak{g}_s . This additionally ensures that the other thermodynamic identity, as well, is carried over to the ϕ dependent formulation, i.e.,

$$\left.\frac{\partial s}{\partial \rho}\right|_{e,\phi} = -\frac{\mu}{T}. \quad (2.12)$$

In this manner, even though (generically) different interpolating forms are assumed for the various involved quantities at the outset, it is eventually retrieved that they all have to be identical. Due to this simplification, partially differentiating Eq. (2.8) with respect to the phase indicator at constant e and ρ results in

$$\begin{aligned}\left.\frac{\partial s}{\partial \phi}\right|_{e,\rho} &= -\frac{1}{T} (e_s - e_l) \mathfrak{g}'_s(\phi) + \frac{\mu}{T} (\rho_s - \rho_l) \mathfrak{g}'_s(\phi) + (s_s - s_l) \mathfrak{g}'_s(\phi) \\ &= -\frac{1}{T} (\omega_s - \omega_l) \mathfrak{g}'_s(\phi)\end{aligned} \quad (2.13)$$

where ω_s and ω_l are the grand potential densities of the solid and liquid phases, respectively. We now cater to the relatively high stability of solid and liquid states by adding an extra term to Eq. (2.1) that depresses the entropy of the intermediate states. Therefore, the final entropy density is

$$s = s_s(T, \mu) \mathfrak{g}_s(\phi) + s_l(T, \mu) \mathfrak{g}_l(\phi) - s_{\text{dw}}(\phi) \quad (2.14)$$

where $s_{\text{dw}}(\phi)$ is a typical double well function. Note that, it is very important for the “excess” term $s_{\text{dw}}(\phi)$ to be independent of T and μ , since otherwise, the required forms of the relations Eqs. (2.11) and (2.12) will be disturbed. On the other hand, if this specific form of the new term is utilized, the Eqs. (2.11) and (2.12) are unaffected while Eq. (2.13) is modified to

$$\left. \frac{\partial s}{\partial \phi} \right|_{e,\rho} = -\frac{1}{T} ((\omega_s - \omega_l) \mathbf{g}'_s(\phi) + T s'_{\text{dw}}(\phi)). \quad (2.15)$$

With the help of the relations derived so far, the governing equations for solidification can be obtained from the following entropy functional by demanding positive entropy production in each subvolume. The form of the functional we choose is

$$S = \int s_{\text{S}}(T, \mu, \phi, \nabla \phi) dV := \int \left(s(T, \mu, \phi) - \frac{s_{\text{G}}}{2} (\nabla \phi)^2 \right) dV \quad (2.16)$$

where S is the entropy of the sub-region considered, $s(T, \mu, \phi)$ is the expression of Eq. (2.14) and $\frac{s_{\text{G}}}{2} (\nabla \phi)^2$ marks the entropy deficit in a local region due to phase heterogeneity. Taking the time derivative of the above functional yields

$$\begin{aligned} \frac{dS}{dt} = \int \left(\left. \frac{\partial s(T, \mu, \phi)}{\partial e} \right|_{\rho, \phi} \frac{\partial e}{\partial t} + \left. \frac{\partial s(T, \mu, \phi)}{\partial \rho} \right|_{e, \phi} \frac{\partial \rho}{\partial t} + \frac{\delta S}{\delta \phi} \frac{\partial \phi}{\partial t} \right) dV \\ - \int s_{\text{G}} \frac{\partial \phi}{\partial t} \nabla \phi \cdot \vec{n} dA \end{aligned} \quad (2.17)$$

where the domain of integration is the interior of the subvolume in the first integral and its boundary in the second with \vec{n} being the unit outward normal at each point of the boundary. Owing to Eqs. (2.11) and (2.12), Eq. (2.17) simplifies to

$$\begin{aligned} \frac{dS}{dt} = \int \left(\frac{1}{T} \frac{\partial e}{\partial t} - \frac{\mu}{T} \frac{\partial \rho}{\partial t} + \frac{\delta S}{\delta \phi} \frac{\partial \phi}{\partial t} \right) dV \\ - \int s_{\text{G}} \frac{\partial \phi}{\partial t} \nabla \phi \cdot \vec{n} dA. \end{aligned} \quad (2.18)$$

The positivity of the production rate can be ensured by choosing $\partial e/\partial t$, $\partial \rho/\partial t$ and $\partial \phi/\partial t$ in a manner that is typical of the phase-field approach and that is consistent with the standard mass and energy balance equations in the bulks [27]. That is:

$$\frac{\partial \phi}{\partial t} = M_{\phi} \frac{\partial S}{\partial \phi} = M_{\phi} \left[\frac{1}{T} (\omega_l - \omega_s) \mathbf{g}'_s(\phi) - s'_{\text{dw}}(\phi) + s_{\text{G}} (\nabla^2 \phi) \right], \quad (2.19)$$

$$\frac{\partial \rho}{\partial t} = \nabla \cdot M_{\rho} \nabla (\mu/T), \quad (2.20)$$

$$\frac{\partial e}{\partial t} = -\nabla \cdot (M_T T^2 \nabla (1/T)) = \nabla \cdot (M_T \nabla T). \quad (2.21)$$

Where the cross terms corresponding to the off-diagonal elements of the Onsager matrix are not considered in Eqs. (2.20) and (2.21). Substituting Eqs. (2.19), (2.20) and (2.21) in Eq. (2.18) gives, after some manipulation,

$$\begin{aligned} \frac{dS}{dt} = & \int \left(M_T T^2 (\nabla(1/T))^2 + M_\rho (\nabla(\mu/T))^2 + M_\phi \left(\frac{\delta S}{\delta \phi} \right)^2 \right) dV \\ & - \int \left(\frac{1}{T} M_T T^2 \nabla \left(\frac{1}{T} \right) + \frac{\mu}{T} M_\rho \nabla \left(\frac{\mu}{T} \right) + s_G \frac{\partial \phi}{\partial t} \nabla \phi \right) \cdot \vec{n} dA. \end{aligned} \quad (2.22)$$

The first integral corresponds to the entropy production and is necessarily positive in the current choice of the governing equations as is required by the thermodynamics law. Thus the necessary condition is ensured to be satisfied; for sufficiency, the same has to be shown for the surroundings, however, it is usually assumed to be true without additional analysis. Eq. (2.21) can be re-expressed as

$$\begin{aligned} \frac{\partial e}{\partial t} = & \frac{\partial e}{\partial T} \Big|_{\rho, \phi} \frac{\partial T}{\partial t} + \frac{\partial e}{\partial \rho} \Big|_{T, \phi} \frac{\partial \rho}{\partial t} + \frac{\partial e}{\partial \phi} \Big|_{T, \rho} \frac{\partial \phi}{\partial t} = \nabla \cdot (M_T \nabla T) \\ \implies \frac{\partial T}{\partial t} = & \frac{\partial e}{\partial T} \Big|_{\rho, \phi}^{-1} \left(\nabla \cdot (M_T \nabla T) - \frac{\partial e}{\partial \rho} \Big|_{T, \phi} \frac{\partial \rho}{\partial t} - \frac{\partial e}{\partial \phi} \Big|_{T, \rho} \frac{\partial \phi}{\partial t} \right). \end{aligned} \quad (2.23)$$

Thus, Eqs. (2.19), (2.20) and (2.23) model the solidification of pure compressible systems within the diffuse interface approach which additionally facilitate a separate manipulation of bulk and interface properties. Since the independent variables in the above set of equations are the temperature, number density and the phase-field parameter, the chemical potential μ on the r.h.s of Eq. (2.20) has to be expressed in terms of them with the help of Eq. (2.3). Alternatively, instead of making such inversions, Eqs. (2.20) and (2.21) can be re-expressed in terms of the intensive variables giving rise to evolution equations for T and μ in terms of themselves and the phase indicator.

In this manner, the governing equations are managed to be derived almost solely from the promptings of the thermodynamical principles. The most striking feature of the derivation though, is the fact that even though entropy functional is chosen as the starting point, grand-potential densities naturally enter into the governing equation for the evolution of the phase-field variable. The potentiality of this detail can be realized by recalling that the only major difference between the governing equations of the WBM model and the grand-potential model is that the (Helmholtz) free energy density differences appear as the driving force term in the evolution equation of the phase-field variable in the former whereas their place is taken by the grand-potential densities in the latter. This small difference, however, was all that was sufficient to give the grand-potential model its superiority. However, this came at the cost of compromising on the thermodynamical connection of the model derivation since the starting point had to be changed

to the grand-potential functional. In contrast, in the above method of deriving things, densities of a different thermodynamic potential than the one considered for the starting point functional can very well arise in the governing equations. Hence, this gives a hope that even by starting from the free energy functional and thus staying close to thermodynamical considerations, one may still recover the advantageous decoupled equations that the grand-potential model is famous for.

However, instead of re-doing the calculations for the isothermal alloy solidification case right away, a generic framework is first fashioned by gathering together, in their most generic form, the key ideas that went into the above derivation. The case of isothermal alloy solidification is then studied as a special application of the general formulation.

2.3 Generic formulation

On a closer observation, one finds that there are three important ingredients in the above derivation. These will form the starting hypotheses of the generic formulation. They are

- (H_1) The extensive quantities are interpolated when expressed in terms of the intensive variables.
- (H_2) The “excess” and gradient contributions are implemented in entropy and not in any other extensive variable appearing in the fundamental relation. Further, these terms should be independent of the intensive variables.
- (H_3) The thermodynamic identities that are valid for bulk states also hold true for the intermediate ones.

Once these are ensured, the governing equations facilitating independent control of bulk and interfacial properties fall out readily by the application of the principle of ‘positive entropy production due to internal changes in each subvolume of the space hosting the irreversible process’.

The above recipe will now be employed to model some specific processes, but before that, we point out a ready consequence of the above hypotheses. Which is, as seen in section 2.2, even when one starts off quite generically by assuming different interpolation functions for different quantities, the above impositions naturally recover that they have to be identical. Conversely, this sameness can be realized to be equivalent to hypothesis H_3 and hence can replace it, i.e., if all the interpolations are already chosen alike, then the requirement of H_3 is automatically fulfilled. For future purposes, this equivalent of H_3 will now be explicitly stated.

(H'_3) The forms of the interpolating functions are the same for all the extensive quantities.

Next some applications of the generic formulation are considered.

2.3.1 Isothermal solidification in incompressible binary alloys

Solidification is associated with the release of latent heat. Therefore, if the system is initially undercooled, then as the new solid layers form from the melt, locally there will be a rise in the temperature at the solidification front. Hence, in order to maintain isothermality throughout the system, it is indispensable to employ an external sink. However, this means that in any subvolume where freezing is taking place, the system and the sink are simultaneously operating and as a result, the combined entropy production rate has to be positive not just that of the system. Therefore, the entropy functional of the combination has to be worked with. Instead of doing this, it will be assumed that the sink is a temperature reservoir with a temperature same as that intended to be imposed in the system. As a result, the Helmholtz free energy of the system alone can be looked at owing to it being rigid. This is because, in isothermal irreversible processes in incompressible systems, the negative production rate of Helmholtz free energy of the system is equivalent to the positive entropy production of both the system and the reservoir. Thus, to model isothermal solidification in incompressible alloys, the starting point would be the free energy functional chosen below.

$$F = \int f_{\neq}(\mu, \phi, \nabla\phi) dV := \int \left(f(\mu, \phi) + \frac{f_G}{2} (\nabla\phi)^2 \right) dV \quad (2.24)$$

where the ϕ dependent free energy density $f(\mu, \phi)$ is obtained by interpolating the bulk energies and entropies when expressed in terms of the chemical potential rather than concentration as per the hypothesis H_1 . That is,

$$\begin{aligned} f(\mu, \phi) &= e(\mu, \phi) - Ts(\mu, \phi) \\ &= e_s(\mu)\mathbf{q}_s(\phi) + e_l(\mu)\mathbf{q}_l(\phi) - T(s_s(\mu)\mathbf{q}_s(\phi) + s_l(\mu)\mathbf{q}_l(\phi) - s_{\text{dw}}(\phi)) \\ &= (e_s(\mu) - Ts_s(\mu))\mathbf{q}_s(\phi) + (e_l(\mu) - Ts_l(\mu))\mathbf{q}_l(\phi) + Ts_{\text{dw}}(\phi) \\ &= f_s(\mu)\mathbf{q}_s(\phi) + f_l(\mu)\mathbf{q}_l(\phi) + Ts_{\text{dw}}(\phi). \end{aligned} \quad (2.25)$$

where, f_s and f_l are the Helmholtz free energy densities of the solid and liquid phases, respectively. Notice that the intermediate states penalizing term is only present in $s(\mu, \phi)$ and not in $e(\mu, \phi)$ consistent with H_2 . Also, the above calculation implies that the free energy excess f_{dw} associated with the intermediate state (T, μ, ϕ) is identically $Ts_{\text{dw}}(\phi)$. Similarly, by considering the special case of systems with vanishing latent heats, the free energy gradient coefficient f_G can be realized to be equal to Ts_G .

Next, H_1 also proposes that the concentration has to be interpolated expressed in terms of μ , moreover, as per H'_3 , the interpolating function should be the same as the one used for f . That is,

$$c(\mu) = c_s(\mu)\mathbf{g}_s(\phi) + c_l(\mu)\mathbf{g}_l(\phi). \quad (2.26)$$

Now, following the recipe of section 2.2, μ is expressed in terms of c_s , c_l and (c, ϕ) using $c_s = c_s(\mu)$, $c_l = c_l(\mu)$ and (2.26), respectively. Substituting these at appropriate places of Eq. (2.25) similar to that in Eq. (2.7) yields

$$\begin{aligned} f(\mu(c, \phi), \phi) &= f_s(\mu(c_s))\mathbf{g}_s(\phi) + f_l(\mu(c_l))\mathbf{g}_l(\phi) + f_{\text{dw}}(\phi) \\ \implies f(c, \phi) &= f_s(c_s)\mathbf{g}_s(\phi) + f_l(c_l)\mathbf{g}_l(\phi) + f_{\text{dw}}(\phi), \end{aligned} \quad (2.27)$$

$$\text{i.e., } f(c(\mu), \phi) = f_s(c_s(\mu))\mathbf{g}_s(\phi) + f_l(c_l(\mu))\mathbf{g}_l(\phi) + f_{\text{dw}}(\phi). \quad (2.28)$$

Where, to keep the notation to a minimum, same symbols are used for before and after the substitution. Partially differentiating the above with respect to c at constant ϕ yields

$$\begin{aligned} \left. \frac{\partial f}{\partial c} \right|_{\phi} &= \left. \frac{df_s}{dc_s} \frac{\partial c_s}{\partial c} \right|_{\phi} \mathbf{g}_s(\phi) + \left. \frac{df_l}{dc_l} \frac{\partial c_l}{\partial c} \right|_{\phi} \mathbf{g}_l(\phi) \\ &= \rho\mu_s(c_s(\mu)) \left. \frac{\partial c_s}{\partial c} \right|_{\phi} \mathbf{g}_s(\phi) + \rho\mu_l(c_l(\mu)) \left. \frac{\partial c_l}{\partial c} \right|_{\phi} \mathbf{g}_l(\phi) \end{aligned} \quad (2.29)$$

$$= \rho\mu \left(\left. \frac{\partial c_s}{\partial c} \right|_{\phi} \mathbf{g}_s(\phi) + \left. \frac{\partial c_l}{\partial c} \right|_{\phi} \mathbf{g}_l(\phi) \right). \quad (2.30)$$

where ρ is the number density of the rigid alloy system. To determine the term in the brackets in the above equation, μ in Eq. (2.26) is expressed in terms of (c, ϕ) leading to

$$c = c_s(c, \phi)\mathbf{g}_s(\phi) + c_l(c, \phi)\mathbf{g}_l(\phi). \quad (2.31)$$

Now, partially differentiating the above equation with regard to c fixes the value of the parenthetical term of Eq. (2.30) at unity resulting in

$$\left. \frac{\partial f}{\partial c} \right|_{\phi} = \rho\mu.$$

Partially differentiating Eq. (2.31) with regard to ϕ gives

$$\begin{aligned} \left. \frac{\partial c}{\partial \phi} \right|_c &= \left. \frac{\partial c_s}{\partial \phi} \right|_c \mathbf{g}_s(\phi) + \left. \frac{\partial c_l}{\partial \phi} \right|_c \mathbf{g}_l(\phi) + c_s \mathbf{g}'_s(\phi) + c_l \mathbf{g}'_l(\phi) \\ \implies 0 &= \left. \frac{\partial c_s}{\partial \phi} \right|_c \mathbf{g}_s(\phi) + \left. \frac{\partial c_l}{\partial \phi} \right|_c \mathbf{g}_l(\phi) + (c_s - c_l) \mathbf{g}'_s(\phi). \end{aligned} \quad (2.32)$$

This relation is obtained for the purpose of evaluating $\left. \frac{\partial f}{\partial \phi} \right|_c$. Specifically, partially differentiating Eq. (2.27) with respect to ϕ at constant c gives

$$\begin{aligned} \left. \frac{\partial f}{\partial \phi} \right|_c &= \left. \frac{df_s}{dc_s} \frac{\partial c_s}{\partial \phi} \right|_c \mathbf{g}_s(\phi) + \left. \frac{df_l}{dc_l} \frac{\partial c_l}{\partial \phi} \right|_c \mathbf{g}_l(\phi) + (f_s - f_l) \mathbf{g}'_s(\phi) + f'_{\text{dw}}(\phi) \\ &= \rho \mu \left(\left. \frac{\partial c_s}{\partial c} \right|_\phi \mathbf{g}_s(\phi) + \left. \frac{\partial c_l}{\partial c} \right|_\phi \mathbf{g}_l(\phi) \right) + (f_s - f_l) \mathbf{g}'_s(\phi) + f'_{\text{dw}}(\phi) \\ &= -\rho \mu (c_s - c_l) \mathbf{g}'_s(\phi) + (f_s - f_l) \mathbf{g}'_s(\phi) + f'_{\text{dw}}(\phi) \\ &= (\omega_s - \omega_l) \mathbf{g}'_s(\phi) + f'_{\text{dw}}(\phi) \end{aligned}$$

where the second last equality is due to Eq. (2.32). The isothermal rigid alloy solidification modeling equations can be now derived by differentiating the free energy functional of Eq. (2.24) with respect to time in the following manner

$$\begin{aligned} \frac{dF}{dt} &= \int \left. \frac{\partial f(\mu, \phi)}{\partial c} \right|_\phi \frac{\partial c}{\partial t} dV + \int \left(\left. \frac{\partial f(\mu, \phi)}{\partial \phi} \right|_c - f_G \nabla^2 \phi \right) \frac{\partial \phi}{\partial t} dV + \text{boundary terms} \\ &= \int \mu \rho \frac{\partial c}{\partial t} dV + \int ((\omega_s - \omega_l) \mathbf{g}'_s(\phi) + f'_{\text{dw}}(\phi) - f_G \nabla^2 \phi) \frac{\partial \phi}{\partial t} dV + \text{boundary terms} \end{aligned}$$

and choosing the phase-field and concentration evolution equations as in Eqs. (2.33) and (2.34) so as to guarantee negative Helmholtz free energy production rates due to internal changes and mass transport through diffusion.

$$\frac{\partial \phi}{\partial t} = M_\phi [(\omega_l - \omega_s) \mathbf{g}'_s(\phi) - f'_{\text{dw}}(\phi) + f_G (\nabla^2 \phi)], \quad (2.33)$$

$$\frac{\partial c}{\partial t} = \nabla \cdot (M_c \nabla \mu). \quad (2.34)$$

Once again, strikingly enough, even though free energy functional is considered as the starting point, the grand potential difference between the solid and liquid phases naturally entered into the formulation. Further, when the second of the above equations is rewritten so as to give an evolution equation for chemical potential, the resulting set of governing equations will be identical to those of the grand potential model of Ref. [18].

To summarize, we have managed to arrive at the same advantageous governing equations of the grand-potential model, but in a derivation whose starting point and further progression is mainly driven by thermodynamical considerations.

The derivations for obtaining the decoupled governing equations of non-isothermal solidification in incompressible alloy and pure systems are very similar and are presented in appendix A.4. Before proceeding with further applications, we take a short digression to provide a comparative discussion reviewing the existing models in the light of the present formulation.

2.3.2 Comparative discussion with other models

It is already detailed in the introduction that each of the existing variational models fails in some or the other aspect of a) facilitating separate control of bulk and interfacial properties, b) allowing a unified treatment of multiple cases and c) being framed as emerging solely from the thermodynamic considerations. Since the current formulation seems to have set forth the necessary and sufficient requirements for achieving these, a question now arises: can an explanation be given for why the existing models fall short in the departments they respectively do? It turns out that such a linking can indeed be done as given below.

In the WBM model of isothermal alloy solidification [9], the extensive quantity free energy is interpolated when expressed in terms of yet another extensive variable concentration and the monotonicity argument and mass balance are invoked for thermodynamic consistency [†], hence, as condition (H_1) is not satisfied, the decoupling behavior is not captured. To remedy this while still remaining in the coarse graining philosophy (as opposed to KKS who adopted a two-phase approach [17]), Plapp [18] and Choudhury and Nestler [23] proposed a switch from free energy density to grand-potential density and from concentration to chemical potential, as a result, the necessary and sufficient conditions (H_1) , (H_2) and (H_3) are all fulfilled. Thus, in principle, by starting from the appropriately modified free energy functional and using the same thermodynamically consistent argument of the WBM model, the decoupled equations could have very well been derived as demonstrated in section 2.3.1. However, Plapp [18] and Choudhury and Nestler [23] made a further switch from free energy functional to that of grand-potential and adopted a two-argument approach instead. This unnecessarily lengthens the formulation as it has to be supplemented with further calculations involving a back-construction of the free energy functional to demonstrate consistency (as in appendix A.2.1). Also, in the pure substance solidification derivation of Ref. [18] presented for the purpose of motivating the grand-potential formulation, the excess term is not incorporated in entropy density and thus condition (H_2) is not fulfilled, and as a result, the decoupling is lost (appendix A.2.2). Finally, as it turns out, the success of the grand-potential densities in modeling isothermal solidification has as much to do with the problem itself as the potential because, as shown in appendix A.2.3, the right switch to be made for a unified treatment that includes the non-isothermal processes as well is, in fact, not the grand-potential functional as it violates condition (H_2) , but the one corresponding to the same divided by the temperature. That is, if one were to use a two-argument approach, the

[†]In actuality, a more accurate argument than functional monotonicity is the appropriate sign preservation of the local production rates due to internal changes; even though not explicitly stated, this is indeed ensured in WBM and most other phase-field models.

Legendre transformations of the entropy rather than energy have to be worked with for achieving decoupling in a broader range of systems.

On the other hand is the derivation put forth by Wang *et al.* [28] which produces decoupled equations by utilizing thermodynamically consistent arguments and in which the appropriate Massieu-Planck function naturally arises. However, in their original work, only the case of pure substance solidification is presented and the various steps of the derivation are not stated in their most generic terms. As a result, they can be interpreted in multiple ways leading to two possible reformulations for isothermal alloy solidification (appendices A.3.1 and A.3.2). However, only one of them readily fulfills the requirements of conditions (H_1) - (H_3) and hence the decoupling behavior is only observed in it. Even this, can only handle those systems which have vanishing latent heats of fusion (appendix A.3.2). The other interpretation leads to a model which violates condition (H_2) , hence, it has to be appropriately modified before it can start exhibiting the ideal behavior of facilitating decoupling of bulk and interfacial properties (appendix A.3.1). Both these approaches produces the same governing equations as that of the grand potential model of Ref. [18] and can be readily generalized to multiphase, multi-component systems. As a matter of fact, once (H_2) is explicitly demanded, Wang *et al.* or Penrose and fife's algorithm is superior to the current one as it only utilizes a weaker version of hypothesis (H_1) .

We now get back to the program of applying the generic formulation to specific processes.

2.3.3 Isothermal evolution of multi-phase, multi-component, rigid alloy system

A multi-phase, multi-component model is now developed using the current framework. As the alloy system is considered to be rigid, and further, as isothermal conditions are assumed to prevail, Helmholtz free energy is the relevant thermodynamic potential. Though the derivation is just a generalization of the one carried out for single component systems in section 2.3.1, a detailed presentation is still provided for the sake of completeness.

Let us consider a K component system at a temperature where it can coexist as M different phases. Further, let it be assumed that the overall number density of the system, ρ , is a constant regardless of the phase. Therefore, concentrations of any of the $K - 1$ components are sufficient in specifying the exact state of being of a given phase. Without loss of generality, the first $K - 1$ components are chosen as the independent ones. Let these be referred to as $c_\alpha^1, c_\alpha^2, \dots, c_\alpha^{K-1}$ when speaking about the α^{th} phase. We denote the $K - 1$ tuple $(c_\alpha^1, c_\alpha^2, \dots, c_\alpha^{K-1})$ by c_α for brevity of notation. Therefore, the corre-

sponding volumetric Helmholtz free energy density's dependence on the concentrations is represented as

$$f_\alpha = f_\alpha(c_\alpha) = f_\alpha(c_\alpha^1, c_\alpha^2, \dots, c_\alpha^{K-1}).$$

The chemical potential of the i^{th} component as a function of composition in α^{th} phase is obtained by partially differentiating the above with the concentration of the i^{th} component. That is,

$$\mu^i = \mu^i(c_\alpha) = \mu^i(c_\alpha^1, c_\alpha^2, \dots, c_\alpha^{K-1}) := \frac{\partial f_\alpha(c_\alpha)}{\partial c_\alpha^i} \quad \forall i \in \{1, 2, \dots, K-1\}. \quad (2.35)$$

Let us assume that the $K-1$ equations above in $K-1$ variables are invertible, i.e., when chemical potentials of all the independent components are prescribed, then the corresponding concentrations in the α^{th} phase can be known from the following relations obtained by inverting the equations of Eq.(2.35)

$$c_\alpha^i = c_\alpha^i(\mu) = c_\alpha^i(\mu^1, \mu^2, \dots, \mu^{K-1}) \quad \forall i \in \{1, 2, \dots, K-1\}$$

where μ without any suffix is used to denote the vector of the chemical potentials of all the components, i.e., $\mu = (\mu^1, \mu^2, \dots, \mu^{K-1})$.

A vector valued phase-field variable of N components, $\phi = (\phi_1, \phi_2, \dots, \phi_N)$ is used to mark N grains. Though multiple grains may correspond to the same physical phase, in the following, for simplicity, the N grains are referred to as phases. That is, no distinction is made between two grains of distinct phases from those of the same one. The α^{th} phase is characterized by the α^{th} component taking a value of unity and all the rest assuming a value of zero. For this reason, the ϕ_α component is said to characterize the α^{th} phase and sometimes the latter is even referred to as the ϕ_α phase for brevity. Adopting this terminology, we proceed to develop the model for isothermal phase evolution.

Consistent with the hypotheses H_1 and H'_3 , the free energy density and composition of any of the stable or the intermediate phases for a given value of the chemical potential are interpolated as

$$f = \sum_{\alpha=1}^N f_\alpha(c_\alpha(\mu)) \mathbf{g}_\alpha(\phi) \quad \text{and} \quad (2.36)$$

$$c^i = \sum_{\alpha=1}^N c_\alpha^i(\mu) \mathbf{g}_\alpha(\phi) \quad \forall i \in \{1, 2, \dots, K-1\}, \quad (2.37)$$

respectively. Where, $\mathbf{g}_\alpha(\phi)$ for each $\alpha \in \{1, 2, \dots, N\}$ is an interpolation function satisfying $\mathbf{g}_\alpha(\phi) = 1$ when $\phi_\alpha = 1$, $\mathbf{g}_\alpha(\phi) = 0$ when $\phi_\alpha = 0$ and $\frac{\partial \mathbf{g}_\alpha(\phi)}{\partial \phi_\alpha} = 0$ when $\phi_\alpha = 0$ or 1. Some typical choices of multi-phase interpolation functions are listed in Table 2.1. Next,

the penalizing term is implemented only in the entropy and not in internal energy or composition as per the prescription of condition H_2 leading to the following free energy functional.

$$F = \int \left(\sum_{\alpha=1}^N f_{\alpha}(c_{\alpha}(\mu)) \mathbf{g}_{\alpha}(\phi) + f_{\text{mw}}(\phi) + \frac{f_G}{2} |\nabla \phi|^2 \right) dV \quad (2.38)$$

$$=: \int \left(\mathcal{F} + f_{\text{mw}}(\phi) + \frac{f_G}{2} |\nabla \phi|^2 \right) dV \quad (2.39)$$

where, $f_{\text{mw}}(\phi)$ is a multi-well potential. Differentiating the above with respect to time yields

$$\begin{aligned} \frac{dF}{dt} = \int \sum_{i=1}^{K-1} \left. \frac{\partial \mathcal{F}}{\partial c^i} \right|_{c^j \neq i, \phi} \frac{\partial c^i}{\partial t} dV + \int \sum_{\beta=1}^N \left(\left. \frac{\partial \mathcal{F}}{\partial \phi_{\beta}} \right|_{c, \phi_{\alpha \neq \beta}} + \frac{\partial f_{\text{mw}}}{\partial \phi_{\beta}} - f_G \nabla^2 \phi_{\beta} \right) \frac{\partial \phi_{\beta}}{\partial t} dV \\ + \text{boundary terms.} \end{aligned} \quad (2.40)$$

The partial derivatives $\left. \frac{\partial \mathcal{F}}{\partial c^i} \right|_{c^j \neq i, \phi}$ and $\left. \frac{\partial \mathcal{F}}{\partial \phi_{\beta}} \right|_{c, \phi_{\alpha \neq \beta}}$ will be analyzed next. Before that, we assume that the system of equations given by Eq. (2.37) are invertible leading to μ^i for each i in $\{1, 2, \dots, K-1\}$ being expressible in terms of c and ϕ . That is,

$$\mu^i = \mu^i(c, \phi) = \mu^i(c^1, c^2, \dots, c^{K-1}, \phi_1, \phi_2, \dots, \phi_N) \quad \forall i \in \{1, 2, \dots, K-1\}.$$

Substituting the above relations back in Eq. (2.37) results in

$$\begin{aligned} c^i &= \sum_{\alpha=1}^N c_{\alpha}^i(\mu(c, \phi)) \mathbf{g}_{\alpha}(\phi) \quad \forall i \in \{1, 2, \dots, K-1\} \\ &=: \sum_{\alpha=1}^N c_{\alpha}^i(c, \phi) \mathbf{g}_{\alpha}(\phi) \quad \forall i \in \{1, 2, \dots, K-1\} \\ \implies c^j &= \sum_{\alpha=1}^N c_{\alpha}^j(c, \phi) \mathbf{g}_{\alpha}(\phi) \quad \forall j \in \{1, 2, \dots, K-1\}. \end{aligned}$$

Partially differentiating the above equation with c^i leads to

$$\begin{aligned} \left. \frac{\partial c^j}{\partial c^i} \right|_{c^j \neq i, \phi} &= \sum_{\alpha=1}^N \left. \frac{\partial c_{\alpha}^j(c, \phi)}{\partial c^i} \right|_{c^j \neq i, \phi} \mathbf{g}_{\alpha}(\phi) \quad \forall j \in \{1, 2, \dots, K-1\} \\ \implies \delta_{ji} &= \sum_{\alpha=1}^N \left. \frac{\partial c_{\alpha}^j(c, \phi)}{\partial c^i} \right|_{c^j \neq i} \mathbf{g}_{\alpha}(\phi) \quad \forall j \in \{1, 2, \dots, K-1\}. \end{aligned}$$

Similarly, partially differentiating with respect to ϕ_{β} leads to

$$\begin{aligned} \left. \frac{\partial c^j}{\partial \phi_{\beta}} \right|_{c, \phi_{\alpha \neq \beta}} &= \sum_{\alpha=1}^N \left. \frac{\partial c_{\alpha}^j(c, \phi)}{\partial \phi_{\beta}} \right|_{c, \phi_{\alpha \neq \beta}} \mathbf{g}_{\alpha}(\phi) + \sum_{\alpha=1}^N c_{\alpha}^j(c, \phi) \frac{\partial \mathbf{g}_{\alpha}(\phi)}{\partial \phi_{\beta}} \\ \implies 0 &= \sum_{\alpha=1}^N \left. \frac{\partial c_{\alpha}^j(c, \phi)}{\partial \phi_{\beta}} \right|_{c, \phi_{\alpha \neq \beta}} \mathbf{g}_{\alpha}(\phi) + \sum_{\alpha=1}^N c_{\alpha}^j(c, \phi) \frac{\partial \mathbf{g}_{\alpha}(\phi)}{\partial \phi_{\beta}} \end{aligned}$$

$$\implies \sum_{\alpha=1}^N \frac{\partial c_{\alpha}^j(c, \phi)}{\partial \phi_{\beta}} \Big|_{c, \phi_{\alpha} \neq \beta} \mathbf{g}_{\alpha}(\phi) = - \sum_{\alpha=1}^N c_{\alpha}^j(c, \phi) \frac{\partial \mathbf{g}_{\alpha}(\phi)}{\partial \phi_{\beta}} \quad \forall j \in \{1, 2, \dots, K-1\}.$$

Now consider the partial derivative $\frac{\partial \mathcal{F}}{\partial \phi_{\beta}} \Big|_{c, \phi_{\alpha} \neq \beta}$,

$$\begin{aligned} \frac{\partial \mathcal{F}}{\partial \phi_{\beta}} \Big|_{c, \phi_{\alpha} \neq \beta} &= \sum_{\alpha=1}^N \frac{\partial f_{\alpha}(c_{\alpha}(\mu))}{\partial \phi_{\beta}} \Big|_{c, \phi_{\alpha} \neq \beta} \mathbf{g}_{\alpha}(\phi) + \sum_{\alpha=1}^N f_{\alpha}(c_{\alpha}(\mu)) \frac{\partial \mathbf{g}_{\alpha}(\phi)}{\partial \phi_{\beta}} \\ &= \sum_{\alpha=1}^N \frac{\partial f_{\alpha}(c_{\alpha}(c, \phi))}{\partial \phi_{\beta}} \Big|_{c, \phi_{\alpha} \neq \beta} \mathbf{g}_{\alpha}(\phi) + \sum_{\alpha=1}^N f_{\alpha}(c_{\alpha}(\mu)) \frac{\partial \mathbf{g}_{\alpha}(\phi)}{\partial \phi_{\beta}} \\ &= \sum_{\alpha=1}^N \sum_{j=1}^{K-1} \frac{\partial f_{\alpha}(c_{\alpha}(c, \phi))}{\partial c_{\alpha}^j} \Big|_{c_{\alpha}^k \neq j} \frac{\partial c_{\alpha}^j}{\partial \phi_{\beta}} \Big|_{c, \phi_{\alpha} \neq \beta} \mathbf{g}_{\alpha}(\phi) + \sum_{\alpha=1}^N f_{\alpha}(c_{\alpha}(\mu)) \frac{\partial \mathbf{g}_{\alpha}(\phi)}{\partial \phi_{\beta}} \\ &= \sum_{\alpha=1}^N \sum_{j=1}^{K-1} \mu^j (c_{\alpha}(c, \phi)) \frac{\partial c_{\alpha}^j}{\partial \phi_{\beta}} \Big|_{c, \phi_{\alpha} \neq \beta} \mathbf{g}_{\alpha}(\phi) + \sum_{\alpha=1}^N f_{\alpha}(c_{\alpha}(\mu)) \frac{\partial \mathbf{g}_{\alpha}(\phi)}{\partial \phi_{\beta}} \\ &= \sum_{\alpha=1}^N \sum_{j=1}^{K-1} \mu^j (c_{\alpha}(c(\mu, \phi), \phi)) \frac{\partial c_{\alpha}^j}{\partial \phi_{\beta}} \Big|_{c, \phi_{\alpha} \neq \beta} \mathbf{g}_{\alpha}(\phi) + \sum_{\alpha=1}^N f_{\alpha}(c_{\alpha}(\mu)) \frac{\partial \mathbf{g}_{\alpha}(\phi)}{\partial \phi_{\beta}} \\ &= \sum_{\alpha=1}^N \sum_{j=1}^{K-1} \mu^j \frac{\partial c_{\alpha}^j}{\partial \phi_{\beta}} \Big|_{c, \phi_{\alpha} \neq \beta} \mathbf{g}_{\alpha}(\phi) + \sum_{\alpha=1}^N f_{\alpha}(c_{\alpha}(\mu)) \frac{\partial \mathbf{g}_{\alpha}(\phi)}{\partial \phi_{\beta}} \\ &= \sum_{j=1}^{K-1} \sum_{\alpha=1}^N \mu^j \frac{\partial c_{\alpha}^j}{\partial \phi_{\beta}} \Big|_{c, \phi_{\alpha} \neq \beta} \mathbf{g}_{\alpha}(\phi) + \sum_{\alpha=1}^N f_{\alpha}(c_{\alpha}(\mu)) \frac{\partial \mathbf{g}_{\alpha}(\phi)}{\partial \phi_{\beta}} \\ &= \sum_{j=1}^{K-1} \mu^j \sum_{\alpha=1}^N \frac{\partial c_{\alpha}^j}{\partial \phi_{\beta}} \Big|_{c, \phi_{\alpha} \neq \beta} \mathbf{g}_{\alpha}(\phi) + \sum_{\alpha=1}^N f_{\alpha}(c_{\alpha}(\mu)) \frac{\partial \mathbf{g}_{\alpha}(\phi)}{\partial \phi_{\beta}} \\ &= \sum_{j=1}^{K-1} \mu^j \sum_{\alpha=1}^N -c_{\alpha}^j(c, \phi) \frac{\partial \mathbf{g}_{\alpha}(\phi)}{\partial \phi_{\beta}} + \sum_{\alpha=1}^N f_{\alpha}(c_{\alpha}(\mu)) \frac{\partial \mathbf{g}_{\alpha}(\phi)}{\partial \phi_{\beta}} \\ &= \sum_{\alpha=1}^N \sum_{j=1}^{K-1} -\mu^j c_{\alpha}^j(c, \phi) \frac{\partial \mathbf{g}_{\alpha}(\phi)}{\partial \phi_{\beta}} + \sum_{\alpha=1}^N f_{\alpha}(c_{\alpha}(\mu)) \frac{\partial \mathbf{g}_{\alpha}(\phi)}{\partial \phi_{\beta}} \\ &= \sum_{\alpha=1}^N \left(f_{\alpha}(c_{\alpha}(\mu)) - \sum_{j=1}^{K-1} \mu^j c_{\alpha}^j(c, \phi) \right) \frac{\partial \mathbf{g}_{\alpha}(\phi)}{\partial \phi_{\beta}} \\ &= \sum_{\alpha=1}^N \left(f_{\alpha}(c_{\alpha}(\mu)) - \sum_{j=1}^{K-1} \mu^j c_{\alpha}^j(c(\mu, \phi), \phi) \right) \frac{\partial \mathbf{g}_{\alpha}(\phi)}{\partial \phi_{\beta}} \\ &= \sum_{\alpha=1}^N \omega_{\alpha}(c_{\alpha}(\mu)) \frac{\partial \mathbf{g}_{\alpha}(\phi)}{\partial \phi_{\beta}} \\ &= \sum_{\alpha=1}^N \omega_{\alpha}(\mu) \frac{\partial \mathbf{g}_{\alpha}(\phi)}{\partial \phi_{\beta}}. \end{aligned}$$

Similarly, the other partial derivative $\left. \frac{\partial \mathcal{F}}{\partial c^i} \right|_{c^{j \neq i}, \phi}$, as well, can be analyzed as

$$\begin{aligned}
\left. \frac{\partial \mathcal{F}}{\partial c^i} \right|_{c^{j \neq i}, \phi} &= \sum_{\alpha=1}^N \left. \frac{\partial f_{\alpha}(c_{\alpha}(\mu))}{\partial c^i} \right|_{c^{j \neq i}, \phi} \mathbf{g}_{\alpha}(\phi) \\
&= \sum_{\alpha=1}^N \left. \frac{\partial f_{\alpha}(c_{\alpha}(c, \phi))}{\partial c^i} \right|_{c^{j \neq i}, \phi} \mathbf{g}_{\alpha}(\phi) \\
&= \sum_{\alpha=1}^N \sum_{j=1}^{K-1} \left. \frac{\partial f_{\alpha}(c_{\alpha}(c, \phi))}{\partial c_{\alpha}^j} \right|_{c_{\alpha}^{k \neq j}} \left. \frac{\partial c_{\alpha}^j}{\partial c^i} \right|_{c^{j \neq i}, \phi} \mathbf{g}_{\alpha}(\phi) \\
&= \sum_{\alpha=1}^N \sum_{j=1}^{K-1} \mu^j(c_{\alpha}(c, \phi)) \left. \frac{\partial c_{\alpha}^j}{\partial c^i} \right|_{c^{j \neq i}, \phi} \mathbf{g}_{\alpha}(\phi) \\
&= \sum_{\alpha=1}^N \sum_{j=1}^{K-1} \mu^j(c_{\alpha}(c(\mu, \phi), \phi)) \left. \frac{\partial c_{\alpha}^j}{\partial c^i} \right|_{c^{j \neq i}, \phi} \mathbf{g}_{\alpha}(\phi) \\
&= \sum_{\alpha=1}^N \sum_{j=1}^{K-1} \mu^j(c_{\alpha}(\mu)) \left. \frac{\partial c_{\alpha}^j}{\partial c^i} \right|_{c^{j \neq i}, \phi} \mathbf{g}_{\alpha}(\phi) \\
&= \sum_{\alpha=1}^N \sum_{j=1}^{K-1} \mu^j \left. \frac{\partial c_{\alpha}^j}{\partial c^i} \right|_{c^{j \neq i}, \phi} \mathbf{g}_{\alpha}(\phi) \\
&= \sum_{j=1}^{K-1} \sum_{\alpha=1}^N \mu^j \left. \frac{\partial c_{\alpha}^j}{\partial c^i} \right|_{c^{j \neq i}, \phi} \mathbf{g}_{\alpha}(\phi) \\
&= \sum_{j=1}^{K-1} \mu^j \sum_{\alpha=1}^N \left. \frac{\partial c_{\alpha}^j}{\partial c^i} \right|_{c^{j \neq i}, \phi} \mathbf{g}_{\alpha}(\phi) \\
&= \sum_{j=1}^{K-1} \mu^j \delta_{ji} \\
&= \mu^i.
\end{aligned}$$

Hence, the phase-field and the concentration evolution equations that ensure mass balance through diffusion and negative Helmholtz free energy production in each subvolume are

$$\frac{\partial \phi_{\beta}}{\partial t} = -M_{\phi} \left(\sum_{\alpha=1}^N \omega_{\alpha}(\mu) \frac{\partial \mathbf{g}_{\alpha}(\phi)}{\partial \phi_{\beta}} + \frac{\partial f_{\text{mw}}(\phi)}{\partial \phi_{\beta}} - f_{\text{G}} \nabla^2 \phi_{\beta} \right) \quad \forall \beta \in \{1, 2, \dots, N\} \quad (2.41)$$

and

$$\frac{\partial c^i}{\partial t} = \nabla \cdot (M_c \nabla \mu^i) \quad \forall i \in \{1, 2, \dots, K-1\}. \quad (2.42)$$

2.3.3.1 Summation constraint

Often, an extra requirement of sum of all the components of the phase indicator adding up to unity is additionally demanded. To fulfill this summation rule, in each of the N

equations of Eq. (2.41), an extra term is introduced in the following manner.

$$\frac{\partial \phi_\beta}{\partial t} = -M_\phi \left(\sum_{\alpha=1}^N \omega_\alpha(\mu) \frac{\partial \mathbf{g}_\alpha(\phi)}{\partial \phi_\beta} + \frac{\partial f_{\text{mw}}(\phi)}{\partial \phi_\beta} - f_G \nabla^2 \phi_\beta - \lambda \right) \quad \forall \beta \in \{1, 2, \dots, N\}$$

where

$$\lambda = \frac{1}{N} \sum_{\beta=1}^N \frac{\delta F}{\delta \phi_\beta}$$

with $\frac{\delta F}{\delta \phi_\beta}$ standing for the term inside the braces in Eq. (2.41). This modification is termed as the implementation of the Lagrange multiplier formalism with λ being the multiplier. It has to be made sure that even after such an implementation, the negative production rate is not affected. Since the composition evolution equation is unaltered, only the second integral of Eq. (2.40) is examined for this using the modified expression for $\frac{\partial \phi_\beta}{\partial t}$. The calculations are

$$\begin{aligned} \int \sum_{\beta=1}^N \frac{\delta F}{\delta \phi_\beta} \frac{\partial \phi_\beta}{\partial t} dV &= \int \sum_{\beta=1}^N \frac{\delta F}{\delta \phi_\beta} \left\{ -M_\phi \left(\frac{\delta F}{\delta \phi_\beta} - \lambda \right) \right\} dV \\ &= - \int M_\phi \sum_{\beta=1}^N \frac{\delta F}{\delta \phi_\beta} \left(\frac{\delta F}{\delta \phi_\beta} - \frac{1}{N} \sum_{\beta=1}^N \frac{\delta F}{\delta \phi_\beta} \right) dV \\ &= - \int M_\phi \left[\sum_{\beta=1}^N \left(\frac{\delta F}{\delta \phi_\beta} \right)^2 - \frac{1}{N} \left(\sum_{\beta=1}^N \frac{\delta F}{\delta \phi_\beta} \right)^2 \right] dV. \end{aligned}$$

The square bracket term in the above equation is identically non-negative which can be proved by the application of the Cauchy-Schwarz inequality to the N -component vectors $\left(\frac{\delta F}{\delta \phi_1}, \frac{\delta F}{\delta \phi_2}, \dots, \frac{\delta F}{\delta \phi_N} \right)$ and $(1, 1, \dots, 1)$. Therefore, the requirement of negative production rate is satisfied in the Lagrange multiplier implementation as well. It is necessary to caution that the inclusion of the multiplier only ensures that at any given spatial point, the sum of all the phase-field components remains unchanged as time passes but does not necessarily fix the value of the sum at unity. For the latter, it has to be taken care that the summation constraint is satisfied by the initial condition (sometimes called as initial filling) itself. In the rest of the thesis, whenever Lagrange multipliers are employed, it is to be understood that it is for the purpose of implementing the summation rule and hence the initial filling is consistent with it even when not mentioned explicitly.

2.4 Binary eutectic growth model

The binary eutectic growth model which is the focus of the current thesis will now be deduced from the above model. For reasons that will become more clearer in the next

chapter, the various terms occurring in the phase-field evolution equations will be selected as multiplied to various powers of a parameter ϵ as follows.

$$\frac{\partial \phi_\beta}{\partial t} = -\frac{1}{\tau(\phi)} \left(\sum_{\alpha=1}^N \frac{1}{\epsilon} \omega_\alpha(\mu) \frac{\partial \mathbf{g}_\alpha(\phi)}{\partial \phi_\beta} + \frac{\gamma}{\epsilon^2} \frac{\partial W(\phi)}{\partial \phi_\beta} - \gamma \nabla^2 \phi_\beta \right) \quad \forall \beta \in \{1, 2, \dots, N\} \quad (2.43)$$

where $W(\phi)$ is a dimensionless multi-well form, γ is the interfacial energy specifier and ω_α is grand-potential of the α^{th} phase up to a constant multiple which is the same for each α . The parameter ϵ then happens to be the interfacial width specifier. The function $\tau(\phi)$ interpolates the inverse mobilities of all the possible combinations of the interfaces in such a way that when the phase-field variable has only two non-zero components, then the inverse mobility corresponding to the interface between the phases naturally marked by these components is selected. That is, denoting the inverse mobility of the interface between ϕ_α phase and ϕ_β phase by $\tau_{\alpha\beta}$, $\tau(\phi)$ collapses to this value when all but the α^{th} and β^{th} components of the phase-field variable are zero. Further, the interpolating form should be selected such that it is always positive. An example of such a τ -form which is typically used is presented in Table 2.1 along with some standard multi-well forms that are studied in the current thesis. Visualizations of these multi-wells when restricted to the Gibbs triangle are provided in the next chapter.

Coming to the evolution of the chemical species, as there is only a single independent component, Eq. (2.42) takes the form of Eq. (2.34) however, with c now depending on N phases. It is further re-expressed in terms of ϕ and μ as

$$\begin{aligned} \frac{\partial}{\partial t} \sum_{\alpha=1}^N c_\alpha(\mu) \mathbf{g}_\alpha(\phi) &= \nabla \cdot (M_c \nabla \mu) \\ \implies \sum_{\alpha=1}^N \frac{\partial c_\alpha(\mu)}{\partial \mu} \mathbf{g}_\alpha(\phi) \frac{\partial \mu}{\partial t} + \sum_{\alpha=1}^N c_\alpha(\mu) \frac{\partial \mathbf{g}_\alpha(\phi)}{\partial t} &= \nabla \cdot (M_c \nabla \mu) \end{aligned}$$

The mobility of the chemical transport is related to the diffusivities in each phase resulting in a final form of chemical potential evolution equation:

$$\frac{\partial \mu}{\partial t} = \left(\sum_{\alpha=1}^N \frac{dc_\alpha(\mu)}{d\mu} \mathbf{g}_\alpha(\phi) \right)^{-1} \left[\nabla \cdot \left\{ \left(\sum_{\alpha=1}^N D_\alpha \frac{dc_\alpha}{d\mu} \mathbf{h}_\alpha(\phi) \right) \nabla \mu \right\} - \sum_{\alpha=1}^N c_\alpha(\mu) \frac{\partial \mathbf{g}_\alpha(\phi)}{\partial t} \right] \quad (2.44)$$

where $\{\mathbf{h}_\alpha\}$ are some other interpolation functions which may coincide with $\{\mathbf{g}_\alpha\}$.

Eq. (2.43) and its Lagrange multiplier counterpart, and Eq. (2.44) are of primary concern in the rest of the thesis.

Table 2.1: Examples of some of the standard choices of interpolating and multi-well forms which are repeatedly employed in the thesis.

		Comments	
Interpolating forms	Uncoupled forms	$\mathbf{g}_\alpha(\phi) = \mathbf{g}_S(\phi_\alpha) \forall \alpha$ where \mathbf{g}_S is an interpolating function of the scalar phase-field models	They are the simplest forms due to the absence of mixed products of the components
	Folch-Plapp form	$\mathbf{g}_\alpha(\phi) = \frac{\phi_\alpha^2}{4} \{15(1 - \phi_\alpha)[1 + \phi_\alpha - (\phi_\beta - \phi_\gamma)^2] + \phi_\alpha(9\phi_\alpha^2 - 5)\}$	Presented only for $N = 3$ phases; hence, $\alpha, \beta, \gamma \in \{1, 2, 3\}$
τ -form		$\tau_A = \frac{\sum_{\alpha < \beta} \tau_{\alpha\beta} \phi_\alpha^2 \phi_\beta^2}{\sum_{\alpha < \beta} \phi_\alpha^2 \phi_\beta^2}$	The A in the suffix is to remind that the form gives the arithmetic mean when $\phi_\alpha = \phi_\beta \forall \alpha, \beta$
Multi-well forms	Classical multi-well	$W^C = \sum_{\alpha < \beta} a_{\alpha\beta} \phi_\alpha^2 \phi_\beta^2$	The word classical is used because it is this form that was employed in most of the initial models.
	Folch-Plapp triple-well	$W^{FP} = a [\phi_1^2(1 - \phi_1)^2 + \phi_2^2(1 - \phi_2)^2 + \phi_3^2(1 - \phi_3)^2]$	Symmetric well presented only for $N = 3$ phases

Chapter 3

Asymptotic analysis

3.1 Introduction

The governing equations of eutectic growth obtained in the previous chapter are no different than the ones derived in the traditional grand potential formulation except that the development here is more refined being framed as emerging from thermodynamic first principles. In the same spirit, the current chapter carries out a similar program of refining the next aspect of the phase-field theory, namely, the asymptotic analysis of the developed modeling equations.

Asymptotic analysis is a very helpful tool as it reveals which physical laws of transport and interface evolution are captured by the developed phase-field equations. Even more importantly, it helps select the various modeling parameters such that the performed simulations indeed actually correspond to the exact material system under specification. However, in multi-phase-field analyses, it is often the case that instead of looking at the entire vector valued phase-field variable, only two components at a time are considered for predicting the corresponding binary interface's asymptotic behavior. The dynamics of the higher order inter-phase boundaries like triple, quadruple etc. junctions is left unanalyzed only to be empirically understood later from the numerical results. Only two works, Refs. [30] and [31], exist which handle the higher order junctions on the same footing as the binary interfaces, however, they restrict themselves to the study of triple points. That is, an analysis of the behavior of still higher order junctions is never before attempted. Even in the considered special case, the perturbative analysis is carried out only up to the leading order resulting in a prediction about the configuration around the triple point but not its kinetics. The current chapter aims to remedy this by performing a full-fledged analysis of the developed multi-phase-field model.

Another shortcoming of the practice of analyzing the multi-phase-field equations af-

ter reducing them to the two-phase model is particularly realized in the simulations of the classic directional eutectic growth problem which is the focus of the current thesis. Here, the diffusivities of both the components are approximated to vanish in the solid phases and the kinetic co-efficients of the interfaces that the latter form with the melt are also assumed to be zero. While this poses no problem in the selection of the (inverse) mobilities of the solid-liquid surfaces, the prescription for the solid-solid mobility remains indeterminate. To elaborate, consider the single phase solidification model expressed in the following form.

$$\tau_{\alpha l} \frac{\partial \phi}{\partial t} = \frac{1}{\epsilon} (\omega_l - \omega_\alpha) \mathbf{g}'_\alpha(\phi) - \frac{1}{\epsilon^2} \gamma f'_{\text{dw}}(\phi) + \gamma (\nabla^2 \phi), \quad (3.1)$$

$$\frac{\partial \mu}{\partial t} = \left(\frac{\partial c_\alpha(\mu)}{\partial \mu} \mathbf{g}_\alpha(\phi) + \frac{\partial c_l(\mu)}{\partial \mu} (1 - \mathbf{g}_\alpha(\phi)) \right)^{-1} \left[\nabla \cdot (M_c \nabla \mu) - (c_\alpha(\mu) - c_l(\mu)) \frac{\partial \mathbf{g}_\alpha(\phi)}{\partial t} \right] \quad (3.2)$$

with

$$M_c = D_\alpha \frac{\partial c_\alpha}{\partial \mu} \mathbf{h}_\alpha(\phi) + D_l \frac{\partial c_l}{\partial \mu} (1 - \mathbf{h}_\alpha(\phi)).$$

Where, α and l stand for the solid and melt phases respectively. Further, in the system of interest, both D_α and the kinetic coefficient vanish. This requires performing asymptotic analysis up to three leading orders in the inner coordinates (also called a thin-interface analysis) for a proper connection of the model parameters to the thermo-physical properties of the material system. Then, the desired free boundary problem is recovered up to an order of error of ϵ for which the inverse mobility $\tau_{\alpha l}$ has to be chosen as

$$\tau_{\alpha l} = \epsilon \frac{(c_\alpha(\mu_{\text{eq}}) - c_l(\mu_{\text{eq}}))^2 K}{D_l \frac{dc_l}{d\mu}(\mu_{\text{eq}})}$$

where μ_{eq} is the solid-liquid equilibrium chemical potential at the given temperature and K is a numerical constant dependent on the specific forms of the double-well and the interpolation functions.

However, in the case of α - β solid-solid system of special interest, i.e., $D_\alpha = D_\beta = 0$, the governing equation for the chemical potential evolution, Eq. (3.2), is replaced by

$$\frac{\partial \mu}{\partial t} = - \left(\frac{\partial c_\alpha(\mu)}{\partial \mu} \mathbf{g}_\alpha(\phi) + \frac{\partial c_\beta(\mu)}{\partial \mu} (1 - \mathbf{g}_\alpha(\phi)) \right)^{-1} \left[(c_\alpha(\mu) - c_\beta(\mu)) \frac{\partial \mathbf{g}_\alpha(\phi)}{\partial t} \right]$$

and the phase-field equation remains essentially the same except for the obvious replacement of $\tau_{\alpha l}$ with the solid-solid mobility $\tau_{\alpha\beta}$ and ω_l with ω_β . As a result, the conditions recovered inside the interfacial region are

$$\tau_{\alpha\beta} v = F[\mu(z, t), \phi(z, t)] - \gamma \kappa \quad (3.3)$$

and, throughout the diffuse interface,

$$v \frac{\partial c(\mu)}{\partial z} = v \frac{\partial}{\partial z} (c_\alpha(\mu) \mathbf{g}_\alpha(\phi) + c_\beta(\mu)(1 - \mathbf{g}_\alpha(\phi))) = 0 \quad (3.4)$$

with v and κ being the normal velocity and the curvature of the interface, respectively; z is the spatial variable spanning across the width of the diffuse interface; and F is a functional of the phase-field and chemical potential profiles at any given time t .

The second of the above equations implies that either $v = 0$ or $c(\mu) = \text{constant}$. That is, if the latter were to happen, instead of chemical potential being constant through out the (vanishingly small) width of the interface, as required by the local equilibrium, the composition remains so. However, numerical simulations revealed that the interface is static for various supersaturations around the equilibrium values. Thus, the first alternative is the relevant solution which is picked in the simulations. But then this would imply that nothing about the chemical potential profile can be inferred from the equations. Even if it is assumed to be constant throughout the interface, the l.h.s of Eq. (3.3) vanishes eliminating $\tau_{\alpha\beta}$ altogether from the equations thereby allowing no chance for giving a prescription for the inverse mobility even when next order is considered in order to perform a thin-interface analysis. Thus, the model is plagued with the issue of non-uniqueness. In the wake of this, questions arise as to: Do all the values of $\tau_{\alpha\beta}$ give the same results? Even if they do as far as the binary interfaces are considered, what about the effect on the dihedral angles recovered at the triple junctions and on the triple point speed? Ref. [52] reported a definite presence of an effect of the value of solid-solid mobility on the recovered bicrystal evolution dynamics. Since the lamellar eutectic growth set up is very similar to it, the same should be expected as well. If so, since there is no non-uniqueness in the Jackson-Hunt problem, only a particular value of $\tau_{\alpha\beta}$, if at all any, will give a perfect match with the analytical results. How can this latter be known? Is there a chance of eliminating the non-uniqueness through a more complete asymptotic analysis which includes the investigation of the higher order junctions as well? Much of the effort in the current chapter is directed towards addressing these concerns.

Another motivation for performing a refined asymptotic analysis, although of minor significance, is the following. In the common practice, to reason that a third or ghost phase does not arise in the interfacial region between two phases, it is shown that the absence of it in a neighborhood implies it remaining so for the “next moment”. However, this argument is conditional and very local in time. Hence, in setups where a phase is left unfilled through out the domain it may apply globally for all times, but if the bulk of a phase is present at some part of the domain, its non-zero values permeate the whole domain in due time (in fact instantaneously due to the parabolic nature of the partial differential equation for its component). Thus, in practice, never is the third phase completely absent on a binary interface if its bulk is present somewhere in the domain.

Hence, technically speaking, the argument given for reducing the multi-phase-field model to consider two components at a time is invalid globally.

In summary, a refined asymptotic analysis is indeed very much desired for a stronger justification of the claims made about the recovered free boundary problem. The current chapter aims at developing it. However, for now, the evolution equation of the phase-field (vector) variable alone is studied by assuming that a second field is not present. This will be adjusted appropriately and supplemented with the analysis of the chemical potential equation later in appendix D to form a complete analysis of the eutectic growth model. Further, before performing the asymptotic analysis on the multi-phase-field equations, the corresponding procedure in the case of scalar phase-field variable will now be briefly considered to facilitate a smooth transition when moving on to the vector case.

3.2 Asymptotic analysis of scalar phase-field model

The phase-field evolution equation of concern is as follows.

$$\tau \frac{\partial \phi}{\partial t} = \frac{1}{\epsilon} \Delta f \mathcal{G}'(\phi) - \gamma \frac{1}{\epsilon^2} f'_{\text{dw}}(\phi) + \gamma \nabla^2(\phi). \quad (3.5)$$

In the first step of the asymptotic analysis, it is assumed that the solution to the above equation has an asymptotic expansion of the form

$$\phi = \phi^{(0)} + \epsilon \phi^{(1)} + \epsilon^2 \phi^{(2)} + \dots \quad (3.6)$$

Substituting the above in Eq. (3.5) and separating the orders gives at the leading order

$$f'_{\text{dw}}(\phi^{(0)}) = 0. \quad (3.7)$$

Due to the chosen symmetric form of the function $f_{\text{dw}}(\phi)$, the solutions to the above equation are $\phi^{(0)} = 0$, $\phi^{(0)} = 1/2$ and $\phi^{(0)} = 1$.

If in the domain there were to be regions corresponding to different solutions, then the problem exhibits a boundary (interior) layer behavior. However, it is unclear how to conclude whether or not such distinct regions will exist and if they do, what their distribution in the domain is. Further, traditionally, the $\phi^{(0)} = 1/2$ solution is neglected and only the other two are considered for the analysis. A sound argument for such a move is not typically set forth. These shortcomings can be rectified when we begin to look at the governing equation in faster timescales, namely, $\tau = t/\epsilon^2$ and $\tau = t/\epsilon$.

3.2.1 Timescale $\tau = t/\epsilon^2$

In this timescale, the r.h.s of Eq. (3.5) remains unchanged and the l.h.s modifies to $\frac{\tau}{\epsilon^2} \frac{\partial \phi}{\partial \tau}$, thus requiring the following at the leading order

$$\tau \frac{\partial \phi^{(0)}}{\partial \tau} = -\gamma f'_{\text{dw}}(\phi^{(0)}(x, \tau)). \quad (3.8)$$

Which means that the solution $\phi^{(0)}(x, \tau)$ is in such a way that the corresponding values of the double well are ever decreasing. This can be seen by considering $f_{\text{dw}}(\phi^{(0)}(\tau))$ and differentiating it with respect to time, i.e.,

$$\begin{aligned} \frac{\partial}{\partial \tau} f_{\text{dw}}(\phi^{(0)}(\tau)) &= \frac{\partial}{\partial \phi^{(0)}} f_{\text{dw}}(\phi^{(0)}(x, \tau)) \frac{\partial \phi^{(0)}}{\partial \tau} \\ &= f'_{\text{dw}}(\phi^{(0)}(x, \tau)) \frac{\partial \phi^{(0)}}{\partial \tau} \\ &= -\frac{\gamma}{\tau} (f'_{\text{dw}}(\phi^{(0)}(x, \tau)))^2 \\ &\leq 0. \end{aligned} \quad (3.9)$$

Since the generic shape of a symmetric double well function is as depicted in Fig. B.1 (appendix B.1.1), this means, at regions where the phase-field variable is initially set to a value in the interval $(0, 1/2)$, it decreases progressively, increases in like fashion when in interval $(1/2, 1)$ and remains unchanged where it exactly equals 0 or $1/2$ or 1. Moreover, in the former two regions, it does not ever overshoot the values of 0 and 1 nor runs out before approaching them but exactly tends to them, respectively. This is because, if it overshoots, it violates the requirement of monotonically decreasing behavior of $f_{\text{dw}}(\phi^{(0)}(x, \tau))$, whereas if it converges to some other value, the l.h.s of equation will vanish eventually but the r.h.s remains bounded away from zero. Thus, at this timescale, the changes in the initially set filling are in such a way that extended regions of $\phi^{(0)} = 0$ and $\phi^{(0)} = 1$ are formed and the regions corresponding to $\phi^{(0)} = 1/2$ are sustained without being modified. That is, schematically speaking, an initial profile as shown in Fig 3.1a) tends to the that (in green) in Fig 3.1b). A technically complete argument for the above is presented in appendix B.1.1.

3.2.2 Timescale $\tau = t/\epsilon$

The leading order requirement at this timescale is as in Eq. (3.7) and hence is consistent with the developed microstructure at the previous scale. However, as interior layers exist, it makes sense to perform local analysis by transforming to stretched coordinates centered on the appropriate level set curves. That is, level sets corresponding to any value in $(0, 1)$ for layers separating bulks of $\phi = 0$ from $\phi = 1$, and between $(0, 1/2)$ for

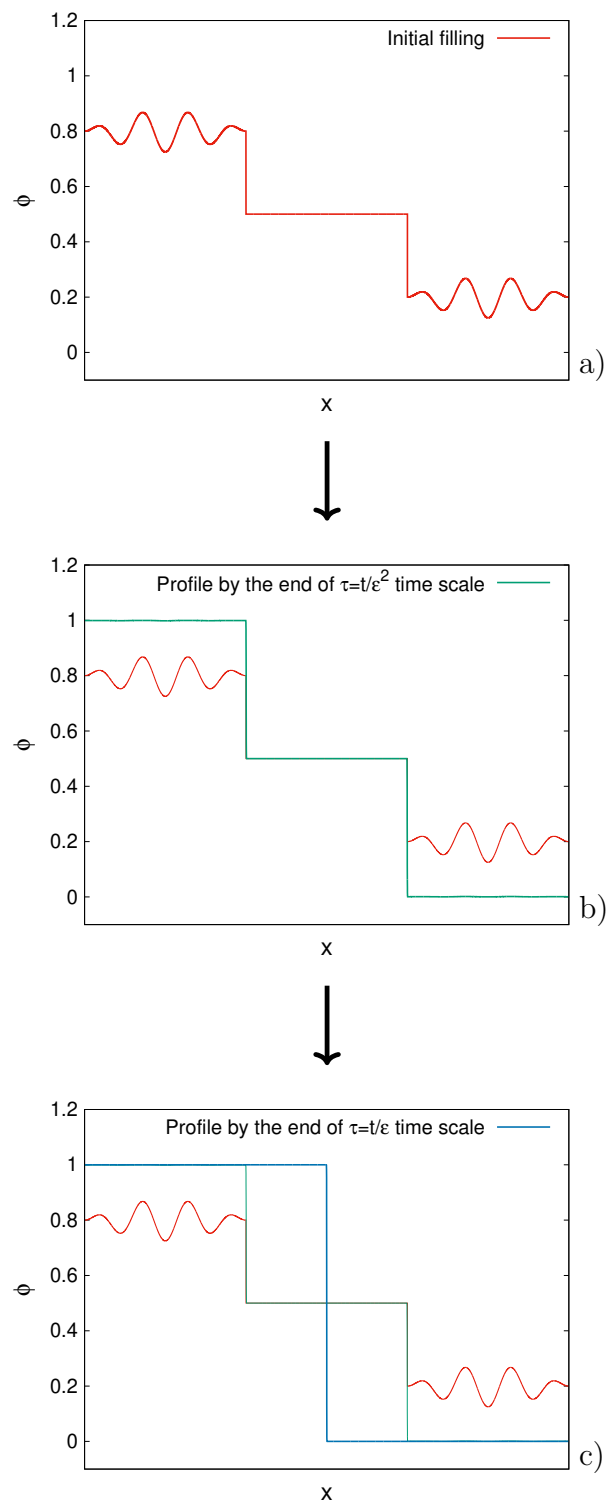


Figure 3.1: The evolution of an initially set profile in the lower timescales $\tau = t/\epsilon^2$ and $\tau = t/\epsilon$. The (red) curve in a) corresponds to the initial filling; the green profile in b) is its state by the “end” of timescale $\tau = t/\epsilon^2$; and the blue one of c) corresponds to that by the end of $\tau = t/\epsilon$ scale. The red and green curves are replotted in later timescales for easy reference.

those intervening the regions of $\phi = 0$ and $\phi = 1/2$, and similarly for the other type of layers. The local coordinates are chosen in a standard fashion typical of the phase-field models of solidification. That is, the distance along the centered level set is one of the coordinates which is here denoted by s and the distance from it along the normal to it, r , as the other. The latter is stretched as $\rho = r/\epsilon$. The transformed governing equations give at the leading order

$$-\tau v^{(0)} \frac{\partial \tilde{\phi}^{(0)}}{\partial \rho} = -\gamma f'_{\text{dw}}(\tilde{\phi}^{(0)}) + \gamma \frac{\partial^2 \tilde{\phi}^{(0)}}{\partial \rho^2} \quad (3.10)$$

where $v^{(0)}$ is the zeroth order term in the asymptotic expansion (in ϵ) of the normal velocity of the base contour whose positive value implies that the interface moves in the direction of positive r . $\tilde{\phi}^{(0)}$ is the leading order term in the local expansion of the phase-field variable. On multiplying both sides of the above equation with $\partial \tilde{\phi}^{(0)}/\partial \rho$ and integrating leads to

$$\tau v^{(0)} \int_{-\infty}^{\infty} \frac{\partial \tilde{\phi}^{(0)}}{\partial \rho} \frac{\partial \tilde{\phi}^{(0)}}{\partial \rho} d\rho = \gamma (f_{\text{dw}}(\phi^{(0)}|_{+}) - f_{\text{dw}}(\phi^{(0)}|_{-})) \quad (3.11)$$

after matching with the outer solution. For the interface between the stable phases, i.e., $\phi = 0$ and $\phi = 1$, the r.h.s of the above equation vanishes implying the static behavior of the interface in this timescale. In contrast, if the interface separates an extended region corresponding to a stable phase from that of $\phi = 1/2$, $v^{(0)}$ is non zero in such a way that the movement of the interface leads to the shrinkage of the $\phi = 1/2$ region. This also rules out the possibility of the generation of fresh $\phi = 1/2$ bulks by the way of breakdown of the interface between $\phi = 0$ and $\phi = 1$ midway. Thus by the ‘‘end’’ of this timescale, only bulks corresponding to $\phi = 0$ and $\phi = 1$ survive (Fig. 3.1c).

3.2.3 Timescale $\tau = t$

The leading order outer analysis in this timescale is presented at the beginning of this section. As extended regions of $\phi = 1/2$ did not survive from the previous timescale, there remains two things to be addressed with regard to this. First, the shrinkage of the $\phi = 1/2$ regions implies that an initial setting like the one shown in Fig. 3.2a) evolves to that in Fig. 3.2b). Whether or not this residual spike survives is yet to be answered. Next, a possibility of regeneration of the bulk regions of $\phi = 1/2$ as a consequence of the dynamics happening at the current scale has to be evaluated. Analysis in the local co-ordinates helps address these issues. At leading order, the requirement is

$$\frac{\partial^2 \tilde{\phi}^{(0)}}{\partial \rho^2} = f'_{\text{dw}}(\tilde{\phi}^{(0)}). \quad (3.12)$$

The only solution of the above differential equation with the limits $\tilde{\phi}^{(0)} \rightarrow 0$ as $\rho \rightarrow \pm\infty$ is $\tilde{\phi}^{(0)} = 0$ thus eliminating the possibility of spiked solutions. The details of the proof are provided in appendix B.1.2. Similar is the analysis for the (inverted) spikes in the $\phi = 1$ bulks. On the other hand, for the regeneration of the $\phi = 1/2$ bulks from the interface between $\phi = 0$ and $\phi = 1$ regions, the interface has to split midway into two segments moving in opposite directions away from each other or in the same direction with the leading one moving faster and the other lagging behind. However, when on a contour corresponding to one such fragments, the recovered leading order requirement is the same Eq. (3.12) but with one of the boundary conditions replaced by $\tilde{\phi}^{(0)} \rightarrow 1/2$ which cannot have solutions. This is because assuming the contrary leads to a contradiction on multiplying Eq. (3.12) by $\frac{\partial \tilde{\phi}^{(0)}}{\partial \rho}$ and integrating the resultant from $-\infty$ to ∞ . Therefore, neither are extended regions of $\phi = 1/2$ exist to begin with nor are they created as the dynamics takes place, thus justifying the common practice of working with only $\phi^{(0)} = 0$ and $\phi^{(0)} = 1$ as the relevant solutions of Eq. (3.7). Continuing the analysis at next order retrieves the standard law of motion by mean curvature in the absence of driving force specifier Δf whereas the following in its presence.

$$\tau v^{(0)} \int_{-\infty}^{\infty} \frac{\partial \tilde{\phi}^{(0)}}{\partial \rho} \frac{\partial \tilde{\phi}^{(0)}}{\partial \rho} d\rho = \Delta f (\mathfrak{g}(\phi^{(0)}|_+) - \mathfrak{g}(\phi^{(0)}|_-)) - \gamma \kappa^{(0)} \int_{-\infty}^{\infty} \frac{\partial \tilde{\phi}^{(0)}}{\partial \rho} \frac{\partial \tilde{\phi}^{(0)}}{\partial \rho} d\rho \quad (3.13)$$

where $\kappa^{(0)}$ is the zeroth order term in the asymptotic expansion of the curvature of the base contour.

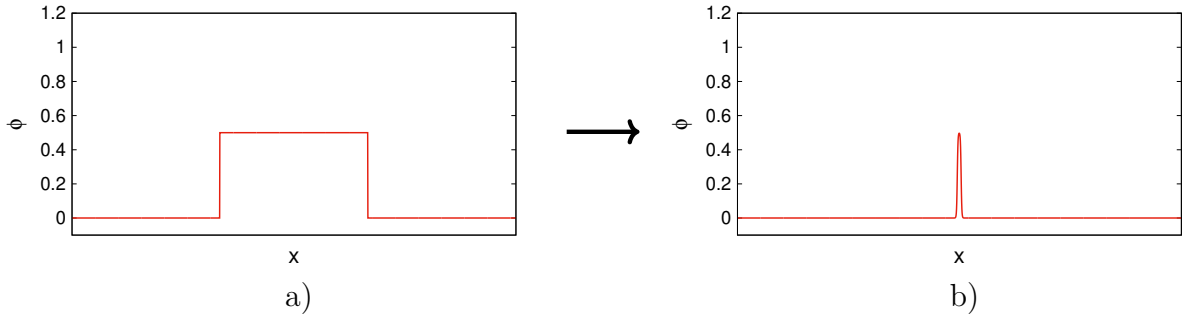


Figure 3.2: Schematic showing the shrinkage of a) an extended region corresponding to $\phi = 1/2$ to b) a spike, as per the prediction of the asymptotic analysis in the $\tau = t/\epsilon$ timescale.

Finally, the illustrations presented in Figs. 3.1 and 3.2 must not be allowed to form an impression that the performed analysis applies only for the case of one spatial dimension. To avoid possible misunderstanding, the various stages in the evolution as predicted by the analysis of the current section are re-demonstrated for a 2D case in Fig. 3.3 when the driving forces are absent. Three circular regions corresponding to $\phi = 0$, 0.5 and 0.8 are filled in the matrix of $\phi = 1$ phase (Fig. 3.3a)). The evolution as per the above

analysis is such that the 0.8 phase is eliminated in the earliest timescale $\tau = t/\epsilon^2$ followed by that of the 0.5 phase in the next scale. Further, the dynamics of the disappearance are different for the different circles. The circle corresponding to 0.8 disappears into 1 retaining its boundary (Fig. 3.3b)). Whereas, the 0.5 circle and the 1 circle disappear by the way of shrinking (Fig. 3.3c) and d), respectively) with the former's rate staying the same throughout its evolution due to Eq. (3.11) while that of the latter increasing with time due to $|v^{(0)}| \propto |\kappa^{(0)}|$ behavior.

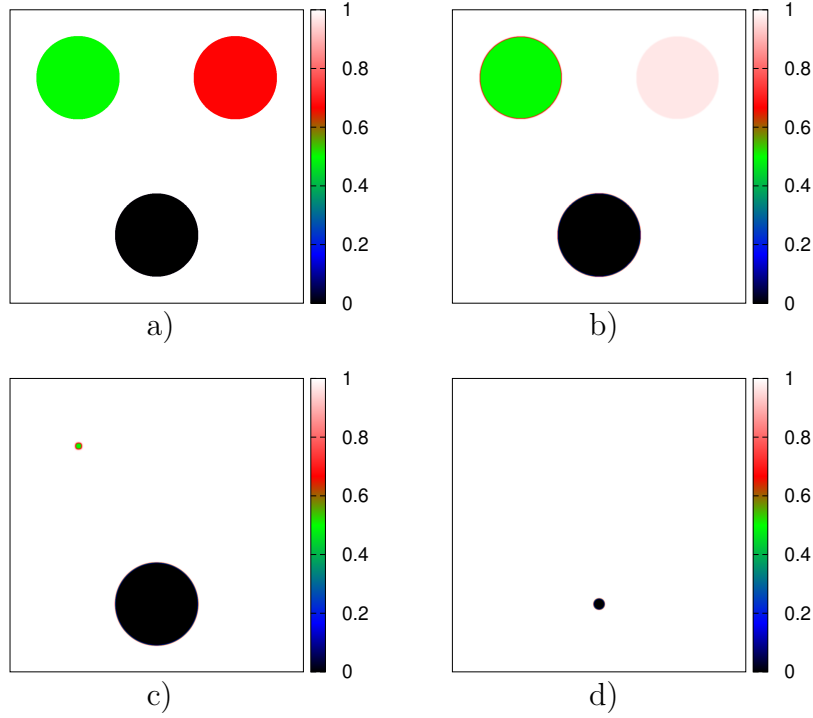


Figure 3.3: Evolution of an initially set phase-field profile in timescales $\tau = t/\epsilon^2$, t/ϵ and t as per the predictions of the current section. The initial filling is shown in a). Profiles towards the end of times scales $\tau = t/\epsilon^2$ and t/ϵ are shown in b) and c), respectively. A late stage in $\tau = t$ scale where the $\phi = 0$ circle almost shrank down is shown in d).

From the insights derived thus far, the matched asymptotic analysis will be carried out next on the multi-phase-field governing equations.

3.3 Multi-phase-field asymptotic analysis of grain growth

The governing equations on which the matched asymptotic analysis is to be performed are as follows.

$$\tau(\phi) \frac{\partial \phi_\beta}{\partial t} = -\frac{\delta F}{\delta \phi_\beta} - \lambda, \quad \beta \in \{1, 2, \dots, N\} \quad (3.14)$$

with

$$\frac{\delta F}{\delta \phi_\beta} = \frac{1}{\epsilon} f_\alpha \frac{\partial \mathbf{g}_\alpha(\phi)}{\partial \phi_\beta} + \frac{1}{\epsilon^2} \gamma \frac{\partial W(\phi)}{\partial \phi_\beta} - \gamma \nabla^2 \phi_\beta$$

and

$$\lambda = \frac{1}{N} \sum_{\beta=1}^N -\frac{\delta F}{\delta \phi_\beta}.$$

Where, α runs over each of the phases and the Einstein's convention of summation over repeated indices is employed. It is to be recalled that ϕ without any suffix refers to the entire phase-field variable $(\phi_1, \phi_2, \dots, \phi_N)$.

As with the scalar phase-field analysis, the behavior of the system of equations Eq. (3.14) is looked at in the $\tau = t/\epsilon^2$ timescale to begin with.

3.3.1 Timescale $\tau = t/\epsilon^2$

The leading order system of equations are

$$\tau(\phi^{(0)}) \frac{\partial \phi_\beta^{(0)}}{\partial \tau} = -\gamma \frac{\partial W(\phi)}{\partial \phi_\beta}(\phi^{(0)}) + \gamma \frac{1}{N} \sum_{\alpha=1}^N \frac{\partial W(\phi)}{\partial \phi_\alpha}(\phi^{(0)}). \quad (3.15)$$

By considering $W(\phi^{(0)}(x, \tau))$ and differentiating it with respect to τ , it can be readily shown by following the arguments of section 2.3.3.1 that the evolution of $\phi^{(0)}(x, \tau)$ as per equation is in such a way that the $W(\phi^{(0)}(\tau))$ reduces monotonically with time τ . Furthermore, since $W(\phi)$ is a well, i.e., bounded below, $W(\phi^{(0)}(x, \tau))$ has to converge eventually. Assuming that $\phi^{(0)}(x, \tau)$ itself converges as $\tau \rightarrow \infty$, then the limit of convergence must be such that the r.h.s of Eq. (3.15) evaluated at it has to vanish for each index β . That is, denoting $\lim_{\tau \rightarrow \infty} \phi^{(0)}(x, \tau)$ by $\phi^{(0)}(x, \infty)$,

$$\begin{aligned} \frac{\partial W(\phi)}{\partial \phi_\beta}(\phi^{(0)}(x, \infty)) &= \frac{1}{N} \sum_{\alpha=1}^N \frac{\partial W(\phi)}{\partial \phi_\alpha}(\phi^{(0)}(x, \infty)) \quad \forall \beta \in \{1, 2, \dots, N\} \\ \implies \frac{\partial W(\phi)}{\partial \phi_\beta}(\phi^{(0)}(x, \infty)) &= \frac{\partial W(\phi)}{\partial \phi_\alpha}(\phi^{(0)}(x, \infty)) \quad \forall \alpha, \beta \in \{1, 2, \dots, N\}. \end{aligned} \quad (3.16)$$

Or, yet in other words, considering a Euclidean geometry for the space of vectors $\phi = (\phi_1, \phi_2, \dots, \phi_N)$, the gradient of $W(\phi)$ at $\phi^{(0)}(x, \infty)$ should point in the $(1, 1, \dots, 1)$ direction. That means, when on such a point on the $\sum_{\beta=1}^N \phi_\beta = 1$ hyperplane (which is actually of interest), the only way to have a change in W by going infinitesimally away from the point is by leaving the plane. Thus, such points are the critical points of $W(\phi)$

when restricted to the $\sum_{\beta=1}^N \phi_{\beta} = 1$ hyperplane. More directly, let us consider this restriction W_R , expressed without loss of generality as

$$W_R(\phi_1, \phi_2, \dots, \phi_{N-1}) = W \left(\phi_1, \phi_2, \dots, \phi_{N-1}, 1 - \sum_{\alpha=1}^{N-1} \phi_{\alpha} \right) \quad \forall \quad 0 \leq \sum_{\alpha=1}^{N-1} \phi_{\alpha} \leq 1.$$

Further, let ${}_R\phi$ stand for $(\phi_1, \phi_2, \dots, \phi_{N-1})$. Then,

$$\begin{aligned} \frac{\partial W_R({}_R\phi)}{\partial \phi_{\beta}} &= \frac{\partial W(\phi)}{\partial \phi_{\beta}} + \frac{\partial W(\phi)}{\partial \phi_N} \frac{\partial}{\partial \phi_{\beta}} \left(1 - \sum_{\alpha=1}^{N-1} \phi_{\alpha} \right) \\ &= \frac{\partial W(\phi)}{\partial \phi_{\beta}} - \frac{\partial W(\phi)}{\partial \phi_N} \quad \forall \beta \in \{1, 2, \dots, N-1\}. \end{aligned}$$

However, the points to which the phase-field vector eventually converges to are such that Eq. (3.16) is fulfilled, implying $\frac{\partial W_R({}_R\phi)}{\partial \phi_{\beta}}({}_R\phi^{(0)}(x, \infty)) = 0 \quad \forall \beta \in \{1, 2, \dots, N-1\}$. That is, they are the critical points of the restriction of $W(\phi)$ to the $\sum_{\beta=1}^N \phi_{\beta} = 1$ hyperplane.

Thus, by the end of this timescale, regions corresponding to the local minima or the local maxima or the saddle points of W_R alone survive. Note that if the Lagrange formulation is not implemented, the points attained are the critical points of $W(\phi)$ itself as the rightmost term of Eq. (3.15) does not occur in such a case.

Before proceeding with further analysis, we now take a short interlude to specialize to the case of three phases ($N = 3$) and set up some associated notation. This is to facilitate an easy visualization of the concepts and arguments to be invoked in the analysis at next orders and also of their predictions. The Gibbs triangle is shown in Fig. 3.4. It will be assumed that $W(\phi)$ is in such a way that the local minima of its restriction $W_R(\phi)$ occur only at the vertices of the triangle, $(1, 0, 0)$, $(0, 1, 0)$ and $(0, 0, 1)$. A critical point necessarily occurs at the centroid of the triangle and only this can be the local maximum. The saddle points can only occur on the lines T_1 , T_2 and T_3 joining the triangle center to the edge centers. Furthermore, it will be assumed that any initial condition pertaining to the region R1 converges to the vertex V1 in the current timescale and similarly for the regions and vertices (R2,R3) and (V2,V3), respectively. The only way a saddle point can be realized by the end of the current timescale is if the initially filled value were to lie on any of the lines T_1 , T_2 and T_3 . Sometimes, the phases are not given explicit names but are referred to by their co-ordinates, for example, as ‘ $(1, 0, 0)$ phase’ or ‘ $(1/3, 1/3, 1/3)$ phase’ etc. The restrictions of the symmetric classical well $W^C = \phi_1^2 \phi_2^2 + \phi_2^2 \phi_3^2 + \phi_3^2 \phi_1^2$ and the Folch-Plapp well $W^{FP} = \phi_1^2(1 - \phi_1)^2 + \phi_2^2(1 - \phi_2)^2 + \phi_3^2(1 - \phi_3)^2$ are depicted in Figs. 3.5 and 3.6, respectively for quick reference and familiarization. It has to be noted that the former is devoid of any local maximum over the plane $\phi_1 + \phi_2 + \phi_3 = 1$ and the saddle point occurs at the triangle center. For W^{FP} , the metastable phases or saddle points are at the edge centers and the unstable phase is at the triangle center. The associated

Hessian matrices immediately verify these facts about the functions. Further it will be assumed that all our wells in the thesis exhibit the same property, i.e., their critical points can be determined by applying the second derivative test just once. Equipped with the details of this special case, we now resume the analysis of next orders.

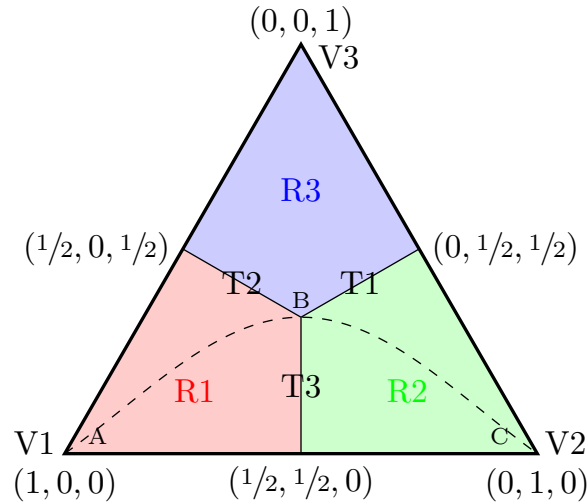


Figure 3.4: Gibbs triangle showing the regions R_1 , R_2 and R_3 which are characterized by their relation to the stable phases (vertices), and the lines T_1 , T_2 and T_3 which are the only choices that are available for the saddle points (the metastable phases) to lie on. A trail ABC passing through the critical point at the centroid is also shown.

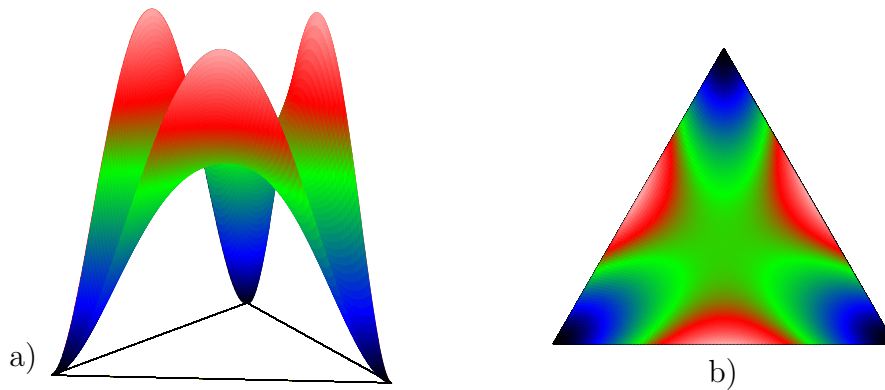


Figure 3.5: Plot of the restriction of the three phase, symmetric classical well $W^C = \phi_1^2 \phi_2^2 + \phi_2^2 \phi_3^2 + \phi_3^2 \phi_1^2$ to the Gibbs triangle; a) as a surface graph over the triangle and b) as a heat map.

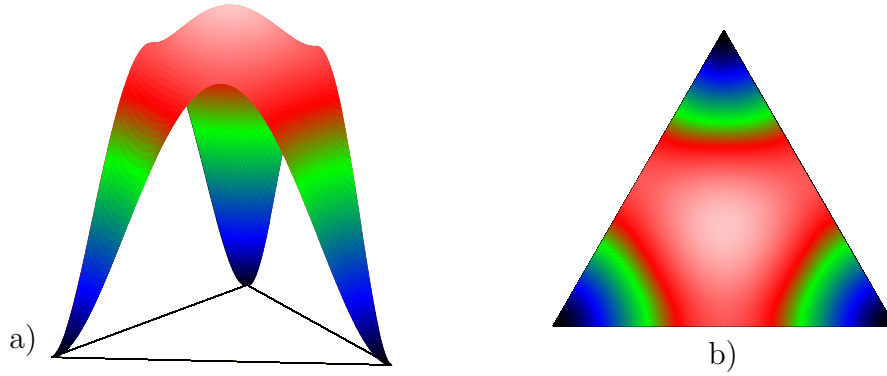


Figure 3.6: Plot of the restriction of the Folch-Plapp well $W^{FP} = \phi_1^2(1 - \phi_1)^2 + \phi_2^2(1 - \phi_2)^2 + \phi_3^2(1 - \phi_3)^2$ to the Gibbs triangle; a) as a surface graph over the triangle and b) as a heat map.

3.3.2 Timescale $\tau = t/\epsilon$

The leading order equations in this timescale are same as those given by Eq. (3.16) and the various solutions extend over the domain in a manner consistent with the developed microstructure at the previous timescale. As bulks of distinct phase-field values coexist, they have to be separated by interior layers and hence it is meaningful to perform a local analysis. However, a question arises as to which contour to choose for centering the local coordinates. Certainly, contour corresponding to a particular value of the phase-field vector variable as a whole cannot be considered as it is unknown whether or not the interface contains such a value. For instance, an interface between $(1, 0, 0)$ and $(0, 1, 0)$ bulks may not have a value of $(1/2, 1/2, 0)$ at any spatial point in the region where it extends. Even if a locus corresponding to a particular value is known to exist, it may not remain intact throughout the course of the evolution and may disintegrate. As an illustration, consider an initial filling in a 1D domain along the path ABC of Fig 3.4. That is, at the left end of the domain, the phase-field is assigned a value of $(1, 0, 0)$ and as one moves into the domain the filling is as per the values encountered on the path eventually reaching $(0, 1, 0)$ at the right end. The evolution at the previous timescale dictates that the regions corresponding to the filling of segments AB and BC with B excluded eventually attain the values of $(1, 0, 0)$ and $(0, 1, 0)$, respectively, and the spatial point corresponding to point B retains the value of $(1/3, 1/3, 1/3)$ as it is a critical point of the restricted multi-well. Thus, here is an instance of the $(1, 0, 0)$ and $(0, 1, 0)$ bulks being separated by $(1/3, 1/3, 1/3)$ point as part of the interface as shown in Fig. 3.7a), at least at the beginning of the timescale. Furthermore, as the dynamics happens, the ϕ_3 component may collapse to some other value or decay altogether as depicted in Figs. 3.7b) and 3.7c), respectively. Thus, it is not advisable to transform to the natural coordinates of a vector valued contour. Rather, since there exists atleast one component which takes distinct values in two adjacent bulks, a switch of coordinate system to such a contour will serve

the purpose. However, a final question remains to be addressed, namely, when contours corresponding to two different components are chosen will the predicted dynamics be consistent? We note that, it is not only going to be consistent but indeed is necessary for a complete analysis in some cases especially where the Lagrange multiplier formulation is not opted for. This topic will be revisited in a while, for now, we proceed with the local analysis.

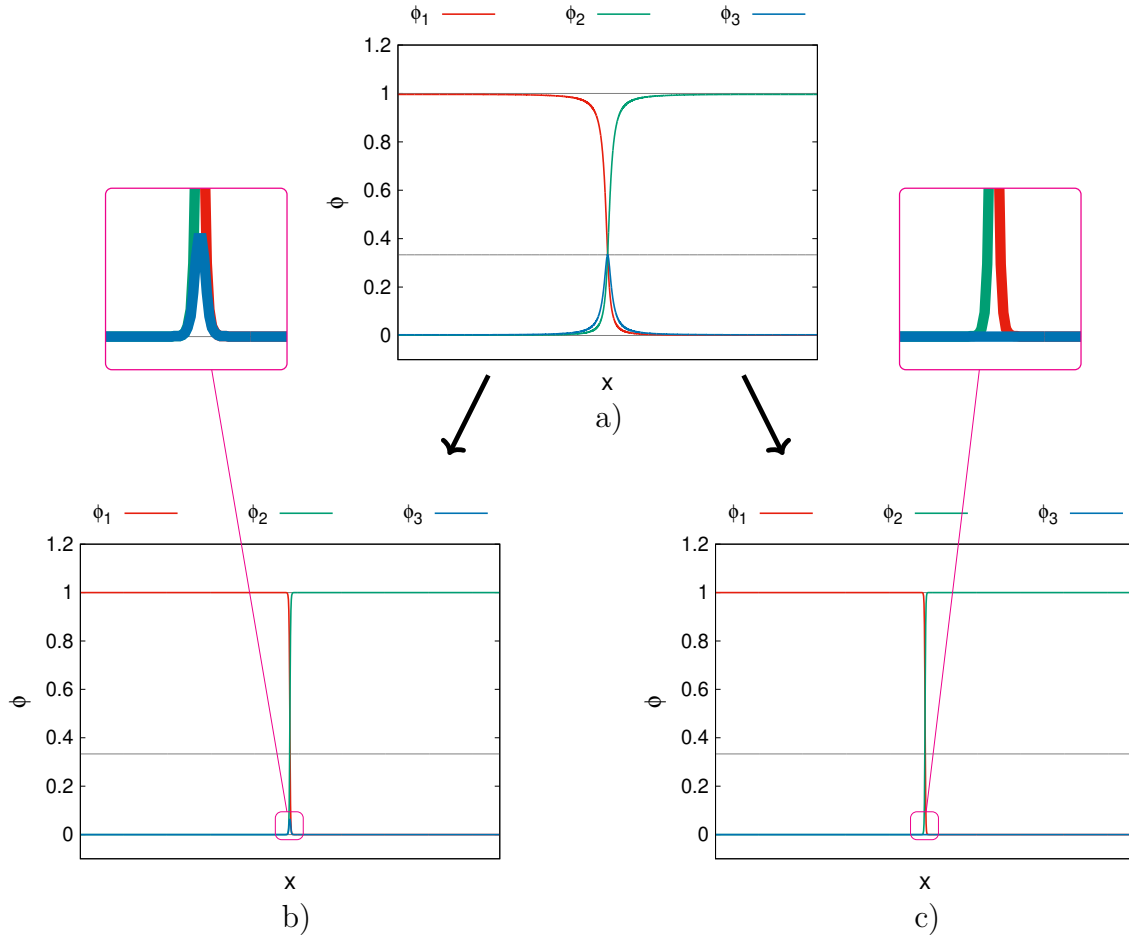


Figure 3.7: Various stages and possibilities for the evolution of an initial profile filled as per the trail ABC of Fig. 3.4. Profile towards the end of the timescale $\tau = t/\epsilon^2$ is schematically shown in a) while b) and c) are two possibilities for its further evolution. In b) the third component survived whereas it disintegrated completely in c) as highlighted by the insets.

Consider two regions corresponding to the critical points of the restricted multi-well that have materialized in the previous timescale from the initial filling. Let a component of the phase-field be such that it takes distinct values in the two regions. By transforming to the natural coordinates of a contour corresponding to an intermediate value of the

component and stretching it as in section 3.2.2, the requirement at the leading order is

$$-\tau(\tilde{\phi}^{(0)})v^{(0)}\frac{\partial\tilde{\phi}_\beta^{(0)}}{\partial\rho} = -\gamma\frac{\partial W(\phi)}{\partial\phi_\beta}(\tilde{\phi}^{(0)}) + \gamma\frac{\partial^2\tilde{\phi}_\beta^{(0)}}{\partial\rho^2} - \tilde{\lambda}^{(0)}$$

where

$$\tilde{\lambda}^{(0)} = \frac{1}{N} \sum_{\beta=1}^N \left(-\gamma\frac{\partial W(\phi)}{\partial\phi_\beta}(\tilde{\phi}^{(0)}) + \gamma\frac{\partial^2\tilde{\phi}_\beta^{(0)}}{\partial\rho^2} \right).$$

Multiplying both sides of the β^{th} equation with $\frac{\partial\tilde{\phi}_\beta^{(0)}}{\partial\rho}$ for each β and summing all the resultant equations gives

$$\begin{aligned} -\tau(\tilde{\phi}^{(0)})v^{(0)}\frac{\partial\tilde{\phi}_\beta^{(0)}}{\partial\rho}\frac{\partial\tilde{\phi}_\beta^{(0)}}{\partial\rho} &= -\gamma\frac{\partial W(\phi)}{\partial\phi_\beta}(\tilde{\phi}^{(0)})\frac{\partial\tilde{\phi}_\beta^{(0)}}{\partial\rho} + \gamma\frac{\partial^2\tilde{\phi}_\beta^{(0)}}{\partial\rho^2}\frac{\partial\tilde{\phi}_\beta^{(0)}}{\partial\rho} - \tilde{\lambda}^{(0)}\sum_{\beta=1}^N\frac{\partial\tilde{\phi}_\beta^{(0)}}{\partial\rho} \\ &= -\gamma\frac{\partial W(\tilde{\phi}^{(0)})}{\partial\rho} + \gamma\frac{\partial^2\tilde{\phi}_\beta^{(0)}}{\partial\rho^2}\frac{\partial\tilde{\phi}_\beta^{(0)}}{\partial\rho} - \tilde{\lambda}^{(0)}\frac{\partial}{\partial\rho}\sum_{\beta=1}^N\tilde{\phi}_\beta^{(0)}. \end{aligned} \quad (3.17)$$

Since the initial filling is demanded to satisfy the summation constraint throughout the domain, the above reduces to

$$-\tau(\tilde{\phi}^{(0)})v^{(0)}\frac{\partial\tilde{\phi}_\beta^{(0)}}{\partial\rho}\frac{\partial\tilde{\phi}_\beta^{(0)}}{\partial\rho} = -\gamma\frac{\partial W(\tilde{\phi}^{(0)})}{\partial\rho} + \gamma\frac{\partial^2\tilde{\phi}_\beta^{(0)}}{\partial\rho^2}\frac{\partial\tilde{\phi}_\beta^{(0)}}{\partial\rho}. \quad (3.18)$$

Note that the exact same condition, Eq. (3.18), is retrieved in the absence of the Lagrange implementation as well. Integrating it leads, upon matching with the outer solution, to

$$v \int_{-\infty}^{\infty} \tau(\tilde{\phi}^{(0)})\frac{\partial\tilde{\phi}_\beta^{(0)}}{\partial\rho}\frac{\partial\tilde{\phi}_\beta^{(0)}}{\partial\rho}d\rho = \gamma(W(\phi|_+) - W(\phi|_-)) \quad (3.19)$$

$$= \gamma(W_{R(r)\phi|_+} - W_{R(r)\phi|_-}) \quad (3.20)$$

in the Lagrange multiplier implementation.

Since the integral on the l.h.s is always positive, the interface moves in the positive r direction if $W_{R(r)\phi|_+} > W_{R(r)\phi|_-}$ and in the negative direction if $W_{R(r)\phi|_+} < W_{R(r)\phi|_-}$ and remains immobile if $W_{R(r)\phi|_+}$ and $W_{R(r)\phi|_-}$ equal each other. That is, the extended regions of low energy critical points expand at the expense of the higher energy ones. This tendency also makes sure that an interface between two equilibrium phases is stable against splitting to give rise to metastable and unstable phases. That is, a perturbation leading to a transition like the one shown in Fig. 3.8 immediately reverts back and the original configuration remains stable. However, when Lagrange multiplier formulation is not implemented a different kind of transition can still be metastable, in that, does not

revert back to the original state for some multi-wells. For example when the multi-well $W^{FP} = \phi_1^2(1 - \phi_1)^2 + \phi_2^2(1 - \phi_2)^2 + \phi_3^2(1 - \phi_3)^2$ is employed not only the phases $(1, 0, 0)$, $(0, 1, 0)$ and $(0, 0, 1)$ exhibit the lowest energy but also the ones like $(0, 0, 0)$, $(1, 1, 0)$, etc. when the phase-field values are not restricted to the $\phi_1 + \phi_2 + \phi_3 = 1$ plane. Therefore, if two profiles shown in Fig. 3.9a) move in opposite directions, the resultant opening created (Fig. 3.9b)) will still be an equilibrium phase, in that, has the same low energy as the original bulk phases and thus the configuration does not revert back due to Eq. (3.19). In the like manner, the transition does not move in the forward direction thereby leading to the expansion of the newly formed phase, either. Thus, only the bulks corresponding to the minima (assuming all of them are equally energetic) of the entire multi-well in the absence of summation constraint and the restricted multi-well in its presence survive by the end of this timescale.

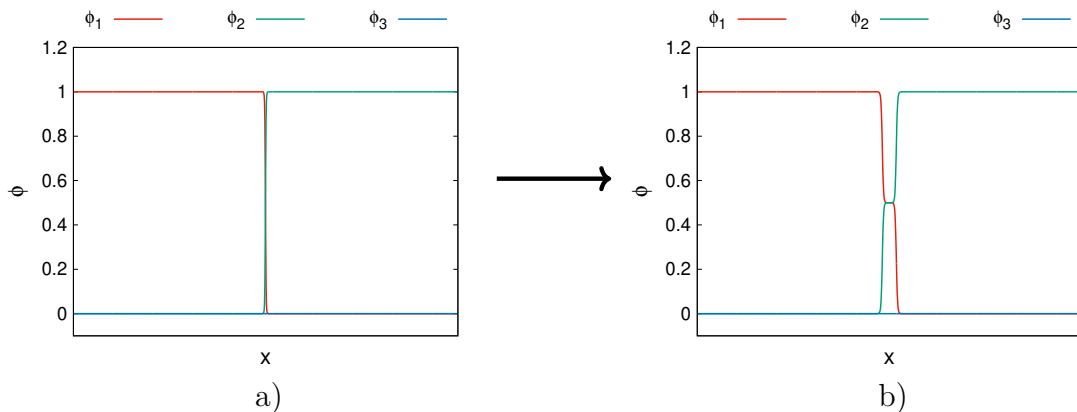


Figure 3.8: Schematic of a perturbation in which the non-zero components ϕ_1 and ϕ_2 (i.e., the components characterizing the stable phases $(1, 0, 0)$ and $(0, 1, 0)$, respectively) split midway giving rise to $(1/2, 1/2, 0)$ phase. This transition is unstable in the current, $\tau = t/\epsilon$, timescale and reverts back immediately.

3.3.3 Timescale $\tau = t$

By the beginning of this timescale, the microstructure consists of bulk equilibrium phases separated by binary interfaces or meeting at a triple or higher order junctions. The outer analysis requirements are consistent with this picture.

We perform a detailed local analysis. It has to be noted that since there are two kinds of phase boundaries, namely, one dimensional binary interfaces and zero dimensional junctions, the interior layer behaviors at both these types of boundaries have to be taken into consideration. While the local analysis for the binary interfaces is carried out in the usual manner viz. by matching with the outer expansions corresponding to the bulks

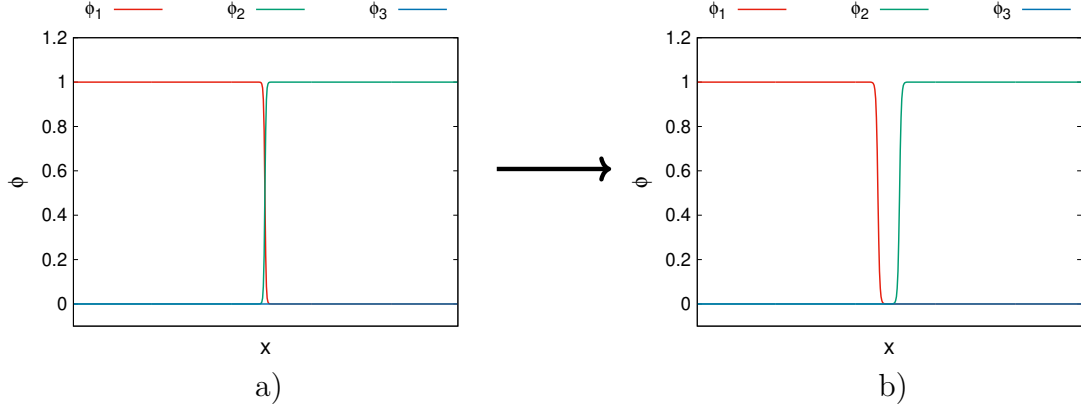


Figure 3.9: Schematic of a perturbation in which the non-zero components ϕ_1 and ϕ_2 (characterizing the stable phases $(1,0,0)$ and $(0,0,1)$, respectively) move apart giving rise to $(0,0,0)$ phase. Depending on the choice of the model, this perturbation may sustain but never grows in the current timescale of $\tau = t/\epsilon$.

as in the above timescale, the junctions have to be treated more carefully as the inner expansions of the binary interfaces themselves behave as the outer expansions along with those of bulk when it comes to the junctions. That is, the local solutions at the junctions have to be matched with different functions along different directions. We begin with the local analysis corresponding to the interior layers that act as the binary interfaces.

3.3.3.1 Leading order local analysis of binary interfaces

At leading order, the requirement is

$$\begin{aligned}
 0 &= -\gamma \frac{\partial W(\phi)}{\partial \phi_\beta}(\tilde{\phi}^{(0)}) + \gamma \frac{\partial^2 \tilde{\phi}_\beta^{(0)}}{\partial \rho^2} + \gamma \frac{1}{N} \sum_{\alpha=1}^N \left(\frac{\partial W(\phi)}{\partial \phi_\alpha}(\tilde{\phi}^{(0)}) - \frac{\partial^2 \tilde{\phi}_\alpha^{(0)}}{\partial \rho^2} \right) \\
 \implies \gamma \frac{\partial^2 \tilde{\phi}_\beta^{(0)}}{\partial \rho^2} &= \gamma \frac{\partial W(\phi)}{\partial \phi_\beta}(\tilde{\phi}^{(0)}) - \gamma \frac{1}{N} \sum_{\alpha=1}^N \frac{\partial W(\phi)}{\partial \phi_\alpha}(\tilde{\phi}^{(0)}) + \gamma \frac{1}{N} \frac{\partial^2}{\partial \rho^2} \sum_{\alpha=1}^N \tilde{\phi}_\alpha^{(0)} \\
 \implies \frac{\partial^2 \tilde{\phi}_\beta^{(0)}}{\partial \rho^2} &= \frac{\partial W(\phi)}{\partial \phi_\beta}(\tilde{\phi}^{(0)}) - \frac{1}{N} \sum_{\alpha=1}^N \frac{\partial W(\phi)}{\partial \phi_\alpha}(\tilde{\phi}^{(0)}). \tag{3.21}
 \end{aligned}$$

The counterpart of the above equation in the case of scalar phase-field variable amounts to evaluating an integral which can be solved in closed form at least for a few choices of the double well. For instance, it is easy to show by explicitly integrating that the archetype bi-quadratic function $\phi^2(1-\phi)^2$ gives hyperbolic tangent solution, $1/2 \pm 1/2 \tanh(\rho)$. Such is not the case with the multi-phase-field models: general methods to express the solutions of Eq. (3.21) are not available. However, a difficulty in the explicit construction of the solution does not, in fact, pose a problem in determining the governing laws or

the properties of the phase-field profiles, as the relevant information can be extracted in a generic manner. For instance, a configuration like the one shown in Fig. 3.10b) results due to the shrinkage of the $(1/2, 1/2, 0)$ bulk separating two extended regions of the equilibrium phase $(1, 0, 0)$ (Fig. 3.10a)). Likewise, an initial filling along the trail of Fig. 3.4 but with an extended region corresponding to point B, i.e., $(1/3, 1/3, 1/3)$, as shown in Fig. 3.11 results in a configuration like the one depicted in Fig. 3.7a) as per the predictions of the previous timescale. Questions as to whether such configurations are retained or do they transition to other profiles to satisfy Eq. (3.21), and if they do, what the characteristics of such solutions are etc., can be answered for a generic multi-well without actually constructing the solution. The analysis easily follows, as noted in Ref. [30], from the proof of a lemma presented in Ref. [53]. The ready adaptation for the case of summation constraint is worked out here for the sake of completeness.

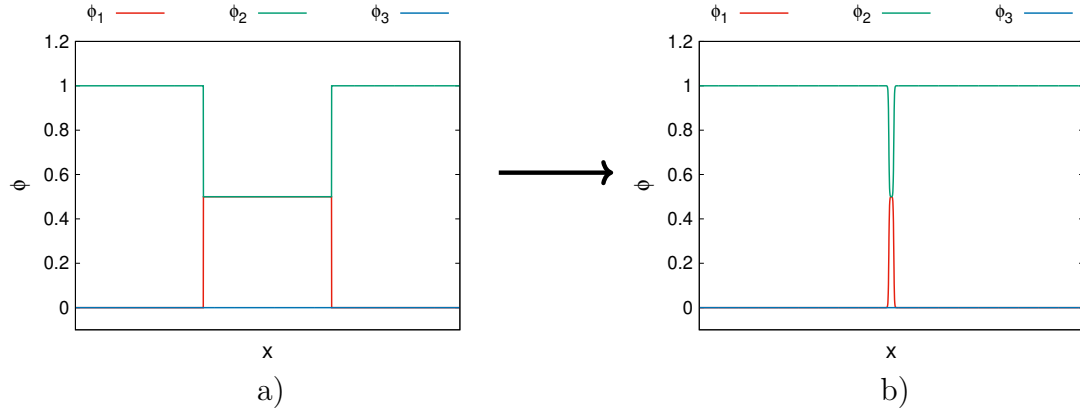


Figure 3.10: Schematic showing the shrinkage of a) an extended region of the $(1/2, 1/2, 0)$ phase resulting in the formation of b) spikes in the profiles of the components ϕ_1 and ϕ_2 as per the prediction of the asymptotic analysis pertaining to the $\tau = t/\epsilon$ timescale.

First of all, it can be readily shown that the so called equi-partition of the interfacial energy between the well and the gradient contributions also holds true in the multi-phase-field case. Multiplying both sides of Eq. (3.21) with $\frac{\partial \tilde{\phi}_\beta^{(0)}}{\partial \rho}$ for each β and summing all the resultant ones to obtain a single equation and, in turn, subsequently integrating the latter from $-\infty$ to any ρ establishes it, which reads

$$\frac{1}{2} \sum_{\beta=1}^N \left(\frac{\partial \tilde{\phi}_\beta^{(0)}}{\partial \rho} \right)^2 = W(\tilde{\phi}^{(0)}). \quad (3.22)$$

Next, we discuss what path on the Gibbs simplex does the solution of Eq. (3.21) correspond to for a given pair of bulk phases at infinity, i.e., the matching conditions. Note that Eq. (3.21) is the Euler-Lagrange equation of the following functional Eq. (3.23)

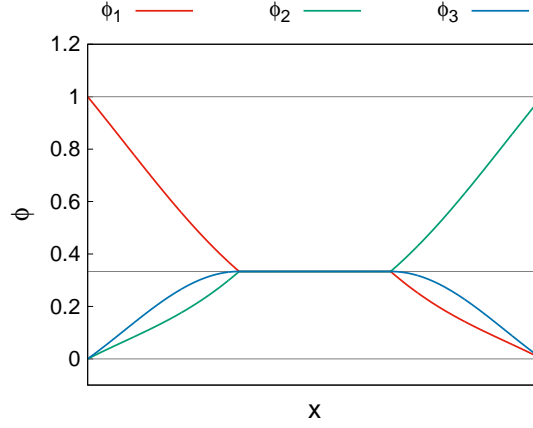


Figure 3.11: An initial filling corresponding to the trail ABC of Fig. 3.4, but with an extended region corresponding to point B, i.e., phase $(1/3, 1/3, 1/3)$.

when $\tilde{\phi}_\beta^{(0)}$ is constrained to the $\sum_{\beta=1}^N \tilde{\phi}_\beta^{(0)} = 1$ hyperplane.

$$\int_{-\infty}^{\infty} \left(\frac{1}{2} \sum_{\beta=1}^N \left(\frac{\partial \tilde{\phi}_\beta^{(0)}}{\partial \rho} \right)^2 + W(\tilde{\phi}^{(0)}) \right) d\rho. \quad (3.23)$$

In other words, the minimizer of the above functional satisfying the far end conditions and the summation rule is a solution of Eq. (3.21). Instead of looking for it, we shift our focus to a different function which fulfills the same matching conditions and also the summation rule but which is, instead, a minimizer of the following functional

$$\sqrt{2} \int_{-\infty}^{\infty} \sqrt{W(\tilde{\phi}^{(0)})} \left| \frac{\partial \tilde{\phi}^{(0)}}{\partial \rho} \right| d\rho. \quad (3.24)$$

In general, the following inequality is true which is a straightforward outcome of the application of the AM \geq GM inequality to the integrand of Eq. (3.23)

$$\sqrt{2} \int_{-\infty}^{\infty} \sqrt{W(\tilde{\phi}^{(0)})} \left| \frac{\partial \tilde{\phi}^{(0)}}{\partial \rho} \right| d\rho \leq \int_{-\infty}^{\infty} \left(\frac{1}{2} \sum_{\beta=1}^N \left(\frac{\partial \tilde{\phi}_\beta^{(0)}}{\partial \rho} \right)^2 + W(\tilde{\phi}^{(0)}) \right) d\rho. \quad (3.25)$$

The equality holds when both the summands of the integrand on the r.h.s happen to equal each other. On the other hand, this is precisely the case for the minimizer of Eq. (3.23) as proved in Eq. (3.22).

Now, a minimizer of Eq. (3.24) need not also minimize Eq. (3.23). In fact, the former need not even satisfy the property of Eq. (3.22). Moreover, the functional of Eq. (3.24) has infinitely many minimizers as given one it can be reparametrized to give another since the functional in question is invariant under reparametrization, i.e, it only depends

on the trace or the path of the curve $\tilde{\phi}^{(0)} = \tilde{\phi}^{(0)}(\rho)$. However, if the path minimizing Eq. (3.24) can be parametrized in such a way that it satisfies the property of Eq. (3.22) while extending from $-\infty$ to ∞ , then such a curve has to be the minimizer of Eq. (3.23) which we are in search of. Furthermore, it can be shown that given a parametrization of the path, such a kind of its reparameterization is indeed possible. The details are as follows.

Let $\gamma_{\min}(\beta) : [-1, 1] \rightarrow \mathbb{R}^N$ be a curve that corresponds to the path that joins two of the minima of the multi-well W and lies completely on the Gibbs-simplex and which minimizes the following weighted distance, Eq. (3.26), among all such other paths.

$$\int_{-1}^1 \sqrt{W(\gamma(\beta))} \left| \frac{d\gamma}{d\beta} \right| d\beta. \quad (3.26)$$

Further, let the arc length of γ_{\min} be bounded away from zero at each point, i.e., $0 < |\gamma'_{\min i}(\beta)| < \infty \forall \beta \in [-1, 1]$ and $\forall i \in \{1, 2, \dots, N\}$. The details related to the existence of such a curve are provided in appendix B.1.3. Now consider the following initial value problem.

$$\frac{d\beta}{d\rho} = \frac{\sqrt{W(\gamma_{\min}(\beta))}}{|\gamma'_{\min}(\beta)|}, \quad \beta(0) = 0. \quad (3.27)$$

The solution of the above problem exists for all of ρ , i.e., $\rho \in (-\infty, \infty)$ with $\beta \rightarrow -1$ as $\rho \rightarrow -\infty$ and $\beta \rightarrow 1$ as $\rho \rightarrow \infty$ (appendix B.1.3). Since such $\beta(\rho)$ exists, the function defined by $\tilde{\phi}^{(0)}(\rho) = \gamma_{\min}(\beta(\rho))$ on $\rho \in (-\infty, \infty)$ is a curve that satisfies the property Eq. (3.22) as can be easily verified and gives the minimum possible value of Eq. (3.23) and hence is the required solution of Eq. (3.21).

To summarize, the zeroth order contribution $\tilde{\phi}^{(0)}(\rho)$ has such a trace on the Gibbs-simplex that its weighted (Euclidean) length measured with $\sqrt{W(\phi)}$ as the weight is the smallest among all other paths joining the two phases whose interface is under consideration. Let us see the implications of this for some specific situations. Particularly, the two questions raised at the beginning of the section about the fates of the configurations in Figs. 3.10 and 3.11 can be very well predicted based on the knowledge of the above result. Firstly, since the two bulks in the situation of Fig. 3.10 correspond to the same equilibrium phase and as the shortest path joining the same point has zero length, such spikes cannot sustain. Next, even though the dynamics at previous timescale predicts a configuration like in Fig. 3.7a) when starting from Fig. 3.11, it will remain so only if the configuration corresponds to the shortest length joining phases $(1, 0, 0)$ and $(0, 1, 0)$ measured using the weight $\sqrt{W(\phi)}$ as in Eq. (3.26). For example, in the case of the multi-well $W^C = \phi_1^2 \phi_2^2 + \phi_2^2 \phi_3^2 + \phi_3^2 \phi_1^2$, a path joining A and B along the edge of the Gibbs-simplex gives a bigger value for the integral Eq. (3.26) due to the higher weight around $(1/2, 1/2, 0)$ (see Fig. 3.5). While a path like the one shown in Fig. 3.4 may not be weighted as

much but is itself long due to its trajectory and hence can raise the value of the integral. Thus, as a compromise, an intermediate path will be chosen and a profile like the one in Fig. 3.7b) will turn out to correspond to the actual solution of Eq. (3.21). Whereas for the function $W^{FP} = \phi_1^2(1-\phi_1)^2 + \phi_2^2(1-\phi_2)^2 + \phi_3^2(1-\phi_3)^2$, the shortest length is along the edge of the simplex and more so after weighing as per Eq. (3.26) (see Fig. 3.6); therefore, this itself will be the expected solution. The simulation results are consistent with these predictions as expanded in the next chapter. Finally, re-generation of metastable phases as per the transformation of Fig. 3.8 is ruled out at the current timescale as well. This can be readily seen by noting that Eq. (3.22) leads to a contradiction upon the application of the limits $\rho \rightarrow \pm\infty$ if the splitting were to sustain.

3.3.3.2 Next-to-leading order local analysis of binary interfaces

The local analysis at the order next to the leading one will be analyzed presently for the binary interfaces. The corresponding equations read

$$- (\tau^{(0)}v^{(0)} + \gamma\kappa^{(0)}) \frac{\partial \tilde{\phi}_\beta^{(0)}}{\partial \rho} = -f_\alpha \frac{\partial \mathbf{g}_\alpha(\phi)}{\partial \phi_\beta}(\tilde{\phi}^{(0)}) - \gamma \frac{\partial}{\partial \phi_\alpha} \frac{\partial W(\phi)}{\partial \phi_\beta}(\tilde{\phi}^{(0)}) \tilde{\phi}_\alpha^{(1)} + \gamma \frac{\partial^2 \tilde{\phi}_\beta^{(1)}}{\partial \rho^2} - \tilde{\lambda}^{(1)} \quad (3.28)$$

with $\tau^{(0)}$ standing for $\tau(\tilde{\phi}^{(0)})$ and $\tilde{\lambda}^{(1)} = \frac{1}{N} \sum_{\beta=1}^N -\frac{\tilde{\delta F}}{\delta \phi_\beta}^{(1)}$ where $-\frac{\tilde{\delta F}}{\delta \phi_\beta}^{(1)}$ is the r.h.s of the above equation excluding $\tilde{\lambda}^{(1)}$. As before, constructing the sum $\frac{\partial \tilde{\phi}_\beta^{(0)}}{\partial \rho} \frac{\partial \tilde{\phi}_\beta^{(0)}}{\partial \rho}$ by appropriately multiplying the above equation for all the occurring indices β and summing them leads to the single equation

$$\begin{aligned} (\tau^{(0)}v^{(0)} + \gamma\kappa^{(0)}) \frac{\partial \tilde{\phi}_\beta^{(0)}}{\partial \rho} \frac{\partial \tilde{\phi}_\beta^{(0)}}{\partial \rho} &= \left(f_\alpha \frac{\partial \mathbf{g}_\alpha(\phi)}{\partial \phi_\beta} + \gamma \frac{\partial}{\partial \phi_\alpha} \frac{\partial W(\phi)}{\partial \phi_\beta}(\tilde{\phi}^{(0)}) \tilde{\phi}_\alpha^{(1)} - \gamma \frac{\partial^2 \tilde{\phi}_\beta^{(1)}}{\partial \rho^2} \right) \frac{\partial \tilde{\phi}_\beta^{(0)}}{\partial \rho} \\ &= f_\alpha \frac{\partial \mathbf{g}_\alpha(\tilde{\phi}^{(0)})}{\partial \rho} + \gamma \frac{\partial}{\partial \phi_\beta} \frac{\partial W(\phi)}{\partial \phi_\alpha}(\tilde{\phi}^{(0)}) \tilde{\phi}_\beta^{(1)} \frac{\partial \tilde{\phi}_\alpha^{(0)}}{\partial \rho} - \gamma \frac{\partial^2 \tilde{\phi}_\beta^{(1)}}{\partial \rho^2} \frac{\partial \tilde{\phi}_\beta^{(0)}}{\partial \rho} \\ &= f_\alpha \frac{\partial \mathbf{g}_\alpha(\tilde{\phi}^{(0)})}{\partial \rho} + \gamma \frac{\partial}{\partial \phi_\alpha} \frac{\partial W(\phi)}{\partial \phi_\beta}(\tilde{\phi}^{(0)}) \tilde{\phi}_\beta^{(1)} \frac{\partial \tilde{\phi}_\alpha^{(0)}}{\partial \rho} - \gamma \frac{\partial^2 \tilde{\phi}_\beta^{(1)}}{\partial \rho^2} \frac{\partial \tilde{\phi}_\beta^{(0)}}{\partial \rho} \\ &= f_\alpha \frac{\partial \mathbf{g}_\alpha(\tilde{\phi}^{(0)})}{\partial \rho} + \gamma \frac{\partial}{\partial \rho} \left(\frac{\partial W(\phi)}{\partial \phi_\beta}(\tilde{\phi}^{(0)}) \right) \tilde{\phi}_\beta^{(1)} - \gamma \frac{\partial^2 \tilde{\phi}_\beta^{(1)}}{\partial \rho^2} \frac{\partial \tilde{\phi}_\beta^{(0)}}{\partial \rho}. \end{aligned}$$

Integrating the above equation with respect to ρ from $-\infty$ to ∞ results in

$$\begin{aligned} \int_{-\infty}^{\infty} (\tau^{(0)}v^{(0)} + \gamma\kappa^{(0)}) \frac{\partial \tilde{\phi}_\beta^{(0)}}{\partial \rho} \frac{\partial \tilde{\phi}_\beta^{(0)}}{\partial \rho} d\rho &= f_\alpha (\mathbf{g}_\alpha(\phi^{(0)}|_+) - \mathbf{g}_\alpha(\phi^{(0)}|_-)) - \gamma \int_{-\infty}^{\infty} \frac{\partial^2 \tilde{\phi}_\beta^{(1)}}{\partial \rho^2} \frac{\partial \tilde{\phi}_\beta^{(0)}}{\partial \rho} d\rho \\ &\quad + \gamma \int_{-\infty}^{\infty} \frac{\partial}{\partial \rho} \left(\frac{\partial W(\phi)}{\partial \phi_\beta}(\tilde{\phi}^{(0)}) \right) \tilde{\phi}_\beta^{(1)} d\rho. \end{aligned}$$

Integrating by parts the first integral on the r.h.s followed by the application of the matching conditions gives

$$\int_{-\infty}^{\infty} (\tau^{(0)}v^{(0)} + \gamma\kappa^{(0)}) \frac{\partial\tilde{\phi}_{\beta}^{(0)}}{\partial\rho} \frac{\partial\tilde{\phi}_{\beta}^{(0)}}{\partial\rho} d\rho = f_{\alpha} (\mathbf{g}_{\alpha}(\phi^{(0)}|_{+}) - \mathbf{g}_{\alpha}(\phi^{(0)}|_{-})) - \gamma \int_{-\infty}^{\infty} \frac{\partial^3\tilde{\phi}_{\beta}^{(0)}}{\partial\rho^3} \tilde{\phi}_{\beta}^{(1)} d\rho \\ + \gamma \int_{-\infty}^{\infty} \frac{\partial}{\partial\rho} \left(\frac{\partial W(\phi)}{\partial\phi_{\beta}}(\tilde{\phi}^{(0)}) \right) \tilde{\phi}_{\beta}^{(1)} d\rho. \quad (3.29)$$

To evaluate the second term on the r.h.s of the above equation, Eq. (3.21) is differentiated with respect to ρ leading to

$$\frac{\partial^3\tilde{\phi}_{\beta}^{(0)}}{\partial\rho^3} = \frac{\partial}{\partial\rho} \left(\frac{\partial W(\phi)}{\partial\phi_{\beta}}(\tilde{\phi}^{(0)}) \right) - \frac{1}{N} \sum_{\alpha=1}^N \frac{\partial}{\partial\rho} \left(\frac{\partial W(\phi)}{\partial\phi_{\alpha}}(\tilde{\phi}^{(0)}) \right) \\ \Rightarrow \frac{\partial^3\tilde{\phi}_{\beta}^{(0)}}{\partial\rho^3} \tilde{\phi}_{\beta}^{(1)} = \frac{\partial}{\partial\rho} \left(\frac{\partial W(\phi)}{\partial\phi_{\beta}}(\tilde{\phi}^{(0)}) \right) \tilde{\phi}_{\beta}^{(1)} - \frac{1}{N} \sum_{\alpha=1}^N \frac{\partial}{\partial\rho} \left(\frac{\partial W(\phi)}{\partial\phi_{\alpha}}(\tilde{\phi}^{(0)}) \right) \sum_{\beta=1}^N \tilde{\phi}_{\beta}^{(1)} \\ = \frac{\partial}{\partial\rho} \left(\frac{\partial W(\phi)}{\partial\phi_{\beta}}(\tilde{\phi}^{(0)}) \right) \tilde{\phi}_{\beta}^{(1)}.$$

As a consequence, Eq. (3.29) simplifies to

$$\int_{-\infty}^{\infty} \left(\tau(\tilde{\phi}^{(0)})v^{(0)} + \gamma\kappa^{(0)} \right) \frac{\partial\tilde{\phi}_{\beta}^{(0)}}{\partial\rho} \frac{\partial\tilde{\phi}_{\beta}^{(0)}}{\partial\rho} d\rho = f_{\alpha} (\mathbf{g}_{\alpha}(\phi^{(0)}|_{+}) - \mathbf{g}_{\alpha}(\phi^{(0)}|_{-})). \quad (3.30)$$

Since the layer under investigation corresponds to a binary interface, on one far end only one of the \mathbf{g}_{α} s takes the value unity and the rest all vanish, similarly, for the other infinity. Hence, the r.h.s of Eq. (3.30) turns out to be the difference between the bulk energies of the two equilibrium phases whose interface is in question. Thus, the Gibbs-Thomson condition is retrieved. As mentioned in chapter 2, typically, the inverse mobility function $\tau(\tilde{\phi}^{(0)})$ includes the values corresponding to all the possible binary interface types in such a way that when only two of the components are non zero, it reduces precisely to the value of the interface between the phases that are naturally marked by the components. Thus, the above form warns against the use of a multi-well whose shortest weighted path between two equilibrium phase-field values is not along the line joining them, i.e., the respective edge of the Gibbs-simplex. This is because, if the binary interface between two phases were to assume non zero values of any other component not naturally marking them, then the dynamics recovered for it would have an effective mobility different from its own. This could be extremely restrictive as will be demonstrated in the next chapter.

Finally, when Lagrange multiplier is not implemented, it was shown in the previous timescale that an equilibrium phase may emerge due to the movement of the contours

corresponding to the different components in opposite directions (Fig. 3.9). However, the transition neither moved forward nor backwards as there was no driving force for either of them. In contrast, in the current timescale, Eq. (3.30) dictates that such an emerged phase may continue to grow or shrink back depending on the numerical values of the bulk energies of the components marking the phases. For example, in situation of Fig. 3.9 when the bulk energies are both positive then the contours move apart as per Eq. (3.30) leading to the materialization of the $(0, 0, 0)$ phase and when negative they move into each other leading to the formation of the $(1, 1, 0)$ phase. In summary, when multi-wells like $W^{FP} = \phi_1^2(1-\phi_1)^2 + \phi_2^2(1-\phi_2)^2 + \phi_3^2(1-\phi_3)^2$ and $W^C = \phi_1^2\phi_2^2 + \phi_2^2\phi_3^2 + \phi_3^2\phi_1^2$ are employed without the implementation of the summation constraint, then one is forced to include at least one among $(0, 0, 0)$ or $(1, 1, 0)$ etc., as one of the equilibrium phases of interest.

Next, the local analysis around the zero-dimensional phase boundaries, i.e., the triple or higher order junctions is considered.

3.3.3.3 Leading order local analysis of junctions

Let us consider a junction between M number of phases as shown in Fig. 3.12 for a representative case of $M = 5$. Tangents to each of the involving binary interfaces can be drawn at the junction and rays can be attached to these resulting in a structure that resembles a free body diagram of a point mass as depicted in Fig. 3.13, especially when the lengths are chosen proportional to the associated interfacial energies. As time passes, these rays can move apart or towards each other or rotate in unison about the point of their origin depending on the dynamics. Thus, the motion of the junction is marked by the position and velocity of the center while the motion of the interfaces relative to it by the evolution of the ray diagram. In the local analysis corresponding to the junction to be carried out presently, the question of what kind of ray diagrams are permissible can be addressed. For example, is it possible to have three interfaces orienting themselves in such a way that their ray diagram is as in Fig. 3.13b)? Can a junction between three phases with interfacial energies of 1, 2 and 4 units between them exhibit a stable motion? Such questions can be answered from the succeeding analysis.

To perform the local analysis, a co-ordinate transformation is made to an axis centered on the junction and the coordinates are stretched. That is, if $(x_*(t), y_*(t))$ marks the locus of the junction with respect to time, a change of axis $(x, y, t) \rightarrow (\zeta, \xi, t)$ is made such that $\zeta = \frac{x - x_*(t)}{\epsilon}$ and $\xi = \frac{y - y_*(t)}{\epsilon}$. If it is further rotated to orient with the i^{th} interface encountered when moving in the counter clockwise direction from the ζ -axis, as shown in Fig. 3.12 then the resultant coordinates are indicated using a suffix that marks the

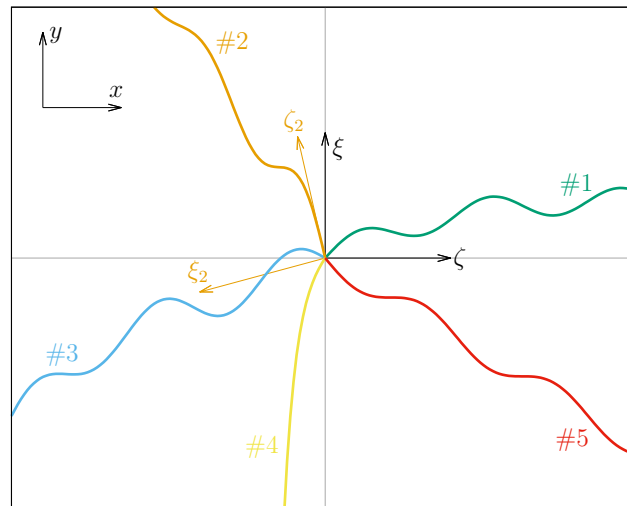


Figure 3.12: Figure showing $M = 5$ interfaces meeting to form a junction. $x - y$ is the laboratory coordinate frame corresponding to the outer co-ordinates and $\zeta - \xi$ is the local frame. The interfaces are numbered with reference to the ζ -axis by starting there and moving in the counter clockwise direction. The local coordinate system rotated so as to align the ζ -axis with the tangent of an interface and suffixed with the number assigned to the latter is also shown exemplarily for the second interface.

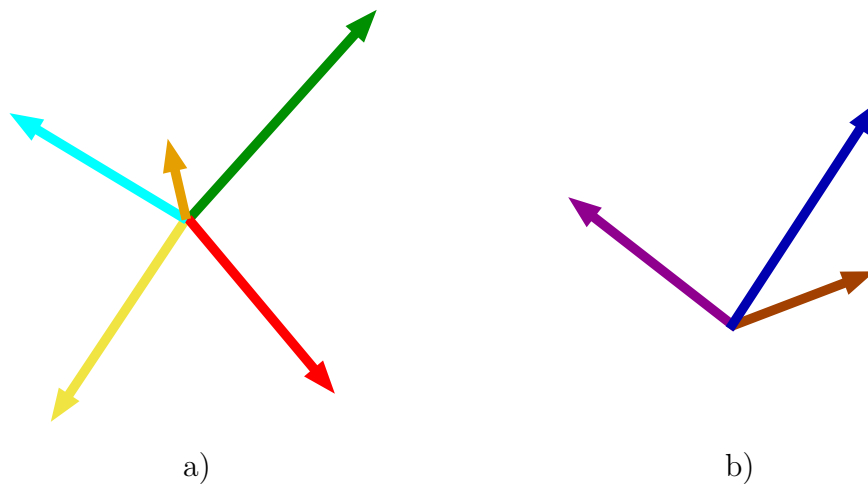


Figure 3.13: Some example ray-diagram constructions; a) corresponds to the interfacial configuration of Fig. 3.12 while b) gives an instance of a ray diagram of a special kind (please refer to the main text).

interface, i.e., (ζ_i, ξ_i) . Therefore,

$$\begin{bmatrix} \zeta_i \\ \xi_i \end{bmatrix} = \begin{bmatrix} \cos \theta_i(t) & \sin \theta_i(t) \\ -\sin \theta_i(t) & \cos \theta_i(t) \end{bmatrix} \begin{bmatrix} \zeta \\ \xi \end{bmatrix} \quad (3.31)$$

where $\theta_i(t)$ is the angle made at time t by the i^{th} interface (encountered while moving in counter clockwise direction) with the ζ -axis (which, in turn, is aligned with the laboratory frame's x -axis (see Fig. 3.12)). The phase-field variable expressed in the (ζ, ξ, t) coordinate system is denoted by $\overset{\perp}{\phi}$, i.e., by definition, $\overset{\perp}{\phi}(\zeta, \xi, t; \epsilon) = \phi(\epsilon\zeta + x_*(t), \epsilon\xi + y_*(t), t; \epsilon)$.

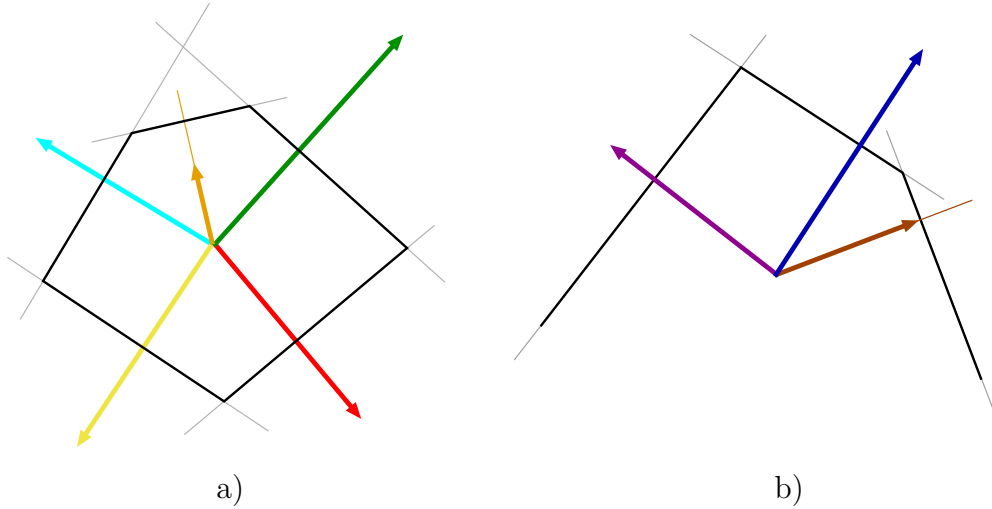


Figure 3.14: Figure showing the polygonal constructions for the ray diagrams of Fig. 3.13; a) corresponds to Fig. 3.13a) while b) to Fig. 3.13b).

Thus the leading order equations are

$$\begin{bmatrix} 0 \\ 0 \\ \cdot \\ \cdot \\ \cdot \\ 0 \end{bmatrix} = \begin{bmatrix} 1 - \frac{1}{N} & -\frac{1}{N} & \cdots & -\frac{1}{N} \\ -\frac{1}{N} & 1 - \frac{1}{N} & \cdots & -\frac{1}{N} \\ \cdot & \cdot & \cdots & \cdot \\ \cdot & \cdot & \cdots & \cdot \\ \cdot & \cdot & \cdots & \cdot \\ -\frac{1}{N} & -\frac{1}{N} & \cdots & 1 - \frac{1}{N} \end{bmatrix} \begin{bmatrix} \frac{\partial W(\phi)}{\partial \phi_1}(\overset{\perp}{\phi}^{(0)}) - \left(\frac{\partial^2 \overset{\perp}{\phi}_1^{(0)}}{\partial \zeta^2} + \frac{\partial^2 \overset{\perp}{\phi}_1^{(0)}}{\partial \xi^2} \right) \\ \frac{\partial W(\phi)}{\partial \phi_2}(\overset{\perp}{\phi}^{(0)}) - \left(\frac{\partial^2 \overset{\perp}{\phi}_2^{(0)}}{\partial \zeta^2} + \frac{\partial^2 \overset{\perp}{\phi}_2^{(0)}}{\partial \xi^2} \right) \\ \cdot \\ \cdot \\ \cdot \\ \frac{\partial W(\phi)}{\partial \phi_N}(\overset{\perp}{\phi}^{(0)}) - \left(\frac{\partial^2 \overset{\perp}{\phi}_N^{(0)}}{\partial \zeta^2} + \frac{\partial^2 \overset{\perp}{\phi}_N^{(0)}}{\partial \xi^2} \right) \end{bmatrix} \quad (3.32)$$

The above equations have to be fulfilled for all of the \mathbb{R}^2 space, however, to begin with, a smaller region is considered and then it is enlarged to equal the whole space. To construct the region, perpendiculars are drawn to the rays at equal distance σ from the center. When the innermost envelope of these lines forms a closed figure, for example like in Fig. 3.14a), then that becomes the required region. On the other hand, when a closed figure does not form as for the case of the ray diagram of Fig. 3.13b) as illustrated in Fig. 3.14b), the figure is closed by arbitrarily drawing a line to join the two hanging edges. Thus, the region in which Eq. (3.32) is considered is a closed convex polygon with the number of sides equal or one greater than the number of interfaces. For the moment, the former case is considered, the adjustments when going to the latter are straightforward as will become clear shortly. The polygonal region of “size” σ will be denoted by the symbol \diamond_σ and its boundary by $\partial\diamond_\sigma$ in the subsequent analysis. In the next step, the Eq. (3.32) is left multiplied with $\left(\frac{\partial \hat{\phi}_1^{(0)}}{\partial \zeta} \quad \frac{\partial \hat{\phi}_2^{(0)}}{\partial \zeta} \quad \dots \quad \frac{\partial \hat{\phi}_N^{(0)}}{\partial \zeta} \right)$ which will lead to the following owing to the initial filling satisfying the summation rule throughout the domain and its subsequent preservation through Lagrange multiplier implementation.

$$\left(\frac{\partial^2 \hat{\phi}_\alpha^{(0)}}{\partial \zeta^2} + \frac{\partial^2 \hat{\phi}_\alpha^{(0)}}{\partial \xi^2} \right) \frac{\partial \hat{\phi}_\alpha^{(0)}}{\partial \zeta} = \frac{\partial W(\phi)}{\partial \phi_\alpha} (\hat{\phi}^{(0)}) \frac{\partial \hat{\phi}_\alpha^{(0)}}{\partial \zeta}. \quad (3.33)$$

In the above equation as well as the following steps, the summation convention is used only with regard to index α . Next, Eq. (3.33) is integrated over the polygonal region that is just constructed:

$$\begin{aligned} & \int_{\diamond_\sigma} \frac{\partial^2 \hat{\phi}_\alpha^{(0)}}{\partial \zeta^2} \frac{\partial \hat{\phi}_\alpha^{(0)}}{\partial \zeta} dV + \int_{\diamond_\sigma} \frac{\partial^2 \hat{\phi}_\alpha^{(0)}}{\partial \xi^2} \frac{\partial \hat{\phi}_\alpha^{(0)}}{\partial \zeta} dV = \int_{\diamond_\sigma} \frac{\partial W(\hat{\phi}^{(0)})}{\partial \zeta} dV \\ \Rightarrow & \frac{1}{2} \int_{\diamond_\sigma} \frac{\partial}{\partial \zeta} \left(\frac{\partial \hat{\phi}_\alpha^{(0)}}{\partial \zeta} \frac{\partial \hat{\phi}_\alpha^{(0)}}{\partial \zeta} \right) dV + \int_{\diamond_\sigma} \frac{\partial}{\partial \xi} \left(\frac{\partial \hat{\phi}_\alpha^{(0)}}{\partial \xi} \frac{\partial \hat{\phi}_\alpha^{(0)}}{\partial \zeta} \right) dV - \int_{\diamond_\sigma} \frac{\partial \hat{\phi}_\alpha^{(0)}}{\partial \zeta} \frac{\partial^2 \hat{\phi}_\alpha^{(0)}}{\partial \xi \partial \zeta} dV \\ & = \int_{\diamond_\sigma} \frac{\partial W(\hat{\phi}^{(0)})}{\partial \zeta} dV \\ \Rightarrow & \frac{1}{2} \int_{\diamond_\sigma} \frac{\partial}{\partial \zeta} \left(\frac{\partial \hat{\phi}_\alpha^{(0)}}{\partial \zeta} \frac{\partial \hat{\phi}_\alpha^{(0)}}{\partial \zeta} \right) dV + \int_{\diamond_\sigma} \frac{\partial}{\partial \xi} \left(\frac{\partial \hat{\phi}_\alpha^{(0)}}{\partial \xi} \frac{\partial \hat{\phi}_\alpha^{(0)}}{\partial \zeta} \right) dV - \frac{1}{2} \int_{\diamond_\sigma} \frac{\partial}{\partial \zeta} \left(\frac{\partial \hat{\phi}_\alpha^{(0)}}{\partial \xi} \frac{\partial \hat{\phi}_\alpha^{(0)}}{\partial \xi} \right) dV \\ & = \int_{\diamond_\sigma} \frac{\partial W(\hat{\phi}^{(0)})}{\partial \zeta} dV \end{aligned}$$

\implies

$$\int_{\hat{\Omega}_\sigma} \frac{\partial}{\partial \xi} \left(\frac{\partial \hat{\phi}_\alpha^{(0)}}{\partial \xi} \frac{\partial \hat{\phi}_\alpha^{(0)}}{\partial \zeta} \right) dV = \int_{\hat{\Omega}_\sigma} \frac{\partial}{\partial \zeta} \left\{ W(\hat{\phi}^{(0)}) + \frac{1}{2} \left(\frac{\partial \hat{\phi}_\alpha^{(0)}}{\partial \xi} \frac{\partial \hat{\phi}_\alpha^{(0)}}{\partial \xi} \right) - \frac{1}{2} \left(\frac{\partial \hat{\phi}_\alpha^{(0)}}{\partial \zeta} \frac{\partial \hat{\phi}_\alpha^{(0)}}{\partial \zeta} \right) \right\} dV.$$

Applying the divergence theorem to the above equation leads to

$$\int_{\partial \hat{\Omega}_\sigma} \frac{\partial \hat{\phi}_\alpha^{(0)}}{\partial \xi} \frac{\partial \hat{\phi}_\alpha^{(0)}}{\partial \zeta} \mathbf{n} \cdot \hat{\xi} dS = \int_{\partial \hat{\Omega}_\sigma} \left\{ W(\hat{\phi}^{(0)}) + \frac{1}{2} \left(\frac{\partial \hat{\phi}_\alpha^{(0)}}{\partial \xi} \frac{\partial \hat{\phi}_\alpha^{(0)}}{\partial \xi} \right) - \frac{1}{2} \left(\frac{\partial \hat{\phi}_\alpha^{(0)}}{\partial \zeta} \frac{\partial \hat{\phi}_\alpha^{(0)}}{\partial \zeta} \right) \right\} \mathbf{n} \cdot \hat{\zeta} dS$$

\implies

$$\begin{aligned} \sum_{i=1}^M \int_{\partial(i)} \frac{\partial \hat{\phi}_\alpha^{(0)}}{\partial \xi} \frac{\partial \hat{\phi}_\alpha^{(0)}}{\partial \zeta} \mathbf{n} \cdot \hat{\xi} dS = \\ \sum_{i=1}^M \int_{\partial(i)} \left\{ W(\hat{\phi}^{(0)}) + \frac{1}{2} \left(\frac{\partial \hat{\phi}_\alpha^{(0)}}{\partial \xi} \frac{\partial \hat{\phi}_\alpha^{(0)}}{\partial \xi} \right) - \frac{1}{2} \left(\frac{\partial \hat{\phi}_\alpha^{(0)}}{\partial \zeta} \frac{\partial \hat{\phi}_\alpha^{(0)}}{\partial \zeta} \right) \right\} \mathbf{n} \cdot \hat{\zeta} dS. \end{aligned} \quad (3.34)$$

Where, $\partial(i)$ is the i^{th} side of the polygon that was formed from the perpendicular drawn to the i^{th} interface. For any single such side, the contribution from it to the l.h.s when expressed in the co-ordinates oriented along the associated interface, i.e., (ζ_i, ξ_i) is

$$\int_{\partial(i)} \left(\frac{\partial \hat{\phi}_\alpha^{(0)}}{\partial \xi_i} \frac{\partial \hat{\phi}_\alpha^{(0)}}{\partial \xi} + \frac{\partial \hat{\phi}_\alpha^{(0)}}{\partial \zeta_i} \frac{\partial \hat{\phi}_\alpha^{(0)}}{\partial \xi} \right) \left(\frac{\partial \hat{\phi}_\alpha^{(0)}}{\partial \xi_i} \frac{\partial \hat{\phi}_\alpha^{(0)}}{\partial \zeta} + \frac{\partial \hat{\phi}_\alpha^{(0)}}{\partial \zeta_i} \frac{\partial \hat{\phi}_\alpha^{(0)}}{\partial \zeta} \right) \mathbf{n} \cdot \hat{\xi} dS.$$

In the limit of the size of the polygon becoming arbitrarily large, due to matching, $\frac{\partial \hat{\phi}_\alpha^{(0)}}{\partial \zeta_i}$ vanishes. Therefore, the above integral reduces to

$$\int_{\substack{\partial(i) \\ \sigma \rightarrow \infty}} \left(\frac{\partial \hat{\phi}_\alpha^{(0)}}{\partial \xi_i} \frac{\partial \hat{\phi}_\alpha^{(0)}}{\partial \xi} \right) \left(\frac{\partial \hat{\phi}_\alpha^{(0)}}{\partial \xi_i} \frac{\partial \hat{\phi}_\alpha^{(0)}}{\partial \zeta} \right) \mathbf{n} \cdot \hat{\xi} dS = \int_{\substack{\partial(i) \\ \sigma \rightarrow \infty}} \frac{\partial \hat{\phi}_\alpha^{(0)}}{\partial \xi_i} \frac{\partial \hat{\phi}_\alpha^{(0)}}{\partial \xi_i} \cos \theta_i (-\sin \theta_i) \mathbf{n} \cdot \hat{\xi} dS.$$

Similarly, the r.h.s. of Eq. (3.34) as well modifies in the like manner, together yielding

$$\begin{aligned} - \sum_{i=1}^M \int_{\substack{\partial(i) \\ \sigma \rightarrow \infty}} \frac{\partial \hat{\phi}_\alpha^{(0)}}{\partial \xi_i} \frac{\partial \hat{\phi}_\alpha^{(0)}}{\partial \xi_i} \cos \theta_i \sin \theta_i \mathbf{n} \cdot \hat{\xi} dS = \\ \sum_{i=1}^M \int_{\substack{\partial(i) \\ \sigma \rightarrow \infty}} \left\{ W(\hat{\phi}^{(0)}) + \frac{1}{2} \left(\frac{\partial \hat{\phi}_\alpha^{(0)}}{\partial \xi_i} \frac{\partial \hat{\phi}_\alpha^{(0)}}{\partial \xi_i} \right) \cos^2 \theta_i - \frac{1}{2} \left(\frac{\partial \hat{\phi}_\alpha^{(0)}}{\partial \xi_i} \frac{\partial \hat{\phi}_\alpha^{(0)}}{\partial \xi_i} \right) \sin^2 \theta_i \right\} \mathbf{n} \cdot \hat{\zeta} dS. \end{aligned}$$

Since $\mathbf{n} \cdot \hat{\xi}$ and $\mathbf{n} \cdot \hat{\zeta}$ equal $\sin \theta_i$ and $\cos \theta_i$, respectively, the above equation simplifies to

$$\sum_{i=1}^M \int_{\substack{\partial^{(i)} \\ \sigma \rightarrow \infty}} \left\{ W(\hat{\phi}^{(0)}) + \frac{1}{2} \left(\frac{\partial \hat{\phi}_\alpha^{(0)}}{\partial \xi_i} \frac{\partial \hat{\phi}_\alpha^{(0)}}{\partial \xi_i} \right) \cos^2 \theta_i + \frac{1}{2} \left(\frac{\partial \hat{\phi}_\alpha^{(0)}}{\partial \xi_i} \frac{\partial \hat{\phi}_\alpha^{(0)}}{\partial \xi_i} \right) \sin^2 \theta_i \right\} \cos \theta_i dS = 0$$

\Rightarrow

$$\sum_{i=1}^M \int_{\substack{\partial^{(i)} \\ \sigma \rightarrow \infty}} \left\{ W(\hat{\phi}^{(0)}) + \frac{1}{2} \left(\frac{\partial \hat{\phi}_\alpha^{(0)}}{\partial \xi_i} \frac{\partial \hat{\phi}_\alpha^{(0)}}{\partial \xi_i} \right) \right\} \cos \theta_i dS = 0$$

\Rightarrow

$$\sum_{i=1}^M \int_{\substack{-\infty \\ i^{\text{th}} \text{ interface}}}^{\infty} \left\{ W(\tilde{\phi}^{(0)}) + \frac{1}{2} \left(\frac{\partial \tilde{\phi}_\alpha^{(0)}}{\partial \rho} \frac{\partial \tilde{\phi}_\alpha^{(0)}}{\partial \rho} \right) \right\} d\rho \cos \theta_i = 0.$$

Due to Eq. (3.22), this further implies

$$2 \sum_{i=1}^M \int_{\substack{-\infty \\ i^{\text{th}} \text{ interface}}}^{\infty} \frac{1}{2} \left(\frac{\partial \tilde{\phi}_\alpha^{(0)}}{\partial \rho} \frac{\partial \tilde{\phi}_\alpha^{(0)}}{\partial \rho} \right) d\rho \cos \theta_i = 0$$

\Rightarrow

$$\sum_{i=1}^M (\text{I.E.})_i \cos \theta_i = 0. \quad (3.35)$$

Where, $(\text{I.E.})_i$ is the interfacial energy of the i^{th} interface. Note that the adjustments to be made when one of the constructed sides does not correspond to any of the interfaces like, for instance, the “open side” of Fig. 3.14b) are indeed trivial. However, since the contribution from such an arbitrarily constructed side to Eq. (3.35) is identically zero in the limit of the size of the polygon blowing up, the above condition with M being the number of interfaces meeting at a junction is a necessary requirement to be fulfilled by them at their common meeting point whether or not they give rise to a closed polygon.

Similarly, repeating the above procedure but by starting by left multiplying Eq. (3.32) with $\left(\frac{\partial \hat{\phi}_1^{(0)}}{\partial \xi} \quad \frac{\partial \hat{\phi}_2^{(0)}}{\partial \xi} \quad \dots \quad \frac{\partial \hat{\phi}_N^{(0)}}{\partial \xi} \right)$ instead, leads to the following requirement.

$$\sum_{i=1}^M (\text{I.E.})_i \sin \theta_i = 0. \quad (3.36)$$

The conditions Eqs. (3.35) and (3.36) are reminiscent of the force balance requirement; the first one is the balance of ζ -component and the latter that of ξ , with the interfacial

energies taking the role of the applied forces. Therefore, the questions raised regarding the situations of Fig. 3.14b) and the possibility of having a stable junction between interfaces with energies 1, 2 and 4 units is now easy to answer in the negative. This is because, in the former, it is impossible to balance out the y -components of the “forces”, while the latter don’t satisfy the triangle inequality and hence cannot cancel themselves out. A corollary is that any ray diagram which does not produce a closed polygon upon the construction of the perpendiculars cannot be a valid solution.

3.3.3.4 Next-to-leading order local analysis of junctions

We now proceed with the analysis at the next order. First, the simpler case of the absence of driving forces i.e., $f_\alpha = f_\beta \forall \alpha, \beta$ or, in particular, $f_\alpha = 0 \forall \alpha$, and unit mobility case i.e., $\tau(\phi) = 1$ will be considered; this will be generalized later. The corresponding equations are

$$\begin{bmatrix} -v_x \frac{\partial \hat{\phi}_1^{(0)}}{\partial \zeta} - v_y \frac{\partial \hat{\phi}_1^{(0)}}{\partial \xi} \\ -v_x \frac{\partial \hat{\phi}_2^{(0)}}{\partial \zeta} - v_y \frac{\partial \hat{\phi}_2^{(0)}}{\partial \xi} \\ \cdot \\ \cdot \\ \cdot \\ -v_x \frac{\partial \hat{\phi}_N^{(0)}}{\partial \zeta} - v_y \frac{\partial \hat{\phi}_N^{(0)}}{\partial \xi} \end{bmatrix} = \begin{bmatrix} 1 - \frac{1}{N} & -\frac{1}{N} & \cdots & -\frac{1}{N} \\ -\frac{1}{N} & 1 - \frac{1}{N} & \cdots & -\frac{1}{N} \\ \cdot & \cdot & \cdots & \cdot \\ \cdot & \cdot & \cdots & \cdot \\ \cdot & \cdot & \cdots & \cdot \\ -\frac{1}{N} & -\frac{1}{N} & \cdots & 1 - \frac{1}{N} \end{bmatrix} \begin{bmatrix} -\frac{\partial}{\partial \phi_\alpha} \frac{\partial W(\phi)}{\partial \phi_1} (\hat{\phi}^{(0)}) \hat{\phi}_\alpha^{(1)} + \nabla^2 \hat{\phi}_1^{(1)} \\ -\frac{\partial}{\partial \phi_\alpha} \frac{\partial W(\phi)}{\partial \phi_2} (\hat{\phi}^{(0)}) \hat{\phi}_\alpha^{(1)} + \nabla^2 \hat{\phi}_1^{(1)} \\ \cdot \\ \cdot \\ \cdot \\ -\frac{\partial}{\partial \phi_\alpha} \frac{\partial W(\phi)}{\partial \phi_N} (\hat{\phi}^{(0)}) \hat{\phi}_\alpha^{(1)} + \nabla^2 \hat{\phi}_1^{(1)} \end{bmatrix} \quad (3.37)$$

where $v_x = \frac{d}{dt} x_*(t)$ and $v_y = \frac{d}{dt} y_*(t)$. Left multiplying the above with the row matrix $\left(\frac{\partial \hat{\phi}_1^{(0)}}{\partial \zeta} \quad \frac{\partial \hat{\phi}_2^{(0)}}{\partial \zeta} \quad \cdots \quad \frac{\partial \hat{\phi}_N^{(0)}}{\partial \zeta} \right)$ and integrating over the polygonal construction discussed previously gives

$$\begin{aligned} -v_x \int_{\hat{\square}_\sigma} \frac{\partial \hat{\phi}_\alpha^{(0)}}{\partial \zeta} \frac{\partial \hat{\phi}_\alpha^{(0)}}{\partial \zeta} dV - v_y \int_{\hat{\square}_\sigma} \frac{\partial \hat{\phi}_\alpha^{(0)}}{\partial \xi} \frac{\partial \hat{\phi}_\alpha^{(0)}}{\partial \zeta} dV \\ = - \int_{\hat{\square}_\sigma} \frac{\partial}{\partial \phi_\alpha} \frac{\partial W(\phi)}{\partial \phi_\beta} (\hat{\phi}^{(0)}) \hat{\phi}_\alpha^{(1)} \frac{\partial \hat{\phi}_\beta^{(0)}}{\partial \zeta} dV + \int_{\hat{\square}_\sigma} \nabla^2 \hat{\phi}_\alpha^{(1)} \frac{\partial \hat{\phi}_\alpha^{(0)}}{\partial \zeta} dV. \end{aligned}$$

By the use of divergence theorem twice, the last integral on the r.h.s modifies leading to

$$\begin{aligned}
& -v_x \int_{\hat{\Omega}_\sigma} \frac{\partial \hat{\phi}_\alpha^{(0)}}{\partial \zeta} \frac{\partial \hat{\phi}_\alpha^{(0)}}{\partial \zeta} dV - v_y \int_{\hat{\Omega}_\sigma} \frac{\partial \hat{\phi}_\alpha^{(0)}}{\partial \xi} \frac{\partial \hat{\phi}_\alpha^{(0)}}{\partial \zeta} dV \\
& = - \int_{\hat{\Omega}_\sigma} \frac{\partial}{\partial \phi_\alpha} \frac{\partial W(\phi)}{\partial \phi_\beta} (\hat{\phi}^{(0)}) \hat{\phi}_\alpha^{(1)} \frac{\partial \hat{\phi}_\beta^{(0)}}{\partial \zeta} dV + \int_{\hat{\Omega}_\sigma} \hat{\phi}_\alpha^{(1)} \nabla^2 \frac{\partial \hat{\phi}_\alpha^{(0)}}{\partial \zeta} dV \\
& \quad + \int_{\partial \hat{\Omega}_\sigma} \frac{\partial \hat{\phi}_\alpha^{(0)}}{\partial \zeta} \nabla \hat{\phi}_\alpha^{(1)} \cdot \mathbf{ndS} - \int_{\partial \hat{\Omega}_\sigma} \hat{\phi}_\alpha^{(1)} \nabla \frac{\partial \hat{\phi}_\alpha^{(0)}}{\partial \zeta} \cdot \mathbf{ndS}.
\end{aligned} \tag{3.38}$$

To determine the second volume integral on the r.h.s of the above equation, Eq. (3.32) is differentiated with respect to ζ and the resultant is left multiplied with $(\hat{\phi}_1^{(1)} \hat{\phi}_2^{(1)} \dots \hat{\phi}_N^{(1)})$ and integrated resulting in

$$\int_{\hat{\Omega}_\sigma} \hat{\phi}_\alpha^{(1)} \nabla^2 \frac{\partial \hat{\phi}_\alpha^{(0)}}{\partial \zeta} dV = \int_{\hat{\Omega}_\sigma} \frac{\partial}{\partial \zeta} \left(\frac{\partial W(\phi)}{\partial \phi_\alpha} (\hat{\phi}^{(0)}) \right) \hat{\phi}_\alpha^{(1)} dV$$

while the first one can be manipulated in the following manner

$$\begin{aligned}
\int_{\hat{\Omega}_\sigma} \frac{\partial}{\partial \phi_\alpha} \frac{\partial W(\phi)}{\partial \phi_\beta} (\hat{\phi}^{(0)}) \hat{\phi}_\alpha^{(1)} \frac{\partial \hat{\phi}_\beta^{(0)}}{\partial \zeta} dV & = \int_{\hat{\Omega}_\sigma} \frac{\partial}{\partial \phi_\beta} \frac{\partial W(\phi)}{\partial \phi_\alpha} (\hat{\phi}^{(0)}) \hat{\phi}_\alpha^{(1)} \frac{\partial \hat{\phi}_\beta^{(0)}}{\partial \zeta} dV \\
& = \int_{\hat{\Omega}_\sigma} \frac{\partial}{\partial \phi_\beta} \frac{\partial W(\phi)}{\partial \phi_\alpha} (\hat{\phi}^{(0)}) \frac{\partial \hat{\phi}_\beta^{(0)}}{\partial \zeta} \hat{\phi}_\alpha^{(1)} dV \\
& = \int_{\hat{\Omega}_\sigma} \frac{\partial}{\partial \zeta} \left(\frac{\partial W(\phi)}{\partial \phi_\alpha} (\hat{\phi}^{(0)}) \right) \hat{\phi}_\alpha^{(1)} dV.
\end{aligned}$$

Therefore, the first two terms on the r.h.s of Eq. (3.38) cancel each other out leading to

$$\begin{aligned}
& -v_x \int_{\hat{\Omega}_\sigma} \frac{\partial \hat{\phi}_\alpha^{(0)}}{\partial \zeta} \frac{\partial \hat{\phi}_\alpha^{(0)}}{\partial \zeta} dV - v_y \int_{\hat{\Omega}_\sigma} \frac{\partial \hat{\phi}_\alpha^{(0)}}{\partial \xi} \frac{\partial \hat{\phi}_\alpha^{(0)}}{\partial \zeta} dV = \\
& \quad \int_{\partial \hat{\Omega}_\sigma} \frac{\partial \hat{\phi}_\alpha^{(0)}}{\partial \zeta} \nabla \hat{\phi}_\alpha^{(1)} \cdot \mathbf{ndS} - \int_{\partial \hat{\Omega}_\sigma} \hat{\phi}_\alpha^{(1)} \nabla \frac{\partial \hat{\phi}_\alpha^{(0)}}{\partial \zeta} \cdot \mathbf{ndS}.
\end{aligned} \tag{3.39}$$

Similarly, repeating the analysis but by beginning by left multiplying Eq. (3.37) with $\left(\frac{\partial \overset{\wedge}{\phi}_1^{(0)}}{\partial \xi} \quad \frac{\partial \overset{\wedge}{\phi}_2^{(0)}}{\partial \xi} \quad \dots \quad \frac{\partial \overset{\wedge}{\phi}_N^{(0)}}{\partial \xi} \right)$ leads to

$$\begin{aligned}
-v_x \int_{\hat{\Omega}_\sigma} \frac{\partial \overset{\wedge}{\phi}_\alpha^{(0)}}{\partial \zeta} \frac{\partial \overset{\wedge}{\phi}_\alpha^{(0)}}{\partial \xi} dV - v_y \int_{\hat{\Omega}_\sigma} \frac{\partial \overset{\wedge}{\phi}_\alpha^{(0)}}{\partial \zeta} \frac{\partial \overset{\wedge}{\phi}_\alpha^{(0)}}{\partial \xi} dV = \\
\int_{\partial \hat{\Omega}_\sigma} \frac{\partial \overset{\wedge}{\phi}_\alpha^{(0)}}{\partial \xi} \nabla \overset{\wedge}{\phi}_\alpha^{(1)} \cdot \mathbf{nd}S - \int_{\partial \hat{\Omega}_\sigma} \overset{\wedge}{\phi}_\alpha^{(1)} \nabla \frac{\partial \overset{\wedge}{\phi}_\alpha^{(0)}}{\partial \xi} \cdot \mathbf{nd}S.
\end{aligned} \tag{3.40}$$

The surface integrals appearing in Eqs. (3.39) and (3.40) can be categorized into two types, one containing the gradients of the zeroth order approximation $\overset{\wedge}{\phi}_\alpha^{(0)}$ while the other that of the first order correction $\overset{\wedge}{\phi}_\alpha^{(1)}$. Among these, the former can be shown to vanish identically due to the fundamental requirements of the matching principles when the area of the polygon is made arbitrarily large. Considering explicitly the example of the rightmost integral of Eq. (3.40), we have,

$$\begin{aligned}
\int_{\partial \hat{\Omega}_\sigma} \overset{\wedge}{\phi}_\alpha^{(1)} \nabla \frac{\partial \overset{\wedge}{\phi}_\alpha^{(0)}}{\partial \xi} \cdot \mathbf{nd}S &= \sum_{i=1}^M \int_{\partial(i)} \overset{\wedge}{\phi}_\alpha^{(1)} \nabla \frac{\partial \overset{\wedge}{\phi}_\alpha^{(0)}}{\partial \xi} \cdot \mathbf{nd}S \\
&= \sum_{i=1}^M \int_{\partial(i)} \overset{\wedge}{\phi}_\alpha^{(1)} \left(\frac{\partial}{\partial \zeta_i} \frac{\partial \overset{\wedge}{\phi}_\alpha^{(0)}}{\partial \xi} \hat{\zeta}_i + \frac{\partial}{\partial \xi_i} \frac{\partial \overset{\wedge}{\phi}_\alpha^{(0)}}{\partial \xi} \hat{\xi}_i \right) \cdot \mathbf{nd}S \\
&= \sum_{i=1}^M \int_{\partial(i)} \overset{\wedge}{\phi}_\alpha^{(1)} \left(\frac{\partial}{\partial \zeta_i} \frac{\partial \overset{\wedge}{\phi}_\alpha^{(0)}}{\partial \xi} \right) dS \\
&= \sum_{i=1}^M \int_{\partial(i)} \overset{\wedge}{\phi}_\alpha^{(1)} \left(\frac{\partial}{\partial \xi} \frac{\partial \overset{\wedge}{\phi}_\alpha^{(0)}}{\partial \zeta_i} \right) dS.
\end{aligned} \tag{3.41}$$

However, in the limit that is of interest, $\overset{\wedge}{\phi}_\alpha^{(0)}$ approaches a constant value with regard to ζ_i thus causing the derivative $\frac{\partial \overset{\wedge}{\phi}_\alpha^{(0)}}{\partial \zeta_i}$ to vanish. On the other hand, the matching conditions say that the factor $\overset{\wedge}{\phi}_\alpha^{(1)}$ in the integrand grows arbitrarily large at ζ_i^2 order (appendix B.2). If the rate of the former going to zero is faster than the latter blowing up, the integral vanishes. In the case of local analysis at binary interfaces, it is in fact shown in appendix B.1.3 that the local solution converges to the matching conditions at an exponential rate. It may be speculated that such a state of affairs may also hold

true even in the current case of the solution of the p.d.e. system Eq. (3.32). A rigorous proof is although unavailable, we turn to the special case of triple junction to derive some insights. The explicit solution of the system of equations Eq. (3.32) is presented for the first time by Bollada *et al.* [54] when the chosen well is W^{FP} and the junction is a triple point (see appendix B.3). Indeed, it so happens that an exponential decay is exhibited by $\frac{\partial \overset{\wedge}{\phi}_\alpha^{(0)}}{\partial \zeta_i}$ as ζ_i approaches ∞ as detailed in appendix B.3.2. Invoking the assumption that the behavior remains so for any generic multi-well, the contribution from the above integral to Eq. (3.40) is identically zero.

Before proceeding with the analysis of the other kind of integral, we would like to pause for a moment to re-emphasize our claim that as $\zeta_i \rightarrow \infty$, the first order correction $\overset{\wedge}{\phi}_\alpha^{(1)}$ is of the order ζ_i^2 . This is a rather surprising fact at a first glance because the counterpart matching condition for a binary interface requires that the first order local correction is of the order of the local variable as the latter tends to infinity but not its square. To be precise, the matching condition for first order term of the local expansion at a binary interface is

$$\tilde{\phi}^{(1)}(s, \rho) = \lim_{r \rightarrow \pm 0} \left(\phi^{(1)}(s, r) + \rho \frac{\partial \phi^{(0)}}{\partial r}(s, r) \right) + \mathcal{O}(1) \text{ as } \rho \rightarrow \pm \infty$$

with r marking, as before, the distance along the normal to the interface and ρ being its stretched counterpart. That is, the outer limit of the first order inner correction matches with the inner limit of the first order outer correction plus inner variable times the inner limit of the derivative of the zeroth order term of the outer expansion. It would be tempting to extend this, in a naive way, to higher order interior ‘‘layer’’, i.e, a neighborhood of a junction, in the following manner.

$$\overset{\wedge}{\phi}_\alpha^{(1)}(\zeta_i, \xi_i) = \lim_{s \rightarrow 0} \left(\tilde{\phi}^{(1)}(s, \rho = \xi_i) + \zeta_i \frac{\partial \tilde{\phi}^{(0)}}{\partial s}(s, \rho = \xi_i) \right) + \mathcal{O}(1) \text{ as } \zeta_i \rightarrow \infty \quad (3.42)$$

where s and ρ are the distance along the i^{th} interface and the stretched distance normal to it, respectively. Further, as the local solution corresponding to the binary interfaces is independent of the distance along the interface in the problem we are concerned with, the second term on the r.h.s of the above equation vanishes, thus not requiring to worry about the rate at which the term in the parenthesis of Eq. (3.41) converges to zero. However, such is not the state of affairs as Eq. (3.42) is incomplete. Due analysis shows that the presence of the other degree of freedom ξ_i also has its effect in determining the matching condition and the actual relation is: as $\zeta_i \rightarrow \infty$,

$$\overset{\wedge}{\phi}_\alpha^{(1)}(\zeta_i, \xi_i) = \lim_{s \rightarrow 0} \left(\tilde{\phi}^{(1)}(s, \rho = \xi_i) + \zeta \frac{\partial \tilde{\phi}^{(0)}}{\partial s}(s, \rho = \xi_i) + (-\kappa_{0,i} \zeta_i^2 / 2) \frac{\partial \tilde{\phi}^{(0)}}{\partial \rho}(s, \rho = \xi_i) \right) + \mathcal{O}(1) \quad (3.43)$$

where $\kappa_{0,i}$ is the curvature of the i^{th} interface at the junction evaluated in $\zeta_i - \xi_i$ coordinate system with the convention that a function $\zeta_i = \zeta_i(\xi_i)$ which is concave upwards is positively curved. The derivation of this relation is provided in appendix B.2.2. Since the last term on the r.h.s of the above equation is non-zero in general, the relative rates of vanishing of $\frac{\partial \hat{\phi}_\alpha^{(0)}}{\partial \zeta_i}$ and divergence of $\hat{\phi}_\alpha^{(1)}$ have to be indeed estimated for handling the first kind of integral.

We now carry on with the analysis of the other kind of integral:

$$\begin{aligned}
\int_{\partial \square_\sigma} \frac{\partial \hat{\phi}_\alpha^{(0)}}{\partial \xi} \nabla \hat{\phi}_\alpha^{(1)} \cdot \mathbf{n} dS &= \sum_{i=1}^M \int_{\partial(i)} \frac{\partial \hat{\phi}_\alpha^{(0)}}{\partial \xi} \left(\frac{\partial \hat{\phi}_\alpha^{(1)}}{\partial \zeta_i} \hat{\zeta}_i + \frac{\partial \hat{\phi}_\alpha^{(1)}}{\partial \xi_i} \hat{\xi}_i \right) \cdot \mathbf{n} dS \\
&= \sum_{i=1}^M \int_{\partial(i)} \frac{\partial \hat{\phi}_\alpha^{(0)}}{\partial \xi} \frac{\partial \hat{\phi}_\alpha^{(1)}}{\partial \zeta_i} dS \\
&= \sum_{i=1}^M \int_{\partial(i)} \left(\frac{\partial \hat{\phi}_\alpha^{(0)}}{\partial \zeta_i} \frac{\partial \zeta_i}{\partial \xi} + \frac{\partial \hat{\phi}_\alpha^{(0)}}{\partial \xi_i} \frac{\partial \xi_i}{\partial \xi} \right) \frac{\partial \hat{\phi}_\alpha^{(1)}}{\partial \zeta_i} dS \\
&= \sum_{i=1}^M \frac{\partial \zeta_i}{\partial \xi} \int_{\partial(i)} \frac{\partial \hat{\phi}_\alpha^{(0)}}{\partial \zeta_i} \frac{\partial \hat{\phi}_\alpha^{(1)}}{\partial \zeta_i} dS + \sum_{i=1}^M \frac{\partial \xi_i}{\partial \xi} \int_{\partial(i)} \frac{\partial \hat{\phi}_\alpha^{(0)}}{\partial \xi_i} \frac{\partial \hat{\phi}_\alpha^{(1)}}{\partial \zeta_i} dS.
\end{aligned}$$

Dividing the above with the size of the polygon, i.e., the stretched distance σ at which the perpendiculars are drawn on each tangent ray for constructing the polygon \square_σ , gives

$$\frac{1}{\sigma} \int_{\partial \square_\sigma} \frac{\partial \hat{\phi}_\alpha^{(0)}}{\partial \xi} \nabla \hat{\phi}_\alpha^{(1)} \cdot \mathbf{n} dS = \frac{1}{\sigma} \sum_{i=1}^M \frac{\partial \zeta_i}{\partial \xi} \int_{\partial(i)} \frac{\partial \hat{\phi}_\alpha^{(0)}}{\partial \zeta_i} \frac{\partial \hat{\phi}_\alpha^{(1)}}{\partial \zeta_i} dS + \frac{1}{\sigma} \sum_{i=1}^M \frac{\partial \xi_i}{\partial \xi} \int_{\partial(i)} \frac{\partial \hat{\phi}_\alpha^{(0)}}{\partial \xi_i} \frac{\partial \hat{\phi}_\alpha^{(1)}}{\partial \zeta_i} dS.$$

Note that the polygon growing in size to eventually fill up the entire space is the same as $\sigma \rightarrow \infty$. In this limit, the first summand on the r.h.s vanishes due to matching requirements and exponential decay assumption leaving with

$$\lim_{\sigma \rightarrow \infty} \frac{1}{\sigma} \int_{\partial \square_\sigma} \frac{\partial \hat{\phi}_\alpha^{(0)}}{\partial \xi} \nabla \hat{\phi}_\alpha^{(1)} \cdot \mathbf{n} dS = - \sum_{i=1}^M \frac{\partial \xi_i}{\partial \xi} \kappa_{0,i} \int_{-\infty}^{\infty} \frac{\partial \tilde{\phi}^{(0)}}{\partial \rho} \frac{\partial \tilde{\phi}^{(0)}}{\partial \rho} d\rho$$

i^{th} interface

where $\kappa_{0,i}$ is as in Eq. (3.43).

Thus, emerging as the final outcome of the analysis at this order, the laws governing

the trajectory of the junction are

$$-v_x \lim_{\sigma \rightarrow \infty} \frac{1}{\sigma} \int_{\square_{\sigma}} \frac{\partial \overset{\lambda(0)}{\phi}_{\alpha}}{\partial \zeta} \frac{\partial \overset{\lambda(0)}{\phi}_{\alpha}}{\partial \zeta} dV - v_y \lim_{\sigma \rightarrow \infty} \frac{1}{\sigma} \int_{\square_{\sigma}} \frac{\partial \overset{\lambda(0)}{\phi}_{\alpha}}{\partial \xi} \frac{\partial \overset{\lambda(0)}{\phi}_{\alpha}}{\partial \zeta} dV = - \sum_{i=1}^M \frac{\partial \xi_i}{\partial \zeta} 2\kappa_{0,i} (\text{I.E.})_i \quad (3.44)$$

and

$$-v_x \lim_{\sigma \rightarrow \infty} \frac{1}{\sigma} \int_{\square_{\sigma}} \frac{\partial \overset{\lambda(0)}{\phi}_{\alpha}}{\partial \zeta} \frac{\partial \overset{\lambda(0)}{\phi}_{\alpha}}{\partial \xi} dV - v_y \lim_{\sigma \rightarrow \infty} \frac{1}{\sigma} \int_{\square_{\sigma}} \frac{\partial \overset{\lambda(0)}{\phi}_{\alpha}}{\partial \xi} \frac{\partial \overset{\lambda(0)}{\phi}_{\alpha}}{\partial \xi} dV = - \sum_{i=1}^M \frac{\partial \xi_i}{\partial \xi} 2\kappa_{0,i} (\text{I.E.})_i. \quad (3.45)$$

Note that it will be a disaster if any of the limits on the l.h.s of Eqs. (3.44) and (3.45) blows up. Likewise, if all of them vanish, then instead of obtaining a prescription for junction velocities, a relation to be satisfied by the curvatures of the interfaces at the junction point with regard to their energies will be recovered which eliminates certain configurations and curvatures that are known to be stable (for example the situation of Fig. 3.15). It will now be shown that by assuming some properties that are necessarily fulfilled by the explicit solution put forth by Bollada *et al.* for the triple junction case, these possibilities are eliminated. We elucidate this by considering the second term on the l.h.s of Eq. (3.45). Before that, without loss of generality, we suppose that the interface between the phases ϕ_1 and ϕ_2 is along the ζ axis. Now, consider the smallest square centered around the origin with sides parallel to the ζ and ξ axes and completely containing the polygonal construction \square_{σ} . In the following, this newly constructed square region will be denoted by \square_{σ^*} , and its size by σ^* . Then,

$$\begin{aligned} \int_{\square_{\sigma}} \frac{\partial \overset{\lambda(0)}{\phi}_{\alpha}}{\partial \xi} \frac{\partial \overset{\lambda(0)}{\phi}_{\alpha}}{\partial \xi} dV &\leq \int_{\square_{\sigma^*}} \frac{\partial \overset{\lambda(0)}{\phi}_{\alpha}}{\partial \xi} \frac{\partial \overset{\lambda(0)}{\phi}_{\alpha}}{\partial \xi} dV \leq \int_{-\sigma^*}^{\sigma^*} \int_{-\xi^*}^{\xi^*} \frac{\partial \overset{\lambda(0)}{\phi}_{\alpha}}{\partial \xi} \frac{\partial \overset{\lambda(0)}{\phi}_{\alpha}}{\partial \xi} d\xi d\zeta \quad \text{where } \xi^* \geq \sigma^* \\ &=: \int_{-\sigma^*}^{\sigma^*} I(\zeta, \xi^*) d\zeta \\ &< \int_{-\sigma^*}^{\sigma^*} I(\zeta, \infty) d\zeta. \end{aligned}$$

For the case of a triple junction and the multi-well W^{FP} , $I(\zeta, \infty)$ can be analytically estimated thanks to the explicit solution $\overset{\lambda(0)}{\phi}(\zeta, \xi)$ provided by Bollada *et al.*. In appendix B.3.3.1, it is shown that $I(\zeta, \infty)$ is bounded above by a constant I^* independent

of ζ . Therefore,

$$\frac{1}{\sigma} \int_{\square_{\sigma}} \frac{\partial \phi_{\alpha}^{(0)}}{\partial \xi} \frac{\partial \phi_{\alpha}^{(0)}}{\partial \xi} dV \leq \frac{1}{\sigma} 2\sigma^* I^*.$$

As the size of the polygon σ is increased, since the shape is preserved, the ratio σ^*/σ remains the same. This means, the integral is bounded above for all values of σ .

Further, consider the largest square centered around the origin with sides parallel to the ζ and ξ axes and that is completely contained within the polygon \square_{σ} . Denoting it by \square_{σ^*} and its size by σ_* , we have

$$\begin{aligned} \int_{\square_{\sigma}} \frac{\partial \phi_{\alpha}^{(0)}}{\partial \xi} \frac{\partial \phi_{\alpha}^{(0)}}{\partial \xi} dV &\geq \int_{\square_{\sigma^*}} \frac{\partial \phi_{\alpha}^{(0)}}{\partial \xi} \frac{\partial \phi_{\alpha}^{(0)}}{\partial \xi} dV = \int_{-\sigma^*}^{\sigma^*} \int_{-\sigma^*}^{\sigma^*} \frac{\partial \phi_{\alpha}^{(0)}}{\partial \xi} \frac{\partial \phi_{\alpha}^{(0)}}{\partial \xi} d\xi \\ &\geq \int_0^{\sigma^*} \int_{-\sigma^*}^{\sigma^*} \frac{\partial \phi_{\alpha}^{(0)}}{\partial \xi} \frac{\partial \phi_{\alpha}^{(0)}}{\partial \xi} d\xi \\ &= \int_0^{\sigma^*} I(\zeta, \sigma_*) d\zeta. \end{aligned}$$

In appendix B.3.3.1, by considering the explicit solution of Bollada *et al.*, it is argued that for $\zeta > 0$, $I(\zeta, \sigma_*)$ is always greater than a positive valued, monotonically increasing function which is independent of ζ , let it be denoted by $I_*(\sigma_*)$. Therefore,

$$0 < \frac{1}{\sigma} I_*(\sigma_*) \sigma_* \leq \frac{1}{\sigma} \int_{\square_{\sigma}} \frac{\partial \phi_{\alpha}^{(0)}}{\partial \xi} \frac{\partial \phi_{\alpha}^{(0)}}{\partial \xi} dV.$$

Thus, for all $\sigma > 0$, the ratio $\frac{1}{\sigma} \int_{\square_{\sigma}} \frac{\partial \phi_{\alpha}^{(0)}}{\partial \xi} \frac{\partial \phi_{\alpha}^{(0)}}{\partial \xi} dV$ for the Bollada *et al.* solution is greater than a positive increasing function of σ and is bounded above. Hence, its limit for arbitrarily large values of σ , if it exists, is non-zero. We assume that such a state of affairs to be true even for any other multi-well and a junction of any order, i.e., any number of interfaces meeting at a point. Following a similar argumentation detailed in appendix B.3.3.2, the first limit on the l.h.s of Eq. (3.44) can be shown to be non-vanishing. For the remaining ‘‘mixed integral’’, using Cauchy-Schwarz inequality, it can be related to the product of the unmixed ones and hence the boundedness of the associated ratio, as well, can be readily established. Thus, Eqs. (3.44) and (3.45) prescribe the instantaneous velocity of the junctions.

We now provide a quick example showcasing the above analysis, especially Eqs. (3.44) and (3.45), at work. When three phases with same bulk and interfacial energies are set

up as in Fig. 3.15 where the interfaces 1 and 2 are mirror images of one another with regard to interface 3, the evolution should progress in such a way that the triple junction moves only in the downward direction. The impossibility of the horizontal motion can be easily deduced from the symmetry considerations. When the system is simulated through Eq. (3.14) using the same mobility for all the phase pairs and with the multi-well chosen as W^{FP} , the presented asymptotic analysis around the triple junction first of all stipulates that the angles 1 2 and 3 are all 120° each. Furthermore, as the solution $\phi_\alpha^{(0)}(\zeta, \xi)$ is explicitly known, the limits in Eqs. (3.44) and (3.45) can be computed, if not analytically, at least through numerical means. However, for a quick demonstration, instead of evaluating them in the triangular domain which is the polygonal construction for the given setup, we assume the following which is but a safe assumption and evaluate them in the square domains.

$$\int_{\square_\sigma} (\cdot) dV = \int_{\square_{\sigma^*}} (\cdot) dV + o(\sigma) \quad \text{as } \sigma \rightarrow \infty.$$

The computations in the appendix B.3.3.3 reveal that the integration of $\frac{\partial \phi_\alpha^{(0)}}{\partial \xi} \frac{\partial \phi_\alpha^{(0)}}{\partial \zeta}$ over an arbitrarily large square region is identically zero. Hence, Eqs. (3.44) and (3.45) for the current application reduce to

$$v_x \lim_{\sigma \rightarrow \infty} \frac{1}{\sigma} \int_{\square_{\sigma^*}} \frac{\partial \phi_\alpha^{(0)}}{\partial \zeta} \frac{\partial \phi_\alpha^{(0)}}{\partial \zeta} dV = \sum_{i=1}^3 \frac{\partial \xi_i}{\partial \zeta} 2\kappa_{0,i} \text{ (I.E.)} \quad (3.46)$$

and

$$v_y \lim_{\sigma \rightarrow \infty} \frac{1}{\sigma} \int_{\square_{\sigma^*}} \frac{\partial \phi_\alpha^{(0)}}{\partial \xi} \frac{\partial \phi_\alpha^{(0)}}{\partial \xi} dV = \sum_{i=1}^3 \frac{\partial \xi_i}{\partial \xi} 2\kappa_{0,i} \text{ (I.E.)} \quad (3.47)$$

where (I.E.) is the common interfacial energy of the three involving interfaces. Expanding the r.h.s of the above equations results in

$$v_x I_\zeta = \left(-\sin(\pi/6) \frac{\kappa_{0,1}}{2} - \sin(5\pi/6) \frac{-\kappa_{0,1}}{2} - \sin(3\pi/2) \frac{0}{2} \right) \text{ (I.E.)} = 0$$

$$v_y I_\xi = \left(\cos(\pi/6) \frac{\kappa_{0,1}}{2} + \cos(5\pi/6) \frac{-\kappa_{0,1}}{2} + \cos(3\pi/2) \frac{0}{2} \right) \text{ (I.E.)} = 2\sqrt{3} \kappa_{0,1} \text{ (I.E.)}$$

where I_ζ and I_ξ are the limits in Eqs. (3.46) and (3.47), respectively and are already shown to be non-vanishing. Thus, consistent with the expected behavior, the momentary absence of horizontal motion is predicted. Further, since $\kappa_{0,1}$ is negative due to the shape of the interface, the vertical motion is in the downward direction.

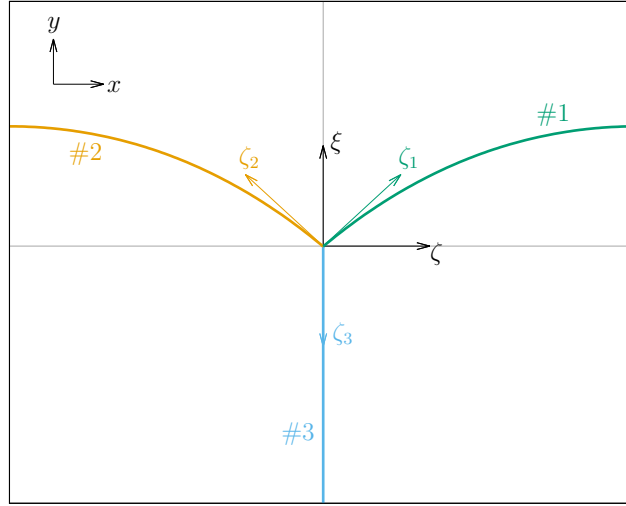


Figure 3.15: Setup considered for demonstrating the accuracy of the asymptotic laws Eqs. (3.44) and (3.45) in predicting the instantaneous motion of a junction.

We finally note that the adjustments to be made for the case of a generic inverse mobility $\tau(\phi)$ and the presence of bulk energies are straightforward and the corresponding counterparts of Eqs. (3.44) and (3.45) are

$$\begin{aligned}
 -v_x \lim_{\sigma \rightarrow \infty} \frac{1}{\sigma} \int_{\hat{\Omega}_\sigma} \tau(\hat{\phi}^{(0)}) \frac{\partial \hat{\phi}_\alpha^{(0)}}{\partial \zeta} \frac{\partial \hat{\phi}_\alpha^{(0)}}{\partial \zeta} dV - v_y \lim_{\sigma \rightarrow \infty} \frac{1}{\sigma} \int_{\hat{\Omega}_\sigma} \tau(\hat{\phi}^{(0)}) \frac{\partial \hat{\phi}_\alpha^{(0)}}{\partial \xi} \frac{\partial \hat{\phi}_\alpha^{(0)}}{\partial \zeta} dV \\
 = - \lim_{\sigma \rightarrow \infty} \frac{1}{\sigma} \int_{\hat{\Omega}_\sigma} f_\alpha \frac{\partial}{\partial \zeta} \mathfrak{g}_\alpha(\hat{\phi}^{(0)}) dV - \sum_{i=1}^M \frac{\partial \xi_i}{\partial \zeta} 2\kappa_{0,i} (\text{I.E.})_i
 \end{aligned} \tag{3.48}$$

and

$$\begin{aligned}
 -v_x \lim_{\sigma \rightarrow \infty} \frac{1}{\sigma} \int_{\hat{\Omega}_\sigma} \tau(\hat{\phi}^{(0)}) \frac{\partial \hat{\phi}_\alpha^{(0)}}{\partial \zeta} \frac{\partial \hat{\phi}_\alpha^{(0)}}{\partial \xi} dV - v_y \lim_{\sigma \rightarrow \infty} \frac{1}{\sigma} \int_{\hat{\Omega}_\sigma} \tau(\hat{\phi}^{(0)}) \frac{\partial \hat{\phi}_\alpha^{(0)}}{\partial \xi} \frac{\partial \hat{\phi}_\alpha^{(0)}}{\partial \xi} dV \\
 = - \lim_{\sigma \rightarrow \infty} \frac{1}{\sigma} \int_{\hat{\Omega}_\sigma} f_\alpha \frac{\partial}{\partial \xi} \mathfrak{g}_\alpha(\hat{\phi}^{(0)}) dV - \sum_{i=1}^M \frac{\partial \xi_i}{\partial \xi} 2\kappa_{0,i} (\text{I.E.})_i.
 \end{aligned} \tag{3.49}$$

Chapter 4

Approaching the asymptotic limits in numerics

4.1 Introduction

The asymptotic analysis of the previous chapter made a rather surprising prediction. Which is, no matter the values of the interfacial mobilities and their interpolating form, the angles recovered at the junctions should always be as in the force balance calculation. That is, considering a three phase system, the angles at the triple junction and the interfacial energies have to fulfill the sine law. However, the computational results seem to be violating this: Eq. (3.14) is numerically solved for $N = 3$ for an initial setup depicted in Fig. 4.1. The choice of the interpolating forms and the multi-well form, and the selection of various material and simulation parameters are as listed in Table 4.1. The chosen values are such that phases ϕ_2 and ϕ_3 are interchangeable and grow at the expense of ϕ_1 . Thus, a moving window technique is implemented in the growth direction as indicated in the figure. The reproduced steady state profile shapes of the growth front for various values of τ_{23} are reported in Fig. 4.2 and the corresponding angles and speeds are tabulated in Table 4.2. The solution of the sharp interface version of the steady state problem* with triple junction angles chosen in accordance with the Young's law is also included in the figure and the table. Clearly, there seems to be a considerable effect of the mobilities on the growth morphologies including the trijunction angles in complete contrast to the predictions of the last chapter.

In actual fact, there is no contradiction whatsoever here as the asymptotic analysis reveals exclusively the vanishing interface width limiting behavior of the system. Hence, the laws it predicts, like Eqs. (3.30), (3.35) and (3.36) etc., need only be valid when ϵ

*The problem statement and the solution steps are presented in appendix C.1.

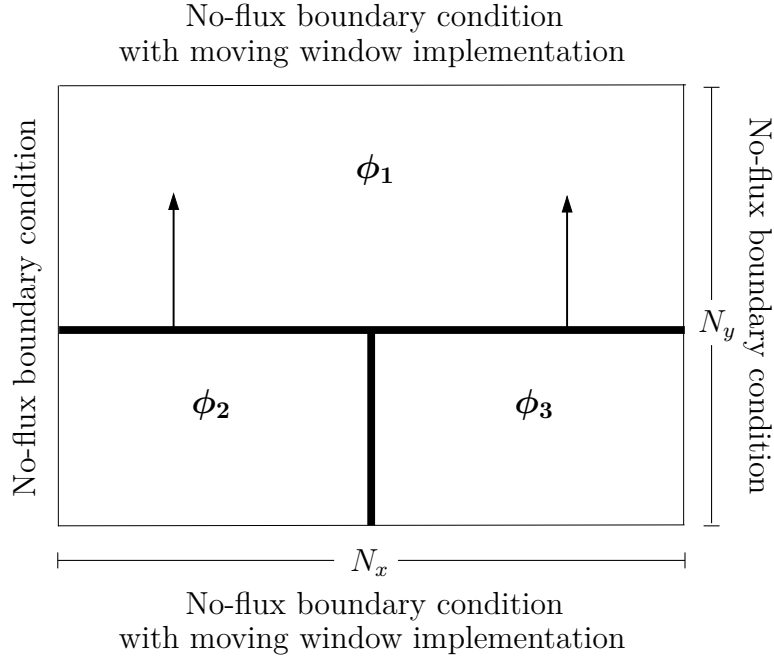


Figure 4.1: A simulation setup used for the study of three phase growth. The growth direction is as depicted by the arrows and accordingly is the implementation of the shifting window.

Table 4.1: Table showing a parameter set used in the study of three phase growth within the setup of Fig. 4.1. N_x and N_y are the number of grid points in the x and y directions, respectively.

f_1	f_2	f_3	γ	τ_{12}	τ_{13}	N_x	N_y	Δx	Δt	ϵ
0.2	0.0	0.0	1.0	1.0	1.0	128	128	0.25	0.0125	1.25
$\{g_\alpha(\phi)\}$				$W(\phi)$				$\tau(\phi)$		
$\{\phi_\alpha^3(10 - 15\phi_\alpha + 6\phi_\alpha^2)\}$				$W^{FP}(\phi)$ with $a = 18$				$\tau_A(\phi)$		

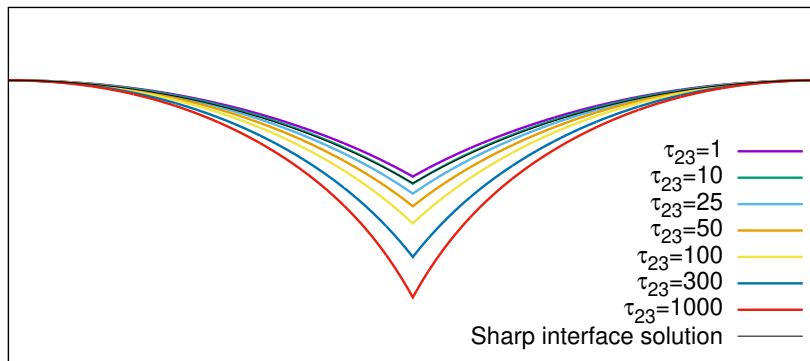


Figure 4.2: Steady state growth fronts realized in the simulations performed with the parameter set of Table 4.1 within the setup of Fig. 4.1 for various values of τ_{23} . Also depicted is the sharp interface theory predicted profile in black.

Table 4.2: Steady state growth speeds realized in the simulations performed with the parameter set of Table 4.1 within the setup of Fig. 4.1 for various values of τ_{23} . Also listed is the sharp interface theory predicted growth speed.

τ_{23}	Recovered angle at the triple junction	Recovered steady state speed (rel. error)
1	29.55724°	0.069110327 (3.50%)
10	31.81860°	0.067431019 (5.84%)
25	34.76556°	0.065186275 (8.98%)
50	38.60122°	0.062458562 (12.79%)
100	42.97858°	0.058963272 (17.67%)
300	52.02093°	0.052690495 (26.43%)
1000	61.14056°	0.045133604 (36.98%)
Sharp interface solution	30.0°	0.071616518

tends to zero and before that a different behavior can indeed be expected. Therefore, in the currently considered example, it might well be the case that the chosen value of $\epsilon = 1.25$ is not sufficiently small, especially more so for $\tau = 1000$ than $\tau = 1$ (i.e., larger values of inverse mobility than smaller ones), and on reducing it, the angles and the steady state speeds may perhaps converge to the analytically predicted values tabulated in the bottom most row of Table 4.2. Nothing can be conclusively confirmed until these tests are performed. In any case, how small is small enough is a question that still needs to be addressed which is a very non-trivial and difficult question to answer analytically. Hence, typically, numerical results are generated for progressively decreasing values of ϵ , and that value at which a further drop in the magnitude results only in a marginal change in the produced results is finalized to be a good enough choice and the subsequent simulation studies are all performed with it.

It has to be emphasized though that this procedure is not as straightforward as it seems to be, as additional considerations have to be taken into account while executing it: Commonly, an explicit finite difference scheme is employed to solve the p.d.e.s modeling solidification in the phase-field approach. In an attempt to simulate low interface widths, if the spatial discretization Δx is fixed and ϵ alone were to be reduced, the number of points corresponding to the interface keeps on decreasing, eventually leading to too few a points to sufficiently resolve it. Thus, one is forced to choose a rule connecting the two; traditionally, ϵ is chosen proportional to the spatial discretization Δx . This demands that

in order to simulate the same physical size of the system and yet decrease the interface width, the grid has to be necessarily made finer. Hence, the computational costs increase as some power of the grid fineness. More elaborately, if a particular discretization length is chosen to begin with, reducing it to half the original value is the same as doubling the fineness of the grid. Hence, the fineness factor is 2 and the number of grid points required to discretize the physical system increases as 2^d where d is the dimension of the domain. As a result, the number of calculations in each time step increase by the same amount. Moreover, since explicit finite difference scheme is concerned with, when the grid spacing is decreased by a factor, for numerical stability, due to the Laplacian nature of the Allen-Cahn equation, the timestep has to be reduced by the square of the factor. Thus, to simulate the same physical size and the same physical time at half the interface width, 2^{d+2} times more computational effort has to be expended.

To utter disappointment, numerical simulations revealed that even this costlier procedure is unable to fetch the vanishing interface width limit behavior: Eq. (3.5) is solved to simulate the evolution in a two phase 1D system starting from an initial setup of the left half of the domain filled with $\phi = 1$ and the right one with $\phi = 0$. The forms of the double well and the interpolation functions are chosen as $f_{\text{dw}}(\phi) = 18\phi^2(1 - \phi^2)$ and $g(\phi) = \phi^3(10 - 15\phi + 6\phi^2)$, respectively. The interfacial energy γ , bulk driving force Δf and the mobility τ are selected as 1.0, 0.1 and 1.0, respectively. As a result, as per the predictions of the asymptotic analysis, the interface should move with a speed of $v^{(0)} = 0.1$ at steady state. The simulated results at various grid finenesses and proportionality constants are reported in Table 4.3. At the base fineness, the simulated speed is correct up to a value of a tenth of the calculated speed when ϵ is varied as four times Δx . As the fineness is increased, instead of tending towards the right value, the simulated results diverged away from it eventually leading to a stagnant but diffuse interface. At higher proportionality constants, the behavior is delayed but remained fundamentally the same as can be witnessed from columns 4 and 5 of the table. Thus, the ϵ proportional to Δx prescription proved to be ineffective in carrying out the interface width reduction investigations.

To sum up, the job is not done just yet when the targeted dynamical laws are shown to be the asymptotic limits of the derived phase-field model. Due efforts have also to be exercised for finding computationally cheaper ways of realizing them. Moreover, for the problems of current interest, the commonly designated method for measuring the convergence is itself seen to be nonrobust. The current chapter of the thesis is dedicated towards working on these issues. Particularly, in the immediate next section, an explanation is provided for the behavior reported in Table 4.3 and an efficacious prescription for realizing the vanishing limit of ϵ in explicit finite difference schemes is put forth. With it at disposal, the rest of the chapter will be dedicated for examining the speed of

Table 4.3: Effect of reducing the interface width by choosing ϵ proportional to Δx on the simulated growth speeds for three different proportionality constants. The expected speed is 0.1 units.

Δx	Fineness factor of the grid	Recovered steady state speed with		
		$\epsilon = 4.0 \times \Delta x$	$\epsilon = 5.0 \times \Delta x$	$\epsilon = 6.0 \times \Delta x$
0.5 (base case)	1	0.090516	0.095858	0.097215
0.5/2	2	0.083321	0.095855	0.097278
0.5/4	4	0.043899	0.095673	0.097293
0.5/8	8	0	0.094919	0.097294
0.5/16	16	0	0.091821	0.097279
0.5/32	32	0	0.078190	0.097217
0.5/64	64	0	0	0.096969
0.5/128	128	0	0	0.095973
0.5/256	256	0	0	0.091879
0.5/512	512	0	0	0.073252
0.5/1024	1024	0	0	0

convergence of the simulations towards the asymptotic behavior predicted in the previous chapter. Along the way, alternate choices of multi-well and interpolating forms are considered from the point of view of reducing the computational costs.

Before we move on, a terminology which will be employed frequently is explicitized. In the rest of the thesis, whenever the grid resolution or fineness is said to be varied, it is for the purposes of changing the interface width. Hence, no distinction is made between the two. That is, from here on, by simulations performed at higher (lower) resolutions or fineness factors, we mean the ones carried out at lower (higher) values of ϵ . The exact amount by which ϵ is reduced (increased) is either explicitly specified as and when it appears or is made sure that it is clear from the context.

4.2 Efficacious ϵ v.s. Δx relations for the numerical realization of the asymptotic limits[†]

Let us consider the following governing equation, a one dimensional version of Eq. (3.5).

$$\tau \frac{\partial \phi}{\partial t} = \frac{1}{\epsilon} \Delta f \mathbf{g}'(\phi) - \gamma \frac{1}{\epsilon^2} f'_{\text{dw}}(\phi) + \gamma \frac{\partial^2 \phi}{\partial x^2}. \quad (4.1)$$

The derivatives $\frac{\partial \phi}{\partial t}$ and $\frac{\partial^2 \phi}{\partial x^2}$ evaluated at a spatial point x and time t can be related to $\phi(x, t + \Delta t)$, $\phi(x - \Delta x, t)$, $\phi(x, t)$ and $\phi(x + \Delta x, t)$ using Mean Value Theorem as

$$\begin{aligned} \left. \frac{\partial \phi}{\partial t} \right|_{(x,t)} &= \frac{\phi(x, t + \Delta t) - \phi(x, t)}{\Delta t} + \Delta t \left. \frac{\partial^2 \phi}{\partial t^2} \right|_{(x,t^*)} \quad \text{for some } t^* \in (t, t + \Delta t) \quad \text{and} \\ \left. \frac{\partial^2 \phi}{\partial x^2} \right|_{(x,t)} &= \frac{\phi(x + \Delta x, t) - 2\phi(x, t) + \phi(x - \Delta x, t)}{(\Delta x)^2} + (\Delta x)^2 \left. \frac{\partial^4 \phi}{\partial x^4} \right|_{(x^*,t)} \\ &\quad \text{for some } x^* \in (x - \Delta x, x + \Delta x). \end{aligned}$$

Therefore, Eq. (4.1) corresponding to the point (x, t) can be re-expressed as

$$\begin{aligned} \tau \frac{\phi(x, t + \Delta t) - \phi(x, t)}{\Delta t} &= \frac{\Delta f}{\epsilon} \mathbf{g}'(\phi(x, t)) - \frac{\gamma}{\epsilon^2} f'_{\text{dw}}(\phi(x, t)) \\ &\quad + \gamma \frac{\phi(x + \Delta x, t) - 2\phi(x, t) + \phi(x - \Delta x, t)}{(\Delta x)^2} \\ &\quad \underbrace{-\tau \Delta t \left. \frac{\partial^2 \phi}{\partial t^2} \right|_{(x,t^*)} + \gamma (\Delta x)^2 \left. \frac{\partial^4 \phi}{\partial x^4} \right|_{(x^*,t)}}. \quad (4.2) \end{aligned}$$

[†]The numerical analysis of this section is performed jointly with Dr. Ing. Amol Subhedar.

However, in finite difference scheme, the above equation neglecting the last two terms is used for evaluating the phase-field value of the later time $t + \Delta t$ from the information pertaining to the current time t . That means, the implicit assumption is that the under-braced part of Eq. (4.2) is negligible compared to the rest of the equation. Invoking a stronger version of this: each of the under-braced terms of Eq. (4.2) is assumed to be minute compared to each of the remaining terms of the equation. That is,

$$\begin{aligned} \tau \Delta t \left| \frac{\partial^2 \phi}{\partial t^2} \Big|_{(x,t^*)} \right| &\ll \tau \left| \frac{\phi(x, t + \Delta t) - \phi(x, t)}{\Delta t} \right| = \tau \left| \frac{\partial \phi}{\partial t} \Big|_{(x,t^{**})} \right|, \\ \tau \Delta t \left| \frac{\partial^2 \phi}{\partial t^2} \Big|_{(x,t^*)} \right| &\ll \frac{1}{\epsilon} |\Delta f \mathbf{g}'(\phi(x, t))|, \\ \tau \Delta t \left| \frac{\partial^2 \phi}{\partial t^2} \Big|_{(x,t^*)} \right| &\ll \frac{\gamma}{\epsilon^2} |f'_{\text{dw}}(\phi(x, t))|, \quad \text{and} \\ \tau \Delta t \left| \frac{\partial^2 \phi}{\partial t^2} \Big|_{(x,t^*)} \right| &\ll \gamma \left| \frac{\phi(x + \Delta x, t) - 2\phi(x, t) + \phi(x - \Delta x, t)}{(\Delta x)^2} \right| = \gamma \left| \frac{\partial^2 \phi}{\partial x^2} \Big|_{(x^{**}, t)} \right| \end{aligned}$$

for some $t^{**} \in (t, t + \Delta t)$ and $x^{**} \in (x - \Delta x, x + \Delta x)$. Similarly,

$$\begin{aligned} \gamma (\Delta x)^2 \left| \frac{\partial^4 \phi}{\partial x^4} \Big|_{(x^*, t)} \right| &\ll \tau \left| \frac{\partial \phi}{\partial t} \Big|_{(x,t^{**})} \right|, \\ \gamma (\Delta x)^2 \left| \frac{\partial^4 \phi}{\partial x^4} \Big|_{(x^*, t)} \right| &\ll \frac{1}{\epsilon} |\Delta f \mathbf{g}'(\phi(x, t))|, \\ \gamma (\Delta x)^2 \left| \frac{\partial^4 \phi}{\partial x^4} \Big|_{(x^*, t)} \right| &\ll \frac{\gamma}{\epsilon^2} |f'_{\text{dw}}(\phi(x, t))|, \quad \text{and} \\ \gamma (\Delta x)^2 \left| \frac{\partial^4 \phi}{\partial x^4} \Big|_{(x^*, t)} \right| &\ll \gamma \left| \frac{\partial^2 \phi}{\partial x^2} \Big|_{(x^{**}, t)} \right|. \end{aligned}$$

The actual solution of Eq. (4.1) is $\tanh((x - vt)/\epsilon)$ for the choice $f_{\text{dw}}(\phi) = 18\phi^2(1 - \phi^2)$ and $\mathbf{g}(\phi) = \phi^3(10 - 15\phi + 6\phi^2)$ with v standing for $\Delta f/\tau$. Therefore, $\frac{\partial^2 \phi}{\partial t^2} \Big|_{(x,t^{**})} = \mathcal{O}\left(\frac{1}{\epsilon^2}\right)$, $\frac{\partial \phi}{\partial t} \Big|_{(x,t^{**})} = \mathcal{O}\left(\frac{1}{\epsilon}\right)$, $\frac{\partial^2 \phi}{\partial x^2} \Big|_{(x,t^{**})} = \mathcal{O}\left(\frac{1}{\epsilon^2}\right)$, and $\frac{\partial^4 \phi}{\partial x^4} \Big|_{(x,t^{**})} = \mathcal{O}\left(\frac{1}{\epsilon^4}\right)$. Hence, the calculations pertaining to the numerical scheme give small errors only when

$$\begin{aligned} \frac{\Delta t}{\epsilon^2} \ll \frac{1}{\epsilon} &\implies \Delta t \ll \epsilon & \frac{(\Delta x)^2}{\epsilon^4} \ll \frac{\Delta f}{\gamma \epsilon} &\implies (\Delta x)^2 \ll \frac{\Delta f}{\gamma} \epsilon^3 \\ \frac{\Delta t}{\epsilon^2} \ll \frac{1}{\epsilon^2} &\implies \Delta t \ll 1 & \frac{(\Delta x)^2}{\epsilon^4} \ll \frac{1}{\epsilon^2} &\implies (\Delta x)^2 \ll \epsilon^2 \\ \frac{\Delta t}{\epsilon^2} \ll \frac{1}{\epsilon^4} &\implies \Delta t \ll \frac{1}{\epsilon^2} & \frac{(\Delta x)^2}{\epsilon^4} \ll \frac{1}{\epsilon^4} &\implies (\Delta x)^2 \ll 1. \end{aligned}$$

Further, since explicit finite difference schemes are used for solving the evolution equation, for numerical stability, Δt has to be chosen such that $\Delta t \leq \frac{\tau(\Delta x)^2}{2d\gamma}$. Therefore, it suffices that the spatial discretization and the interface width specifier satisfy

$$\begin{aligned}(\Delta x)^2 &\ll \frac{1}{\epsilon^2} \\(\Delta x)^2 &\ll 1 \\(\Delta x)^2 &\ll \epsilon \\(\Delta x)^2 &\ll \epsilon^2 \\(\Delta x)^2 &\ll \frac{\Delta f}{\gamma} \epsilon^3.\end{aligned}$$

Of course, the above relations will necessarily be satisfied for a constant ϵ when Δx is brought close to zero. However, when ϵ itself is made to tend to zero, the relative vanishing rates should be carefully chosen so as to satisfy the relations. Specifically, in the limit $\epsilon \rightarrow 0$, the last relation is the significant one, since, once it is ensured to hold, the others are automatically satisfied. Let ϵ be chosen as a power of Δx , i.e., $\epsilon = k(\Delta x)^p$, then the last condition requires

$$(\Delta x)^{2-3p} \ll \frac{\Delta f}{\gamma} k^3. \quad (4.3)$$

The above condition is necessarily ‘eventually satisfied’ when Δx is progressively reduced if and only if $2 - 3p > 0$. In other words, to approach the asymptotic limit of $\epsilon \rightarrow 0$ in numerics by implementing a finite difference explicit scheme, it has to be ensured that $\left((\Delta x)^{\frac{2}{3}}\right) = o(\epsilon)$ as $\Delta x \rightarrow 0$. This explains the failure of the $\epsilon \propto \Delta x$ prescription observed in Table 4.3: When p is chosen as 1, Eq. (4.3) becomes

$$\frac{1}{\Delta x} \ll \frac{\Delta f}{\gamma} k^3. \quad (4.4)$$

For as long as Δx fulfills the above condition, the errors incurred in approximating the partial differential equation with the explicit finite difference equation are small and hence the recovered dynamics is close to the actual behavior. However, as Δx is reduced progressively, it incrementally begins to violate the above requirement and hence results diverging away from the desired behavior are realized. Further, a value of Δx that fails to fulfill Eq. 4.4 for some prefactor k does so by lesser amount for higher values of the latter. Consistent with this, the error in the predicted dynamics drops along each row in Table 4.3. Eq. (4.4) also points out the effect that the driving force Δf and the interfacial energy γ are going to have on the range of allowable grid spacings. It is well known that a large value of the driving force removes points from the interface and hence demands a larger value of the coefficient k for sustaining a stable simulation. On the other

hand, it is usually believed that a low driving force does not pose any such difficulty. In contrast, Eq. (4.4) suggests that when the driving force is too small, an otherwise effective grid spacing leads to undesirable magnitudes of errors. This is demonstrated in Table 4.4 which corresponds to the same simulations as the last column of Table 4.3 but with smaller values of Δf viz $\Delta f = 0.1$ and 0.01 . The lower the driving force, the faster is the approach towards stagnation of the interface. The opposite effect of γ is illustrated in Table 4.5. All these problems can be avoided by choosing $\epsilon \succ (\Delta x)^{\frac{2}{3}}$, this is demonstrated in Tables 4.6, 4.7 and 4.8 where the results of the simulations corresponding to Tables 4.3, 4.4 and 4.5 re-performed but with ϵ chosen as $\epsilon = k\sqrt{\Delta x}$ consistent with Eq. (4.3) are reported. The contrasting behavior of the results converging towards the expected answer when the grid is made finer can be readily recognized.

Table 4.4: Speeds recovered in simulations as interface width is reduced whilst choosing $\epsilon = 6.0 \times \Delta x$ for three different values of the driving force specifier Δf viz. 0.1, 0.01 and 0.001. The expected speeds are 0.1, 0.01 and 0.001, respectively.

Δx	Fineness factor	Recovered speed for		
		$\Delta f = 0.1$	$\Delta f = 0.01$	$\Delta f = 0.001$
0.5 (base case)	1	0.097215	0.0097209	0.00096374
0.5/2	2	0.097278	0.0097287	0.00094050
0.5/4	4	0.097293	0.0097180	0.00083504
0.5/8	8	0.097294	0.0096794	0
0.5/16	16	0.097279	0.0095213	0
0.5/32	32	0.097217	0.0088681	0
0.5/64	64	0.096969	0.0055310	0
0.5/128	128	0.095973	0	0
0.5/256	256	0.091879	0	0
0.5/512	512	0.073252	0	0
0.5/1024	1024	0	0	0

To consolidate, for realizing the vanishing interface width limit behavior of the derived phase-field model in explicit schemes, Δx should be made to vanish faster than ϵ . This implies that the number of grid points corresponding to the interfacial region keeps on scaling up as the interface width is reduced. Also, the numerical recovery of asymptotic limit is a far more expensive procedure than the estimates provided in section 4.1.

Finally, it is worth pointing out that not all the aspects of the numerical analysis

Table 4.5: Simulated steady state speeds as interface width is reduced by choosing $\epsilon = 4.0 \times \Delta x$ for various values of interfacial energy specifier γ . The expected speed is 0.1.

Δx	Fineness factor	Recovered speed for		
		$\gamma = 1.0$	$\gamma = 0.25$	$\gamma = 0.0625$
0.5 (base case)	1	0.090516	0.091987	0.083559
0.5/2	2	0.083321	0.092053	0.090045
0.5/4	4	0.043899	0.090487	0.091959
0.5/8	8	0	0.083318	0.092065
0.5/16	16	0	0.043920	0.090484
0.5/32	32	0	0	0.083313
0.5/64	64	0	0	0.043932
0.5/128	128	0	0	0

Table 4.6: Study of Table 4.3 repeated instead by choosing ϵ proportional to $\sqrt{\Delta x}$ for the same proportionality constants.

Δx	Fineness factor	Recovered steady state speed with		
		$\epsilon = 4.0 \times \sqrt{\Delta x}$	$\epsilon = 5.0 \times \sqrt{\Delta x}$	$\epsilon = 6.0 \times \sqrt{\Delta x}$
0.5 (base case)	1	0.096740570	0.097990192	0.098572284
0.5/2	2	0.098488824	0.099034747	0.099306608
0.5/4	4	0.099269114	0.099526360	0.099657746
0.5/8	8	0.09963862	0.099764334	0.099829382
0.5/16	16	0.099819862	0.099882168	0.099914606
0.5/32	32	0.099910263	0.099941214	0.099957375
0.5/64	64	0.099955217	0.099970638	0.099978705
0.5/128	128	0.099977623	0.099985324	0.099989353
0.5/256	256	0.099988813	0.099992662	0.099994676
0.5/512	512	0.099994408	0.099996333	0.099997339
0.5/1024	1024	0.099997203	0.099998170	0.099998670

Table 4.7: Study of Table 4.4 reperformed instead with $\epsilon = 6.0 \times \sqrt{\Delta x}$.

Δx	Fineness factor	Recovered speed for		
		$\Delta f = 0.1$	$\Delta f = 0.01$	$\Delta f = 0.001$
0.5 (base case)	1	0.098572284	0.009882372	0.000988252
0.5/2	2	0.099306608	0.009941124	0.000994115
0.5/4	4	0.099657746	0.009969976	0.000996997
0.5/8	8	0.099829382	0.009984056	0.000998406
0.5/16	16	0.099914606	0.009992258	0.000999226
0.5/32	32	0.099957375	0.009996080	0.000999608
0.5/64	64	0.099978705	0.009998048	0.000999805
0.5/128	128	0.099989353	0.009999024	0.000999902
0.5/256	256	0.099994676	0.009999511	0.000999951
0.5/512	512	0.099997339	0.009999756	0.000999976
0.5/1024	1024	0.099998670	0.0099998778	0.000999987

Table 4.8: Study of Table 4.5 reperformed instead with $\epsilon = 4.0 \times \sqrt{\Delta x}$.

Δx	Fineness factor	Recovered speed for		
		$\gamma = 1.0$	$\gamma = 0.25$	$\gamma = 0.0625$
0.5 (base case)	1	0.096740570	0.095743965	0.084264066
0.5/2	2	0.098488824	0.098060608	0.092243193
0.5/4	4	0.099269114	0.099064623	0.096129851
0.5/8	8	0.09963862	0.099540896	0.098062178
0.5/16	16	0.099819862	0.099771958	0.099028455
0.5/32	32	0.099910263	0.099886604	0.099513178
0.5/64	64	0.099955217	0.099943431	0.099756302
0.5/128	128	0.099977623	0.099971748	0.099878092
0.5/256	256	0.099988813	0.099985879	0.099939033
0.5/512	512	0.099994408	0.099992943	0.099969510
0.5/1024	1024	0.099997203	0.099996470	0.099984752

associated with the problem are covered in the current presentation: For one, the errors incurred in marching, as per the chosen finite difference scheme, from time t to $t + \Delta t$ are evaluated assuming that the exact solution corresponding to the former time instant is available. Whereas, in actuality, the information available pertaining to time t will only be approximate in nature having been obtained in the same fashion in the preceding timestep. That is, the “instantaneous” errors are calculated without taking into account their propagation along the way. Secondly, typically, a second set of calculations pertaining to passage to a global analysis from the local one presented herein has to be carried out which puts further constraints on the allowable ranges of discretization. This is elucidated by considering the following example, the classical diffusion equation.

$$\frac{\partial c}{\partial t} = D\nabla^2 c.$$

Repeating the calculations of the current section for this equation merely demands that Δt and Δx have to be kept vanishingly small for controlling the errors, i.e., $\Delta t \ll 1$ and $\Delta x \ll 1$. No further condition concerning their relative orders is demanded. However, it is well known that only when Δt is varied as $\Delta t \leq (\Delta x)^2/2dD$ will the explicit finite difference scheme be stable. The equations corresponding to all the grid points have to be simultaneously considered and analyzed for obtaining this result. Such a second layer of analysis is not performed on the entirety of Eq. (4.1), and is not even possible due to its non-linear nature. In spite of this, the behaviors of Tables 4.3, 4.4 and 4.5 have been explained and rectified. Not only that, as will be witnessed next, the relation Eq. (4.3) proved to be efficacious in all the 2D problems and even those involving triple junctions, i.e., multi-phase-field applications notwithstanding the fact that it is derived merely by considering a very specific scalar 1D modeling equation. Seeing that so many details are left out, it should only be considered good fortune that the part that could actually be done was of such immense help in setting straight the prescription for approaching the vanishing interface width limit in numerics.

The numerical performance of the multi-phase-field governing equations will be considered next.

4.3 Numerical realization of the asymptotic behavior of the multi-phase-field model

The asymptotic analysis of the previous chapter predicted that the binary interfaces and the junctions in a multi-grain system have to necessarily exhibit certain general behavior. It will now be tested how easy or difficult it is to realize this in numerical simulations.

4.3.1 Binary interface behavior in numerical simulations

For example, it is demonstrated in section 3.3.3.1 that an interface between two equilibrium phases marks out such a path on the Gibbs-simplex that the weighted distance function Eq. (3.26) is minimized. It is further argued that in the case of the multi-well W^{FP} , the minimizing path for three phase system is along the boundary of the simplex joining the two phases and for W^C , it includes the points from the interior as well. However, this is an asymptotic law, in that, it is realized in the vanishing limit of ϵ . How demanding is the system with regard to the exact numerical value of ϵ will now be analyzed along with what kind of implications this could have on the feasibility of the simulations.

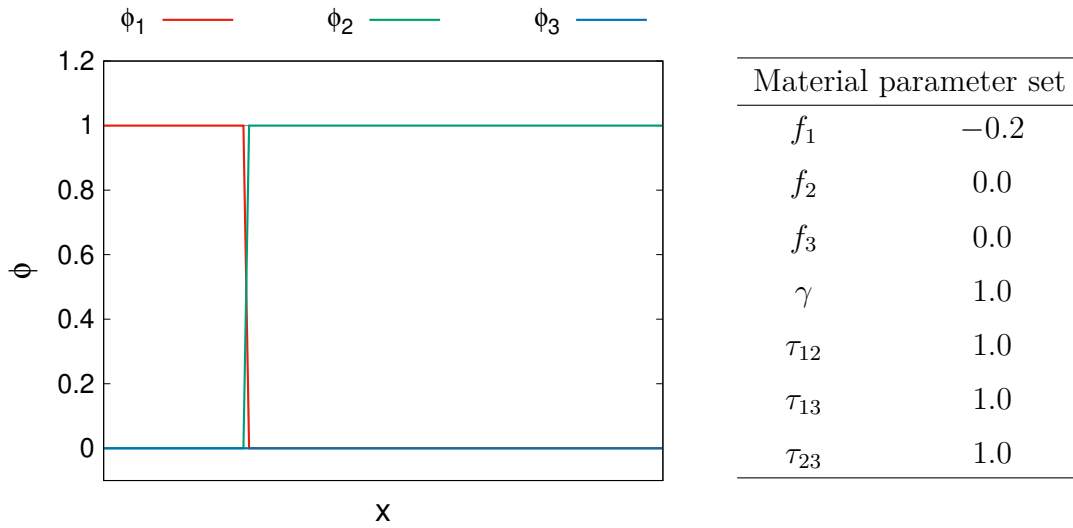


Figure 4.3: Initial filling and material parameter set used in the study of 1D two phase evolution problem through the multi-phase-field model with $N=3$.

A 1D domain is filled with ϕ_1 phase in the left quarter and with ϕ_2 in the remaining portion, a third and final phase is considered for the calculations but left unfilled. That is, the phase-field variable is assigned a value of $(1, 0, 0)$ in the first part and $(0, 1, 0)$ in the latter. Therefore, the summation constraint $\phi_1 + \phi_2 + \phi_3 = 1$ is ensured at the filling stage and the profiles of the components are as shown in Fig. 4.3. With this initial filling, the phase evolution equations Eq.(3.14) are solved once with the multi-well $W^C = 36[\phi_1^2\phi_2^2 + \phi_2^2\phi_3^2 + \phi_3^2\phi_1^2]$ and next with $W^{FP} = 18[\phi_1^2(1 - \phi_1)^2 + \phi_2^2(1 - \phi_2)^2 + \phi_3^2(1 - \phi_3)^2]$ by choosing the bulk energy interpolation forms in an uncoupled fashion with $g_S(\phi) = \phi^3(10 - 15\phi + 6\phi^2)$. The associated phase-field profiles pertaining to some later time and for the material parameter set listed in Fig. 4.3 are shown in Figs. 4.4 and 4.5, respectively. Both of them exhibit the presence of the “ghost phase”, i.e., non zero values of the initially unfilled component ϕ_3 . However, the asymptotic analysis of the previous chapter proposes that up to zeroth order there should be no presence of

ϕ_3 in the second case implying that the contribution seen there is from the higher order corrections to the phase-field variable. This can also be rationalized by taking a closer look at the recovered problem at the order next to the leading one. The corresponding equation pertaining to the component ϕ_3 (from Eq. (3.28)) is

$$-\gamma \frac{\partial^2 \tilde{\phi}_3^{(1)}}{\partial \rho^2} = \frac{1}{3} \left(f_1 \mathcal{G}'_S(\tilde{\phi}_1^{(0)}) + f_2 \mathcal{G}'_S(\tilde{\phi}_2^{(0)}) \right) + \frac{1}{3} \gamma \left((6(\tilde{\phi}_1^{(0)})^2 - 6(\tilde{\phi}_1^{(0)}) + 1) \tilde{\phi}_1^{(1)} + (6(\tilde{\phi}_2^{(0)})^2 - 6(\tilde{\phi}_2^{(0)}) + 1) \tilde{\phi}_2^{(1)} \right). \quad (4.5)$$

If $\tilde{\phi}_3^{(1)} = 0$, then $\tilde{\phi}_1^{(1)} = -\tilde{\phi}_2^{(1)}$ implying

$$0 = \frac{1}{3} \left(f_1 \mathcal{G}'_S(\tilde{\phi}_1^{(0)}) + f_2 \mathcal{G}'_S(\tilde{\phi}_2^{(0)}) \right)$$

which is a contradiction for the current parameter set. Hence, a non zero correction at first order arises from ϕ_3 component. If such is the case, on making ϵ smaller, its contribution should die out whereas it should be sustained in the first (W^C) case. Accordingly, simulations performed with finer grids and ϵ chosen as $\epsilon = k\sqrt{\Delta x}$ recovered this behavior as depicted in Figs 4.6 and 4.7.

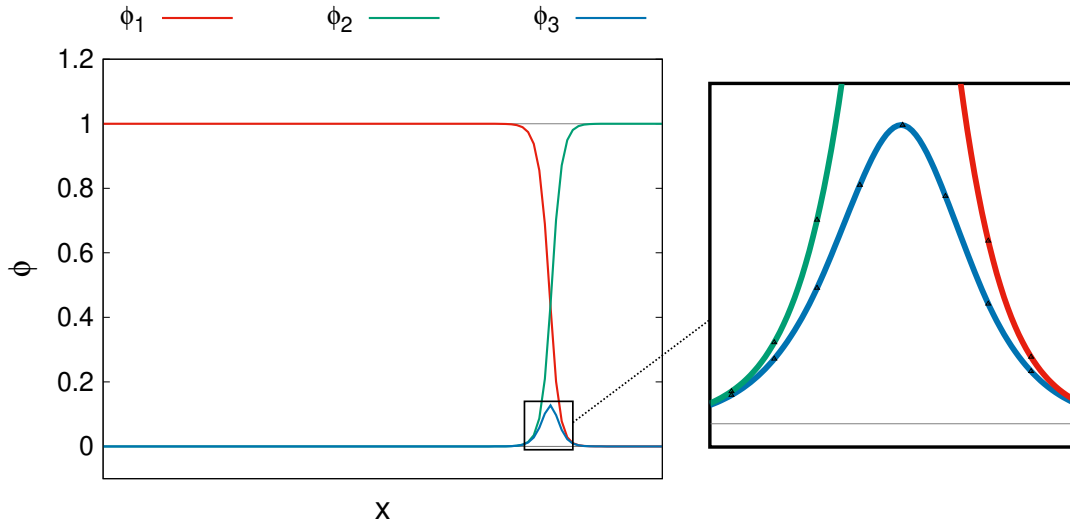


Figure 4.4: Steady state vector phase-field profile simulated using the classical multi-well form $W^C = 36[\phi_1^2\phi_2^2 + \phi_2^2\phi_3^2 + \phi_3^2\phi_1^2]$ from an initial set up and parameter set of Fig. 4.3. The presence of third phase is highlighted by zooming in appropriately.

Next, the recovered steady state speeds, i.e., the predictions of section 3.3.3.2 are investigated. As pointed out there, the W^C multi-well should give rise to a speed different from the desired value due to an effective mobility different from the actual one entering

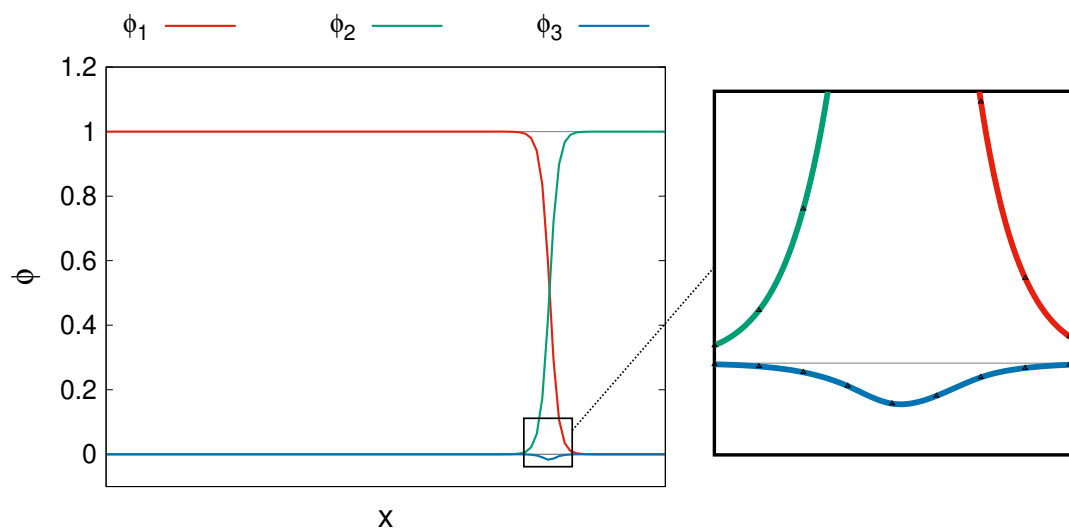


Figure 4.5: Steady state vector phase-field profile simulated using the Folch-Plapp multi-well form $W^{FP} = 18[\phi_1^2(1 - \phi_1)^2 + \phi_2^2(1 - \phi_2)^2 + \phi_3^2(1 - \phi_3)^2]$ from an initial set up and parameter set of Fig. 4.3. The presence of third phase is highlighted by zooming in on the appropriate part.

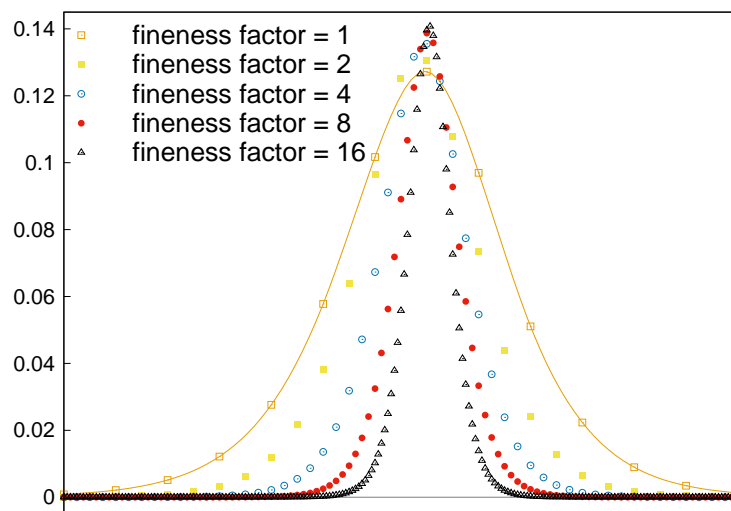


Figure 4.6: Sustenance of third phase at lower interface widths in simulations employing classical multi-well $W^C = 36[\phi_1^2\phi_2^2 + \phi_2^2\phi_3^2 + \phi_3^2\phi_1^2]$.

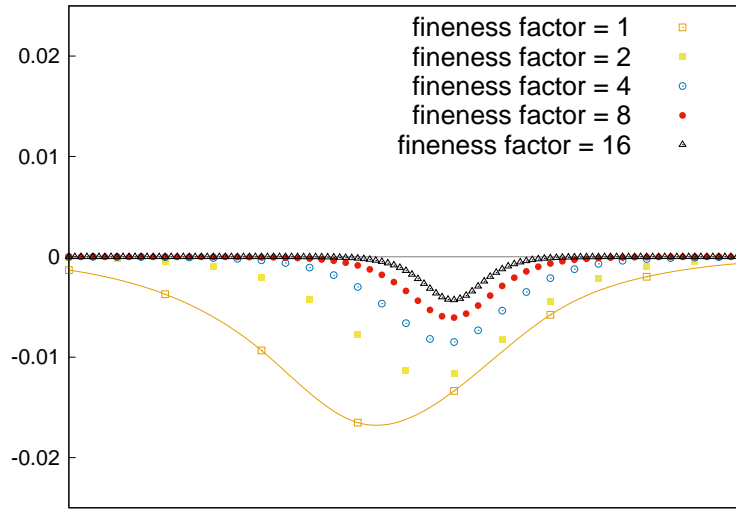


Figure 4.7: Decay of third phase as interface width is reduced in simulations employing Folch-Plapp multi-well $W^{FP} = 18[\phi_1^2(1 - \phi_1)^2 + \phi_2^2(1 - \phi_2)^2 + \phi_3^2(1 - \phi_3)^2]$.

the dynamical law Eq. (3.30). Consistent with this, from the results reported in Fig. 4.8, the steady state speeds can be seen to tend toward a value different from the right result of Velocity = Mobility \times Bulk driving force = $1.0 \times (0.0 - (-0.1)) = 0.1^\ddagger$. Whereas, as depicted in Fig. 4.9, the desired value is recovered in those simulations in which W^{FP} is employed.

It will now be argued that even though elimination of the third phases at the leading order can in principle recover the right dynamics of the phase evolution, it is not entirely sufficient. This is because, in some circumstances, for instance when the mobility of the ghost phase is extremely small (irrespective of which phase it forms the interface with), in spite of it occurring in trace amounts, the speed of the entire interface may be significantly affected. This is demonstrated using the Folch-Plapp well in the following. The highest resolution studied in Figs. 4.6- 4.9, that is, a grid fineness of 16 times the base value considered in these figures is chosen for re-performing the simulations but for higher and higher values of τ_{13} and τ_{23} . The results are reported in Fig. 4.10 which indicate a significant drop in the steady state speed from the expected value of 0.1. In other words, a resolution of 16 times the base value which was satisfactory for lower values of τ_{13} and τ_{23} , proved to be insufficient when the third phase is highly immobile. The origin of this behavior can be uncovered by continuing the asymptotic analysis of section 3.3.3.2 at next order, i.e., by performing a thin-interface analysis.

[‡]It has to be emphasized that when a and $a_{\alpha\beta}$ of Table 2.1 are fixed at 18 and 36, respectively, as done in the current case, then for an accurate modeling of the system ' f_α 's should not be the bulk energies of the phases but twice these values. Hence the calculation of bulk driving force is as $0.0 - (-0.1)$ and not as $0.0 - (-0.2)$.

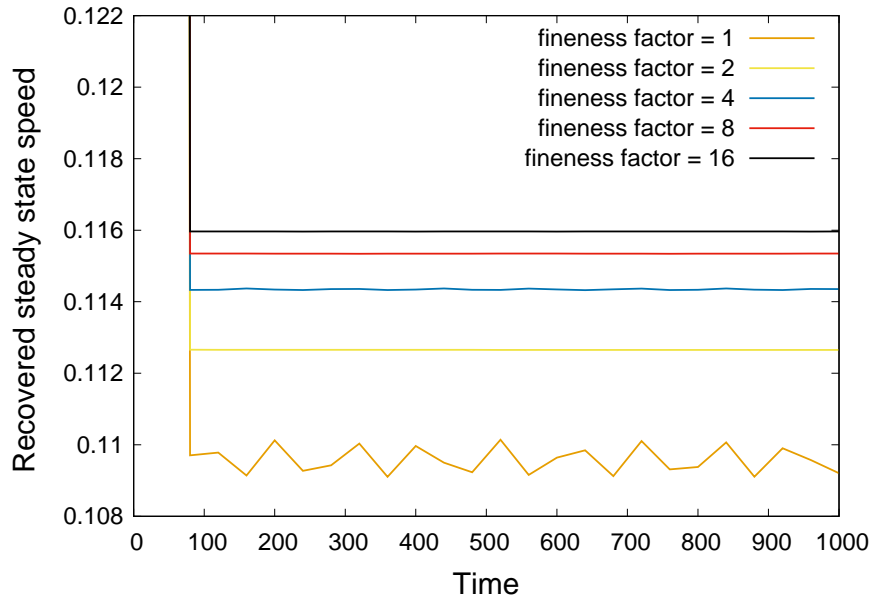


Figure 4.8: Convergence of the steady state speed as the interface width is reduced in simulations employing the classical well $W^C = 36[\phi_1^2\phi_2^2 + \phi_2^2\phi_3^2 + \phi_3^2\phi_1^2]$. The value approached is different from the desired result of 0.1 due to the presence of the third phases at zeroth order.

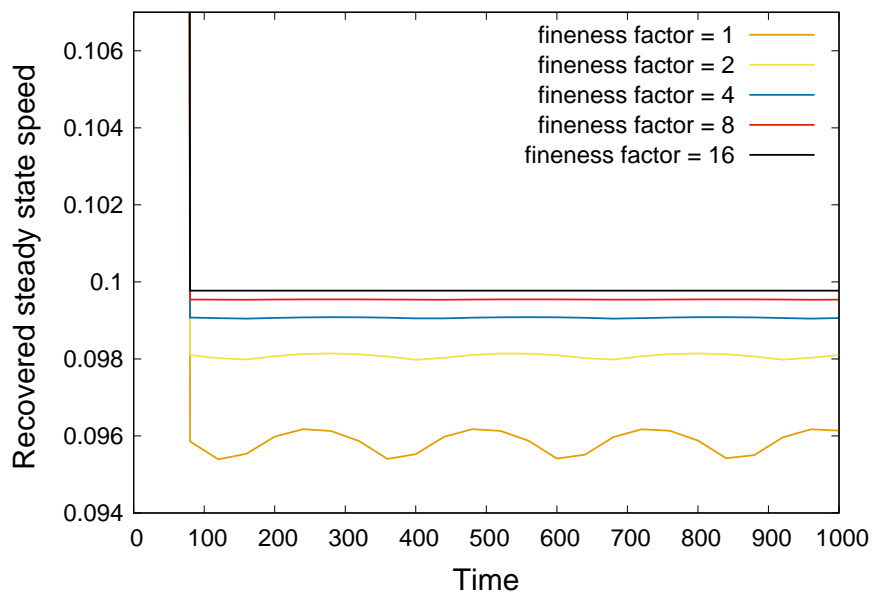


Figure 4.9: Convergence of the steady state speed as the interface width is reduced in simulations employing the Folch-Plapp well $W^{FP} = 18[\phi_1^2(1 - \phi_1)^2 + \phi_2^2(1 - \phi_2)^2 + \phi_3^2(1 - \phi_3)^2]$. The value approached is the same as the desired result of 0.1 due to the absence of third phases at the zeroth order.

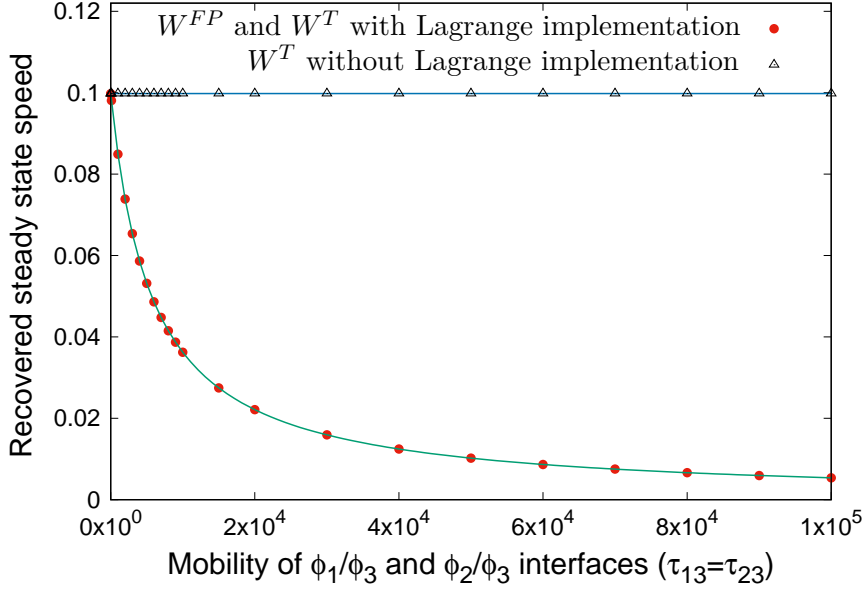


Figure 4.10: Effect of ghost phase mobility on the recovered planar growth kinetics for the Foch-Plapp well with Lagrange implementation and for the Toth well with and without Lagrange implementation. The highest resolution that is studied in Figs. 4.6–4.9 is used for this investigation. The targeted value is 0.1. Lines are drawn connecting the points for easy reference.

4.3.1.1 Thin interface analysis of binary interfaces

Without loss of generality, we assume that the interface under study is between phases ϕ_1 and ϕ_2 . The requirement at this order is

$$\begin{aligned}
& -(\tau_{12}v^{(0)} + \gamma\kappa^{(0)}) \frac{\partial \tilde{\phi}_\beta^{(1)}}{\partial \rho} - (\tau_{12}v^{(1)} + \gamma\kappa^{(1)}) \frac{\partial \tilde{\phi}_\beta^{(0)}}{\partial \rho} - \tau^{(1)}(\tilde{\phi}^{(0)}, \tilde{\phi}^{(1)})v^{(0)} \frac{\partial \tilde{\phi}_\beta^{(0)}}{\partial \rho} \\
& = -f_\alpha \frac{\partial^2 \mathbf{g}_\alpha(\phi)}{\partial \phi_\gamma \partial \phi_\beta}(\tilde{\phi}^{(0)})\tilde{\phi}_\gamma^{(1)} - \frac{\gamma}{2} \frac{\partial^3 W(\phi)}{\partial \phi_\gamma \partial \phi_\alpha \partial \phi_\beta}(\tilde{\phi}^{(0)})\tilde{\phi}_\alpha^{(1)}\tilde{\phi}_\gamma^{(1)} \\
& \quad - \gamma \frac{\partial^2 W(\phi)}{\phi_\alpha \partial \phi_\beta}(\tilde{\phi}^{(0)})\tilde{\phi}_\alpha^{(2)} + \gamma \frac{\partial^2 \tilde{\phi}_\beta^{(2)}}{\partial \rho^2} + \gamma(\kappa^{(0)})^2 \rho \frac{\partial \tilde{\phi}_\beta^{(0)}}{\partial \rho} - \tilde{\lambda}^{(2)}.
\end{aligned}$$

where $\tilde{\lambda}^{(2)} = \sum_{i=1}^N -\frac{\delta F}{\delta \phi_\beta}^{(2)}$ with $-\frac{\delta F}{\delta \phi_\beta}^{(2)}$ standing for the r.h.s of the above equation excluding $\tilde{\lambda}^{(2)}$.

Mimicking the standard calculations for the scalar phase-field solidification model and manipulating mixed derivatives in a characteristic manner as done in chapter 3, the

following relation is derived from the above.

$$\begin{aligned}
2(\tau_{12}v^{(0)} + \gamma\kappa^{(0)}) \int_{-\infty}^{\infty} \frac{\partial\tilde{\phi}_{\beta}^{(1)}}{\partial\rho} \frac{\partial\tilde{\phi}_{\beta}^{(0)}}{\partial\rho} d\rho + (\tau_{12}v^{(1)} + \gamma\kappa^{(1)}) \int_{-\infty}^{\infty} \frac{\partial\tilde{\phi}_{\beta}^{(0)}}{\partial\rho} \frac{\partial\tilde{\phi}_{\beta}^{(0)}}{\partial\rho} d\rho \\
+ v^{(0)} \int_{-\infty}^{\infty} \tau^{(1)}(\tilde{\phi}^{(0)}, \tilde{\phi}^{(1)}) \frac{\partial\tilde{\phi}_{\beta}^{(0)}}{\partial\rho} \frac{\partial\tilde{\phi}_{\beta}^{(0)}}{\partial\rho} d\rho = 0.
\end{aligned} \tag{4.6}$$

In the scalar model analyses, the counterpart of the first integral of Eq. (4.6) vanishes due to the terms of the integrand obeying some symmetry properties. The appropriately modified symmetry requirements for the multi-phase case are readily satisfied by the current choices of the multi-well and the interpolating forms, hence, the same holds in the current situation as well. The second term on the l.h.s carries the first order correction to the Gibbs-Thomson law recovered at the previous order, i.e., Eq. (3.30). The third term, however, does not arise in a scalar phase-field model and is only exclusive to the current case. As a result, the dynamical law is retrieved in the former up to an order of error of ϵ^2 . Only when an additional field of composition or temperature is considered, this level of accuracy is lost and it is necessary to introduce the thin-interface corrections into the τ parameter to re-gain it; otherwise, it is automatically captured. Whereas, in a multi-phase-field model, if it is not taken care that the third integral of Eq. (4.6) vanishes, the Gibbs-Thomson condition is retrieved only up to the zeroth order even when an additional transport field is absent. However, executing a thin-interface correction is not an advisable solution to overcome this problem as it would require evaluating the third integral of Eq. (4.6) which, in turn, demands a knowledge of $\tilde{\phi}^{(1)}$ which is hard to solve for. Hence, causing the integral to vanish altogether is the only feasible option. Fortunately, this is not as difficult a task as it would seem on a first look, at least when the τ -form of Table 2.1 is employed. This is because, the latter has the property that if only two and the same two components of $\tilde{\phi}^{(0)}$ and $\tilde{\phi}^{(1)}$ are non-vanishing, then $\tau_A^{(1)}(\tilde{\phi}^{(0)}, \tilde{\phi}^{(1)})$ vanishes identically. That means, all the above discussion boils down to being able to eliminate the third phases not only at the leading order but also at least at the one next to it.

Currently, the root cause for the invalidity of $\tilde{\phi}_3^{(1)} = 0$ is the non vanishing behavior of the r.h.s. of Eq. (4.5), or in other words, the choice of the interpolation functions. Instead of the currently chosen interpolating forms, if the ones given in Ref. [22] are used, the third phase can be eliminated even at first order. Thus, this is one of the ways in which this problem can be solved. However, the scope of the solution is very limited as it is specific to three-phase systems. One way of generalizing this to any number of phases is to choose interpolation functions which satisfy the following set of sufficient conditions among which the first three are anyway the standard requirement and only the remaining

two are additional:

$$\mathbf{g}_\alpha(\phi_\alpha = 0) = 0, \quad (4.7a)$$

$$\mathbf{g}_\alpha(\phi_\alpha = 1) = 1, \quad (4.7b)$$

$$\frac{\partial \mathbf{g}_\beta}{\partial \phi_\beta}(\phi_\beta = 1) = 0, \quad (4.7c)$$

$$\frac{\partial \mathbf{g}_\alpha}{\partial \phi_\beta}(\phi_\beta = 0) = 0 \quad \text{and} \quad (4.7d)$$

$$\sum_{\beta=1}^N \frac{\partial \mathbf{g}_\alpha}{\partial \phi_\beta} \Big|_{\sum_{\gamma=1}^N \phi_\gamma=1} = 0. \quad (4.7e)$$

However, by now, the multi-well can start creating a problem as it may not necessarily provide a vanishing contribution to the evolution equations of all the unfilled phases. Thus, in conjunction with the new kind of interpolation functions, a multi-well fulfilling the following conditions will completely address the issue. In fact, in such a case, there will no longer be a necessity of the Lagrange multiplier implementation and yet the summation property will be preserved (i.e., the Lagrange multiplier is identically zero). The said conditions on the multi-well are

$$\frac{\partial W}{\partial \phi_\beta}(\phi_\beta = 0) = 0, \quad (4.8a)$$

$$\sum_{\beta=1}^N \frac{\partial W}{\partial \phi_\beta} \Big|_{\sum_{\alpha=1}^N \phi_\alpha=1} = 0 \quad \text{and} \quad (4.8b)$$

$$\frac{\partial}{\partial \phi_\alpha} \frac{\partial W}{\partial \phi_\beta}(\phi_\beta = 0) = 0 \quad \text{when } \alpha \neq \beta. \quad (4.8c)$$

It is unknown if all the conditions of Eq. (4.7) can be simultaneously satisfied or not; no examples are known to exist so far. Such being the state of affairs, the multi-well of Eq. (4.8) is especially attractive because even when only the first four conditions of Eq. (4.7) are satisfied, it guarantees that the third phases remain suppressed without erupting up to the first order. However, the trade off is that the summation property may not be necessarily satisfied. But again, this does not stand as an major obstacle in modeling systems where summation rule is important because a significant part of the phase-field variable satisfies the rule as it still holds at the zeroth order. An instance of such an all advantageous multi-well indeed exists which is proposed by Toth *et.al.* which takes the form

$$W^T = a \left(\sum_{\alpha=1}^N \frac{\phi_\alpha^4}{4} + \sum_{\substack{\alpha=1, \beta=1 \\ \alpha \neq \beta}}^{N,N} \frac{\phi_\alpha^2 \phi_\beta^2}{4} - \sum_{\alpha=1}^N \frac{\phi_\alpha^3}{3} - \frac{1}{12} \right) \quad (4.9)$$

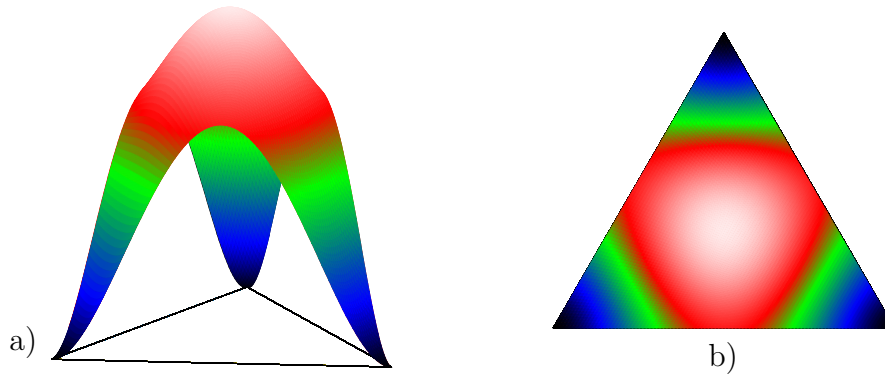


Figure 4.11: Plot of the restriction of the three phase Toth's well (i.e., W^T of Eq.(4.9) for $N = 3$) to the Gibbs triangle; a) as a surface graph over the triangle and b) as a heat map.

and is visualized over the Gibbs-simplex in Fig. 4.11. The results of simulations of Figs. 4.4–4.9 re-performed employing this well and without Lagrange multiplier implementation are depicted in Fig. 4.12 and with it in Fig. 4.13. In the first case, no third phase arose and in the latter, the rise and subsequent subsiding of it is the exact same as that seen in the case with W^{FP} . Of course, the latter is due to the fact that the governing equations with Toth well merge with those with the Plapp one when Lagrange multipliers are turned on. This implies that the behavior of the green curve in Fig. 4.10 gets bettered to that of the blue one in the first case while it remains the same in the latter. Other multi-wells that suppress the third phases up to the first order when summation constraint is not imposed have a similar form as that of Eq. (4.9) and are frequently employed [55–59]. However, they break the constraint even at the zeroth order and only the Toth's well is an exception. Unfortunately, the latter only handles the case of equal interfacial energies for all the involving interfaces. A generalization to asymmetric cases is currently not known.

In summary, the Folch-Plapp formulation of Ref. [22], although ensures the summation property and as well as eliminates the third phases for both equal and unequal interfacial energies, is only valid for three phases. Toth's well, on the other hand, recovers the summation rule to a significant level and can be applied to more than three phases, however, a generalization to unequal interfacial energies is currently unavailable. Finally, the classical well W^C can be easily extended to arbitrary interfacial energies and any number of phases but produces third phases at the zeroth order itself.

Before we end the discussion, we note that although in principle the third phases cannot be eliminated at zeroth order when using the classical well, a way to minimize them is to add a higher order term $G\phi_1^2\phi_2^2\phi_3^2$ to the multi-well which penalizes the middle portion of the Gibbs-simplex without affecting the edges or vertices. Higher the strength G of this higher order term, higher is the penalty. However, increasing G would also

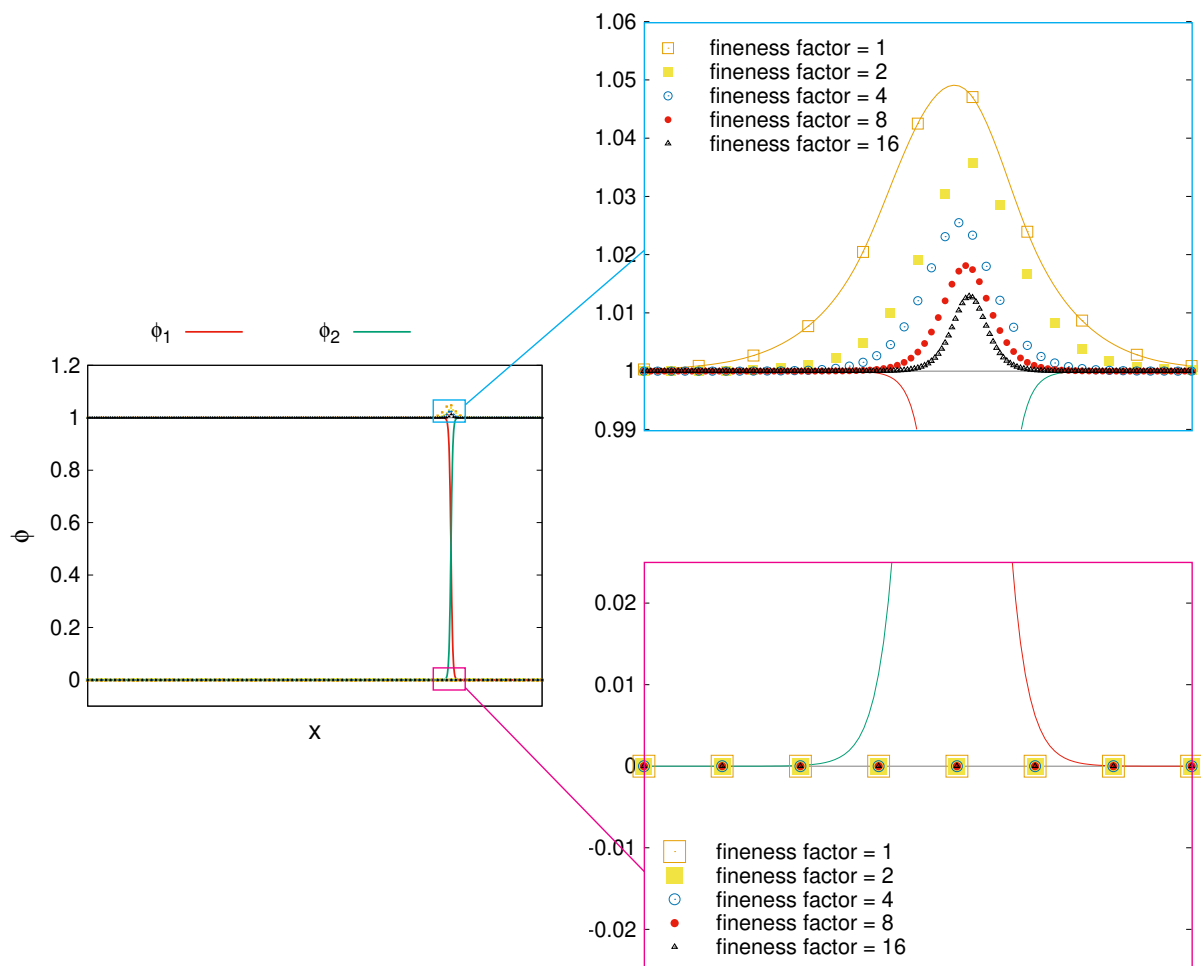


Figure 4.12: Simulated results at various grid discretizations obtained using Toth's well in the absence of Lagrange multiplier implementation. The zoomed in figure on the top shows the sum of all the components $\phi_1 + \phi_2 + \phi_3$ and the one on the bottom shows the absence of springing up of the ghost phase.

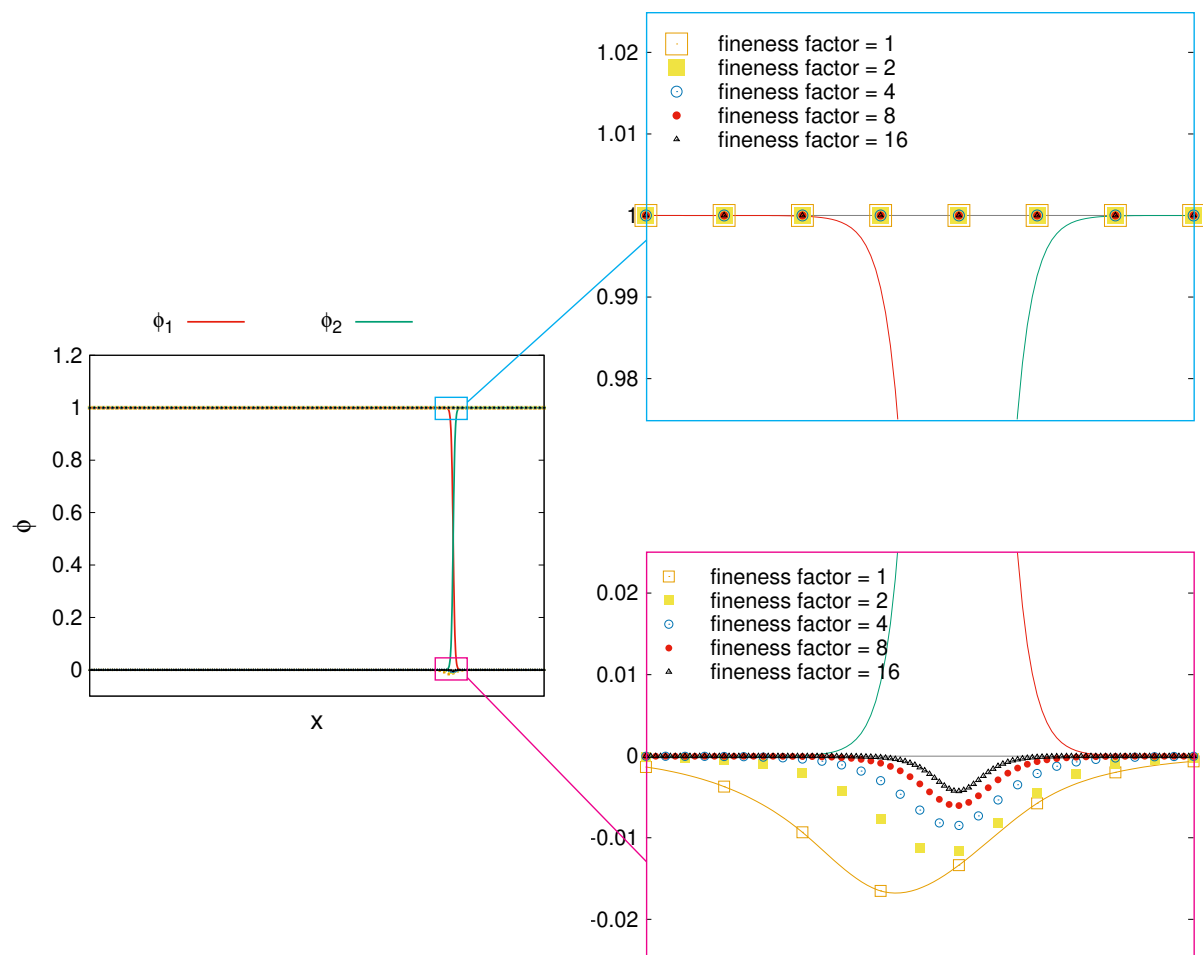


Figure 4.13: Simulated results at various grid finesses obtained using Toth's well and a Lagrange multiplier implementation. The zoomed in figure on the top shows the sum of all the components $\phi_1 + \phi_2 + \phi_3$ and the one on the bottom shows the rise of the ghost phase and its progressive suppression at higher resolutions similar to that found in the case of Folch-Plapp well in Fig. 4.7.

require using a smaller grid spacing to avoid numerical instabilities and thus proving to be not that advantageous after all. A similar observation of having to compromise on the fineness of the grid discretization when lifting the heights of one of the saddle points was made by Folch and Plapp in Ref. [22].

We now move on to the numerical recovery of the asymptotic laws predicted for the triple junction dynamics. Particularly, we look at the recovery of the Young’s law.

4.3.2 Triple junction behavior in numerical simulations

The apparent influence of the mobilities on the triple junction angles in the motivating example presented at the beginning of the chapter can now be explained on the basis of the above discussion to be an artifact of larger “interface widths”. Thus, as the latter is reduced, each of the colored profiles in Fig. 4.2 is expected to gradually change, eventually merging into the dark one (i.e., the theoretical profile). Likewise, the front velocities are supposed to converge to the appropriate value. This is demonstrated in Fig. 4.14 and Table 4.9 for an inverse mobility of $\tau_{23} = 100$ where the simulations are performed at various finenesses of grid by choosing Toth’s well W^T with $a = 36$ and switching off the Lagrange multiplier implementation to minimize third phases. The relation between ϵ and the grid spacing Δx is varied as $\epsilon = 5.0 \times \Delta x$. Even though it has just been reasoned that such a prescription will eventually prove futile for studying the convergence with regard to interface width in numerical simulations, it is still employed to take advantage of the faster downsizing of the interface width it has to offer, at least until the problem begins to show up. Correspondingly, the profiles are seen to incrementally improve

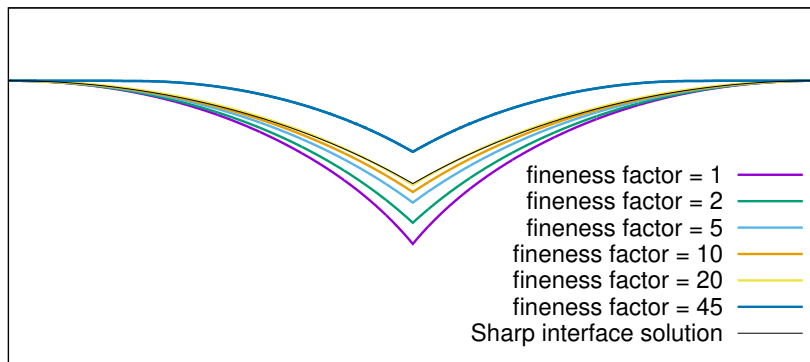


Figure 4.14: The $\tau_{23} = 100$ case of Fig. 4.2 re-studied at various degrees of grid fineness using Toth’s multi-well $W^T = 36 \left(\frac{\phi_1^4 + \phi_2^4 + \phi_3^4}{4} + \frac{\phi_1^2 \phi_2^2 + \phi_2^2 \phi_3^2 + \phi_3^2 \phi_1^2}{2} - \frac{\phi_1^3 + \phi_2^3 + \phi_3^3}{3} - \frac{1}{12} \right)$ and by turning off the Lagrange multiplier implementation. The prescription of $\epsilon = 5.0 \times \Delta x$ is utilized for the simulations with the resolution of Table 4.1 corresponding to fineness factor = 2.

until a resolution of $20\times$ after which they suddenly behave in an eccentric manner. The

Table 4.9: Steady state angles and speeds recovered for the growth fronts of Fig. 4.14.

Fineness factor	Recovered angle at the triple junction	Recovered steady state speed (rel. error)
1	50.26812°	0.055692812 (22.23%)
2	42.65556°	0.059691085 (16.65%)
5	36.56480°	0.063862144 (10.83%)
10	33.52546°	0.066000236 (7.84%)
20	31.78469°	0.067073856 (6.34%)
40	30.26082°	0.062963142 (12.08%)
Sharp interface solution	30.0°	0.071616518

abnormal behavior is suspected to be emerging from the inefficacy of the ϵ proportional to Δx selection. However, it is not feasible to test this for the current parameter set as it would require going up to over 900 times higher resolution when using $\epsilon = 5.0\sqrt{\Delta x}$. Therefore, a different parameter set is simulated exclusively for testing this hypothesis. The analysis of section 4.2 also proposes that the $\epsilon \propto \Delta x$ scheme fails faster at lower driving forces; thus, by reducing the latter, this hypothesis may be tested. However, when the bulk driving force is too small, one may run into the problem of the solid phases shrinking rather than growing due to their curvatures. Thus, to control the curvatures, larger lengths in the lateral direction are chosen and a parameter set is designed which is listed in Table 4.10. The associated simulation results are reported in Figs. 4.15 and 4.16, and in Table 4.11. In the $\epsilon = 4.5 \times \Delta x$ simulations, after a fineness of $8\times$, the front motion stopped abruptly whereas when $\epsilon = 4.5 \times (\Delta x)^{0.6}$, at $40\times$, that is, at even smaller interface widths, the profile behaved in a normal fashion. Thus, it can be concluded that the sudden change in the profile shape in Fig. 4.14 is an outcome of the restrictive choice of the relation between interface width and spatial discretization.

Table 4.10: A parameter set designed to prove that the jump behavior of Fig. 4.14 is due to the $\epsilon \propto \Delta x$ selection.

f_1	f_2	f_3	γ	τ_{12}	τ_{13}	τ_{23}	N_x	N_y	Δx	Δt
0.50	0.0	0.0	1.0	1.0	1.0	1.0	64	32	1.0	$0.2 \times (\Delta x)^2$
$\{g_\alpha(\phi)\}$				$W(\phi)$			$\tau(\phi)$			
$\{\phi_\alpha^3(10 - 15\phi_\alpha + 6\phi_\alpha^2)\}$				$W^T(\phi)$ with $a = 36$			$\tau_A(\phi)$			

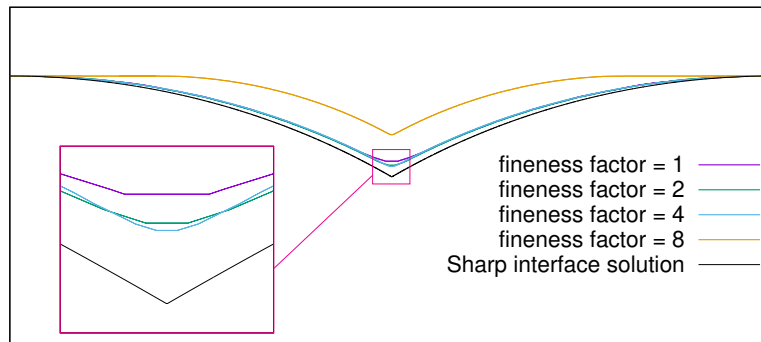


Figure 4.15: Simulation results at various degrees of fineness of the grid obtained by varying ϵ as $\epsilon = 4.5 \times \Delta x$. The values of Table 4.10 are chosen for the base resolution.

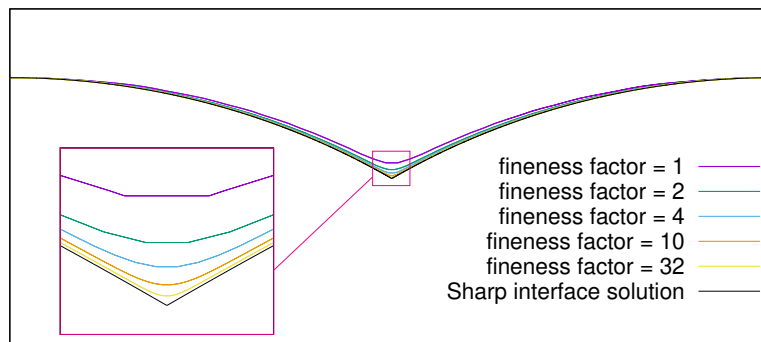


Figure 4.16: Simulation results at various degrees of fineness of the grid obtained by varying ϵ as $\epsilon = 4.5 \times (\Delta x)^{0.6}$. The values of Table 4.10 correspond to the base resolution.

Table 4.11: Steady state speeds recovered for the growth fronts of a) Fig. 4.15 and b) Fig. 4.16.

a)		b)	
Fineness of the grid	Recovered speed with $\epsilon = 4.5 \times \Delta x$	Fineness of the grid	Recovered speed with $\epsilon = 4.5 \times (\Delta x)^{0.6}$
1	0.009057744	1	0.009057744
2	0.009172148	2	0.009493199
4	0.009012258	4	0.009644454
6	0.008199712	6	0.009697528
7	0.006742424	8	0.009722445
8	-2.025757E-13	10	0.009736554
		20	0.009765793
Sharp interface solution	0.009790374	32	0.009776316
		40	0.009779809

We will now try to figure out the reason behind the lethargic convergence in Fig. 4.14. Note that in the case of section 4.3.1, a third phase which isn't supposed to occur has emerged and due to its low mobility, it retarded the motion of the interface. Such a thing cannot be happening in the present case as it is made sure that the chosen model, i.e., the usage of Toth potential and the choice of leaving out Lagrange multiplier implementation ensures that the binary interfaces are free from the third phases up to first order. Thus, the retarded motion must be emerging solely from the interplay happening at the triple junction. Specifically, the reason has to do with the particular choice of the inverse mobility function $\tau(\phi)$ chosen as $\tau_A(\phi)$.

Consider the schematic of Fig. 4.17 and let us assume that the simulation parameter set is as given in Table 4.1 except may be for a replacement of W^{FP} with W^T . The regions marked A and B which are well removed from the triple point see a bulk driving force of 0.1 and an inverse mobility of 1.0 due to the $\tau_A(\phi)$ merging into τ_{12} and τ_{13} , respectively, at zeroth order. Whereas, the region marked C has the values of all the phase-field components around $1/3$ and as a rough estimate sees an inverse mobility of $\frac{1 \times 1/3 \times 1/3 + 1 \times 1/3 \times 1/3 + 100 \times 1/3 \times 1/3}{1/3 \times 1/3 + 1/3 \times 1/3 + 1/3 \times 1/3} = 34$ and possibly not a strikingly different overall driving force. Hence, the region C has almost the same propensity to grow but its mobility is

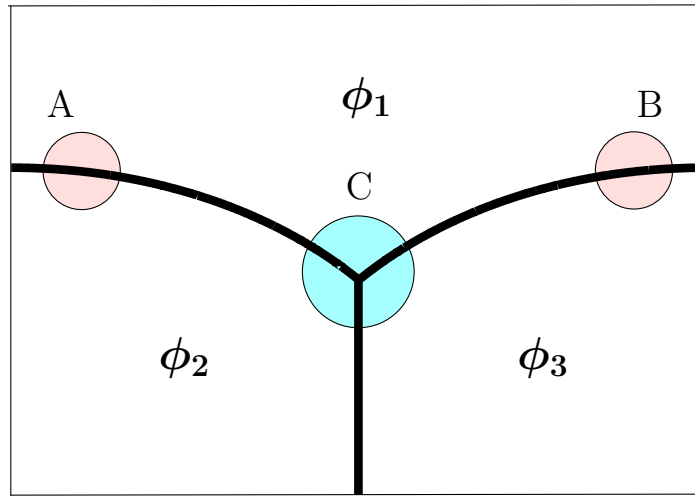


Figure 4.17: Schematic of the steady state profile of the three grain growth within the setup of Fig. 4.1, with triple junction region and regions well removed from it highlighted.

much lower compared to regions A and B and hence the interface gets pinned to some extent at the triple junction. Further, as ϵ is reduced, the percentage of the front region that is associated with low mobility reduces and the pinning is relaxed. Eventually, in the sharpest of the interface widths, only the triple point, i.e, a set of measure zero sees a different value and hence the pinning effect is completely eliminated. Thus, to solve the problem of delayed convergence without having to adopt the costly approach of ϵ

reduction, a different interpolation form for $\tau(\phi)$ may be chosen. Particularly, if $\tau(\phi)$ is averaged in a harmonic fashion $\tau_{\text{H}}(\phi)$ given by

$$\frac{1}{\tau_{\text{H}}(\phi)} = \frac{\sum_{\alpha < \beta} \frac{1}{\tau_{\alpha\beta}} \phi_{\alpha}^2 \phi_{\beta}^2}{\sum_{\alpha < \beta} \phi_{\alpha}^2 \phi_{\beta}^2} \quad (4.10)$$

as opposed to the arithmetic one $\tau_{\text{A}}(\phi)$ of Table 2.1, the value seen at regions A and B is still unity but the one seen at C is around 3 instead of 30. Therefore, the hinging of the triple junction can be drastically reduced. Results of simulations performed at various

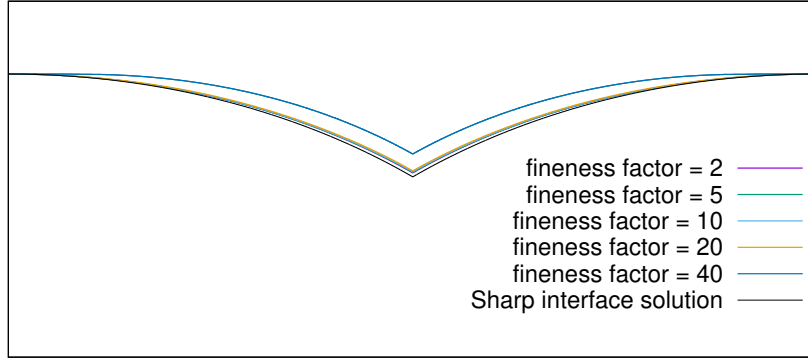


Figure 4.18: Simulations of Fig. 4.14 re-performed with inverse mobility interpolation chosen in a harmonic fashion as in Eq. (4.10).

Table 4.12: Steady state angles and speeds recovered for the growth fronts of Fig. 4.18.

Fineness factor	Recovered angle at the triple junction	Recovered steady state speed (rel. error)
1	35.78360°	0.067906155 (5.18%)
2	29.75446°	0.068478003 (4.38%)
5	29.48043°	0.068868911 (3.84%)
10	29.43619°	0.068930519 (3.75%)
20	29.63458°	0.068655565 (4.13%)
40	29.19031°	0.063279723 (11.64%)
Sharp interface solution	30.0°	0.071616518

resolutions but for the new τ -form are reported in Fig. 4.18 and Table 4.12. Note that the recovered angle and speed of advancement of the surface are very close to the theoretical values even at low resolutions. Once again, the abrupt behavior in the profile shape can be witnessed at large resolutions due to the ϵ proportional to Δx scheme of reducing

the interface width. Simulations re-done instead by choosing $\epsilon \propto (\Delta x)^{0.6}$ eliminated this as evident from Fig. 4.19 and Table 4.13. Not only that, the quality of convergence is also higher: A slight gap between the sharp interface solution and the simulated profiles persisted in Fig. 4.18 even at values of grid fineness in the ideal range. Whereas, no such visible gap is seen in the case of $\epsilon = 5.0 \times (\Delta x)^{0.6}$. Further, the growth speed is also seen to attain the steady state value in a clean fashion in the latter case without an oscillatory behavior observed in the former (not reported).

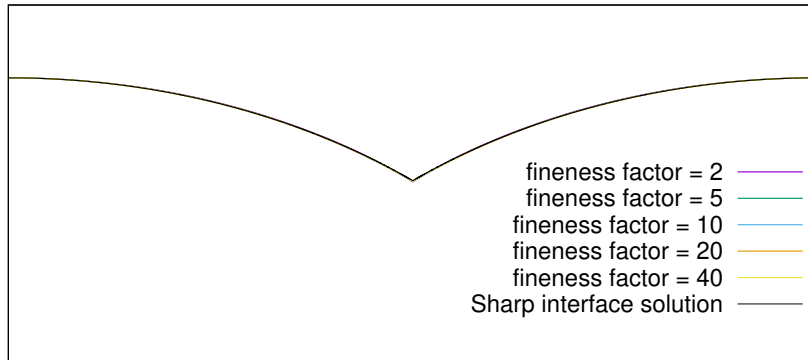


Figure 4.19: Simulations of Fig. 4.18 re-performed by instead varying ϵ as $\epsilon = 5.0 \times (\Delta x)^{0.6}$.

Table 4.13: Steady state angles and speeds recovered for the growth fronts of Fig. 4.19.

Fineness factor	Recovered angle at the triple junction	Recovered steady state speed (rel. error)
1	35.44136°	0.068944773 (3.73%)
2	32.10509°	0.069987781 (2.27%)
5	30.68639°	0.070741189 (1.22%)
10	30.39941°	0.071060387 (0.78%)
20	30.25262°	0.071261178 (0.50%)
40	30.15823°	0.071388989 (0.32%)
Sharp interface solution	30.0°	0.071616518

Though the change in the form used for interpolating the mobilities solved the particular problem at hand, it is in no way an all inclusive solution. Arithmetic average of a set of numbers stays close to the largest of the values while the harmonic one to that of the smallest. Hence, in the current example, where it is advantageous to pick the smaller value, harmonic form proved to be efficacious. However, in problems where the binary front of interest is itself less mobile and a part of it is contributed from a triple junction

which is highly mobile, then the reverse situation would occur. That is, it would then be beneficial to pick a larger value instead of a smaller one and hence arithmetic form, in principle, will turn out to be the better choice among the two. Like the arithmetic form led to a pinning of the triple junction in the current case, in such a situation, a protrusion of the junction is likely to take place with the rest of the front lagging behind. However, simulations performed with the same parameter set as used for Fig. 4.19 except for a reversal of the inverse mobility values as $\tau_{12} = 100$, $\tau_{13} = 100$ and $\tau_{23} = 1$ did not produce any such protrusion or as a matter of fact, any huge differences in the computational results as can be seen from the first two rows of Table 4.14 and from the second and third columns of Table 4.15. The arithmetic form is seen to be only a little better than the harmonic one both in terms of the front shapes and their growth speeds. Hightened differences can be seen at larger driving forces as shown in Table 4.16. Where, for the resolutions 1 and 2, the harmonic form gave rise to an oscillatory instability while the arithmetic one remained stable, and at resolution 4, the former exhibited a protrusion. However, as is typically the case, the interface widths required to retrieve results up to the same level of accuracy are smaller at higher driving forces. Hence, though better than the harmonic one, the arithmetic form itself behaved badly (i.e., convergence is very lethargic) as is evident from the table. Strikingly, even though a huge difference is seen among the profile shapes, the recovered growth speeds deviated only slightly as revealed by Table 4.17.

Thus, a form of mobility interpolation function which can successfully handle all the setups is yet to be devised.

At this juncture, it may be of interest to consider a τ -formulation proposed by Steinbach [19] which does not involve any kind of averaging or interpolation. The governing equations in such a model read

$$\frac{\partial \phi_\alpha}{\partial t} = -\frac{1}{N} \sum_{\substack{\beta=1 \\ \beta \neq \alpha}}^N \frac{1}{\tau_{\alpha\beta}} \left(\frac{\delta F}{\delta \phi_\alpha} - \frac{\delta F}{\delta \phi_\beta} \right) \quad \forall \alpha \in \{1, 2, \dots, N\} \quad (4.11)$$

where the variational derivatives have the standard form as those of Eq. (3.14). It has to be cautioned, however, that the bulk energy interpolating forms have to be necessarily chosen as $\mathbf{g}_\alpha(\phi) = \phi_\alpha \forall \alpha \in \{1, 2, \dots, N\}$. It will now be shown that even with these equations, the binary interfaces being free of any other phases at leading order and the force balance requirement holding true at the junctions are both recovered in the limit of $\epsilon \rightarrow 0$.

First of all, it is easy to recognize that the summation rule property is facilitated by the above equations. Next, in the local coordinates pertaining to a binary interface, the

Table 4.14: Simulations performed with the parameter set used for Fig. 4.19 but with three different mobility formulations and a modification of the inverse mobility values as $\tau_{12} = \tau_{13} = 100$ and $\tau_{23} = 1$. That is, the growth front is made less mobile and the mobility of the interface between the two grains on the bottom is enhanced.

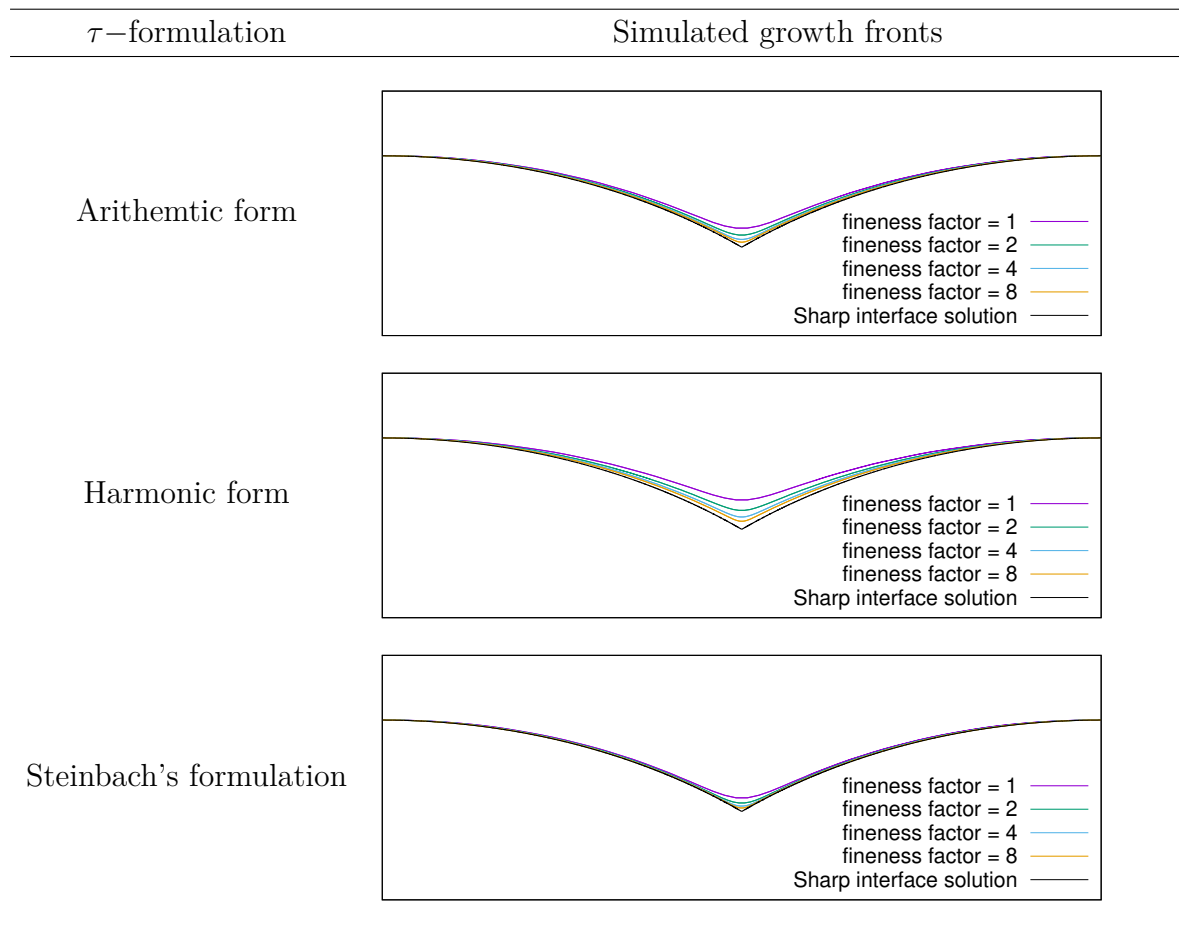


Table 4.15: Steady state angles and speeds recovered for the growth fronts of Table 4.14.

Fineness factor	Speed recovered with		
	Arithmetic form	Harmonic form	Steinbach's formulation
1	0.000710319	0.000744610	0.000921221
2	0.000714586	0.000735689	0.000934725
4	0.000716372	0.000729509	0.000941852
8	0.000716966	0.000725348	0.000945626
Sharp interface theory predicted speed			0.00071616518

Table 4.16: Simulations of Table 4.14 reperformed but with 10 times larger driving force, i.e., with $f_1 = 2.0$, $f_2 = 0.0$ and $f_3 = 0.0$.

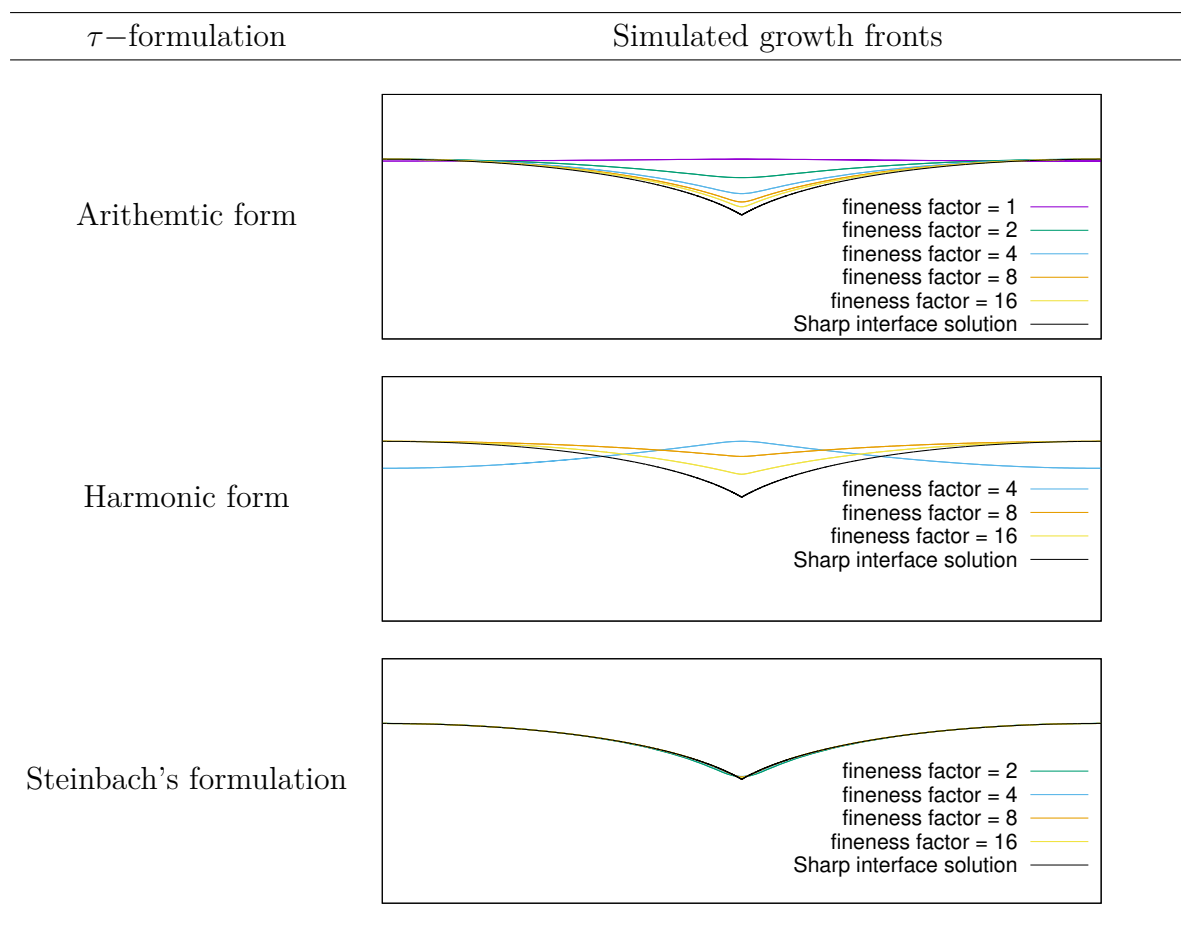


Table 4.17: Steady state angles and speeds recovered for the growth fronts of Table 4.16.

Fineness factor	Speed recovered with		
	Arithmetic form	Harmonic form	Steinbach's formulation
1	0.01175377	Unstable	Unstable
2	0.01055376	Unstable	0.01438601
4	0.01011871	0.01031806	0.01353602
8	0.00996935	0.01002834	0.01326541
16	0.00991464	0.00993977	0.01316515
Sharp interface theory predicted speed			0.00987556

requirement at the leading order is

$$\begin{bmatrix} 0 \\ 0 \\ \cdot \\ \cdot \\ \cdot \\ 0 \end{bmatrix} = \frac{1}{N} \begin{bmatrix} \frac{1}{\tau_{1*}} & -\frac{1}{\tau_{12}} & \cdots & -\frac{1}{\tau_{1N}} \\ -\frac{1}{\tau_{21}} & \frac{1}{\tau_{2*}} & \cdots & -\frac{1}{\tau_{2N}} \\ \cdot & \cdot & \cdots & \cdot \\ \cdot & \cdot & \cdots & \cdot \\ \cdot & \cdot & \cdots & \cdot \\ -\frac{1}{\tau_{N1}} & -\frac{1}{\tau_{N2}} & \cdots & \frac{1}{\tau_{N*}} \end{bmatrix} \begin{bmatrix} -\gamma \frac{\partial W(\phi)}{\partial \phi_1}(\tilde{\phi}^{(0)}) + \gamma \frac{\partial^2 \tilde{\phi}_1^{(0)}}{\partial \rho^2} \\ -\gamma \frac{\partial W(\phi)}{\partial \phi_2}(\tilde{\phi}^{(0)}) + \gamma \frac{\partial^2 \tilde{\phi}_2^{(0)}}{\partial \rho^2} \\ \cdot \\ \cdot \\ \cdot \\ -\gamma \frac{\partial W(\phi)}{\partial \phi_N}(\tilde{\phi}^{(0)}) + \gamma \frac{\partial^2 \tilde{\phi}_N^{(0)}}{\partial \rho^2} \end{bmatrix} \quad (4.12)$$

where $\tau_{\alpha\beta} = \tau_{\beta\alpha}$ as usual, and $\tau_{\alpha*}$ is given by

$$\frac{1}{\tau_{\alpha*}} = \sum_{\substack{\beta=1 \\ \beta \neq \alpha}}^N \frac{1}{\tau_{\alpha\beta}}.$$

It can be readily verified that a column matrix with all the entries being the same belongs to the null space of the above matrix $\left\{ \frac{1}{\tau_{\alpha\beta}} \right\}$. Further, if it is assumed that they are the only kind of vectors that are present in the null space, the requirement on the leading order phase-field variable is

$$\gamma \frac{\partial^2 \tilde{\phi}_\alpha^{(0)}}{\partial \rho^2} - \gamma \frac{\partial W(\phi)}{\partial \phi_\alpha}(\tilde{\phi}^{(0)}) = f(\tilde{\phi}^{(0)}) \quad \forall \alpha \in \{1, 2, \dots, N\}$$

for some function $f(\tilde{\phi}^{(0)})$. Summing up all the equations above, i.e., over all α , the function turns out to be $f(\tilde{\phi}^{(0)}) = -\frac{\gamma}{N} \sum_{\beta=1}^N \frac{\partial W(\phi)}{\partial \phi_\beta}$ owing to $\tilde{\phi}^{(0)}$ satisfying the summation rule. Thus, the requirements at the leading order are indeed the same as Eq. (3.21). Hence, the same analysis and the conclusions of section 3.3.3.1 apply as far as the leading order is considered even when Steinbach kind of τ -formulation is utilized. Similar analysis also recovers that the force balance conditions Eqs.(3.35) and (3.36) have to be fulfilled. In contrast, the analysis of the later orders does not continue to hold and has to be performed separately whose implications will be revisited in a while.

Strikingly, redoing the simulations but with the Steinbach form of τ -formulation leads to a better and faster recovery of the triple junction angles as evident from Table 4.14. Even in the case of higher driving forces, i.e., the parameter set corresponding to Table 4.16, it is seen that the Steinbach implementation is superior even when compared to the arithmetic form of inverse mobilities interpolation. This state of things may give the impression that Steinbach's formulation might in fact be the desired full-fledged solution

unlike the arithmetic or harmonic ones which are only better under certain circumstances. However, this is not the case as established by the following setup, Fig. 4.20. Where, the phase ϕ_2 has higher bulk energy compared to the other two phases and hence the latter have a driving force to eat up the former. However, the mobilities of the interfaces formed by the ϕ_1 phase are 100 times smaller than the one between ϕ_2 and ϕ_3 . As a result, the former barely move and the interfacial motion is predominantly as indicated by the arrow in the figure. A sequence of simulation images verifying this is presented in Fig. 4.21. With the initial filling as in Fig. 4.20 and with the parameter set of Table 4.18 considered as the base resolution, simulations are performed employing the arithmetic, harmonic and Steinbach forms of τ -implementation for various interface thicknesses. The prescription of $\epsilon = 5.0 \times \Delta x$ is utilized for reducing the interface widths. The recovered results are as indicated in Fig. 4.22 where the $\phi_2 = 0.5$ contours are plotted after appropriate normalization.

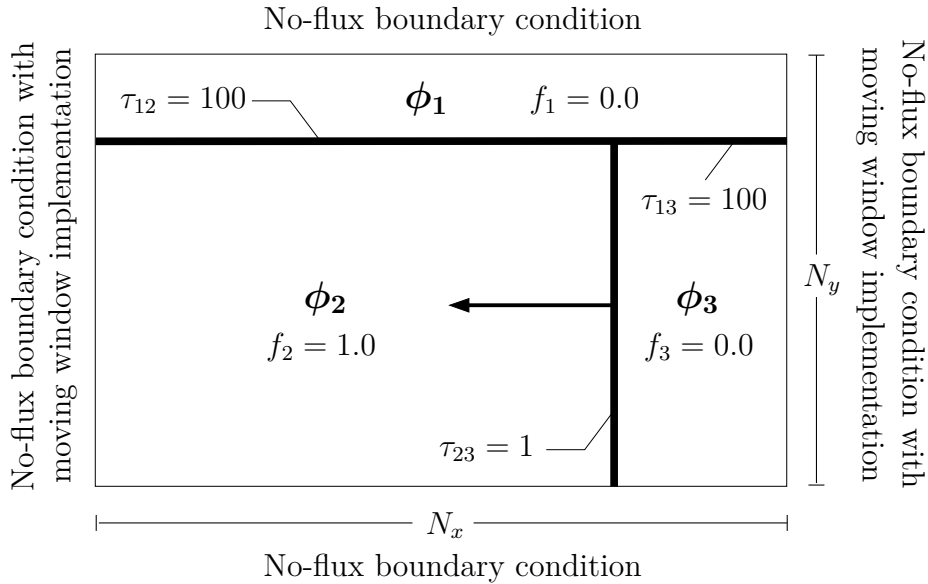


Figure 4.20: A simulation setup used for the study of three phase growth. The growth direction is as depicted by the arrow and accordingly is the implementation of the shifting window.

Table 4.18: Table showing a parameter set used for the study of three phase evolution within the setup of Fig. 4.20.

f_1	f_2	f_3	γ	$\tau_{12} = \tau_{13}$	τ_{12}	N_x	N_y	Δx	Δt	ϵ	$W(\phi)$
0.0	1.0	0.0	1.0	100.0	1.0	64	40	0.5	$0.2(\Delta x)^2$	$5.0\Delta x$	$W^T(\phi)$

As per the asymptotic analysis requirements, a $120^\circ - 120^\circ - 120^\circ$ angle breakdown is expected due to all the interfacial energies being the same. Whereas, in the arithmetic simulations, as before, a pinning effect is felt while the Steinbach case reproduced a

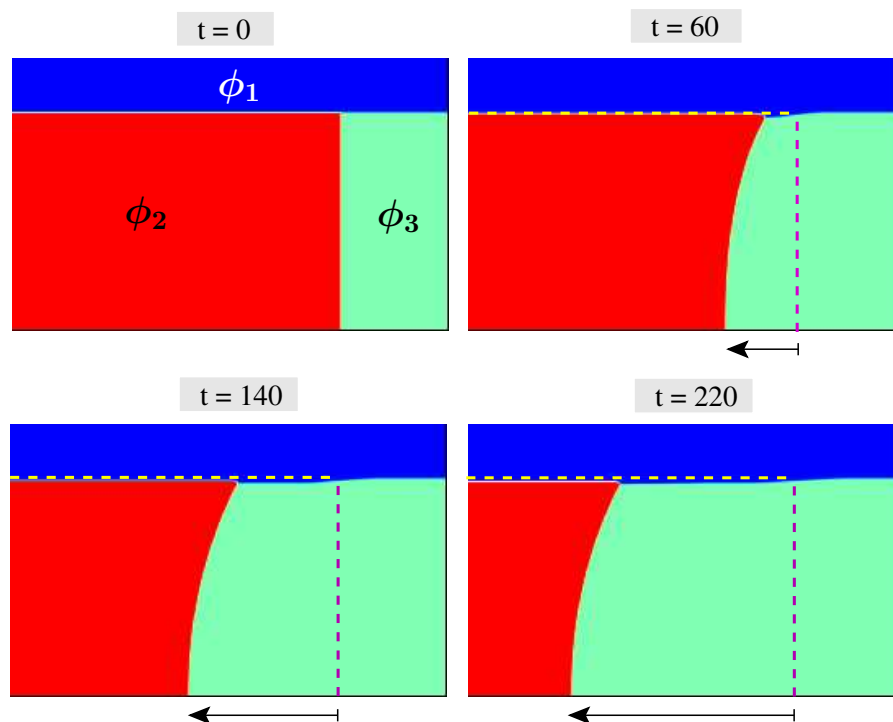


Figure 4.21: A sequence of simulation images illustrating the general growth tendency of the three phase system indicated in Fig. 4.20

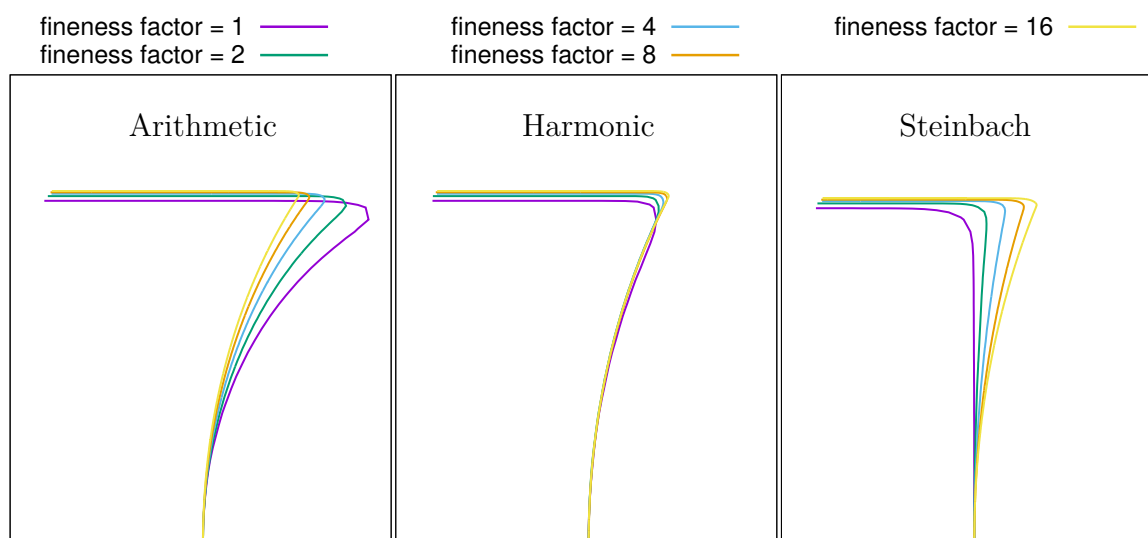


Figure 4.22: Simulated $\phi_2 = 0.5$ contours indicating the slow convergence of the arithmetic and Steinbach formulations compared to the harmonic τ -interpolation for the setup of Fig. 4.20 and the base resolution parameter set listed in Table 4.18.

highly mobile triple junction leading to an almost retention of the originally imposed right angle between the solid-solid and solid-liquid interfaces. Only the harmonic interpolation stayed close to the theoretically predicted behavior. On increasing the resolution, both the arithmetic and Steinbach profiles changed tending more and more closer to those of the harmonic form which remained almost the same as the low resolution one and close to the asymptotic requirement. At still higher resolutions, effects pertaining to the problematic $\epsilon \propto \Delta x$ selection began to be seen.

Thus, it is demonstrated that the Steinbach's method, after all, is not the all encompassing solution to the problem of finding a τ -formulation that is not too restrictive with regard to the interface width. Furthermore, while this is in relation to the recovery of the interfacial configuration at the junctions, the kinetics of interface evolution is also not recovered as per the desired Gibbs-Thomson condition, Eq. (3.30). This is a direct consequence of the fact that the leading order behaviors (in the matched asymptotic analyses) of Eqs. (3.14) and (4.11) are the same but the higher ones are different. Which is also evident from the reported simulated steady state speeds of Tables 4.15 and 4.17. Questions like what dynamical law, instead, is recovered and how to adjust it as per the requirement etc., and, even before that, why should the bulk energy interpolating forms be necessarily linear (i.e., $g_\alpha(\phi) = \phi_\alpha$) when borrowing Steinbach's form of equations are beyond the scope of this thesis and hence are not dealt into further. Irregardless, the takeaway is that the search for a universal τ -formulation is not over yet and remains to be continued.

Hence, to sum up the entire chapter, an asymmetric phase-field model (especially with regard to interfacial energies and interfacial mobilities) that is not too restrictive in terms of the transition layers' size specifier, ϵ , is yet to be formulated.

Before closing, we point out that the numerical verification of the laws prescribing the triple point's instantaneous velocity has only been implicit in nature in contrast to the other tests conducted in the current chapter. To elaborate, in the case of binary interfaces, the leading order and the next-to-leading order analyses of chapter 3 predicted the absence or presence of third phases up to zeroth order and the kinetic law of interfacial evolution Eq. (3.30), respectively. These are accordingly verified separately and sequentially in section 4.3.1. Even in the case of trijunctions, the predicted conformity to Young's law is examined explicitly. Whereas, the outcomes of the next order, namely, Eqs. (3.48) and (3.49) are not studied in isolation but only in combination with the dynamics of the interfacial points far removed from the junction. That is, instead of testing the triple point's motion independently, the evolution of the entire growth front is scrutinized in the comparisons of Figs. 4.14, 4.15 and 4.16 etc., and Tables. 4.9, 4.11 and 4.12 etc. Although of prime relevance is actually the latter, worrying about the former can give

some fresh insights. In fact, this time around, something about the asymptotic laws can be guessed from the converging simulation results. Note that the relation between the trijunction speed and the curvature of the symmetric growth front at the junction point used by the sharp interface theory is Eq. (C.3). This means, we have a target for what the integrals of Eqs. 3.48 and 3.49 have to evaluate to which will help guide their analytical derivation or estimation. This may also further help in conjecturing and proving some general statements about the integrals. In any case, they can always be computed numerically—though with much difficulty—and the agreement with Eq. C.3 can be realized explicitly. A deeper venture into these topics is not of immediate interest and hence is left out of the thesis. That said, we do justify why we are so confident about obtaining Eq. C.3 upon calculating the limits of Eqs. 3.48 and 3.49 for the current case: If a different condition were to result, it would imply that the attainment of steady state is impossible. Since the simulation results strongly point to the contrary, this possibility can be safely dismissed.

Finally, we report that while the asymptotic behavior predicted in chapter 3 for the timescale of actual relevance viz. $\tau = t$ is verified in the current chapter, the simulated behavior is also seen to be accordingly consistent for the earlier timescales $\tau = t/\epsilon^2$ and t/ϵ as well. In fact, the illustrations of chapter 3 like Figs. 3.1, 3.2, 3.3 etc, though claimed to be just schematics there, were actually obtained from simulations. The number of grid points allocated to the bulks were at least a few orders higher than those in the interfaces; hence was the apparent absence of the diffuseness of the latter.

We conclude by reminding that only the simple grain growth model is considered in the current chapter and the previous one. Supplementing it with the analysis of the chemical potential governing equation and thus extending it to the problem of multi-phase binary alloy solidification (Eqs. (2.43) and (2.44)) is carried out in appendix D. No matter how good the corresponding prescriptions may turn out to be, it still stands that the choices of penalizing functions available for the alloy solidification model are the same as for the simple grain growth one. Since a generic asymmetric multi-well remains unconstructed so far, this means that the former's applicability is limited as well. This concern will be taken up for the next chapter.

Chapter 5

Final considerations and eutectic growth simulations

5.1 Introduction

One of the main realizations in the previous chapter has been that a generic multi-phase-field model capable of permitting arbitrary specification of interfacial energies for the involving phase-pairs remains unformulated so far. On the other hand, in eutectic systems—investigating whose solidification through the phase-field methodology stands to be one of the prime objectives of the current thesis—the energies of all the solid-solid and the solid-liquid interfaces are seldom the same. Fortunately, one need not despair of having hit a dead end, as the first statement is only exclusive to models employing well potentials. The situation improves if what are called obstacle potential implementations are instead adopted. In which, primarily, multi-obstacle forms are exploited for penalizing the intermediate states instead of the multi-well forms. This is the only generic solution that is currently available to tackle the problem of arbitrary choice of interfacial energies. Of course, this is not to mean that the new implementations are devoid of any other additional costs, as the mathematical analyzability has to be traded off in order to employ them. But before that, it is worth emphasizing that if the problem of concern is limited to cooperative growth of binary eutectics in regular morphologies, well potential implementations handling it effectively and efficiently do exist.

First of all, it is to be realized that the essence of the entire previous chapter can be summed up in a simple statement. Which is, a numerically ideal phase-field model is the one which ensures a) elimination of third phases at zeroth and first orders in the asymptotic expansion of the phase-field variable, and b) confinement of the mobility values of the junction regions within appropriate ranges. The second of the above is not

always possible as it requires some level of foreknowing the impending evolution within the junction neighborhoods. However, for directional solidification of binary eutectics forming regular morphologies, it can be promptly carried out: Since infinite kinetics is assumed for the solid-liquid interfaces, their inverse mobilities are proportional to ϵ as given by Eq. (D.17). Thus, no matter what value is chosen for the mobility of the solid-solid interface, as the growth tendency is known, an appropriate (arithmetic or harmonic) form of interpolating function can be employed for the inverse mobility function $\tau(\phi)$. Similarly, to achieve the target a), the multi-well and the bulk energy interpolating functions have to be appropriately selected catering to the asymmetry in the properties. While such a selection cannot be made in the most generic of the cases at the present day, for three phase systems however, examples do exist like the asymmetric extension to the Folch-Plapp well proposed by themselves [22] or a pair-wise well (i.e., of the classical kind) put forth by Bollada *et al.* [54]. Thus, as far as the problem of interest of the current thesis i.e., directional solidification of binary alloys forming regular morphologies is concerned, multi-phase-field models involving well potentials indeed suffice. In spite of this, we turn our attention to an alternative approach which is *to use obstacle potentials in conjunction with Gibbs-simplex projection and active phases implementation*. The reason being that it has wider applicability as opposed to the former which falls short merely when moving on to a ternary system in the same (directional) setup. Also, the fact that obstacle potential implementations are equally popular and widespread, if not more, is another reason for investigating them, since, after all, one of the main objectives of the thesis is to test and enhance the soundness of the contemporary phase-field treatments of cooperative growth. The immediate next section exposes the details and nuances of the just mentioned alternative practice. Once familiarized, it is first applied to various test cases before moving on to the application to eutectic growth.

5.2 Multi-obstacle potential phase-field models

We only consider the case where summation constraint is demanded. The essential difference between the well and the obstacle forms is that the derivatives at phase indicator values marking the stable phases do not vanish for the latter. The simplest of the examples can be described as having only a single maximum at or around the center of the hyper-simplex, $(\frac{1}{N}, \frac{1}{N}, \dots, \frac{1}{N})$, with no other critical points anywhere else. For easy visualization of the explanations, we presently specialize to the case of three phases. The standard and simplest symmetric obstacle form $W_{\text{obs}}(\phi) = \phi_1\phi_2 + \phi_2\phi_3 + \phi_3\phi_1$ is depicted in Fig. 5.1. Due to its shape, no matter what the initial filling within the simplex is, the phase-field values tend to go out of it. This can be easily rationalized by ignoring, for the time being, the effect of the gradient energy terms in the obstacle potential version

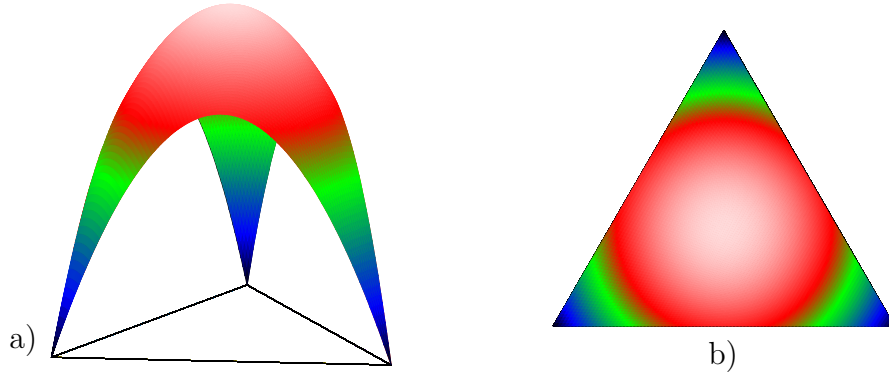


Figure 5.1: Plot of the restriction of the obstacle potential form $W_{obs} = \phi_1\phi_2 + \phi_2\phi_3 + \phi_3\phi_1$ to the Gibbs triangle; a) as a surface graph over the triangle and b) as a heat map.

of Eq. (3.14) and assuming that $f_\alpha = 0 \quad \forall \alpha$. Then, the evolution would be as per

$$\tau(\phi) \frac{\partial \phi_\beta}{\partial \tau} = -\frac{1}{\epsilon^2} \gamma \frac{\partial W_{obs}(\phi)}{\partial \phi_\beta} + \frac{1}{\epsilon^2} \gamma \frac{1}{3} \sum_{\alpha=1}^3 \frac{\partial W_{obs}(\phi)}{\partial \phi_\alpha} \quad \forall \beta \in \{1, 2, 3\}. \quad (5.1)$$

That is, in such a way that the potential reduces with time (see section 3.3.1). However, as the derivatives of the obstacle potential do not vanish at the edges or vertices of the simplex, the phase-field values are not constrained within it. Hence, to bring them back, a Gibbs-simplex projection algorithm is implemented in each time step at the core of which is the following observation: the only sub-region of the $\sum_{\alpha=1}^N \phi_\alpha = 1$ hyperplane where all the components are positive is the Gibbs-simplex. Hence, all projection algorithms essentially entail distributing, one after the other, in some order, the values of the phase-field components that are negative over rest of the non-zero valued components. Some examples of such projection algorithms can be found in Refs. [60–62]. It should be noted that this implementation also almost takes care of eliminating the third phases. For example, consider a filling like the one shown in Fig 4.3. The evolution equation for the third component under the current assumptions reads

$$\frac{\partial \phi_3}{\partial t} \approx -\frac{1}{\epsilon^2} \gamma (\phi_1 + \phi_2) - \frac{1}{3} \left[-\frac{1}{\epsilon^2} \gamma (\phi_2 + \phi_3) - \frac{1}{\epsilon^2} \gamma (\phi_1 + \phi_3) - \frac{1}{\epsilon^2} \gamma (\phi_1 + \phi_2) \right]. \quad (5.2)$$

For an infinitesimal time Δt soon after the simulation is started, the above equation implies

$$\begin{aligned} \frac{\Delta \phi_3}{\Delta t} &\approx -\frac{1}{\epsilon^2} \gamma (1) - \frac{1}{3} \left[-\frac{1}{\epsilon^2} \gamma (\phi_2 + 0) - \frac{1}{\epsilon^2} \gamma (\phi_1 + 0) - \frac{1}{\epsilon^2} \gamma (1) \right] \\ &= -\frac{1}{\epsilon^2} \gamma + \frac{2}{3} \left[\frac{1}{\epsilon^2} \gamma \right] \\ &= -\frac{1}{3} \frac{1}{\epsilon^2} \gamma. \end{aligned}$$

Hence, the ghost phase arises with a negative value and hence is instantly eliminated in the same time step by the Gibbs-simplex projection implementation. However, the above heuristics assumed that the gradient energy terms are negligible which may not be true and when included in Eq. (5.2) may give rise to a situation where the rising of the ghost phase takes place with it assuming positive values. To avoid this, more weightage is given to the potential term so that the contribution from the gradient energy terms is superseded. This is carried out by making the potential landscape more steeper, for example, by the addition of a higher order term like $G\phi_1\phi_2\phi_3$. Thus, even with an obstacle potential, confinement of the phase-field values to the Gibbs-simplex and avoidance of ghost or third phases is accomplished. To reinforce this further, the so called ‘active phases implementation’ is adopted. In which, at every grid point, all the phase-field components with at least one non-vanishing spatial (partial) derivative are first identified. The phases characterized by these components are referred to as being active at the point under consideration and the evolution equations of only these phases are solved. Note that such an implementation also brings in the additional advantage of reducing the computational costs.

From the description of the obstacle models, it is very clear that they are highly impermissible to mathematical analysis. This is because at some grid points, only some of the governing equations are solved and at some others, the whole set. Further, the subset that is solved may vary from one part of the domain to the other. On top of all this, the constant interference in the form of the execution of the Gibbs-simplex projection is neither expressible as some changes to be made to the existing set of ‘p.d.e.’s nor as some additional equations to be appended to them. Nor can it be realized as an imposition of certain interior or boundary conditions. In short, the operations performed cannot be realized as standard IBVP problems, and therefore, the theory of partial differential equations or those of numerical or asymptotic analyses of IBVPs cannot be of any help. Some other different kind of techniques, as well, are not available. Hence, the analytical treatment of such an implementation is close to impossible. However, it has to be mentioned that in the case of binary interfaces away from junctions, i.e., in regions with at most two active phases, analysis is in fact possible. In such a case, away from the interfaces and within the bulks, the governing equations are not solved. While within the interfacial region, the solved equations will only have the interference of the Gibbs-simplex projection as amounting to an implementation of a boundary condition. As together these correspond to a BVP, a mathematical analysis of the same rigour as carried out for the evolution equations involving well potentials is indeed possible. In connection with this, it has to be mentioned that all the previous treatments of such two phase obstacle potential models are either faulty or not fully detailed; a recent work by Paul Hoffrogge and the current author among others has this rectified [63]. Thus,

the efficacy of the model in recovering the evolution dynamics of the binary interfaces in the asymptotic limit is thoroughly established. For the validation with regard to capturing the junction behavior however, we turn to the simulation results generated from the model and compare them with the sharp interface predictions. Once this is done, the obstacle potential model will be applied to the problem of isothermal directional solidification of some real eutectic systems.

5.3 Three grain evolution

The evolution of three grains within the setup of Fig 4.1 served as a nice benchmark example to test the performance of the multi-well model considered in chapter 3. Hence, we use the same case study to examine the performance of the multi-obstacle model. Before that, the modeling equations to be solved are explicitly written down.

In principle, replacing $W(\phi)$ of Eq. (3.14) with the higher order term introduced obstacle form viz.

$$W_{\text{obs}} = a \left(\sum_{\substack{\alpha=1 \\ \alpha < \beta}}^{N,N} \sum_{\beta=1}^{N,N} a_{\alpha\beta} \phi_\alpha \phi_\beta \right) + \sum_{\substack{\alpha=1 \\ \alpha < \beta < \delta}}^{N,N,N} G \phi_\alpha \phi_\beta \phi_\delta \quad (5.3)$$

followed by turning on the Gibbs-simplex projection and active phases implementation will give rise to a multi-obstacle model. However, a further change in the gradient terms is also made giving rise to the following governing equations.

$$\tau(\phi) \frac{\partial \phi_\beta}{\partial t} = -\frac{\delta F}{\delta \phi_\beta} - \lambda, \quad \beta \in \{1, 2, \dots, N\} \quad (5.4)$$

with

$$\frac{\delta F}{\delta \phi_\beta} = \frac{1}{\epsilon} f_\alpha \frac{\partial q_\alpha(\phi)}{\partial \phi_\beta} + \frac{1}{\epsilon^2} \gamma \frac{\partial W_{\text{obs}}(\phi)}{\partial \phi_\beta} - \gamma \left(\frac{\partial}{\partial x_i} \frac{\partial q(\phi, \nabla \phi)}{\partial \left(\frac{\partial \phi_\beta}{\partial x_i} \right)} - \frac{\partial q(\phi, \nabla \phi)}{\partial \phi_\beta} \right)$$

and

$$\lambda = \frac{1}{N} \sum_{\beta=1}^N -\frac{\delta F}{\delta \phi_\beta}$$

where $\{x_i\}$ are the spatial coordinates and $q(\phi, \nabla \phi)$ stands for

$$q(\phi, \nabla \phi) = \sum_{\substack{\alpha=1 \\ \alpha < \beta}}^{N,N} a_{\alpha\beta} (\phi_\alpha \nabla \phi_\beta - \phi_\beta \nabla \phi_\alpha) \cdot (\phi_\alpha \nabla \phi_\beta - \phi_\beta \nabla \phi_\alpha).$$

The advantage of such pair-wise selected gradient terms is that when the a of Eq. (5.3) is appropriately selected viz. $16/\pi^2$, the interfacial energy of the $\phi_\alpha - \phi_\beta$ pair can be directly substituted for $\gamma a_{\alpha\beta}$. That is, $\gamma a_{\alpha\beta}$ appears as the coefficient of the curvature term in the Gibbs-Thomson relation for the $\alpha - \beta$ interface. An additional advantage is that the widths of the interfaces between all the phase pairs happen to be the same for a given ϵ irrespective of their energies.

The governing equations Eq. (5.4) are solved for the setup of Fig. 4.1 for various parameter sets. Particularly, the energies of the involving interfaces are varied by adjusting $a_{\alpha\beta}$ parameter and the resultant triple junction dynamics is compared with the sharp interface expectations. For having the possibility of a steady state behavior, the interfacial energies of 1 – 2 and 1 – 3 interfaces are chosen alike. The material and simulation parameter sets studied are listed in Tables 5.1, 5.3 and 5.5. Taking the grid finenesses mentioned in these tables as the base resolutions, behaviors at lower interface widths are investigated. For reducing the interface width, the prescription of $\epsilon = 4.0 \times (\Delta x)^{0.6}$ is employed. The numerical implementation is carried out in the massive-parallel multiphysics framework PACE3D. The results corresponding to the cases of Tables 5.1, 5.3 and 5.5 are reported in Figs. 5.2, 5.3 and 5.4, respectively and in Tables 5.2, 5.4 and 5.6, respectively.

The level of agreement between the sharp interface predictions and the simulated results is observed to be inferior to that seen in chapter 4. The simulations with the dataset of Table 5.1 correspond to the exact same sharp interface problem as those of Table 4.18. The latter being the ones with the right choices made for the ϵ v.s. Δx dependence and the mobility interpolating form. Furthermore, the interfacial thicknesses of both the studies are roughly the same at each resolution. However, the recovered results are not as accurate. Though the steady state speed and the triple junction angles deviated in a similar fashion as those observed in Table 4.18, the profile shapes did not agree well at lower resolutions. Further, the disagreement is even more pronounced in the asymmetric case where smaller trijunction angles are expected. To elaborate, when the interfacial energies, i.e., $\gamma a_{\alpha\beta}$ are as given in the Table 5.3, the force balance expects that the $\phi_1 - \phi_2$ and $\phi_1 - \phi_3$ interfaces make 14.47751° angle each with the horizontal at the junction point and the recovered value is off by almost 53% at a grid spacing of 128×128 . The steady state speed, however, is not as deviant at 6.67% of the sharp interface predicted value. A different state of affairs is seen for the data set of Table 5.5 where the expected angle is 56.44269° . Here, at the same resolution, i.e., corresponding to the grid spacing 128×128 , the recovered results are within 2% of the sharp interface predictions and the profiles also stayed close to each other. However, the trijunction angles seem to be converging to a value slightly different (about 1° off) from the theoretically expected one. The behaviors seem to be bettering with respect to the profile shapes

Table 5.1: A parameter set employed for simulating the three grain evolution in the setup of Fig. 4.1 using obstacle potential.

f_1	f_2	f_3	γ	τ_{12}	τ_{13}	τ_{23}	N_x	N_y	Δx	Δt	ϵ
0.1	0.0	0.0	1.0	1.0	1.0	1000.0	64	64	0.5	$0.1(\Delta x)^2$	$4.0(\Delta x)^{0.6}$
$\{g_\alpha(\phi)\}$			$W(\phi)$				$\tau(\phi)$				
$\{\phi_\alpha^3(10 - 15\phi_\alpha + 6\phi_\alpha^2)\}$			$W_{\text{obs}}(\phi)$ with $a = 16/\pi^2$, $a_{12} = a_{13} = 1.0$ and $a_{23} = 1.0$				$\tau_{\text{H}}(\phi) = \frac{\sum_{\alpha < \beta} \phi_\alpha \phi_\beta}{\sum_{\alpha < \beta} \frac{1}{\tau_{\alpha\beta}} \phi_\alpha \phi_\beta}$				

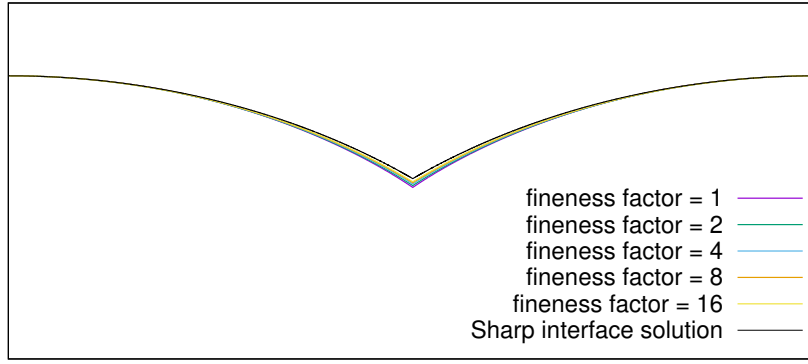


Figure 5.2: Steady-state growth fronts obtained in the three grain evolution simulations in the setup of Fig. 4.1 for the parameter set of Table. 5.1.

Table 5.2: Steady state speeds recovered for the growth fronts of Fig. 5.2.

Fineness factor	Recovered angle at the triple junction	Recovered steady state speed (rel. error)
1	34.06606°	0.067522228 (5.72%)
2	32.66199°	0.068958415 (3.71%)
4	31.78831°	0.069830746 (2.49%)
8	31.27829°	0.070386818 (1.72%)
16	30.93965°	0.070744657 (1.22%)
Sharp interface solution	30.0°	0.071616518

Table 5.3: A parameter set employed for simulating the three grain evolution within the setup of Fig. 4.1 using obstacle potential..

f_1	f_2	f_3	γ	τ_{12}	τ_{13}	τ_{23}	N_x	N_y	Δx	Δt	ϵ
0.1	0.0	0.0	1.0	1.0	1.0	1000.0	64	64	0.5	$0.1(\Delta x)^2$	$4.0(\Delta x)^{0.6}$
$\{g_\alpha(\phi)\}$				$W(\phi)$				$\tau(\phi)$			
$\{\phi_\alpha^3(10 - 15\phi_\alpha + 6\phi_\alpha^2)\}$				$W_{\text{obs}}(\phi)$ with $a = 16/\pi^2$, $a_{12} = a_{13} = 1.0$ and $a_{23} = 0.5$				$\tau_{\text{H}}(\phi) = \frac{\sum_{\alpha < \beta} \phi_\alpha \phi_\beta}{\sum_{\alpha < \beta} \frac{1}{\tau_{\alpha\beta}} \phi_\alpha \phi_\beta}$			

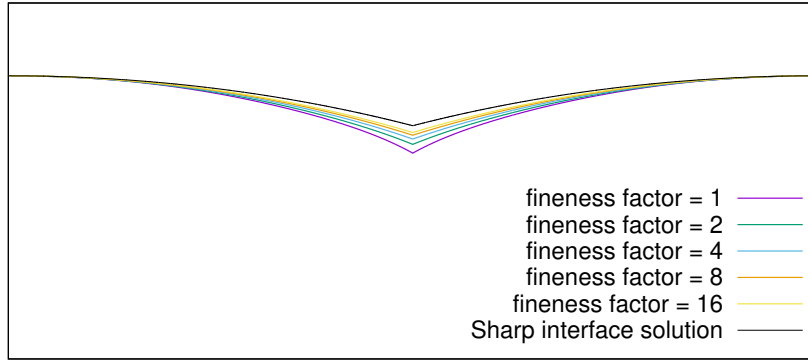


Figure 5.3: Steady-state growth fronts obtained in the three grain evolution simulations within the setup of Fig. 4.1 for the parameter set of Table. 5.3.

Table 5.4: Steady state speeds recovered for the growth fronts of Fig. 5.3.

Fineness factor	Recovered angle at the triple junction	Recovered steady state speed (rel. error)
1	29.01687°	0.077213551 (9.41%)
2	22.15349°	0.079540432 (6.68%)
4	19.25656°	0.081200973 (4.73%)
8	17.64173°	0.082391265 (3.33%)
16	16.62569°	0.083239259 (2.34%)
Sharp interface solution	14.47751°	0.085231233

Table 5.5: A parameter set employed for simulating the three grain evolution within the setup of Fig. 4.1 using obstacle potential..

f_1	f_2	f_3	γ	τ_{12}	τ_{13}	τ_{23}	N_x	N_y	Δx	Δt	ϵ
0.1	0.0	0.0	1.0	1.0	1.0	1000.0	64	64	0.5	$0.1(\Delta x)^2$	$4.0(\Delta x)^{0.6}$
$\{g_\alpha(\phi)\}$			$W(\phi)$				$\tau(\phi)$				
$\{\phi_\alpha^3(10 - 15\phi_\alpha + 6\phi_\alpha^2)\}$			$W_{\text{obs}}(\phi)$ with $a = 16/\pi^2$, $a_{12} = a_{13} = 0.6$ and $a_{23} = 1.0$				$\tau_{\text{H}}(\phi) = \frac{\sum_{\alpha < \beta} \phi_\alpha \phi_\beta}{\sum_{\alpha < \beta} \frac{1}{\tau_{\alpha\beta}} \phi_\alpha \phi_\beta}$				

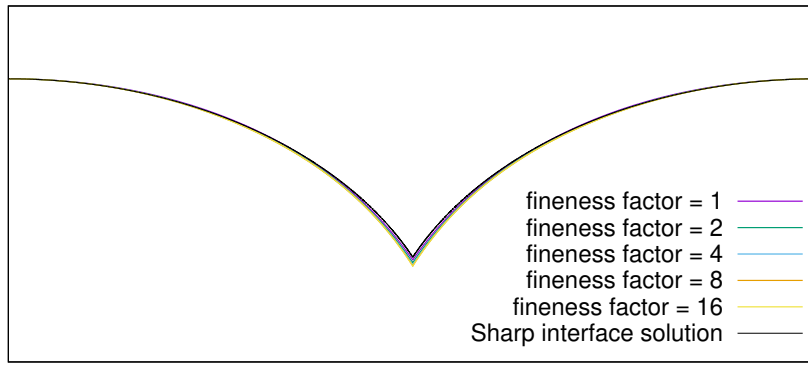


Figure 5.4: Steady-state growth fronts obtained in the three grain evolution simulations within the setup of Fig. 4.1 for the parameter set of Table. 5.5.

Table 5.6: Steady state speeds recovered for the growth fronts of Fig. 5.4.

Fineness factor	Recovered angle at the triple junction	Recovered steady state speed (rel. error)
1	55.05770°	0.074118701 (3.14%)
2	55.79540°	0.074986111 (2.01%)
4	56.71898°	0.075406968 (1.46%)
8	57.22332°	0.075621037 (1.18%)
16	57.42547°	0.075753067 (1.01%)
Sharp interface solution	56.44269°	0.076521789

when the driving forces are lowered as demonstrated in appendix E.1; the same, however, cannot be said about the recovered steady state speeds.

From the above comparisons and those in appendix E.1, it is clear that the triple junction dynamics is sufficiently captured by the employed obstacle potential model in an overall sense at least at low driving forces. It will now be tested whether the accuracy remains the same even after coupling with an additional field like composition. That is, the performance of the model in the case of eutectic growth will be studied.

5.4 Isothermal, directional eutectic growth

The multi-phase-field equations modeling binary alloys' phase evolution and involving obstacle potential are Eq. (5.4) with f_α replaced by $\omega_\alpha(\mu)$, and Eq. (2.44). We employ these equations to study the lamellar and rod growth morphologies and kinetics of NiZr-NiZr₂ eutectic alloys. The eutectic point temperature T_E of the NiZr-NiZr₂-melt system is 1305.9K; solidification at an undercooling $\Delta T = 5.9\text{K}$ is studied in the simulations. The relevant thermophysical data of this eutectic system is gathered from the literature. For temperatures in the range around the considered undercooling, the diffusivities of the Ni and Zr atoms in the melt are reported to be similar in magnitudes in Ref. [64], these values are utilized for the simulations. The grand-potential v.s. chemical potential dependencies of the NiZr, NiZr₂ and liquid phases are obtained from the CALPHAD database composed by K. Hashimoto and T. Abe [65], and published by the National Institute for Materials (NIMS), Japan. To reduce the computational effort, the Gibbs free energy v.s. composition curves of the CALPHAD database are approximated by parabolae of the form $A_\nu c^2 + B_\nu c + C_\nu$ with A_ν , B_ν and C_ν being the coefficients corresponding to phase $\nu \in \{\text{NiZr}, \text{NiZr}_2, \text{liquid}\}$, and c standing for the mole fraction of the Zr component. Due to the stoichiometric nature of NiZr and NiZr₂ solids, the Gibbs free energy data of each of these phases is restricted to a single point at any given temperature in the CALPHAD database. Using these, sharp parabolae are constructed to ensure that the compositions of the forming solids stay close to their stoichiometric values. Next, the surface energies of the NiZr-liquid and NiZr₂-liquid interfaces are calculated from the prescription provided in Ref. [66]. The NiZr-NiZr₂ interfacial energy is not available in the literature, hence a value in the typical range is selected at $\gamma_{\text{NiZr NiZr}_2} = 0.5$.

What remains is the selection of the inverse mobilities $\tau_{\text{NiZr,liquid}}$, $\tau_{\text{NiZr}_2,\text{liquid}}$ and $\tau_{\text{NiZr,NiZr}_2}$, and the solid-solid diffusivity. Since the growth front is considered to display infinite kinetics by the sharp interface theory of eutectic growth, i.e., the Jackson-Hunt analysis, we choose the inverse mobility values as per the suggestion of the thin-interface analysis. As discussed in the introduction of chapter 3, no prescription is derivable for the

solid-solid inverse mobility; hence, we select a large value (say more than 3000 times the highest of those of solid-liquid interfaces) and employ a harmonic form for τ interpolation. Also, in keeping with the JH analysis, the diffusivities in the solids are chosen to be

Table 5.7: Thermo-physical parameters of the NiZr-NiZr₂ system corresponding to near eutectic temperatures. Symbols α , β and l are used to mark the NiZr, NiZr₂ and melt phases, respectively. f is the fineness factor.

Parameter	Value	Units	Source
$\gamma a_{\alpha l} =: \sigma_{\alpha l}$	0.41045	J m ⁻²	[66]
$\gamma a_{\beta l} =: \sigma_{\beta l}$	0.32161	J m ⁻²	[66]
$\gamma a_{\alpha\beta} =: \sigma_{\alpha\beta}$	0.50	J m ⁻²	Chosen
$D_l^{\text{Ni}} = D_l^{\text{Zr}} =: D$	5.5×10^{-10}	m ² s ⁻¹	[64]
$D_\alpha^{\text{Ni}} = D_\alpha^{\text{Zr}}$	0	m ² s ⁻¹	Chosen
$D_\beta^{\text{Ni}} = D_\beta^{\text{Zr}}$	0	m ² s ⁻¹	Chosen
T_E	1305.9	K	CALPHAD database composed by K.Hashimoto and T.Abe from [67], [68] & [69]
A_l	$1.588011084 \times 10^{10}$	J m ⁻³	fitting of CALPHAD data
B_l	$-1.447070021 \times 10^{10}$	"	"
C_l	$-0.8072730376 \times 10^{10}$	"	"
A_α	$45.54332460 \times 10^{10}$	"	"
B_α	$-45.08872107 \times 10^{10}$	"	"
C_α	10.00350×10^{10}	"	"
A_β	$48.09219457 \times 10^{10}$	"	"
B_β	$-63.67410307 \times 10^{10}$	"	"
C_β	20.00350×10^{10}	"	"
γG	7.5	J m ⁻²	Chosen
$\Delta x = \Delta y$	$30.0 \times 10^{-10} / f$	m	—
ϵ	$5.0 \times \Delta x$	m	—
$\tau_{\alpha l}$	$1.697220 \times 10^{17} \times \epsilon$	J s m ⁻⁴	Thin interface analytics [23]
$\tau_{\beta l}$	$0.441306 \times 10^{17} \times \epsilon$	J s m ⁻⁴	Thin interface analytics [23]
$\tau_{\alpha\beta}$	$3.0 \times \tau_{\alpha l} \times 1000 \times f$	J s m ⁻⁴	Chosen
Δt	$(90.0 - 180.0) \times 10^{-11}$	s	—

vanishing identically, and hence, the anti-trapping current terms are appropriately implemented. Note that the forms of the thin-interface limit correction and the anti-trapping current term derived in appendix D are only specific to the well models, the obstacle potential counterparts are presented in Ref. [23] which are adopted for our simulations.

The above mentioned data is collected in Table 5.7 for quick reference where, and as well as in the rest of the current chapter and the next two, α , β and l are used to mark NiZr, NiZr₂ and melt phases, respectively.

Before proceeding on to the cooperative growth studies, that the solid-melt system of interest (i.e., with solid diffusivity = 0 and surface mobility = ∞) is adequately modeled by the implemented thin-interface limit correction and the anti-trapping current terms is first cross-checked. For this, planar solidification of NiZr alloy is simulated at various interface widths and the recovered steady state speeds are compared with the sharp interface solution. The details are presented in appendix E.2 along with the findings which indicate that the performance is satisfactory enough. Thus, backed up by the success in the two bench-mark cases considered in section 5.3 and appendix E.2, the model is next applied to study the cooperative growth of NiZr-NiZr₂ alloys. Solidification from melts at eutectic composition is exclusively looked at.

5.4.1 Lamellar growth

5.4.1.1 Simulation setup

The setup considered for lamellar growth simulations is depicted in Fig. 5.5. An initial seed of each of the solid phases is filled and is shifted backwards in the moving window technique after it grows to such a height that a melt height of three times the width of the domain is present in front of the solids. The melt is filled at a composition corresponding to the invariant point. Periodic boundary conditions are applied in the lateral directions and Neumann and Dirichlet conditions are applied in the growth direction as depicted in the figure. Hence, only one repetitive unit of the lamellar structure is explicitly simulated. We call its width the lamellar spacing and denote it by λ . The recovered growth morphologies and kinetics as λ is varied are presented in the following.

5.4.1.2 Simulation results

Simulations for the lamellar spacings ranging from $0.15\mu m$ to $0.33\mu m$ are performed at three different interface widths. The prescription of $\epsilon \propto \Delta x$ is employed to exploit the faster downscaling of the interface thickness. Note that due to the additional field that has to be solved for, and at each grid point at that, the eutectic growth simulations are far more costlier than the plain grain growth studies of section 5.3. Hence, investigation of only three resolutions was feasible corresponding to a reduction of interface width by four times. Had the $\epsilon \propto \sqrt{\Delta x}$ prescription been employed, the computational costs needed for achieving the same amount of downsizing would have been tremendously high. At

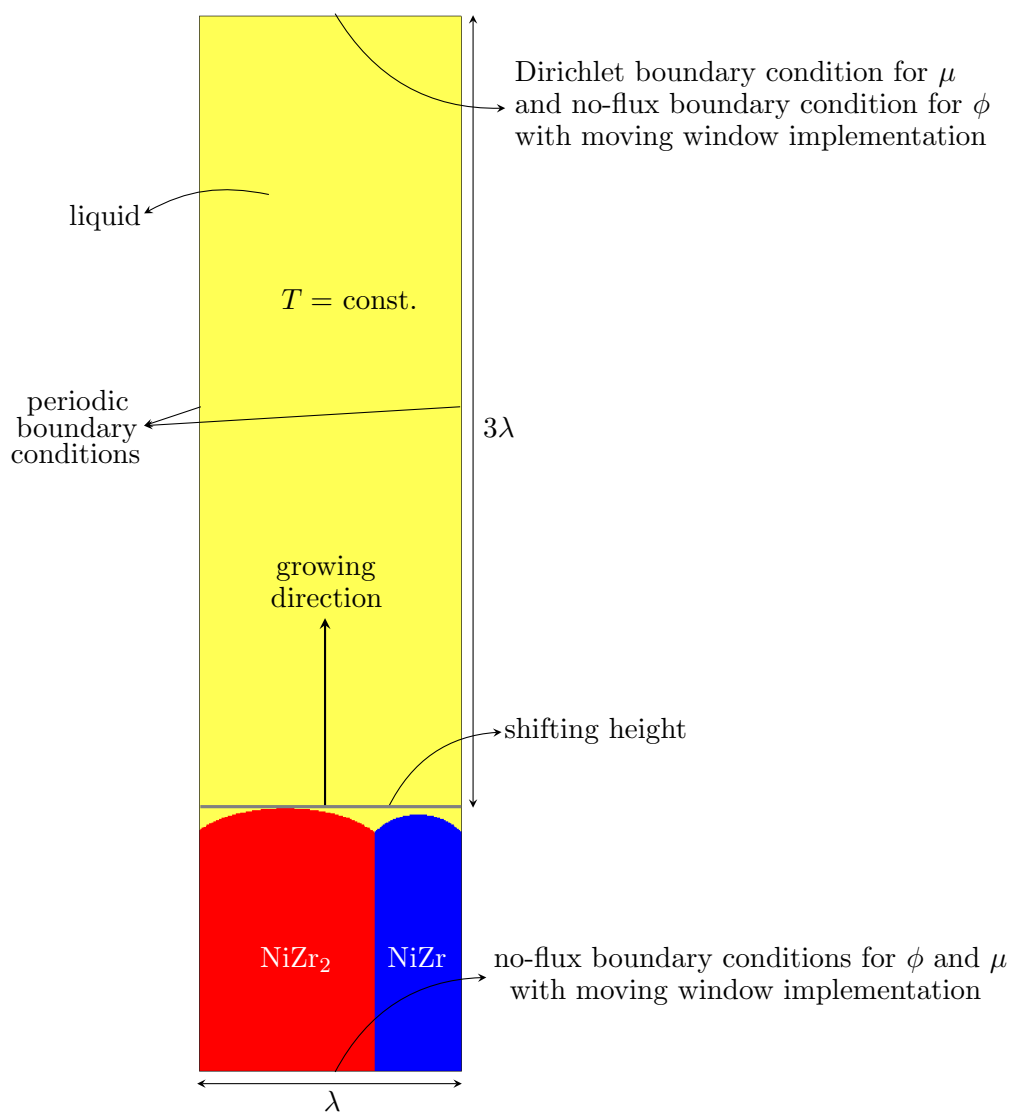


Figure 5.5: The setup used for the simulation of cooperative lamellar growth of NiZr and NiZr_2 solids.

the lowest or base resolution, the smallest lamellar spacing studied corresponds to a size of 50 grid cells.

The maximum deviation of the simulated solid phase compositions from the stoichiometric values is within 0.1% of the latter and the phase fractions are correct up to 1% of the tie-line requirement. The latter indicates that the chosen melt height of three times the lamellar spacing ahead of the solidification front is not too restrictive for the applied Dirichlet condition (viz. the melt composition corresponding to the invariant point).

The angles at the triple junction recovered in the simulations are listed in Table 5.8 for all the three resolutions along with the Young's law requirement. The observed pattern, broadly speaking, can be described as a fluctuating but over all slow convergence towards the theoretically expected values. The angle subtended by the NiZr₂-liquid surface is

Table 5.8: Triple junction angles subtended by the NiZr-liquid and NiZr₂-liquid interfaces that are recovered in the simulations as interface width is reduced whilst choosing $\epsilon \propto \Delta x$. The angles are measured with respect to the horizontal (i.e., axis perpendicular to the growth direction). Symbols α , β and l mark the NiZr, NiZr₂ and melt phases, respectively.

Lamellar spacing (in μm)	Resolution =1		Resolution =2		Resolution =4	
	$\theta_{\beta l}$	$\theta_{\alpha l}$	$\theta_{\beta l}$	$\theta_{\alpha l}$	$\theta_{\beta l}$	$\theta_{\alpha l}$
0.150	42.22°	41.23°	40.27°	42.01°	39.94°	45.78°
0.165	41.54°	38.78°	40.34°	42.44°	38.22°	47.56°
0.180	40.59°	38.17°	39.21°	43.73°	38.41°	47.72°
0.195	40.25°	39.52°	40.08°	44.29°	38.92°	47.17°
0.210	39.93°	39.57°	39.04°	44.85°	38.72°	46.55°
0.225	39.70°	40.48°	39.54°	44.63°	38.32°	48.08°
0.240	40.17°	43.25°	39.21°	45.30°	38.40°	47.27°
0.255	40.05°	42.30°	38.45°	45.82°	38.47°	47.08°
0.270	39.69°	39.39°	38.94°	45.23°	37.21°	48.79°
0.285	39.10°	42.26°	38.19°	45.67°	38.16°	47.40°
0.300	39.05°	41.46°	38.31°	46.17°	36.11°	48.05°
0.315	38.38°	43.00°	38.13°	45.71°	37.03°	47.76°
0.330	38.60°	44.35°	37.48°	45.75°	37.35°	47.40°
Young's law values	$\theta_{\beta l} = 35.1079^\circ$		$\theta_{\alpha l} = 50.1334^\circ$			

seen to converge rather slowly almost seeming that it might even tend to a value higher

than the expected magnitude of 35.1079° . The behavior of the NiZr-melt interface is comparatively better, but the values are still off by 2–3 degrees at the highest resolution considered. Better agreement at larger spacings than at smaller ones is a definite trend observed at all resolutions. Next, the computed growth kinetics is examined.

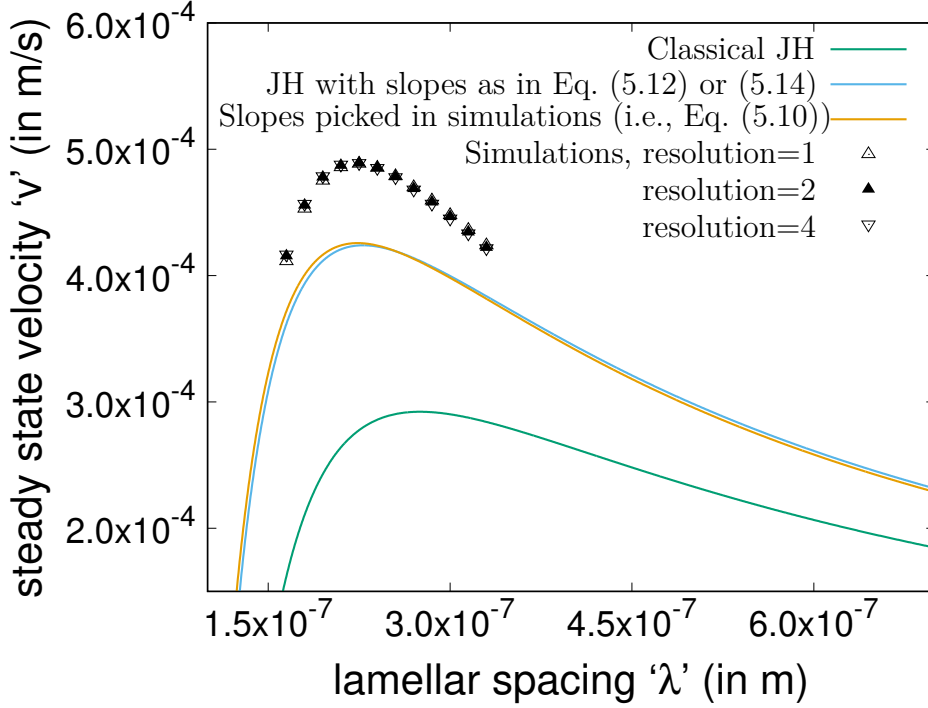


Figure 5.6: NiZr-NiZr₂ lamellar growth kinetics predicted by the JH relation for various choices of the slopes prescription, and their comparison with the simulation results at various interface widths.

The steady state speed versus lamellar spacing curves generated from the simulations are reported in Fig. 5.6 and in Table E.12 of appendix E.3. Unlike the trijunction angles, the change in the values as the resolution is increased is minute.

The analytical kinetics relation derived by Jackson and Hunt is as follows

$$v = \frac{\Delta T - \frac{1}{(m^\beta - m^\alpha)} (m^\beta \Gamma_\alpha \langle \kappa \rangle_\alpha - m^\alpha \Gamma_\beta \langle \kappa \rangle_\beta)}{\frac{\lambda}{D} \left(\frac{-m^\alpha m^\beta}{m^\beta - m^\alpha} \right) \left[(c_{\beta E} - c_{\alpha E}) \left(\frac{\mathcal{P}(\eta_\alpha)}{\eta_\alpha} + \frac{\mathcal{P}(\eta_\beta)}{\eta_\beta} \right) \right]} \quad (5.5)$$

where D is the common diffusivity of the two atomic species constituting the binary system; η_β is the phase fraction of the β phase and η_α that of α in the tie-line construction pertaining to the three equilibrium concentrations at eutectic temperature; m^α and m^β are the slopes of the α -liquidus and β -liquidus lines at the invariant point, respectively; $c_{\alpha E}$ and $c_{\beta E}$ are the equilibrium concentrations of the α and β phases at eutectic

temperature, respectively; the function $\mathcal{P}(\eta)$ is given by

$$\mathcal{P}(\eta) = \sum_{n=1}^{\infty} \frac{1}{(n\pi)^3} \sin^2(\pi n\eta);$$

and the terms $\Gamma_{\alpha}\langle\kappa\rangle_{\alpha}$ and $\Gamma_{\beta}\langle\kappa\rangle_{\beta}$ can be further expanded as

$$\Gamma_{\alpha}\langle\kappa\rangle_{\alpha} = \frac{2T_E \sigma_{\alpha l} \sin \theta_{\alpha l}}{\eta_{\alpha} L_{\alpha} \lambda} \quad \text{and} \quad \Gamma_{\beta}\langle\kappa\rangle_{\beta} = \frac{2T_E \sigma_{\beta l} \sin \theta_{\beta l}}{\eta_{\beta} L_{\beta} \lambda} \quad (5.6)$$

where, T_E is the eutectic point temperature; L_{α} and L_{β} are the latent heats of fusion of the α and β phases, respectively; $\theta_{\alpha l}$ and $\theta_{\beta l}$ are the acute angles w.r.t. horizontal at the triple junction made by the α -liquid and β -liquid interfaces, respectively; and finally, $\sigma_{\alpha l}$ and $\sigma_{\beta l}$ are the interfacial energies of the α -liquid and β -liquid interfaces, respectively. The predicted behavior as per this equation is also plotted in Fig. 5.6 under the name ‘Classical JH’. A huge disagreement can be seen between the analytical and the numerical results. The lamellar width at which the maximum in the velocity occurs is referred to as the characteristic spacing and is denoted by λ_{JH} . It has a special significance within the JH theory as the selection of morphology and operating state in a freely growing system are based upon it. The simulated λ_{JH} is off in the simulations by about -18.18% and the associated speed by 67.38% .

We now move on to see the respective behaviors in the rod growth case.

5.4.2 Rod growth

5.4.2.1 Simulation setup

As mentioned before, the simulation studies of the isothermal co-operative growth of NiZr and NiZr₂ solids in the current thesis are confined to solidification from melts at eutectic point composition. As the invariant point is almost twice as close to one of the phases (NiZr₂) as to the other (NiZr), a rod growth morphology, as opposed to a lamellar one, is more likely to occur [29, 70] in thicker samples. Further, as all the phases are treated to be isotropic, the arrangement of rods is expected to assume a hexagonal pattern [48, 70, 71]. Hence, to simulate such a growth under the ambient conditions: A 3D domain with rectangular cross-section of sides ratio $1 : \sqrt{3}$ and containing an initial seed of one whole rod in the center and a quarter of a rod in each corner as depicted in Fig. 5.7 is setup as the starting configuration. Periodic boundary conditions are applied on the sides to model an infinite domain of hexagonally arranged rods. At the bottom of the domain, a Neumann boundary condition is used and at the top, on the liquid side, a Dirichlet boundary condition is employed. Temperature variations are not implemented in the setup, hence, isothermal conditions prevail in the whole simulation domain. As

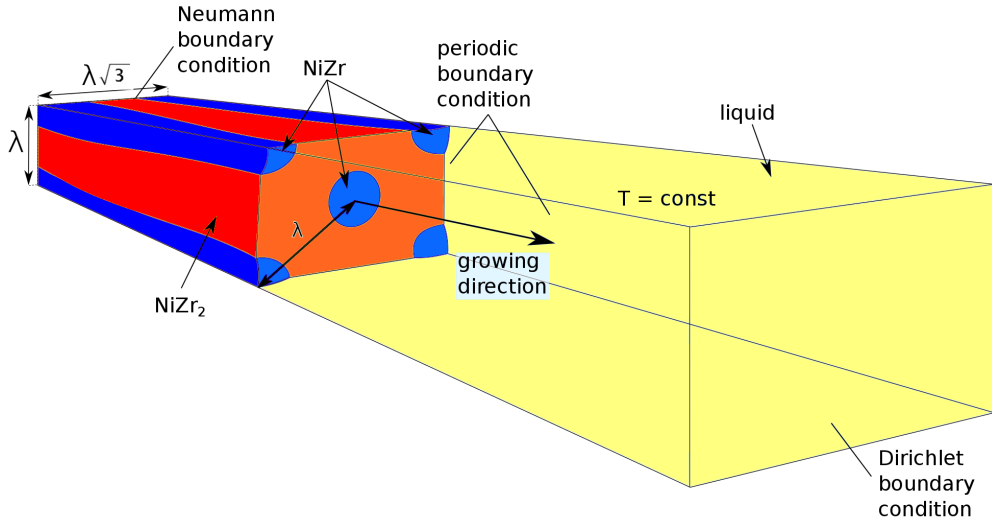


Figure 5.7: Setup applied for the simulation of hexagonally arranged rods.

in the lamellar growth studies, a temperature corresponding to an undercooling of 5.9 K is chosen. To model an infinitely large domain of melt above the solidification front, a liquid height of three times the rod spacing is used and a moving window technique [72] is employed. By varying the lateral dimensions of the domain while preserving the aspect ratio, various inter-rod spacings can be examined and their influence on growth kinetics can be studied. In this study, five different rod spacings between 60 to 90 voxel cells corresponding to physical lengths between 0.18 and 0.27 μm are investigated. This corresponds to domain sizes from 60×105 to 90×157 voxel cells for the rectangular simulations. While these comprise the base resolution studies, $\epsilon \propto \Delta x$ prescription is employed for reducing the interface thickness. As the 3D simulations are expensive compared to 2D lamellar ones, this time, investigation of only two grid finesses was possible. Each simulation is performed on up to 721 cores for at least 5 million time steps on the Hazel Hen supercomputer at the High-Performance Computing Center, Stuttgart (HLRS) to ensure the attainment of steady state.

5.4.2.2 Simulation results

The stoichiometric nature of the NiZr and NiZr₂ solid phases is aptly captured in the simulations as the maximum deviation of the composition from the expected values is found to be within 0.1%. Further, the volume fractions, as well, are consistent with the tie-line construction with the maximum error being within 0.5% of the expected values, twice as good as that recovered for the lamellar simulations. Thus, an undesirable influence of the domain sizes on the simulated results that could have potentially arisen

is successfully avoided.

The angles made by the NiZr-melt and NiZr₂-melt surfaces with the plane perpendicular to the growth direction are presented in Table 5.9. The convergence is better and much faster compared to that observed for the lamellar growth simulations.

Table 5.9: Triple “junction” angles subtended by the NiZr-liquid and NiZr₂-liquid surfaces recovered in the rod growth simulations as interface width is reduced whilst choosing $\epsilon \propto \Delta x$. The angles are measured with respect to the plane perpendicular to the growth direction. Symbols α , β and l mark the NiZr, NiZr₂ and melt phases, respectively.

Lamellar spacing (in μm)	Resolution =1		Resolution =2	
	$\theta_{\beta l}$	$\theta_{\alpha l}$	$\theta_{\beta l}$	$\theta_{\alpha l}$
0.180	35.07°	41.59°	36.27°	47.61°
0.195	36.74°	44.73°	36.78°	47.75°
0.210	38.89°	44.54°	37.11°	47.64°
0.225	34.05°	44.89°	36.73°	47.43°
0.240	37.31°	44.34°	36.94°	47.02°
0.255	37.15°	44.99°	36.99°	46.87°
0.270	37.07°	44.60°	37.43°	46.47°
Young’s law values	$\theta_{\beta l} = 35.1079^\circ$		$\theta_{\alpha l} = 50.1334^\circ$	

The steady state growth speeds are as depicted in Fig. 5.8 where comparison is also made with the predictions of the JH theory. For the case of rod growth, the $v - \lambda - \Delta T$ relation derived by Jackson and Hunt is the same as Eq. (5.5) except that the square bracket term in the denominator is replaced by

$$(c_{\beta E} - c_{\alpha E}) \sum_{n=1}^{\infty} \frac{J_1^2(\sqrt{\eta_\alpha} \gamma_n)}{\gamma_n^3 J_0^2(\gamma_n)} 4 \sqrt{\frac{\sqrt{3}}{2\pi}} \left(1 + \frac{\eta_\alpha}{\eta_\beta}\right) \quad (5.7)$$

where J_0 and J_1 are Bessel functions of orders 0 and 1, respectively and γ_n is the n^{th} zero of $J_1(x)$. Compared to the classical calculations, the simulated λ_{JH} is off by -27.928% and the maximum velocity is different by a staggering 91.677% .

An inquiry into the possible reasons behind the huge deviation observed between the analytical and the computational results of Figs. 5.6 and 5.8 should most obviously constitute the next topic of the study. The following section is dedicated for the same.

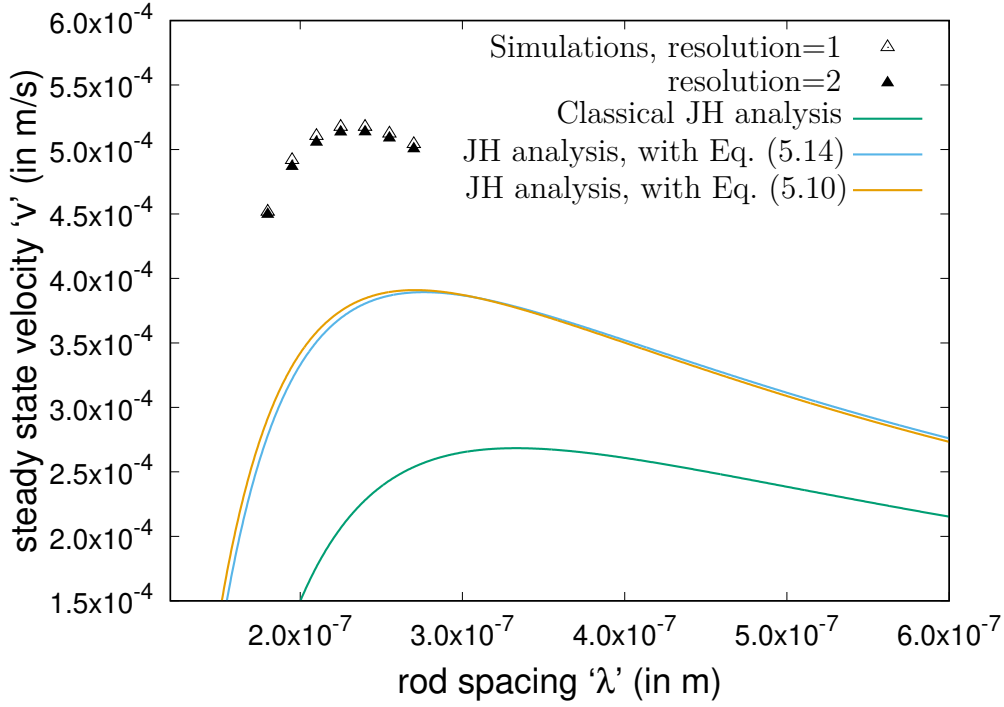


Figure 5.8: Comparison of NiZr-NiZr₂ rod growth kinetics predicted by the JH relation for various choices of the slopes formula with those of the simulations pertaining to various interface widths.

5.4.3 Discussion of results

5.4.3.1 Accounting the huge deviation observed between the simulations and the classical JH

First of all, let us begin by asking the following question: are the governing equations solved by Jackson and Hunt, and the asymptotic limit of the implemented phase-field model identical? This might be surprising coming at this point as it is already explicitly mentioned in chapter 1 that they indeed are. Whereas, a preliminary look at Eq. (5.5) gives the impression that this might not be the actual case. The reason being that a lot of terms associated with the invariant point enter the theoretical relation whereas the simulations correspond exclusively to an undercooled temperature. No information pertaining to the eutectic point, except for the initial filling which is but a choice, is utilized for carrying out the simulations. Also, the interfacial kinetics law captured by the employed phase-field model is (see Ref. [23])

$$\mu - \mu_{\text{eq}} = \frac{\sigma_{sl}\kappa}{(c_s(\mu_{\text{eq}}) - c_l(\mu_{\text{eq}}))}, \quad (5.8)$$

whereas Eq. (5.5) is deduced from an entirely different looking relation which is (see chapter 6)

$$\Delta T = -m^s(c_l(x) - c_E) + \Gamma_s \kappa. \quad (5.9)$$

Where, Γ_s is the Gibbs-Thomson coefficient of the solid-liquid interface at the eutectic temperature and c_E is the eutectic point concentration, indicating, once again, that Eq. (5.5) has very many terms pertaining to the invariant point. On the other hand, the various terms in Eq. (5.8) correspond to that temperature at which the interfacial evolution is in question, i.e., the undercooled temperature $T_{UC} = T_E - \Delta T$. Nonetheless, Eqs. (5.8) and (5.9) are not as disparate as they appear to be and the gap between them can be bridged as follows.

Consider Eq. (5.8); since the free energy v.s. concentration dependence is chosen in a parabolic form, it can be re-written as

$$\begin{aligned} \frac{\sigma_{sl}\kappa}{(c_s(\mu_{eq}) - c_l(\mu_{eq}))} &= \mu - \mu_{eq} = 2A_l c_l + B_l - (2Ac_l^{eq} + B_l) \\ &= 2A_l(c_l - c_l^{eq}(T)) \\ &= 2A_l(c_l - c_l^{eq}(T_E) + c_l^{eq}(T_E) - c_l^{eq}(T)) \\ &= 2A_l(c_l - c_l^{eq}(T_E) + \frac{c_l^{eq}(T_E) - c_l^{eq}(T)}{\Delta T} \Delta T) \end{aligned}$$

\implies

$$\Delta T = -m_*^s(c_l - c_E) + \frac{m_*^s \sigma_{sl}\kappa}{2A_l(c_s(\mu_{eq}) - c_l(\mu_{eq}))}$$

where m_*^s is

$$m_*^s = \frac{T_E - T_{UC}}{c_l^{eq}(T_E) - c_l^{eq}(T_{UC})}. \quad (5.10)$$

Thus, Eq. (5.8) takes an identical form as that of Eq. (5.9). Hence, instead of choosing m^α and m^β of Eq. (5.5) as the tangents of the liquidii lines at the eutectic point, if the secant formula as given in Eq. (5.10) is chosen; and likewise, if Γ_α and Γ_β are chosen as

$$\Gamma_\alpha = \frac{m_*^\alpha \sigma_{\alpha l}}{2A_l(T_{UC})(c_\alpha^{eq}(T_{UC}) - c_l^{eq}(T_{UC}))} \quad \text{and} \quad \Gamma_\beta = \frac{m_*^\beta \sigma_{\beta l}}{2A_l(T_{UC})(c_\beta^{eq}(T_{UC}) - c_l^{eq}(T_{UC}))}, \quad (5.11)$$

then an improved agreement between the theoretical and numerical results can be obtained. That is, the Jackson-Hunt and the limiting problem of the phase-field model are not exactly identical until the slopes and the Gibbs-Thomson coefficients are appropriately adjusted in the former.

At this juncture, we point out that the importance of using the same information in the analytical calculations as in the simulations is also recognized by some previous investigators, for instance, in Ref. [73]. A formula for the liquidus slopes is derived in this work as well as in Ref. [74] and is as follows

$$m^s(T) = \frac{(c_s^{\text{eq}}(T) - c_l^{\text{eq}}(T)) \frac{\partial \mu_l}{\partial c}(c_l^{\text{eq}}(T), T)}{\left(\frac{\partial \omega_s}{\partial T}(\mu_{\text{eq}}(T), T) - \frac{\partial \omega_l}{\partial T}(\mu_{\text{eq}}(T), T) \right)}. \quad (5.12)$$

To evaluate the various terms of $m^s(T_E)$ to be used in Eq. (5.5), the same CALPHAD database as utilized in the computational studies is employed. Further, to make the temperature derivatives $\partial \omega_\nu / \partial T$ more relevant, they are approximated as $(\omega_\nu(\mu_{\text{eq}}(T_E), T_E) - \omega_\nu(\mu_{\text{eq}}(T_{UC}), T_{UC})) / \Delta T$. The slopes thus evaluated are then used to compute the Gibbs-Thomson coefficients Γ_α and Γ_β to be substituted in Eq. (5.5) from

$$\Gamma_s(T_E) = \frac{m^s(T_E) \sigma_{sl}}{2A_l(T_E)(c_s^{\text{eq}}(T_E) - c_l^{\text{eq}}(T_E))}. \quad (5.13)$$

However, it is to be pointed out that the relation given by Eq. (5.12) is flawed as it is derived in Ref. [73] by replacing a total derivative with a partial one. Hence, it may potentially give some non-meaningful results. For instance, in the case of a different binary alloy system, namely, Aluminium-Copper, one of the solids pair forming a eutectic are *alpha-Aluminium* and AlCu₂ (θ -phase). However, when the slopes of their liquidii are evaluated at the common meeting point using Eq. (5.12), both of these turn out to be positive. Hence as per $L_s = T_E / \Gamma_s$, the latent heat of one of the phases has to be negative which is obviously non-physical. The correct formula should instead be

$$m^s(T) = \frac{(c_s^{\text{eq}}(T) - c_l^{\text{eq}}(T)) \frac{\partial \mu_l}{\partial c}(c_l^{\text{eq}}(T), T)}{\left\{ \left(\frac{\partial \omega_s}{\partial T}(\mu_{\text{eq}}(T), T) - \frac{\partial \omega_l}{\partial T}(\mu_{\text{eq}}(T), T) \right) - (c_s^{\text{eq}}(T) - c_l^{\text{eq}}(T)) \frac{\partial \mu}{\partial T}(c_l^{\text{eq}}(T), T) \right\}}. \quad (5.14)$$

We point out that even though the individual slopes and thus the Gibbs-Thomson coefficients calculated from them are predicted erroneously if Eq. (5.12) is adopted, both Eqs. (5.12) and (5.14) give the exact same results when used to evaluate Eq. (5.5) via Eq. (5.13).

The analytical results obtained by appropriately utilizing Eqs. (5.14) and (5.10) (i.e., in conjunction with Eq. (5.13) and (5.11), respectively) are also plotted in Fig. 5.6. No big difference is seen between the two but a huge improvement from the original curve is realized. Thus, the disparity between the theoretical and the numerical λ_{JH} dropped to -0.67% and the one between the associated maximum velocities to 14.89% . In the similar

fashion, the huge deviations observed in the rod growth case are lessened to -11.439% for the λ_{JH} and 31.570% for the maximum speed; the improvement is pictorially depicted in Fig 5.8.

5.4.3.2 Evaluating the credibility of the modeled system properties

We now ask the question how expectable it is that the slopes calculated from the secant formula of Eq. (5.10) give such contrasting results compared to the ones obtained directly from the phase diagram. Note that the undercooling under consideration is very small at a value of 5.9 K; further, typically in phase diagrams, the liquidii do not curve a lot. Thus, one should most reasonably expect that the difference in the former and the latter slopes should be very minute. Does that mean that the observed kinetics is so sensitive to the change in the magnitudes of m^α and m^β ? The formula of Eq. 5.5, on the contrary, does not seem to be suggesting so as perturbing these values by a small amount only alters the recovered speed at most at the same rate—implicating that the values retrieved from Eq. (5.10) in the current study are not so similar to those of the precise values from the phase diagram. Indeed, it is found that while the latter are $m^\alpha = -3571.4285$ K and $m^\beta = 1313.1313$ K, the values evaluated using the former are $m^\alpha = -1435.861$ K and $m^\beta = 1861.099$ K. That means, in a span of 5.9 K, the magnitude of the NiZr-liquidus slope dropped by more than half times the original value, clearly indicating that a huge blunder has been committed somewhere while modeling the system properties.

For instance, maybe the sharpnesses of the free energy curves of the solid phases are not high enough or the liquid's fitting is grossly erroneous. As mentioned earlier, the Gibbs free energy versus composition data of the solid phases is limited to a single point each (at any given temperature) in the CALPHAD database owing to the fact that they are stoichiometric in nature. These values for the current system, as extracted from the database through the software package PANDAT, are reproduced in Table 5.10. The

Table 5.10: CALPHAD data of the constituting solids of NiZr-NiZr₂ eutectic system corresponding to an undercooling of 5.9K, as extracted using the software package PANDAT.

Solid phase	CALPHAD data for $T = T_{UC} = T_E - 5.9\text{K}$ (Zr mole fraction, molar free energy)
NiZr	(0.500503, -115478.82 J/mol)
NiZr ₂	(0.667203, -107133.78 J/mol)

parabolaes of these phases are constructed in such a way that the coordinates given in the table happen to be the respective common tangent points. For the data provided for the liquid phase, a polynomial regression is used for fitting the curve while taking care that

the range of compositions used is small enough. To cater to the stoichiometric nature of the solids, the parabolae constructed for them are made at least 25 times sharper than the liquid curve as can be verified from Table 5.7. While it is true that a more accurate fitting is indeed possible for the liquid phase and the solids' parabolae can be made even sharper, it is not going to make the results any better. This is because to have the slopes that are evaluated through Eq. (5.10) stay close to the precise values $m^\alpha = -3571.4285\text{K}$ and $m^\beta = 1313.1313\text{K}$, the common tangent between the NiZr curve and the liquid one should hit the latter at $c = 0.613194$ and the one between the NiZr₂ and liquid curves at $c = 0.607049$. However, using the data directly from the CALPHAD database, it so turns out that it is impossible for such a thing to happen no matter how sharp the solids' parabolae are. This is because the tangent lines to the liquid at these points when extended do not pass from below the appropriate coordinates of Table 5.10. The exact common tangent points when used, retrieves the magnitudes of $m^\alpha = -2352.472\text{K}$ and $m^\beta = 1062.872\text{K}$ for the slopes. This is the best that could be done in terms of getting closer to the exact values from the phase diagram; i.e., they are still off by an appreciable amount. To worsen things, the corresponding deviation between the v v.s. λ curves is seen to increase when they are used, which is illustrated by the red curve in Fig. 5.9.

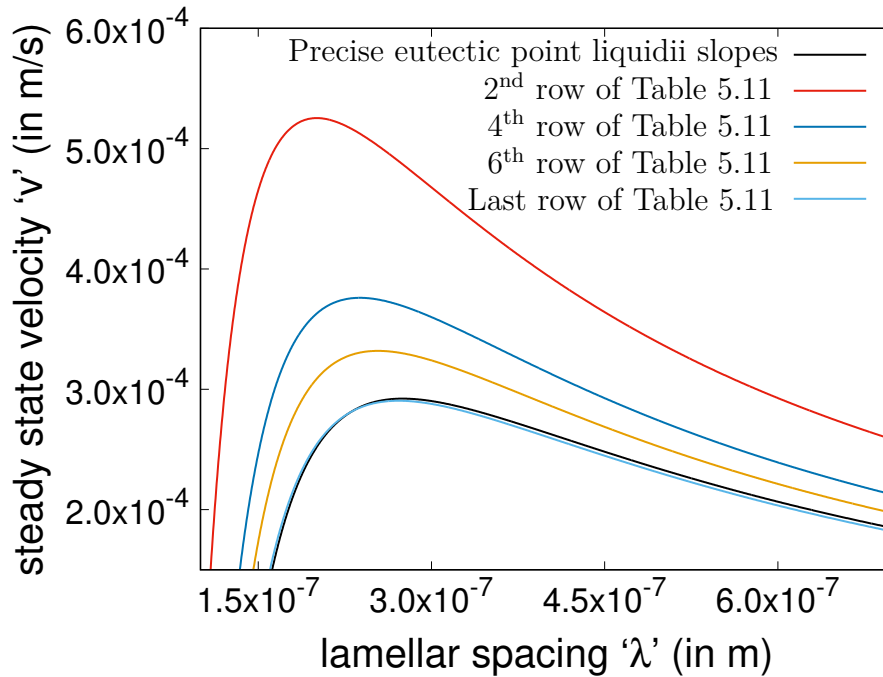


Figure 5.9: NiZr-NiZr₂ lamellar JH results (i.e., from Eq. (5.5)) for various slopes m_α and m_β . The dark curve corresponds to the classical analysis, i.e., with the precise slopes at the eutectic point chosen from the phase diagram and hence is the same as the green curve of Fig. 5.6. The others correspond to the slopes from various rows of Table 5.11.

The culprit is the presentation of the data in the software packages. If the number of

sample points is changed when extracting the free energy versus composition data through PANDAT, it is seen that the coordinates given in Table 5.10 are shifted horizontally in the manner presented in Table 5.11. That is, as the sampling size is increased, the bulk free energies remain fixed but tend to correspond more and more to the exact stoichiometric values. On the other hand, the liquid's data is only refined but not translated in the free energy-composition plane. Therefore, the common tangents made by the parabola fits of the solids with the liquid one will change implying that the secant-formula slopes picked up in simulations (i.e., estimates from Eq. (5.10)) will modify. Further, the observed gradation is such that as the bulk free energies are made to correspond to the exact stoichiometric compositions, the slopes tend to converge into the correct range as revealed by Table 5.11. Accordingly, the associated kinetics curves approach the classical JH one as illustrated by Fig. 5.9. Any sustained deviation is due to the difference in the magnitudes of the Gibbs-Thomson coefficients used: while Eq. (5.11) is utilized for obtaining the coloured curves, the same but with the exact values substituted for slopes and with T_{UC} replaced by T_E is employed for the dark one.

Table 5.11: The NiZr and NiZr₂ CALPHAD data extracted by the PANDAT software when the number of sample points are changed by fixing the Zr mole fraction range as ‘0.48 to 0.68’. Also listed are the liquidii slopes estimated from Eq. (5.10) by utilizing the common tangents made with the melt data.

Number of sampling points	Extracted data for NiZr ($c, -115478.82$ J/mol)	Extracted data for NiZr ₂ ($c, -107133.78$ J/mol)	Slopes from Eq. (5.10) (in K)	
			NiZr	NiZr ₂
100	$c = 0.501010$	$c = 0.667710$	-1815.664	0866.615
200	$c = 0.500503$	$c = 0.667203$	-2352.472	1062.872
300	$c = 0.500334$	$c = 0.667034$	-2608.311	1152.231
500	$c = 0.500200$	$c = 0.666900$	-2854.378	1235.602
700	$c = 0.500143$	$c = 0.666843$	-2973.790	1275.124
1000	$c = 0.500100$	$c = 0.666800$	-3071.317	1306.755
-	$c = 0.500$	$c = 0.66667$	-3322.072	1387.582

5.4.3.3 Rationalizing the residual errors

After correcting for the slope formula, the error in the steady state speed in Fig. 5.6 is seen to settle at just under 15%. This level of matching may not arise all the time as indicated by the results for the previously mentioned Al-AlCu₂ eutectic system, depicted

in Fig. 5.10. It can be seen that the formula of Eq. (5.14) and the one which corresponds to the slopes entering the asymptotic law, namely, Eq. (5.10) are not as close. Further, a disparity of 24.37% is seen between the analytical result employing Eq. (5.10) and the numerically predicted maximum speed; the error in the simulated λ_{JH} is -7.77% .

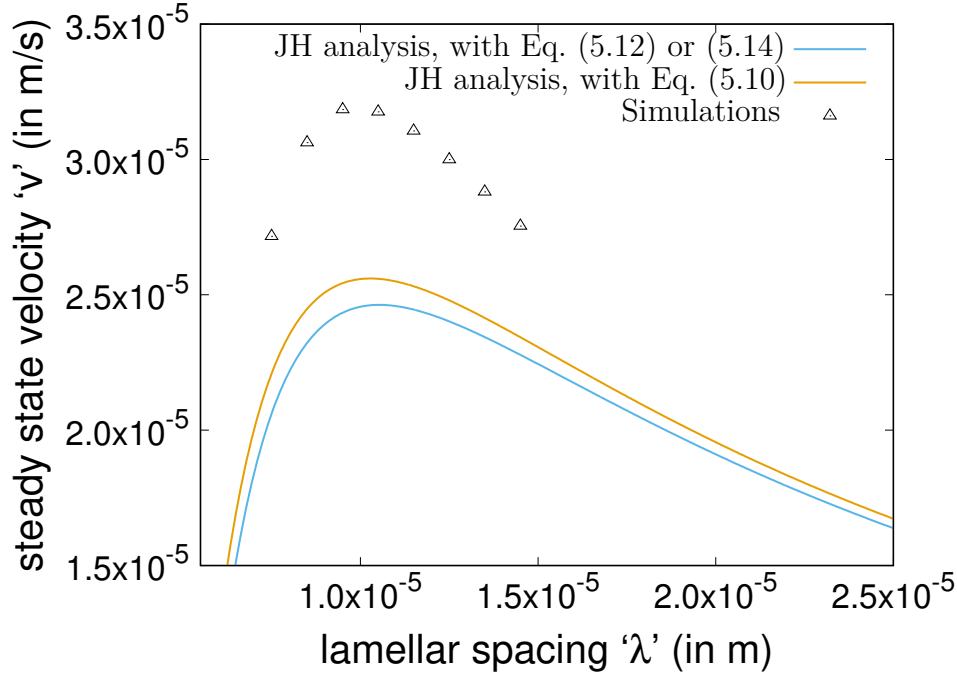


Figure 5.10: Comparison of Al-AlCu₂ lamellar growth kinetics predicted by the JH relation Eq. (5.5) when the slopes and Gibbs-Thomson coefficients are approximated as in Ref. [73] (i.e., Eqs. (5.12) and (5.13)) and when chosen as the ones picked in simulations (i.e., Eqs. (5.10) and (5.11)) with those of the computational results.

Even for the NiZr-NiZr₂ system, the errors increased as reported in Fig. E.7 of appendix E.3 when the solid-solid interfacial energy is modified to $\sigma_{\alpha\beta} = 0.60 \text{ J m}^{-2}$. It has to be noted that the applied change, first and foremost, has the effect of increasing the magnitudes of trijunction angles $\theta_{\alpha l}$ and $\theta_{\beta l}$. Likewise, while the reported results for the Al-AlCu₂ system correspond to an interfacial energies combination such that the triple junction angles are 60° each, on reducing which to 30° , the errors in the predicted kinetics dropped as reported in Fig. E.8. These behaviors point to the trend that larger the angles at the triple junction, higher is the deviation between the JH and the computational results. This gradation is of course not surprising because larger trijunction angles imply higher curvatures of the solidification front whereas the latter are not accounted in the JH calculations leading to Eq. (5.5). That is, we have come to a point where any remaining disagreement is more likely to be an outgrowth of an imperfection in the JH theory rather than the employed phase-field model. All the care that need to be taken in optimizing the latter is catered to and the performance is validated through interface

width reduction studies in appropriate “penultimate-level” benchmark cases. Even the filled up gap of Figs. 5.6 and 5.8 was brought about by matching the slope values in the JH theory to those captured in the simulations rather than modifying the numerical model. That is, slowly and naturally, the focus is shifting from refining the diffuse interface formulation to refining the connection between the phase-field and JH treatments, and finally to improving the sharp interface analysis itself.

That the residual gap is an outcome of the neglect of surface curvatures can also be rationalized in a slightly different way by contrasting with the findings for the rod growth. Even here, the gap between the analytical and the numerical results decreased when the slopes and the Gibbs-Thomson coefficients are chosen as per Eqs. (5.10) and (5.11), respectively as indicated by Fig. 5.8. However, the final deviation in the recovered maximum speed is 31.570%, i.e., twice as high as compared to the lamellar one for the exact same parameter set. A lamellar growth front is curved in “one direction” while remaining flat in the other, whereas transformation fronts of rod growth are curved in both the directions. Thus, in a rough sense, the following can be claimed: by possessing curvature in an additional dimension, the growth fronts of rod morphologies are usually more curved than the lamellar ones for the same feature spacing within a given system; and since the JH analysis ignores surface curvatures, the predicted results deviate by a larger amount in the former than the latter. The next few chapters extensively deal with testing these claims where it will indeed be verified that the residual gaps are due to the planar interface assumption of the JH analysis.

Before passing on to them, we point out that in the case of simple grain growth, not only the simulated steady state speeds but also the front shapes are compared with those of the sharp interface theory; whereas in directional eutectic solidification, the comparison is limited to the interfacial kinetics and mere triple junction angles. That is, instead of comparing the entire growth front only the configuration at the triple point is tested. The classical analysis does present a scheme for predicting the profile shapes at least for the case of lamellar growth. However, a refined version of it is proposed in the next chapter, hence this comparative study is postponed to a later point after its presentation.

Part III

Refinements in the sharp interface analysis of eutectic growth

Chapter 6

Jackson-Hunt analysis of lamellar growth

6.1 Introduction

Theoretical attempts at understanding eutectic growth date back to as early as 1926 [75], when Hultgren [76] proposed a co-operative growth mechanism centrally involving diffusional processes. This has later been recasted in a mathematical language [77] with attempts at solving it taking place simultaneously [77, 78]. For two decades, though acknowledged, the equally important role of the capillarity effects was not accounted into the theory, when it was finally carried out by Zener in his monumental paper in 1946 [79]. Later, Zener's analysis is rendered more rigorous by the likes of Hillert [80] and Tiller [81]* until finally it is given a coherent and comprehensive form by Jackson and Hunt in 1966 [29]. Ever since, this celebrated theory has been referred to as the Jackson-Hunt analysis and is used extensively in estimating the local temperature conditions of the experimental microstructures and, in recent times, in benchmarking simulation studies. But that is not to say that the theory was complete; it still employed a number of restrictive approximations, and the subsequent times have periodically seen articles proposing improvements and newer extensions to the formulation.

For instance, one of the major themes of the approximations has been the smallness of the growth speeds, and the associated simplifications are shown to give rise to considerable errors especially when analyzing off-eutectic solidification. This is exposed and remedied to some extent by Donaghey and Tiller [82] while further rectifications are furnished by Trivedi *et. al.* [83], Ludwig *et. al.* [84] and Zheng *et. al.* [85] through methods

*In fact, it is Tiller who made the switch from the isothermal growth considered by Zener to the case where directional solidification is led by a moving positive temperature gradient.

involving various levels of mixture of analytical and numerical techniques. Similarly, generalizations to multi-component systems [86], non-invariant reactions [74, 87, 88] and diffusion in solids [73] etc. have also been carried out.

Another approximation that has been long standing is the planar interface assumption. Beginning from Scheil [77], it persisted in all the later reformulations including the classical JH analysis and all its subsequent improvements and extensions. An exception is the work of Series *et. al.* [89] who used an electric analog method for solving the diffusion equation [89], and, Folch and Plapp [22] adopted a boundary-integral method. A completely analytical solution though, has never been proposed before. In the current chapter, this is remedied by putting forth a scheme for incorporating and as well as self-consistently predicting the curvatures of the solidification front [90, 91]. Approximations related to the smallness of the growth speeds or Péclet numbers are also relaxed. We begin with a derivation of the sharp interface governing equations of the directional lamellar eutectic growth process.

6.2 Sharp interface governing equations of lamellar eutectic growth

Consider the setup shown in schematic Fig. 6.1, where the shaded regions represent the solid phases α and β comprising the binary eutectic and the unshaded region, the melt l . The setup is imagined to be repeated indefinitely in the lateral direction (x -axis) to produce a lamellar structure. As also mentioned in the previous chapter, the width of the smallest representative unit is referred to as the lamellar spacing or the lamellar width and is denoted by λ . To begin with, the temperature in the entire system is assumed to be held at a constant value T . The practical case of directional growth led by a moving positive temperature gradient is handled later. Owing to the undercooling ΔT of the melt, the solids form at its expense which at steady state grow at a constant rate v . Neglecting advection in the liquid and diffusion in the solids, the only processes that are operative are the diffusion in the former, mass transport across the solidification front, the capillarity driven Gibbs-Thomson effects at the moving surface and the Young's law at triple junctions.

Mass balance in the liquid reads

$$\frac{\partial c}{\partial t} = D \left(\frac{\partial^2 c}{\partial x^2} + \frac{\partial^2 c}{\partial z^2} \right) \quad (6.1)$$

where $c(x, z, t)$ is the mole fraction of the solute atoms and D is the diffusivity in the liquid phase which is assumed to be the same for both the components. Since the concentration

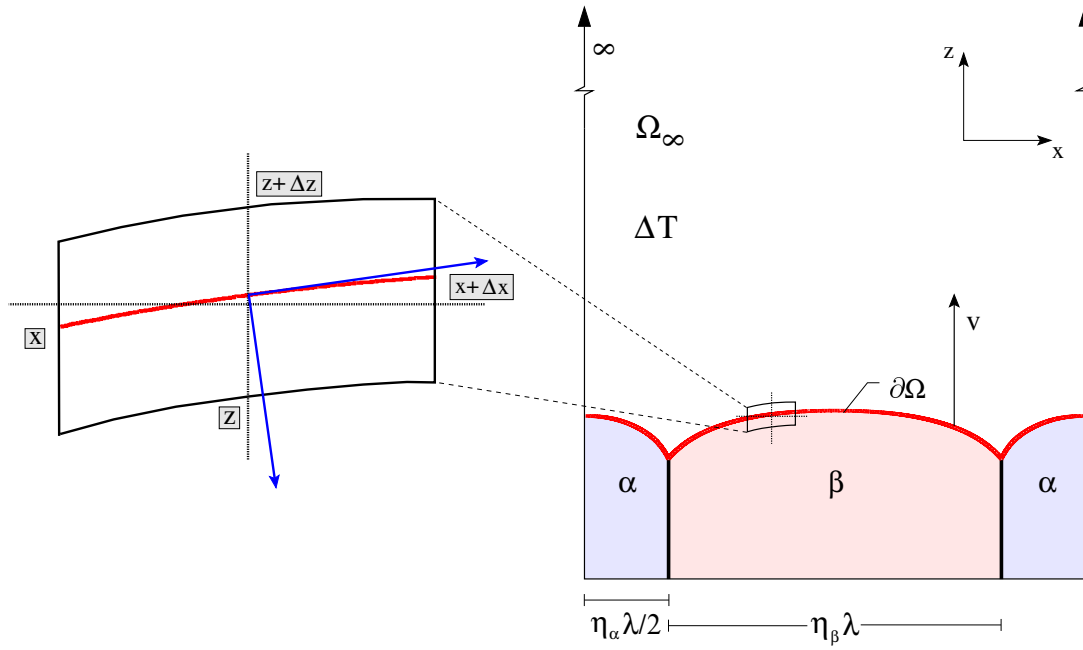


Figure 6.1: Schematic of one representative unit of the lamellar eutectic undergoing a directional growth under isothermal conditions. The zoomed in part shows a control volume over a small region of the solidification front.

profile is steadily moving upward, Eq. 6.1 rewrites as

$$\begin{aligned}
 & \lim_{\Delta t \rightarrow 0} \frac{c(x, z, t + \Delta t) - c(x, z, t)}{\Delta t} = D \nabla^2 c \\
 \Rightarrow & \lim_{\Delta t \rightarrow 0} \frac{c(x, z - v \Delta t, t) - c(x, z, t)}{\Delta t} = D \nabla^2 c \\
 \Rightarrow & \lim_{\Delta t \rightarrow 0} v \frac{c(x, z - v \Delta t, t) - c(x, z, t)}{v \Delta t} = D \nabla^2 c \\
 \Rightarrow & \lim_{v \Delta t \rightarrow 0} v \frac{c(x, z - v \Delta t, t) - c(x, z, t)}{v \Delta t} = D \nabla^2 c,
 \end{aligned}$$

renaming $v \Delta t$ to Δz leads to

$$\begin{aligned}
 \lim_{\Delta z \rightarrow 0} v \frac{c(x, z - \Delta z, t) - c(x, z, t)}{\Delta z} &= D \nabla^2 c \\
 \Rightarrow -v \frac{\partial c}{\partial z} &= D \nabla^2 c.
 \end{aligned}$$

This is the governing equation for transport in the liquid. For mass balance across the interface, consider the control volume shown in the zoomed in portion of Fig. 6.1. At the beginning of an infinitesimal time interval Δt , let the transformation front be at the bottom of the control element; as this time elapses, let it reach its top. The solute mass exchanged through the walls during this period accounts for the difference observed

within the cell. That is

$$\begin{aligned} & \left(\vec{J} \Big|_{z+\Delta z} \cdot \vec{n} \Delta s \Delta t - \vec{J} \Big|_z \cdot \vec{n} \Delta s \Delta t \right) + \left(\vec{J} \Big|_x \cdot \vec{t} \Delta z \Delta t - \vec{J} \Big|_{x+\Delta x} \cdot \vec{t} \Delta z \Delta t \right) \\ & = \Delta x \Delta z (c_s(x) - c_l(x)) \rho. \end{aligned}$$

Where $c_l(x)$ and $c_s(x)$ are the concentrations immediately adjacent to the surface corresponding to co-ordinate x in the liquid and solid phases, respectively. ρ is the overall number density assumed to be the same in all the three phases (just like during the phase-field modeling of the growth process). The diffusion in the solids is considered to be negligible, therefore the above reduces to

$$\begin{aligned} & \vec{J} \Big|_{z+v\Delta t} \cdot \vec{n} \Delta s \Delta t + \left(\vec{J} \Big|_x \cdot \vec{t} v \Delta t \Delta t - \vec{J} \Big|_{x+\Delta x} \cdot \vec{t} v \Delta t \Delta t \right) = \Delta x v \Delta t (c_s(x) - c_l(x)) \rho \\ \implies & \vec{J} \Big|_{z+v\Delta t} \cdot \vec{n} \Delta s + \left(\vec{J} \Big|_x \cdot \vec{t} v \Delta t - \vec{J} \Big|_{x+\Delta x} \cdot \vec{t} v \Delta t \right) = \Delta x v (c_s(x) - c_l(x)) \rho. \end{aligned}$$

In the limit of Δt tending to zero, this becomes

$$\vec{J} \Big|_z \cdot \vec{n} \Delta s = \Delta x v (c_s(x) - c_l(x)) \rho.$$

A further limit of vanishing Δx leads to

$$\vec{J} \Big|_z \cdot \vec{n} \frac{ds}{dx} = v (c_s(x) - c_l(x)) \rho.$$

Thus, the governing equations are

$$D \nabla^2 c + v \frac{\partial c}{\partial z} = 0 \quad \forall z > p(x) + vt \quad (6.2a)$$

$$D \left(\frac{\partial c}{\partial x} \vec{n} \cdot \hat{i} + \frac{\partial c}{\partial z} \vec{n} \cdot \hat{j} \right) \frac{ds}{dx} \Big|_{p(x)+vt} = v (c_l(x) - c_s(x)) \quad (6.2b)$$

$$c(-x, z, t) = c(x, z, t) \quad (6.2c)$$

$$p(-x) = p(x) \quad (6.2d)$$

$$c(x, z, t) = c(x + \lambda, z, t) \quad (6.2e)$$

$$p(x) = p(x + \lambda) \quad (6.2f)$$

$$\Delta T = -m(c_l(x) - c_E) + \Gamma \kappa \quad (6.2g)$$

where $p(x)$ is the shape of the transformation front. Due to steady state behavior, as time passes, the profile shape does not change and only translates upwards with speed v thus marking the liquid region by $\{(x, z) : z > p(x) + vt\}$. The symmetry of the setup around the z -axis is conveyed by Eqs. (6.2c) and (6.2d) while Eqs. (6.2e) and (6.2f) cater to its periodicity. The last equality is the Gibbs-Thomson relation with the kinetic undercooling term suppressed. Where, m is the slope of the liquidus and Γ is the Gibbs-Thomson coefficient corresponding to the solid-melt pair present at $(x, p(x) + vt, t)$, and

κ is the curvature of the front there. c_E is the solute concentration at the invariant point of phase diagram. For some values of the abscissa, $c_s(x)$ corresponds to the α phase and for some others to that of β . To emphasize this, $c_s(x)$ is replaced by $c^\nu(x)$ with ν used to index the phases α and β . Further, since $c_l(x)$ is the concentration in the liquid layer immediately adjacent to the solid-liquid interface, by definition, it equals $c(x, p(x) + vt)$.

For the sake of easeness in the later treatment, especially for error analysis, a few transformations are implemented on the equations. Firstly, the co-ordinate system is transformed to a frame attached to the interface. Next, the x and z co-ordinates are scaled by the lamellar width λ . Finally, the concentration field is modified by subtracting the far-field value c_∞ from it. That is

$$\begin{aligned}(x, z, t) &\rightarrow (x, z - vt, t) \\ (x, z) &\rightarrow \left(\frac{x}{\lambda}, \frac{z}{\lambda}\right) \\ c &\rightarrow c - c_\infty \\ \implies p(x) &\rightarrow \frac{1}{\lambda}p(\lambda x).\end{aligned}$$

Thus, the governing equations modify to

$$\nabla^2 c + \frac{v\lambda}{D} \frac{\partial c}{\partial z} = 0 \quad \forall z > p(x), x \in [-1/2, 1/2] \quad (6.3a)$$

$$\nabla c \cdot \vec{n} \left. \frac{ds}{dx} \right|_{p(x)} = \frac{v\lambda}{D} (c(x, p(x)) + c_\infty - c^\beta(x)) \quad \forall -\frac{\eta_\beta}{2} < x < \frac{\eta_\beta}{2} \quad (6.3b)$$

$$= \frac{v\lambda}{D} (c(x, p(x)) + c_\infty - c^\alpha(x)) \quad \forall \left[-\frac{1}{2}, \frac{1}{2}\right] \setminus \left[-\frac{\eta_\beta}{2}, \frac{\eta_\beta}{2}\right] \quad (6.3c)$$

$$\lim_{z \rightarrow \infty} c(x, z) = 0 \quad (6.3d)$$

$$c(-x, z) = c(x, z) \quad (6.3e)$$

$$c(x, z) = c(x + 1, z) \quad (6.3f)$$

$$\Delta T = -m^\beta (c(x, p(x)) + c_\infty - c_E) + \Gamma_\beta \kappa \quad \forall -\frac{\eta_\beta}{2} < x < \frac{\eta_\beta}{2} \quad (6.3g)$$

$$= -m^\alpha (c(x, p(x)) + c_\infty - c_E) + \Gamma_\alpha \kappa \quad \forall \left[-\frac{1}{2}, \frac{1}{2}\right] \setminus \left[-\frac{\eta_\beta}{2}, \frac{\eta_\beta}{2}\right] \quad (6.3h)$$

$$p(x) \text{ is consistent with the Young's law at } -\eta_\beta/2 \text{ and } \eta_\beta/2. \quad (6.3i)$$

Where, same symbols $x, z, c(x, z)$ and $p(x)$ are used for before and after the transformations for simplicity of notation. m^α and m^β are respectively the α -liquidus and β -liquidus slopes at the eutectic point evaluated with respect to the component whose concentration is being worked with. Γ_α and Γ_β are the Gibbs-Thomson coefficients of the α -liquid and β -liquid interfaces, respectively. Note that due to the shift to the moving co-ordinate frame, the time variable is completely eliminated and the free-boundary

problem is replaced by a boundary value problem. Of course, whose boundary is not specified a priori but has to be determined as part of the solution. That is, the problem statement is to find a $c(x, z)$, η_β , v and $p(x)$ such that Eqs. (6.3a)- (6.3i) are satisfied when all other involved parameters are provided. Although the $v - \lambda - \Delta T$ relation is of actual interest, it would anyway warrant finding the others.

6.3 ZOLPA problem in stoichiometric systems

It is a challenging task to solve the above problem in its full scale, hence, simpler versions of it are first looked at and later on, the various complexities are supplied. For example, the special case in which the forming solids are stoichiometric intermetallics is only considered to begin with. Further, the Péclet number $v\lambda/D$ is considered to be negligible and hence the term containing it in Eq. (6.3a) is ignored; such a move is commonly referred to as the low Péclet number approximation. Also, $c(x, p(x))$ in Eqs. (6.3b) and (6.3c) is retained only up to zeroth order in Péclet number—also called as the zeroth order approximation. Finally, the function $p(x)$ is assumed to be given rather than an unknown to be determined.

The restriction to the case of stoichiometric systems brings in a number of simplifications. On one hand it replaces functions $c^\alpha(x)$ and $c^\beta(x)$ with constants c^α and c^β , the stoichiometric compositions of the phases, and on the other, it readily fixes the volume fractions of the constituting phases η_α and η_β at the respective lever rule values. Before presenting the associated calculations, a notation is introduced where the melt region corresponding to one lamellar width as shown in Fig. 6.1 and below the line $z = z_*$ is denoted by Ω_{z_*} , i.e., $\Omega_{z_*} = \{(x, z) : p(x) < z < z_*, x \in [-1/2, 1/2]\}$. The vertical boundaries and the horizontal boundary $z = z_*$ on the top are denoted by $\partial\Omega_{z_*v}$ and $\partial\Omega_{z_*h}$, respectively. The solid-liquid interface is denoted by $\partial\Omega$ and thus the entire boundary $\partial\Omega_{z_*}$ is the union of all these, $\partial\Omega_{z_*} = \partial\Omega_{z_*v} \cup \partial\Omega_{z_*h} \cup \partial\Omega$. Hence, in this notation, the whole of the melt region is marked as Ω_∞ and its boundary as $\partial\Omega_\infty = \partial\Omega_{\infty h} \cup \partial\Omega$. For convenience, ϵ is used to denote the Péclet number $v\lambda/D$ in the rest of the chapter. Now, integrating Eq. (6.3a) in the region Ω_{z_*} for some z_* leads to

$$\begin{aligned} & \int_{\Omega_{z_*}} \left(\nabla^2 c + \epsilon \frac{\partial c}{\partial z} \right) dV = 0 \\ \implies & \int_{\partial\Omega_{z_*}} \nabla c \cdot \vec{n} ds + \int_{\partial\Omega_{z_*}} c \vec{n} \cdot \hat{z} ds = 0 \\ \implies & \int_{\partial\Omega_{z_*h}} \nabla c \cdot \vec{n} ds + \int_{\partial\Omega} \nabla c \cdot \vec{n} ds + \int_{\partial\Omega_{z_*h}} c \vec{n} \cdot \hat{z} ds + \int_{\partial\Omega} c \vec{n} \cdot \hat{z} ds = 0 \end{aligned}$$

$$\implies \int_{\substack{-1/2 \\ z=z_*}}^{1/2} \left(\frac{\partial c}{\partial z} \right) dx + \int_{\partial\Omega} \nabla c \cdot \vec{n} ds + \int_{\substack{-1/2 \\ z=z_*}}^{1/2} c dx + \int_{\partial\Omega} c \vec{n} \cdot \hat{z} ds = 0$$

In the limit of $z_* \rightarrow \infty$, this becomes

$$\begin{aligned} & \int_{\partial\Omega} \nabla c \cdot \vec{n} ds + \int_{\partial\Omega} c \vec{n} \cdot \hat{z} ds = 0 \\ \implies & \int_{-1/2}^{1/2} (c(x, p(x)) + c_\infty - c^\nu(x)) dx - \int_{-1/2}^{1/2} c(x, p(x)) dx = 0 \\ \implies & c_\infty - \int_{-\eta_\beta/2}^{\eta_\beta/2} c^\beta(x) dx - \int_{[-\frac{1}{2}, \frac{1}{2}] \setminus [-\frac{\eta_\beta}{2}, \frac{\eta_\beta}{2}]} c^\alpha(x) dx = 0 \quad (6.4) \\ \implies & c_\infty - \int_{-\eta_\beta/2}^{\eta_\beta/2} c^\beta dx - \int_{[-\frac{1}{2}, \frac{1}{2}] \setminus [-\frac{\eta_\beta}{2}, \frac{\eta_\beta}{2}]} c^\alpha dx = 0 \\ \implies & c_\infty = c^\beta \eta_\beta + c^\alpha (1 - \eta_\beta). \quad (6.5) \end{aligned}$$

Thus, the phase fractions are readily determined. As a result, since the profile shape $p(x)$ (consistent with the just derived volume fractions) is assumed to be given, all that remains to be computed are the steady-state concentration field and the growth speed.

Typically, a Fourier series route is taken to solve for the solute distribution. The series

$$c(x, z) = a_0 e^{-\epsilon z} + \sum_{m=1}^{\infty} a_m \cos(k_m x) e^{-q_m z} \quad (6.6)$$

with

$$q_m = \frac{\epsilon}{2} + \sqrt{k_m^2 + \frac{\epsilon^2}{4}} \quad \text{and} \quad k_m = 2\pi m.$$

can be readily seen to satisfy Eqs. (6.3a), (6.3d)-(6.3f). It can be shown (appendix F.1.1) that except for the plane wave component, the rest of the series is of the first order in Péclet number as the latter is made to vanish. Hence, to implement zeroth order approximation is to retain only the plane wave contribution in the boundary condition pertaining to the solid-liquid interface. Due to this, an additional simplification arises in case of the stoichiometric systems which is that even the plane wave term can be effectively dropped from the analysis of the BVP (which will become clear shortly). This further helps tremendously in estimating the errors associated with the various approximations that have been invoked.

In summary, the ZOLPA problem in stoichiometric systems is to find an a_0 , an ϵ and a $c(x, z)$ satisfying

$$\nabla^2 c = 0 \quad \forall z > p(x), x \in [-1/2, 1/2] \quad (6.7a)$$

$$\nabla c \cdot \vec{n} \left. \frac{ds}{dx} \right|_{p(x)} = \epsilon (a_0 e^{-\epsilon p(x)} + c_\infty - c^\beta) \quad \forall -\frac{\eta_\beta}{2} < x < \frac{\eta_\beta}{2} \quad (6.7b)$$

$$= \epsilon (a_0 e^{-\epsilon p(x)} + c_\infty - c^\alpha) \quad \forall \left[-\frac{1}{2}, \frac{1}{2}\right] \setminus \left[-\frac{\eta_\beta}{2}, \frac{\eta_\beta}{2}\right] \quad (6.7c)$$

and Eqs. (6.3d)-(6.3i), given c^α , c^β , c_∞ and a consistent η_β and $p(x)$. The method we adopt is as follows.

6.3.1 Computation of the steady state concentration field

The generic solution of Eq. (6.7a) satisfying Eqs. (6.3d)-(6.3f) is

$$c(x, z) = a'_0 e^{-\epsilon z} + \sum_{m=1}^{\infty} a_m \cos(k_m x) e^{-k_m z}. \quad (6.8)$$

Furthermore, the plane wave co-efficient a'_0 is chosen to be identically equal to a_0 . Note that this would then give rise to the quantity $\epsilon a_0 e^{-\epsilon p(x)}$ on the l.h.s of Eqs. (6.7b) and (6.7c) as well, thus canceling out the term from both sides of the equation. This is the reason it is claimed previously that in stoichiometric systems, the implementation of the zeroth order approximation effectively amounts to ignoring the zeroth order term for the manipulation of the equations. Substituting the Fourier series in Eqs. (6.7b) and (6.7c) gives

$$\sum_{m=1}^{\infty} a_m (k_m \sin(k_m x) p'(x) - k_m \cos(k_m x)) e^{-k_m p(x)} = -\epsilon w(x).$$

where $\epsilon w(x)$ is used to denote the r.h.s of the boundary condition after eliminating the plane wave term from both sides. Integrating the above leads to

$$\sum_{m=1}^{\infty} a_m \phi_m(x) := \sum_{m=1}^{\infty} a_m \sin(k_m x) e^{-k_m p(x)} = \epsilon \int_0^x w(x) dx =: \epsilon W(x). \quad (6.9)$$

Computing the solution $c(x, z)$ is to find the coefficients $\{a_m\}$ satisfying Eq. (6.9). For this, the latter is multiplied with $\phi_n(x) := \sin(k_n x) e^{-k_n p(x)}$ and the resultant is integrated from $-1/2$ to $1/2$ leading to

$$\sum_{m=1}^{\infty} \tilde{a}_m A_{mn} = W_n \quad (6.10)$$

where A_{mn} stands for $\int_{-1/2}^{1/2} \phi_m(x)\phi_n(x)dx$, W_n for $\int_{-1/2}^{1/2} W(x)\phi_n(x)dx$ and $\tilde{a}_m = a_m/\epsilon$. Corresponding to each natural number ‘ n ’, an equation of the above type exists where ‘ \tilde{a}_m ’s are unknown. In other words, an infinite system of linear equations in ‘ \tilde{a}_m ’s has resulted. The finite reductions of this infinite system are studied for approximately determining the solution of the ZOLPA solute distribution. In particular, the series in Eq. (6.10) is truncated at N terms for each n belonging to $\{1, 2, \dots, N\}$. This system of N linear equations is solved for \tilde{a}_m $m \in \{1, 2, \dots, N\}$. The ‘ \tilde{a}_m ’s thus estimated are substituted back into Eq. (6.10) to see if the equality is approximately fulfilled and if the error decreases as N is increased. Fortunately, it is observed that this indeed holds true for typical front shapes, and that too, with as few as 5-10 terms in the truncation sufficing to approximate the r.h.s to a very satisfactory degree as demonstrated in Fig 6.2. Furthermore, the

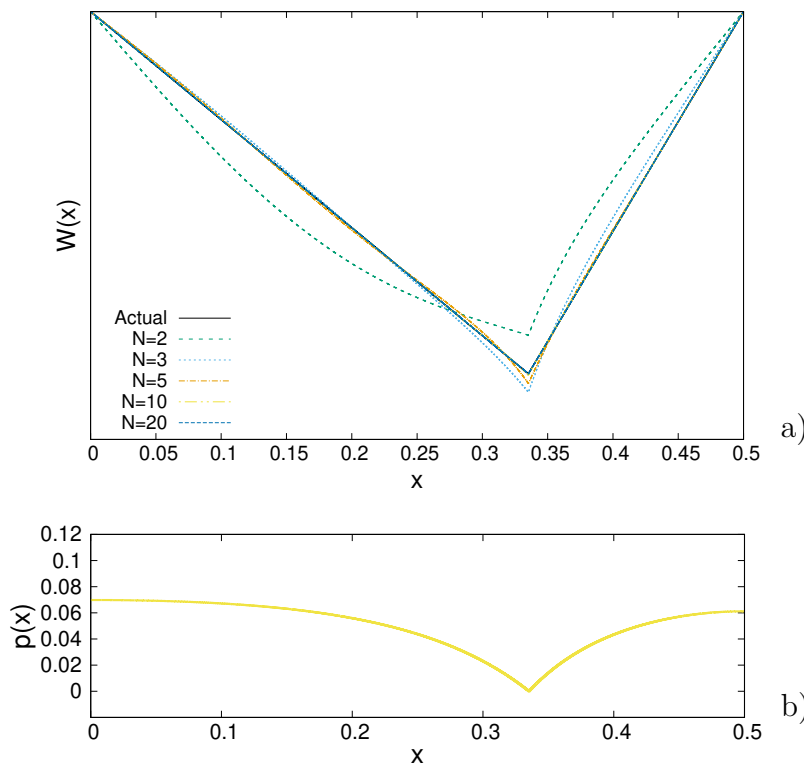


Figure 6.2: a): Typical shape of the function $W(x)$ of Eq. (6.9) (labelled ‘Actual’ in the figure), and its reconstruction from the series on the l.h.s truncated up to N terms for various N . The profile shape $p(x)$ used for the calculations is borrowed from the simulations of section 5.4.1.2 and is presented in b).

associated speed of convergence is found to be faster than when the conventional Fourier series partial sums are considered to approximate $w(x)$; i.e., with $p(x) = 0$ in Eq. (6.9). The \tilde{a}_m s thus determined are substituted into the truncated series of Eq. (6.8) to approximate the steady state concentration field in the zeroth order and low Péclet number

approximations. It is worth emphasizing that the above discussion implies that apart from the plane wave component, the rest of the solution is of the order of Péclet number. Finally, it is to be noted that the dot products A_{mn} cannot be evaluated analytically in a closed form except for a very few simple and unrealistic shapes of $p(x)$. As a result, numerical methods need to be employed to deal with the typical front shapes found in experimental or simulated microstructures.

Thus, the solution Eq. (6.8) is determined except for the plane-wave term. The latter is estimated next along with the steady state speed v .

6.3.2 Calculation of the steady state growth speed

Once the concentration field is estimated, the steady state speed can be found from a calculation similar to the one proposed in the original Jackson-Hunt paper. The key is to use the Gibbs-Thomson condition, Eqs. (6.3g) and (6.3h), averaged over each of the phases. Which read

$$\langle \Delta T \rangle_\alpha = -m^\alpha \langle c_\infty + c - c_E \rangle_\alpha + \Gamma_\alpha \langle \kappa \rangle_\alpha, \quad (6.11)$$

$$\langle \Delta T \rangle_\beta = -m^\beta \langle c_\infty + c - c_E \rangle_\beta + \Gamma_\beta \langle \kappa \rangle_\beta, \quad (6.12)$$

where the angle brackets $\langle \cdot \rangle_\alpha$ denote an averaging operation on the quantity placed inside it over α -liquid interface in one lamellar width; the angle brackets $\langle \cdot \rangle_\beta$ are similarly defined with the averaging carried out over β -liquid interface. Substituting $c(x, z)$ determined in section 6.3.1 into the above equations leads to

$$\Delta T = -m^\alpha b_0 - m^\alpha a_0 \zeta_0^\alpha - m^\alpha \epsilon \zeta_1^\alpha + \Gamma_\alpha \langle \kappa \rangle_\alpha, \text{ and} \quad (6.13)$$

$$\Delta T = -m^\beta b_0 - m^\beta a_0 \zeta_0^\beta - m^\beta \epsilon \zeta_1^\beta + \Gamma_\beta \langle \kappa \rangle_\beta \quad (6.14)$$

where, $b_0 = c_\infty - c_E$. Using ν as an index to indicate solid phases α and β , ζ_0^ν and ζ_1^ν stand for

$$\zeta_0^\nu = \frac{1}{\eta_\nu} \int_\nu e^{-\epsilon p(x)} dx \text{ and} \quad (6.15)$$

$$\zeta_1^\nu = \frac{1}{\eta_\nu} \int_\nu \left(\sum_{m=1}^N \tilde{a}_m \cos(k_m x) e^{-k_m p(x)} \right) dx \quad (6.16)$$

where the integration is considered within the interval $[-1/2, 1/2]$ for all abscissae where the phase ν is in contact with the liquid. Eliminating a_0 from Eqs. (6.13) and 6.14 results in

$$\epsilon = \frac{\left(m^\beta \zeta_0^\beta - m^\alpha \zeta_0^\alpha \right) \Delta T - \left(m^\beta \zeta_0^\beta \Gamma_\alpha \langle \kappa \rangle_\alpha - m^\alpha \zeta_0^\alpha \Gamma_\beta \langle \kappa \rangle_\beta \right) + m^\alpha m^\beta b_0 \left(\zeta_0^\beta - \zeta_0^\alpha \right)}{-m^\alpha m^\beta \left(\zeta_0^\beta \zeta_1^\alpha - \zeta_0^\alpha \zeta_1^\beta \right)} \quad (6.17)$$

and eliminating ΔT leads to

$$a_0 = \frac{-(m^\beta - m^\alpha) b_0 + \Gamma_\beta \langle \kappa \rangle_\beta - \Gamma_\alpha \langle \kappa \rangle_\alpha - \epsilon (m^\beta \zeta_1^\beta - m^\alpha \zeta_1^\alpha)}{(m^\beta \zeta_0^\beta - m^\alpha \zeta_0^\alpha)}. \quad (6.18)$$

If ζ_0^α and ζ_0^β are known then the steady state speed and all the co-efficients a_m , $m \in \{0, 1, \dots, N\}$ will be known, that is, the concentration field will be determined. However, the former cannot be computed as they themselves contain the unknown ϵ which is being determined. Nevertheless, an approximation can be obtained by expanding ζ_0^α and ζ_0^β in terms of ϵ and retaining only up to first order terms when ΔT is expressed as a function of Péclet number. The resultant expressions for steady state speed and the plane-wave coefficient are

$$v = \frac{\Delta T - \frac{1}{(m^\beta - m^\alpha)} (m^\beta \Gamma_\alpha \langle \kappa \rangle_\alpha - m^\alpha \Gamma_\beta \langle \kappa \rangle_\beta)}{\frac{\lambda}{D} \left(\frac{-m^\alpha m^\beta}{m^\beta - m^\alpha} \right) \left[\left(\frac{\Gamma_\beta \langle \kappa \rangle_\beta - \Gamma_\alpha \langle \kappa \rangle_\alpha}{m^\beta - m^\alpha} - b_0 \right) (g_\beta - g_\alpha) + (\zeta_1^\alpha - \zeta_1^\beta) \right]}. \quad (6.19)$$

$$a_0 = \frac{-b_0(m^\beta - m^\alpha) + \Gamma_\beta \langle \kappa \rangle_\beta - \Gamma_\alpha \langle \kappa \rangle_\alpha - \frac{v\lambda}{D} (m^\beta \zeta_1^\beta - m^\alpha \zeta_1^\alpha)}{\left[(m^\beta - m^\alpha) - \frac{v\lambda}{D} (m^\beta g_\beta - m^\alpha g_\alpha) \right]}. \quad (6.20)$$

Where, $g_\nu = \langle p(x) \rangle_\nu$ and the approximation $|(m^\beta g_\beta - m^\alpha g_\alpha) / (m^\beta - m^\alpha)| \leq 1$ is invoked in deriving Eq. (6.19). The terms $\Gamma_\alpha \langle \kappa \rangle_\alpha$ and $\Gamma_\beta \langle \kappa \rangle_\beta$ are as given by Eq. (5.6)

Thus the steady state speed and all the co-efficients a_m , $m \in 0, 1, \dots, N$ are determined and hence so is the ZOLPA concentration field. Since a lot of approximations went into the analysis, it is natural to ask how accurate the derived solutal field and the steady state speeds are. This is taken up in appendix F.

6.3.3 Construction of the self-consistent interface shape

The analysis so far has been carried out under the assumption that the front shape is provided a priori. Whereas, in actuality, it is supposed to be the job of the JH theory to determine it. This shortcoming will be remedied presently.

Attempts to determine the shape of the solidification front were made in the original JH theory itself and by Hillert [80] prior to that. As per their approach, the solute distribution field is computed by first assuming that the interface is planar everywhere except in a vanishing neighborhood around the triple junctions. Next, the Gibbs-Thomson

relation of Eqs. (6.3g) and (6.3h) is integrated leading to

$$\int_{\eta_\beta/2}^x \frac{\lambda}{\Gamma_\alpha} (\Delta T - m^\alpha (c_\infty - c_E + c(x, p(x)))) dx - \sin \theta_{\alpha l} = \frac{-p'(x)}{\sqrt{1 + (p'(x))^2}} \quad \forall \quad \frac{\eta_\beta}{2} < x < \frac{1}{2} \quad (6.21)$$

and

$$\int_{\eta_\beta/2}^x \frac{\lambda}{\Gamma_\beta} (\Delta T + m^\beta (c_\infty - c_E + c(x, p(x)))) dx + \sin \theta_{\beta l} = \frac{-p'(x)}{\sqrt{1 + (p'(x))^2}} \quad \forall \quad 0 \leq x < \frac{\eta_\beta}{2}. \quad (6.22)$$

After this, the just derived concentration field is substituted in place of $c(x, p(x))$ in the above equations and the resultant are solved for $p(x)$. The profile shape thus derived resembles the ones typically found in the experiments of lamellar growth in thin films. That means, by starting from a planar front and using the associated growth speed and the solute distribution field, when the profile shape is tried to be reconstructed, one deviating considerably from the flat profile is retrieved. Put in these terms, it may sound that the calculations are not self-consistent, however, when the procedure is interpreted as a first step in a iterative process, it instantly gives hope that by continuing it, a convergence may be obtained. That is, if the derived profile shape is used to compute the solutal field using the method of sections 6.3.1 and 6.3.2, a new $p(x)$ can be computed by combining it with Eqs. (6.21) and (6.22). Repeating this process for a few more iterations, if the difference between the constructed profiles tends to vanish, then a self-consistent profile is generated. Thus, the interface shape can be evaluated from within the theory.

We note that in the classical theory, only the first step in the iterative process is possible to be carried out as the analysis is limited to the planar front. Beginning from the second iteration, solutal field corresponding to a curved front has to be evaluated. Although not analyzed in the original work, as pointed out before, in a different investigation, Ref. [89], Series *et. al.* have used an electric analog method to solve the BVP to estimate the solute distribution and hence make it possible to carry the iterative process forward through to convergence up to the desired level of tolerance. A completely theoretical estimation is now possible owing to the curvature informed analysis developed in this chapter. Finally, it is worth emphasizing that when the interface is planar, g_ν s are identically unity. Moreover, since $c^\alpha = c_{\alpha E}$ and $c^\beta = c_{\beta E}$ for stoichiometric systems, $\zeta_1^\alpha - \zeta_1^\beta$ also merges with $(c_{\beta E} - c_{\alpha E}) \left(\frac{\mathcal{P}(\eta_\alpha)}{\eta_\alpha} + \frac{\mathcal{P}(\eta_\beta)}{\eta_\beta} \right)$ of Eq. (5.5). That is, the first iteration coincides with the Jackson-Hunt calculation.

6.4 Complete solution in stoichiometric systems and applications

The zeroth order and low Péclet number approximations will now be relaxed. This will be followed by the application of the theory to NiZr-NiZr₂ eutectic system.

6.4.1 Relaxing the zeroth order and low Péclet number approximations

In section 6.3.3, for evaluating the solute distribution field in each iteration, the algorithm of section 6.3.1 is used. However, the latter gives the concentration field pertaining to the governing equations in which the low Péclet number and the zeroth order approximations are implemented. This is rectified next.

Substituting Eq. (6.6) in Eqs. (6.7b) and (6.7c) gives

$$\begin{aligned} \sum_{m=1}^{\infty} a_m (-k_m \sin(k_m x) p'(x) + q_m \cos(k_m x)) e^{-q_m p(x)} &= \epsilon \sum_{m=1}^{\infty} a_m \cos(k_m) e^{-q_m p(x)} + \epsilon w(x) \\ \implies \sum_{m=1}^{\infty} a_m (k_m \sin(k_m x) p'(x) + \tilde{q}_m \cos(k_m x)) e^{-q_m p(x)} &= -\epsilon w(x) \end{aligned}$$

where

$$\begin{aligned} \tilde{q}_m &= \frac{\epsilon}{2} - \sqrt{k_m^2 + \frac{\epsilon^2}{4}} \\ \implies \sum_{m=1}^{\infty} a_m \frac{-\tilde{q}_m}{k_m} \phi_m(x) &:= \sum_{m=1}^{\infty} a_m \frac{-\tilde{q}_m}{k_m} \sin(k_m x) e^{-q_m p(x)} = \epsilon \int_0^x w(x) dx = \epsilon W(x). \end{aligned} \tag{6.23}$$

As Eq. 6.23 is similar in form as Eq. 6.9, the appropriately modified procedure of section 6.3.1 can be utilized to obtain the coefficients a_m . However, only the ϵ on the r.h.s, i.e., the one multiplying $w(x)$ has to be treated as an unknown, and for the ones in ϕ_m and \tilde{q}_m , the value estimated in the previous iteration with the help of Eq. (6.17) is used. Similarly, instead of the approximated formulae Eqs. (6.19) and (6.20), the complete versions themselves viz. Eqs. (6.17) and (6.18) can be employed. This now raises the question: what about the first iteration where there is no previous step to choose the epsilon from? For this, an initial guess of $\epsilon = 0$ is selected. In other words, as far as the first iteration is concerned, low Péclet number and zeroth order approximations are still implemented. Since the interface shape is also planar for this step, it exactly coincides with the JH computation.

6.4.2 Application to NiZr-NiZr₂ system

Next, the improved analysis is applied to study the kinetics of NiZr-NiZr₂ eutectic lamellae and the results are compared with those of the classical JH.

6.4.2.1 Isothermal eutectic solidification

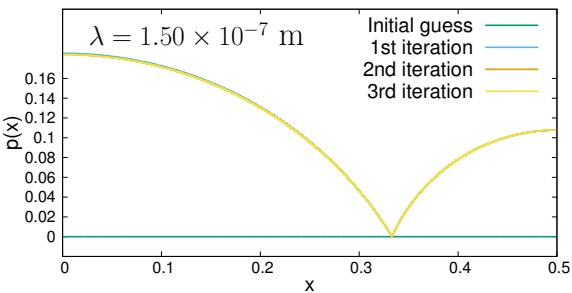
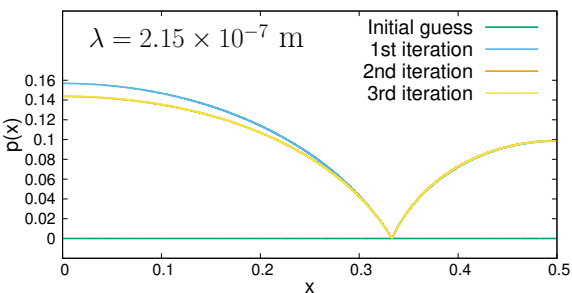
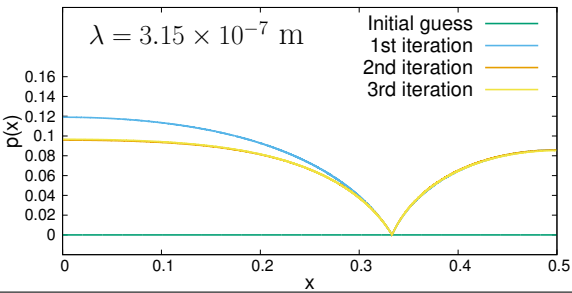
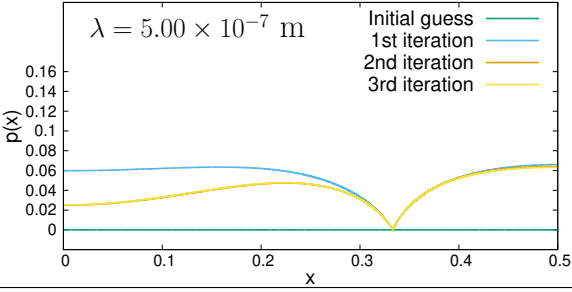
The isothermal cooperative precipitation of NiZr and NiZr₂ intermetallic phases from a melt at eutectic composition is first looked at for an undercooling 5.9 K. Some of the required thermophysical data of this system is already provided in Table 5.7 where α is used to denote the NiZr phase and β the NiZr₂. However, to bring out more effectively the extent to which curvatures can influence the results, the solid-solid interfacial energy given in the table is modified to $\sigma_{\alpha\beta} = 0.65\text{J/m}^2$. As a result, the Young's law angles at the triple junction change to $\theta_{\alpha l} = 66.0217^\circ$ and $\theta_{\beta l} = 58.7582^\circ$ from the values given in Table 5.8. The remaining data needed for performing the theoretical calculations is listed in Table 6.1.

Table 6.1: Thermo-physical parameters of the NiZr-NiZr₂ system corresponding to near eutectic temperatures. Symbols α , β and l mark the NiZr, NiZr₂ and melt phases, respectively.

Parameter	Value	Units	Source
ΔT	5.9	K	Chosen
c^α	0.5000	-	CALPHAD
c^β	0.6667	-	CALPHAD
c_E	0.611542	-	CALPHAD
η_β	0.66912	-	Tie line construction
m^α	-1435.861	K	Combining Table 5.7 with Eq. (5.10)
m^β	1861.099	K	Combining Table 5.7 with Eq. (5.10)
Γ_α	1.612713×10^{-7}	m^1K	Combining Table 5.7 with Eq. (5.11)
Γ_β	3.212049×10^{-7}	m^1K	Combining Table 5.7 with Eq. (5.11)

The iterative procedure of section 6.4.1 is implemented for this system and the estimated profiles and Péclet numbers at various stages of the iterative process are reported in Table 6.2 for the lamellar spacings mentioned in the plots. The last column reports the specific velocity numbers defined as the ratios of the growth speeds predicted by the curvature informed analysis to those of the planar ZOLPA ones. Since the first iteration corresponds exactly to the latter, the associated specific velocity number is identically unity in each case. From the rest of the entries of the table, it is readily evident that the rate of convergence of the iterative process is very fast not requiring more than 2-3

Table 6.2: Reconstructed profiles at various iterations tabulated along with the corresponding Péclet numbers and specific velocities for different spacings.

Reconstructed interface profiles	Iteration	Péclet number ($\times 10^{-2}$)	Specific velocity number
 <p>$\lambda = 1.50 \times 10^{-7}$ m</p>	1st	10.67509	1.00000
	2nd	14.33678	1.343013
	3rd	14.34336	1.343629
	4th	14.34330	1.343623
	5th	14.34329	1.343623
	6th	14.34329	1.343623
 <p>$\lambda = 2.15 \times 10^{-7}$ m</p>	1st	11.23973	1.00000
	2nd	14.62715	1.301379
	3rd	14.57055	1.296344
	4th	14.56365	1.295729
	5th	14.56322	1.295691
	6th	14.56336	1.295704
 <p>$\lambda = 3.15 \times 10^{-7}$ m</p>	1st	18.69191	1.00000
	2nd	23.22298	1.242408
	3rd	22.86347	1.223175
	4th	22.84262	1.222059
	5th	22.84259	1.222058
	6th	22.84357	1.222110
 <p>$\lambda = 5.00 \times 10^{-7}$ m</p>	1st	24.62012	1.00000
	2nd	28.10377	1.141496
	3rd	27.08720	1.100206
	4th	27.05099	1.098735
	5th	27.05404	1.098859
	6th	27.05464	1.098884

iterations to come considerably close to the final result. The fact that the specific velocity numbers are all greater than unity indicates that faster kinetics can be expected for a curved front compared to a flatter one. This is further corroborated by the first three rows of the table from where it can be qualitatively seen that higher the “curvedness” of an interface, larger is the deviation of the growth speed from that of the planar one. It is to be noted that in all the converged reconstructed profiles, the triple junction angles are fixed at the same values as given by the Young’s law. Thus, the above mentioned curvedness means more than just the overall curvature of the profile; the portion of the interface over which this curvature is distributed also plays a key role in determining the specific velocity numbers. In the third row, the profile is considerably flat at the left end and gets curved as the triple junction is approached, whereas in the first, it is curved right from the beginning. Correspondingly, larger specific velocity numbers are witnessed for the latter than the former. An effect typically seen at larger spacings, namely, a “dip” at the center of the growth front is also successfully retrieved in our calculations. Further, the difference between the first iteration and the converged profile is more pronounced when the surface dip occurs. This implies that the classical theory predicts inaccurate interface shapes at larger lamellar widths as it is limited to only one iteration. The converged profile of the last row is curved throughout its extent similar to the one in the first row and unlike the one in the third. In spite of this, the specific velocity number is lower indicating that the sign of curvature is equally crucial in regulating the kinetics as does the magnitude. The specific velocity numbers for all the self-consistent profiles constructed in this study when plotted as a function of lamellar spacing display an interesting linear trend as depicted in Fig. 6.3. The growth speeds corresponding to these profiles are compared with those of the classical results in Fig. 6.4. Also shown in Figs 6.3 and 6.4 are the results pertaining to the self-consistent profiles of the ZOLPA problem, i.e., of section 6.3.

Figure 6.5 shows the higher-order contribution to the solute distribution at the interface, $c_*(x, p(x)) := \sum_{m=1}^{\infty} a_m \cos(k_m x) \exp(-k_m p(x))$, divided by the Péclet number for the final profiles tabulated in Table 6.2. The corresponding flat interface counterparts are also plotted. On comparing the two, it can be seen that the concentration spread at the interface is lowered if we account for the interface curvature. The profiles $c_*(x, p(x))/\epsilon$ corresponding to the curved interfaces tend to get closer to those of the plane ones in the left portions of the plots, eventually overshooting them. This can be readily attributed to the sign change of the interface curvature in these regions.

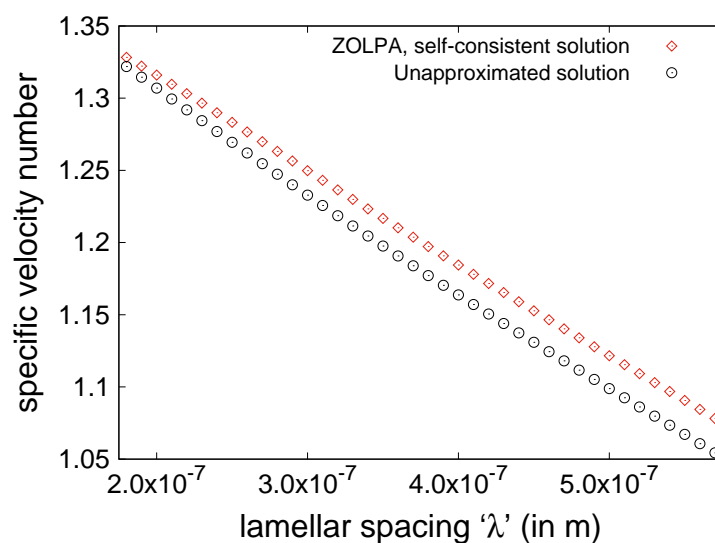


Figure 6.3: Specific velocity number—defined as the ratio between the steady-state velocity predicted by the curvature informed theory to that by the classical JH analysis—calculated for the self-consistently obtained profiles and plotted as function of lamellar widths. Both the cases of ZOLPA and the complete solution are presented.

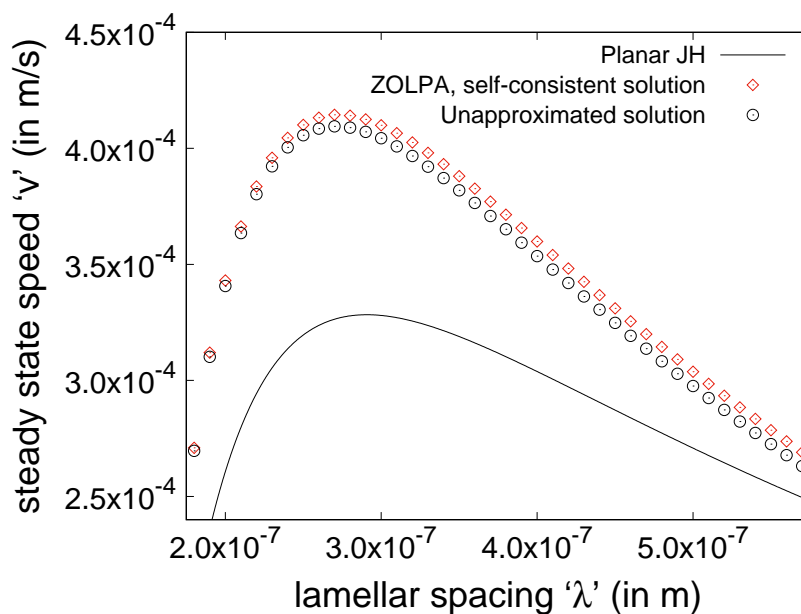


Figure 6.4: Comparison of growth kinetics predicted by the classical and the extended JH analyses.

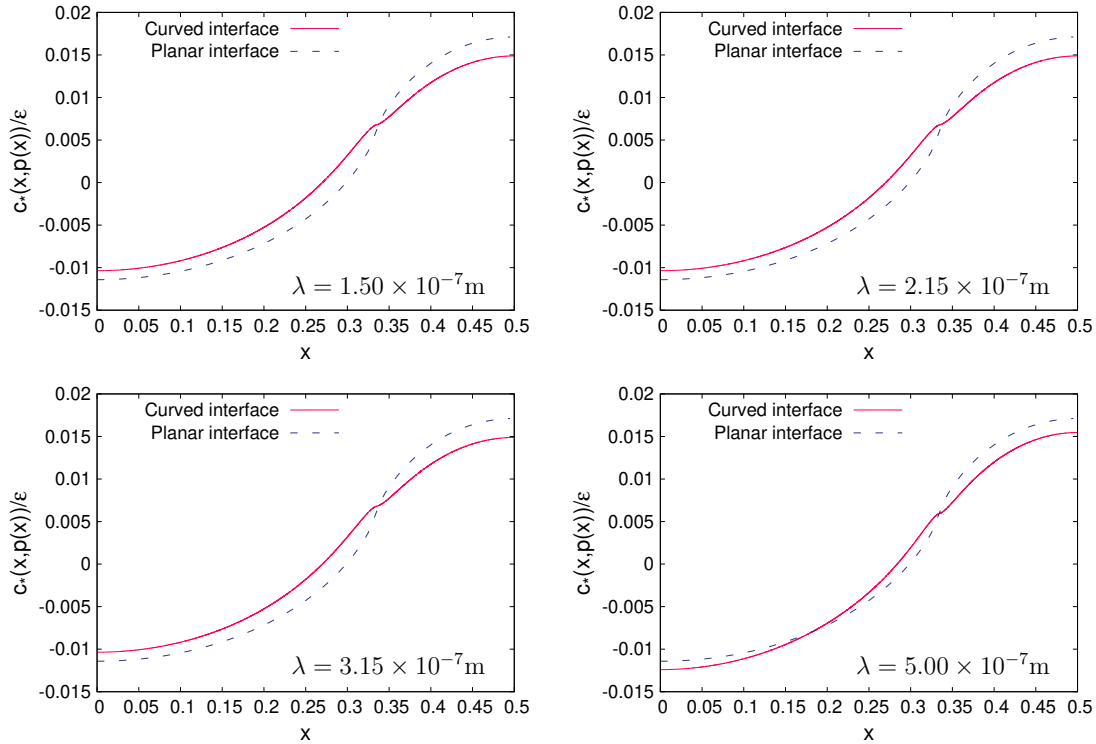


Figure 6.5: Higher order contribution to the interfacial solute distribution $c_*(x, p(x))$ divided by the Péclet number for the converged interfaces of Table 6.2 compared with their flat interface counterparts.

6.4.2.2 Isothermal off-eutectic solidification

It will now be demonstrated that the classical theory can predict more inaccurate results in the cases of solidification from off-eutectic melts. To make this more conspicuous, the parameter set of NiZr-NiZr₂ system will be modified further. Though the equations utilized for the iterative process, viz. Eqs. (6.17) and (6.18) may not readily suggest how this tuning has to be done, their approximated version Eqs. (6.19) and (6.20) can give some pointers. The key idea is to draw a significant contribution from the $b_0(g_\beta - g_\alpha)$ term which was zero in the eutectic case. First of all, it has to be recognized that the numerator of the $v - \lambda - \Delta T$ relation of the ZOLPA problem, i.e., Eq. (6.19) is exactly the same as the classical one, the difference arises only in the square bracket term of the denominator. That means, the effect of the details of the profile shape on the growth kinetics is completely captured by this term; for this reason, we call it the geometric factor. For the hypo-eutectic cases which we are going to consider, b_0 is negative, hence, in order to reduce the magnitude of the geometric factor and thereby have a higher deviation between the classical and the current theories, a g_β appropriately smaller than g_α has to be chosen. This can be achieved when the contact angle at the triple junction, subtended

Table 6.3: Reconstructed profile shapes at characteristic lamellar spacings (λ_{JH}) for various off-eutectic cases. Also listed are the geometry and kinetics related data of the converged profiles and the respective classical geometric factors.

Reconstructed interface profiles	Geometry and kinetics related data
<p style="text-align: center;">$\Delta = 0$</p>	$(\eta_\alpha, \eta_\beta) = (1/3, 2/3)$ $\lambda_{JH} = 2.10 \times 10^{-7} \text{ m}$ $\zeta_1^\alpha - \zeta_1^\beta = 1.685583 \times 10^{-2}$ $(G.F)_{\text{classical}} = 2.096901 \times 10^{-2}$ Péclet number = 19.68526×10^{-2} Specific vel. no. = 1.242881
<p style="text-align: center;">$\Delta = -1/6$</p>	$(\eta_\alpha, \eta_\beta) = (1/2, 1/2)$ $\lambda_{JH} = 1.75 \times 10^{-7} \text{ m}$ $\zeta_1^\alpha - \zeta_1^\beta = 1.847609 \times 10^{-2}$ $(G.F)_{\text{classical}} = 2.258084 \times 10^{-2}$ Péclet number = 19.08013×10^{-2} Specific vel. no. = 1.309173
<p style="text-align: center;">$\Delta = -1/3$</p>	$(\eta_\alpha, \eta_\beta) = (2/3, 1/3)$ $\lambda_{JH} = 1.75 \times 10^{-7} \text{ m}$ $\zeta_1^\alpha - \zeta_1^\beta = 1.915846 \times 10^{-2}$ $(G.F)_{\text{classical}} = 2.096592 \times 10^{-2}$ Péclet number = 20.82117×10^{-2} Specific vel. no. = 1.428725
<p style="text-align: center;">$\Delta = -7/15$</p>	$(\eta_\alpha, \eta_\beta) = (4/5, 1/5)$ $\lambda_{JH} = 1.95 \times 10^{-7} \text{ m}$ $\zeta_1^\alpha - \zeta_1^\beta = 1.851440 \times 10^{-2}$ $(G.F)_{\text{classical}} = 1.697562 \times 10^{-2}$ Péclet number = 25.64073×10^{-2} Specific vel. no. = 1.912197

by the β phase (i.e., the NiZr₂ phase) is chosen at a smaller value. Thus, we modify the magnitude of $\sigma_{\beta l}$ to 0.21392 and that of $\sigma_{\alpha\beta}$ further to 0.50895, respectively, such that the $\theta_{\beta l}$ further changes from 58.7582° to 38.76°. We note that compared to the magnitude of the geometric factor, its first summand is typically at least three orders smaller, hence, the care taken above is sufficient for the current purpose of showing that the specific velocity numbers can rise for off-eutectic solidifications. The associated results for various “off-eutecticness” $\Delta = (c_\infty - c_E)/(c_\beta - c_\alpha) = 0, -1/6, -1/3, -7/15$ are composed in Table 6.3 for an undercooling of 5.9 K. The reported findings correspond to the characteristic lamellar spacing (λ_{JH}) at every off-eutectic composition. The phase fractions, geometric factor corresponding to the planar front (i.e., the classical geometric factor), contributions from the last term (i.e., $\zeta_1^\alpha - \zeta_1^\beta$) of the geometric factor corresponding to the converged profiles, and the Péclet numbers and specific velocity numbers pertaining to the same are also listed in the table.

It can be seen that the convergence of the iterative process slows down as the deviation from eutectic composition increases. Further, the profile constructed in the first iteration differs markedly from that of the converged one indicating the limitation of the classical theory as only the first step of the iteration is possible in it. The disparity in the predicted maximal front speeds is seen to rise up to 91%. Close to eutectic composition, the contribution from the $\zeta_1^\alpha - \zeta_1^\beta$ is significantly larger than that of $b_0(g_\beta - g_\alpha)$, whereas at off-eutectic compositions, the latter dominates. Thus, the boundary layer term is not negligible, unlike the near eutectic systems. Moving further away from the eutectic composition, the former can behave in the opposite manner, i.e., take up values larger than the classical geometric factor as apparent from the fourth column of the table. It is straightforward to envisage systems in which a fortuitous reduction in the deviation between the curved and the planar theories occurs. For instance, in the current system, this can happen at hyper-eutectic compositions or if g_β were to be greater than g_α in the hypo-eutectic cases. Similarly, speeds smaller than the classically predicted values can, in principle, occur at off-eutectic compositions. We note that though Eqs. (6.19) and (6.20) are utilized for presenting the reasoning, the calculations pertaining to Table 6.3 have actually been performed within the unapproximated scheme itself, that is, through the algorithm of section 6.4.1.

6.5 Other extensions

6.5.1 Modifications for directional solidification led by imposed moving temperature gradient

Experimentally, the most convenient way to carry out directional solidification is to apply a positive temperature gradient and pull the sample at a given velocity. That is to hold the speed of growth as a constant rather than the temperature in the system. Hence, borrowing Eqs. (6.17) and (6.18) (which is derived for isothermal solidification) to analyze directional solidification implies invoking an additional approximation that the average interface undercooling is the same for both the product phases. It is apparent that in directionally solidifying alloys, this condition is not satisfied in general as the average front undercooling is determined by the surface profile shape and the imposed temperature gradient. However, the typical gradients employed for metallic systems are of the range of 10 – 100 K/mm. Assuming a maximum “height” of curved interfaces to be 0.2 times the lamellar spacing and by noting that the typical lamellar widths in metallic eutectics are of the order of $10^{-7} - 10^{-6}$ m, the maximum temperature variation across the interface is merely about 0.02 K. Hence, for front undercoolings of the magnitude of 1 K, the error becomes negligible. Nevertheless, for the sake of completeness, the following straightforward modifications can be suggested for the treatment of directional solidification. Notice that $\langle \Delta T \rangle_\alpha$ and $\langle \Delta T \rangle_\beta$ in Eqs. (6.11) and (6.12) are equal in the isothermal case, whereas, under an imposed temperature gradient they become

$$\langle \Delta T \rangle_\alpha = \Delta T_{\text{tr.jn.}} + G\lambda g_\alpha, \text{ and} \quad (6.24)$$

$$\langle \Delta T \rangle_\beta = \Delta T_{\text{tr.jn.}} + G\lambda g_\beta \quad (6.25)$$

where, $\Delta T_{\text{tr.jn.}}$ is the undercooling at the triple junction, G is the imposed thermal gradient, and g_α and g_β are as before. Therefore, we have the same relations for a_0 and the kinetics relation in the case of directional solidification as given in Eqs. (6.18) and (6.17), except that the terms $\Gamma_\alpha \langle \kappa \rangle_\alpha$ and $\Gamma_\alpha \langle \kappa \rangle_\beta$ are replaced by $\Gamma_\alpha \langle \kappa \rangle_\alpha - G\lambda g_\alpha$ and $\Gamma_\beta \langle \kappa \rangle_\beta - G\lambda g_\beta$, respectively and ΔT is replaced by $\Delta T_{\text{tr.jn.}}$. Similarly, for the calculation of interface shapes, the procedure remains the same except that the ΔT term in Eqs. (6.21) and (6.22) is replaced by $\Delta T_{\text{tr.jn.}} + p(x)|_{\text{prev}} G\lambda$, where $p(x)|_{\text{prev}}$ is the profile obtained in the previous iteration step.

6.5.2 Non-stoichiometric systems

The governing equations of section 6.2 have been derived without making any assumption about the stoichiometric nature or lack thereof of the eutectic solids. Hence, the same

apply for all binary systems. However, $c^\alpha(x)$ and $c^\beta(x)$ will no longer be constants for non-stoichiometric systems. Instead, the following relates them to the concentration of the contacting melt $c_l(x)$.

$$c^\nu(x) = \Lambda^\nu c_l(x) - \Lambda^\nu c_E + c_{\nu E}, \quad (6.26)$$

where $c^{\nu E}$ is the equilibrium concentration of ν phase at eutectic temperature; c^E is the eutectic point concentration; and Λ^ν is the solute distribution coefficient corresponding to phase ν as defined in Ref. [74]. The boundary condition after substituting the Fourier series representation of the solute distribution is the same as Eq. (6.23), except that $w(x)$ has to be modified to

$$w(x) = c_\infty + \Lambda^\nu c_E - c_{\nu E} - \Lambda^\nu (c_\infty + a_0 e^{-\epsilon p(x)} + u)$$

with ν taking up the “values” α or β appropriately depending on the coordinate x . Hence, as before, for the first iteration, planar ZOLPA problem is solved. However, unlike the stoichiometric case, a_0 is still present in the boundary condition pertaining to the growth front. Not only that, the undetermined solution u is itself present in the r.h.s. Further, the phase fractions themselves are not known as Eq. (6.4) does not apply.

To handle this, in the first step, an algorithm proposed by Senninger and Voorhees [74] or Lahiri and Choudhury [88] is borrowed and appropriately adapted. Thus, the phase-fractions and the concentration field and the a_0 are obtained which are then used in conjunction with Eqs. (6.21) and (6.22) to estimate the curved profile $p(x)$. Next, the same procedure as in the stoichiometric case is employed to update ϵ , a_0 and $p(x)$ over a number of iterations until a satisfactory level of convergence is attained; except, Eqs. (6.17) and (6.18) are preferred over Eqs. (6.19) and (6.20). One caveat though is that the mass balance across the solid-liquid boundary requires that c_∞ and a_0 be related to each other as

$$c_\infty = \frac{[c_{\nu E} \eta_\nu - c_E \Lambda^\nu \eta_\nu]}{(1 - \Lambda^\nu \eta_\nu)} + \int_{-1/2}^{1/2} \frac{\Lambda^\nu (u + a_0 e^{-\epsilon p(x)})}{(1 - \Lambda^\nu \eta_\nu)} dx \quad (6.27)$$

It is this c_∞ obtained using the u , a_0 , $p(x)$ and ϵ estimated in the previous iteration that is used in each new iteration. That is, an undesirable feature of the analysis is that the far-field composition is re-predicted and updated in each step of the iterative process; hence, it is important to verify that it converges and remains close to the originally given value. Finally, it must be pointed out that, that the Fourier terms apart from the constant and the plane wave are of first order in Péclet number even in the current case as in stoichiometric systems is another detail that needs to be demonstrated. This can be done, for example, by appropriately splitting the BVP into two new ones and individually analyzing them as presented in Ref. [91]. Generalizing further to the imposed temperature gradient case is straightforward in the light of section 6.5.1.

Chapter 7

Jackson-Hunt analysis of rod growth

7.1 Introduction

It is shown in the previous chapter that relaxing the planar growth front assumption modifies the velocity v.s. lamellar spacing curve in such a direction that the typical deviations reported between the classical Jackson-Hunt predicted and the phase-field generated results are reduced. Since the flat interface approximation is also implemented in the analysis of rod growth morphologies, the next natural step is to relax it in the latter case as well. The current chapter deals with the details of it.

However, it must be pointed out that in the case of fibrous eutectic growth, non-accountance of the surface curvatures is not the only geometry related assumption implemented in the classical theory. The periodicity of the embedding of the rods inside the matrix and its rotational symmetry is also not rigorously catered to: First of all, it has to be recalled that the determination of the steady state solute distribution in the melt ahead of the growing eutectic solid is one of the crucial elements of the JH theory. Since the distribution of the constituent phases within the solid forms a periodic pattern, the concentration evaluation can be restricted to any representative unit. In the case of lamellar growth in chapter 6, the latter is chosen as one lamellar width while for rod growth, any unit cell may be chosen. To qualify as a unit cell, a sub-region needs to satisfy the property that its rigid translations by integral multiples of some finite set of vectors can be made to span the entire domain without overlaps. A few examples of such units for the case of interest of hexagonal rod distribution are shown in Fig. 7.1 with dark solid lines. The rectangular unit R is employed for the numerical studies of chapter 5. Whereas, in the classical theory, the circular sub region C is chosen as the representative unit with the size of the circle equalling the area of the hexagonal unit cell H that it is superposed on. Further, a zero flux condition is imposed at the perimeter

of the circle which furnishes the simplification of reducing the 3D problem of rod growth into an effectively 2D problem due to circular symmetry. However, some fundamental differences are brought in. For instance, as circles do not tile the plane, some of the domain is unaccounted altogether while some other regions are considered twice; hence, the global hexagonal symmetry and periodic behavior are completely stripped off from the problem. It is unknown if the solutions from two overlapping circles are consistent in the common region and are compatible with the zero boundary flux conditions of both the circles. Moreover, the assumption of zero flux at the circular boundary is itself unfounded. The compatibility of the solutions from three overlapping circles when extended into the unspanned region surrounded by them remains unaddressed. In view of all these alterations, the circular representative unit approximation is relaxed in the subsequent sections along with the planar surface assumption. A parallelogram shaped primitive unit cell as exemplified by unit P of Fig. 7.1 is worked with for the analysis.

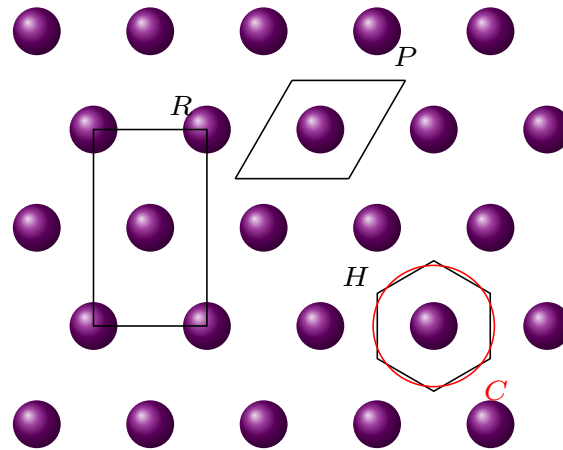


Figure 7.1: Hexagonal lattice showing three different unit cells and the circular representative unit considered in the classical JH theory.

7.2 Extension of the classical JH theory of rod growth

The derivation follows the standard steps of (i) determining the steady state solute distribution in the melt in the representative unit and (ii) substituting it in the generalized Gibbs-Thomson equation to obtain the kinetics relation. The revision is performed in two steps; first, only the hexagonal symmetry is accounted, i.e., by still considering a planar interface as in the classical analysis, this is then followed by the incorporation of surface curvatures.

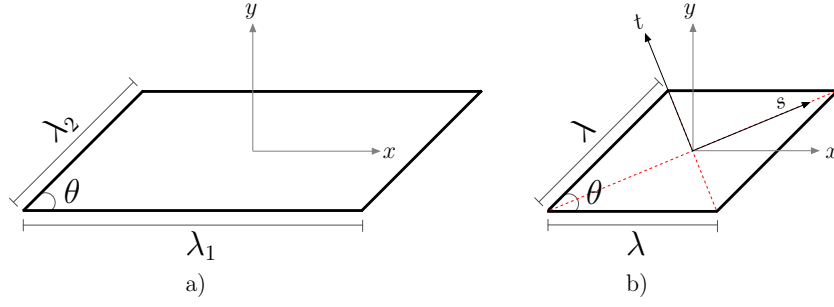


Figure 7.2: Schematic of a) a unit cell of a generic lattice with the co-ordinate axis (x, y, z) and b) a primitive unit cell of equal sides with the (x, y, z) and the (s, t, z) co-ordinate axes. The z -axis is normal to the plane of the paper.

7.2.1 Incorporation of hexagonal symmetry

To start off, a generic lattice for the arrangement of rods is considered, i.e., the unit cell is as shown in Fig. 7.2a) for some λ_1 , λ_2 and θ . The problem reduces to the special case of hexagonal symmetry when $\lambda_1 = \lambda_2$ and $\theta = \pi/3$. The co-ordinate axis is oriented in such a way that the x -axis is parallel to the base of the parallelogram, the z -axis points in the direction of growth, and the origin lies above the center of the unit cell. The x , y and z axes are scaled by λ_1 , λ_2 and $\sqrt{\lambda_1\lambda_2}$, respectively. The solute distribution is transformed by subtracting far-field concentration c_∞ from it. Then, by following the derivation of section 6.2, the governing equations for the transformed steady state solute distribution in the melt in a scaled frame attached to the solid-liquid surface can be written down as:

$$\frac{1}{\lambda_1^2} \frac{\partial^2 c}{\partial x^2} + \frac{1}{\lambda_2^2} \frac{\partial^2 c}{\partial y^2} + \frac{1}{\lambda_1\lambda_2} \frac{\partial^2 c}{\partial z^2} + \frac{v}{D\sqrt{\lambda_1\lambda_2}} \frac{\partial c}{\partial z} = 0 \quad (7.1a)$$

$$\left(\frac{\lambda_2}{\lambda_1} \frac{\partial c}{\partial x} \frac{\partial p}{\partial x} + \frac{\lambda_1}{\lambda_2} \frac{\partial c}{\partial y} \frac{\partial p}{\partial y} - \frac{\partial c}{\partial z} \right) = \frac{v\sqrt{\lambda_1\lambda_2}}{D} (c_l(x, y) - c_s(x, y)) \quad (7.1b)$$

$$c(x + 1, y, z) = c(x, y, z) = c(x + (\lambda_2/\lambda_1) \cos \theta, y + \sin \theta, z) \quad (7.1c)$$

$$\lim_{z \rightarrow \infty} c(x, y, z) = 0 \quad (7.1d)$$

where $c(x, y, z)$ transformed concentration, i.e., the mole fraction of the solute atoms at the spatial point (x, y, z) minus the far-field value; v is the speed of advancement of solid-liquid transformation front; D is the diffusivity of the solute or the solvent atoms in the melt with the assumption that both the species have same diffusivity; $p(x, y)$ is the solid-liquid interface profile; and, $c_l(x, y)$ and $c_s(x, y)$ are, respectively, the untransformed concentrations in the liquid and solid layers that are in contact with each other at the point corresponding to the co-ordinates x and y , hence, by definition, $c_l(x, y) = c_\infty + c(x, y, p(x, y))$. Without loss of generality, we label the phase that forms rods as α phase and the matrix as β phase. This is also consistent with our notation so far for the

application to rod growth of NiZr-NiZr₂ composite from melts of eutectic composition. As NiZr and NiZr₂ are stoichiometric, we assume α and β to be of like nature with the concentrations c^α and c^β , respectively. Thus, for a portion at the center of the unit cell, $c_s(x, y)$ takes the value c^α and for the remaining portion, it takes the value c^β . As before, to remind ourselves of this fact, we rename $c_s(x, y)$ by $c^\nu(x, y)$ with ν functioning as an index to denote α or β depending on (x, y) . Further, for the time being, we assume the solid-liquid surface to be planar with $p(x, y) = 0$. Thus, the boundary condition Eq. (7.1b) becomes

$$-\frac{\partial c}{\partial z} = \frac{v\sqrt{\lambda_1\lambda_2}}{D}(c_\infty + c(x, y, 0) - c^\nu(x, y)). \quad (7.2)$$

The generic solution of Eq. (7.1a) satisfying Eqs. (7.1c) and (7.1d) is as follows

$$c = \sum_{m=0}^{\infty} \sum_{n=-\infty}^{\infty} A_{ij} \cos(k_i x + q_{ij} y) e^{-Q_{ij} z} + B_{ij} \sin(k_i x + q_{ij} y) e^{-Q_{ij} z} \quad (7.3)$$

where

$$k_i = 2\pi i, \quad q_{ij} = k_j \operatorname{cosec} \theta - \frac{\lambda_2}{\lambda_1} k_i \cot \theta,$$

and Q_{ij} satisfies

$$Q_{ij}^2 - \frac{v\sqrt{\lambda_1\lambda_2}}{D} Q_{ij} - \left(\frac{\lambda_2}{\lambda_1} k_i^2 + \frac{\lambda_1}{\lambda_2} q_{ij}^2 \right) = 0.$$

We now make the formulation specific to the case $\lambda_1 = \lambda_2$. Under the assumption that the rods are circular cylinders, such a case gives rise to additional symmetries, namely, the diagonals of the unit cell act as mirror elements. Hence, the solute distribution should meet the following mirror symmetry requirements about the diagonals

$$c(x, y, z) = c(x \cos \theta + y \sin \theta, x \sin \theta - y \cos \theta, z) \quad \text{and} \quad (7.4)$$

$$c(x, y, z) = c(-x \cos \theta - y \sin \theta, -x \sin \theta + y \cos \theta, z). \quad (7.5)$$

We denote the inter rod spacing by λ ($=\lambda_1=\lambda_2$) and the Péclet number, $v\lambda/D$ by ϵ . In chapter 6, it is proved that in the low Péclet number and the zeroth order approximations, the solute distribution for lamellar growth is correct up to first order in Péclet number. In the case of $\lambda_1 = \lambda_2$, from the similarity of the governing equations of the lamellar and rod growth, it can be argued that this order result also holds for the latter. Hence, we work in these approximations in the current article. Thus, the mirror symmetry requirements, Eqs. (7.4) and (7.5) along with the low Péclet number approximation modify the undetermined solute distribution of Eq. (7.3) to the following.

$$\sum_{\substack{m=0, n=0 \\ (m,n) \neq (0,0) \\ (m+n) \equiv 0 \pmod{2}}}^{\infty, \infty} A_{mn} \cos\left(\frac{m\pi}{\cos(\theta/2)} s\right) \cos\left(\frac{n\pi}{\sin(\theta/2)} t\right) e^{-\kappa_{mn} z} + A_0 e^{-\epsilon z} \quad (7.6)$$

where

$$\begin{aligned} s &= x \cos(\theta/2) + y \sin(\theta/2), \\ t &= -x \sin(\theta/2) + y \cos(\theta/2), \quad \text{and} \\ \kappa_{mn} &= \sqrt{\left(\frac{m\pi}{\cos(\theta/2)}\right)^2 + \left(\frac{n\pi}{\sin(\theta/2)}\right)^2}. \end{aligned}$$

Further, the zeroth order approximation modifies the boundary condition, Eq. (7.2), to

$$-\frac{\partial c}{\partial z} = \epsilon(c_\infty + A_0 - c^\nu(x, y)). \quad (7.7)$$

Since circular cross-section is assumed for the rods, the expanded version of the above is

$$-\frac{\partial c}{\partial z} = \frac{v\sqrt{\lambda_1\lambda_2}}{D}(c_\infty + A_0 - c^\alpha) \quad \forall (x, y) \text{ such that } x^2 + y^2 < r_\alpha^2 \quad (7.8a)$$

$$= \frac{v\sqrt{\lambda_1\lambda_2}}{D}(c_\infty + A_0 - c^\beta) \quad \text{in the rest of the unit cell} \quad (7.8b)$$

where r_α is the radius of the alpha fibers.

To completely determine the solute distribution, the coefficients A_{mn} and A_0 have to be determined. This is done by substituting the series of Eq. (7.6) in Eq. (7.8) and employing the ‘dotting on both sides’ method. However, working with the existing coordinate system makes the calculations quite cumbersome; hence, we make the coordinate transformation, $(x, y, z) \rightarrow (s, t, z)$ (see Fig. 7.2b) which is a rotation of axes about z -axis by $\theta/2$ radians in counter-clockwise direction. Therefore, the dot products in the new coordinates evaluate to

$$A_{mn}\kappa_{mn} \sin \theta = \frac{4\epsilon(c^\beta - c^\alpha)}{(1 + \delta_{m0} + \delta_{n0})} \iint_{u^2+v^2 \leq r_\alpha^2} \cos\left(\frac{m\pi}{\cos(\theta/2)}u\right) \cos\left(\frac{n\pi}{\sin(\theta/2)}v\right) du dv \quad (7.9)$$

where δ_{m0} and δ_{n0} are Kronecker deltas. Making a further change of axis to polar coordinates, namely, $(s, t) \rightarrow (r, \varphi)$, the above dot products become

$$\begin{aligned} A_{mn}\kappa_{mn} \sin \theta &= \frac{4\epsilon(c^\beta - c^\alpha)}{(1 + \delta_{m0} + \delta_{n0})} \int_0^{r_\alpha} \int_0^{2\pi} \cos\left(\frac{m\pi}{\cos(\theta/2)}u\right) \cos\left(\frac{n\pi}{\sin(\theta/2)}v\right) d\varphi r dr \\ &= \frac{2\epsilon(c^\beta - c^\alpha)}{(1 + \delta_{m0} + \delta_{n0})} \left[\int_0^{r_\alpha} \int_0^{2\pi} \cos\left(\frac{m\pi}{\cos(\theta/2)}r \cos \varphi + \frac{n\pi}{\sin(\theta/2)}r \sin \varphi\right) d\varphi r dr \right. \\ &\quad \left. + \int_0^{r_\alpha} \int_0^{2\pi} \cos\left(\frac{m\pi}{\cos(\theta/2)}r \cos \varphi - \frac{n\pi}{\sin(\theta/2)}r \sin \varphi\right) d\varphi r dr \right] \end{aligned} \quad (7.10)$$

$$= \frac{4\epsilon(c^\beta - c^\alpha)}{(1 + \delta_{m0} + \delta_{n0})} \int_0^{r_\alpha} \int_0^{2\pi} \cos(r\kappa_{mn} \sin \varphi) d\varphi r dr \quad (7.11)$$

which evaluate to

$$\begin{aligned}
 A_{mn}\kappa_{mn} \sin \theta &= \frac{8\pi r_\alpha \epsilon (c^\beta - c^\alpha)}{\kappa_{mn} (1 + \delta_{m0} + \delta_{n0})} \int_0^{r_\alpha} r J_0(r\kappa_{mn}) r dr \\
 \implies A_{mn} &= \frac{8\pi r_\alpha \epsilon (c^\beta - c^\alpha)}{\kappa_{mn}^2 (1 + \delta_{m0} + \delta_{n0}) \sin \theta} J_1(r_\alpha \kappa_{mn})
 \end{aligned} \tag{7.12}$$

where J_0 and J_1 are Bessel functions of orders 0 and 1, respectively. The co-efficients being proportional to the Péclet number establishes the self-consistency with the zeroth order approximation. Now that the higher order terms are estimated, as in the lamellar analysis, A_0 and the $v - \lambda - \Delta T$ relation can be derived by substituting the liquid concentration at the transformation front in the averaged generalized Gibbs-Thomson equations with the kinetic undercooling term neglected. However, the planar solidification front assumption is still present in the formulation at this stage; this is generalized next.

7.2.2 Incorporation of surface curvatures

Since the presence or absence of curvature in a transformation front is independent of its translational and rotational symmetry, the undetermined solute distribution for the case of curved solid-liquid surface for $\lambda_1 = \lambda_2$ is still given by Eq. (7.6). However, the associated boundary condition in the zeroth order approximation is different from Eq. (7.8) as the surface profile $p(x, y)$ is not constant throughout the unit cell. Instead, it reads as the following

$$\left(\frac{\partial c}{\partial x} \frac{\partial p}{\partial x} + \frac{\partial c}{\partial y} \frac{\partial p}{\partial y} - \frac{\partial c}{\partial z} \right) = \epsilon (c_\infty + A_0 e^{-\epsilon p(x,y)} - c^\nu(x, y)) \tag{7.13}$$

with $c^\nu(x, y)$ chosen appropriately. As in section 7.2.1, we work with the co-ordinate system (s, t, z) instead of (x, y, z) to simplify the calculations. Thus, after the change of axes, the boundary condition at the solid-liquid interface becomes

$$\left(\frac{\partial c}{\partial s} \frac{\partial p}{\partial s} + \frac{\partial c}{\partial t} \frac{\partial p}{\partial t} - \frac{\partial c}{\partial z} \right) = \epsilon (c_\infty + A_0 e^{-\epsilon p(s,t)} - c^\nu(s, t)) \tag{7.14}$$

where, for simplicity of notation, same symbols p and c are used to denote the solid-liquid interface profile and the solute distribution in the (s, t, z) axis, respectively. The form of the equation does not change because the new and old co-ordinates are related to each other by an orthogonal transformation; here, a rotation. Substituting Eq. (7.6) in Eq. (7.14) yields

$$\sum_{\substack{m=0, n=0 \\ (m,n) \neq (0,0) \\ (m+n) \equiv 0 \pmod{2}}}^{\infty, \infty} A_{mn} R_{mn}(s, t) = -\epsilon (c_\infty - c^\nu(s, t)) \tag{7.15}$$

where R_{mn} is given by

$$R_{mn} = \left(p_m \sin(p_m s) \cos(q_n t) \frac{\partial p}{\partial s} + q_n \cos(p_m s) \sin(q_n t) \frac{\partial p}{\partial t} - \sqrt{p_m^2 + q_n^2} \cos(p_m s) \cos(q_n t) \right) e^{(-\sqrt{p_m^2 + q_n^2} p(s,t))}$$

with p_m and q_n standing for $\frac{m\pi}{\cos(\theta/2)}$ and $\frac{n\pi}{\sin(\theta/2)}$, respectively.

Evaluating the co-efficients A_{mn} from Eq. (7.15) determines the solute distribution completely. However, as the functions $R_{mn}(s, t)$ are not orthogonal to each other, computing the co-efficients is not as straightforward as it was for the case of planar solid-liquid interface, in section 7.2.1. However, the workaround presented for the lamellar case in section 6.3.1 can be adapted to overcome this. For an efficient implementation of it, we re-represent the component functions of the series in the LHS of Eq. (7.15) by using a single index instead of two. The mapping we adopt, which relates the single and double index representations is as follows.

$$(m, n) \longrightarrow k = m + \frac{(m+n)^2}{4} \quad (7.16a)$$

$$\left(m = k - \left[\sqrt{k} \right]^2, n = 2 \left[\sqrt{k} \right] - m \right) \longleftarrow k \quad (7.16b)$$

where $[\cdot]$ is the operator corresponding to the greatest integer or the floor function. The co-efficients, A_{mn} and the functions $R_{mn}(s, t)$ are renamed to a_k and $r_k(s, t)$, respectively when expressed in the single index notation. Thus, Eq. (7.15) becomes

$$\sum_{k=1}^{\infty} a_k r_k(s, t) = \epsilon w(s, t) \quad (7.17)$$

where $\epsilon w(s, t)$ stands for the RHS of Eq. (7.15). We now present the “recipe” for obtaining the co-efficients a_k . The functions $r_l(s, t)$, $l \in \{1, 2, 3, \dots\}$ are used as test functions and inner products are calculated as shown in Eq.(7.18) to obtain an infinite system of equations linear in a_k .

$$\begin{aligned} \iint_{\text{unit cell}} \left(\sum_{k=1}^{\infty} a_k r_k(s, t) \right) r_l(s, t) ds dt &= \epsilon \iint_{\text{unit cell}} w(s, t) r_l(s, t) ds dt \quad (7.18) \\ \implies \sum_{k=1}^{\infty} a_k \iint_{\text{unit cell}} r_k(s, t) r_l(s, t) ds dt &= \epsilon \iint_{\text{unit cell}} w(s, t) r_l(s, t) ds dt \\ \implies \sum_{k=1}^{\infty} a_k X_{kl} &= \epsilon w_l. \quad (7.19) \end{aligned}$$

The finite reductions of the infinite linear system of Eq. (7.19) when solved, give approximations to a_k . The accuracy of the approximations can be tested by substituting

them into the truncated series of Eq. (7.17) and verifying if it converges to $\epsilon w(s, t)$. The convergence along three sample directions $(1, 0)$, $(1/\sqrt{2}, 1/\sqrt{2})$ and $(0, 1)$ of the s - t plane is shown in Fig. 7.3 for one of the transformation fronts obtained in the rectangular unit cell simulations of section 5.4.2. The steady state solid-liquid surfaces of simulations are fit to appropriate mathematical functions (see sections 7.2.3 and 8.2), and the latter are used as $p(s, t)$ for the calculations. Though the convergence of the approximation

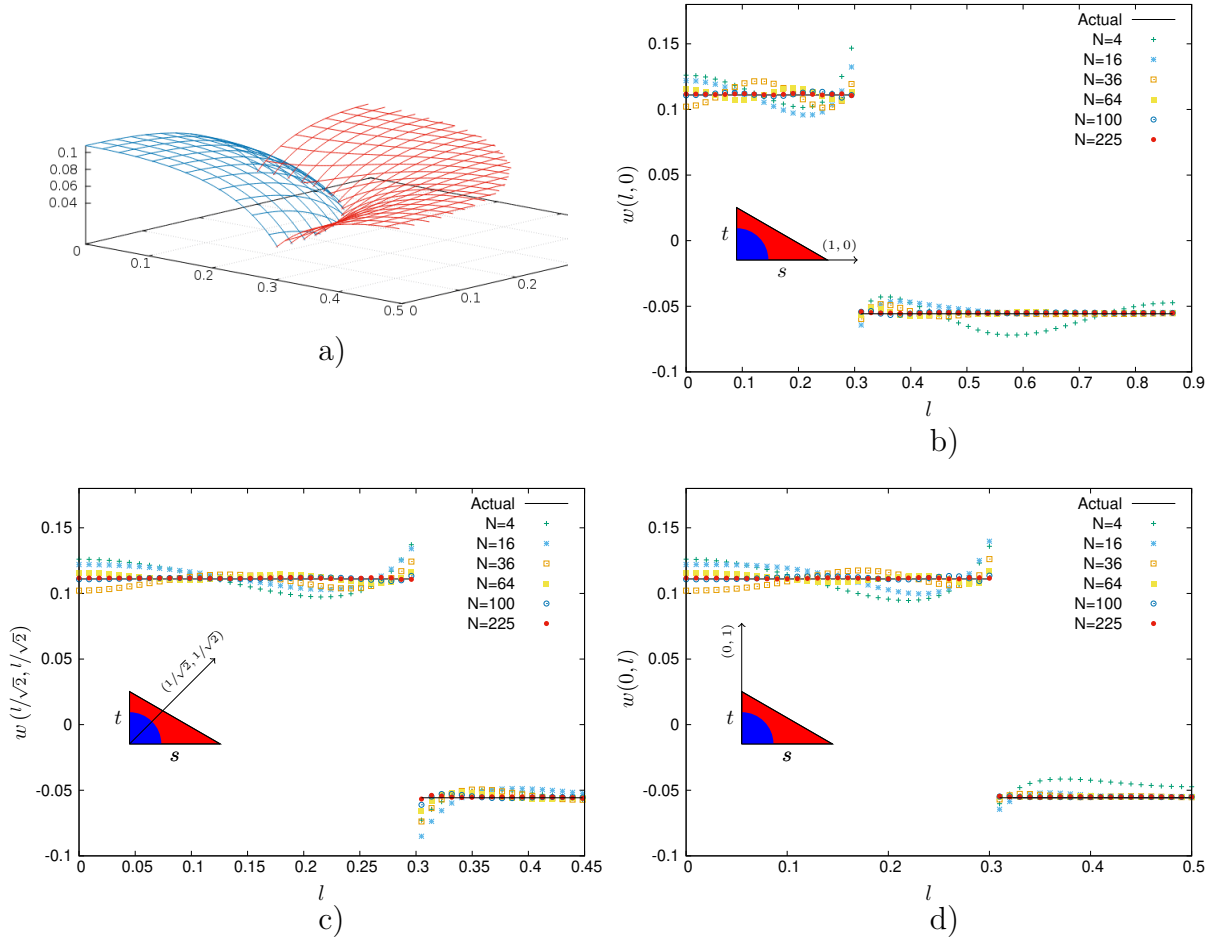


Figure 7.3: a): One of the solidification surfaces obtained in the simulations of section 5.4.2. The red mesh corresponds to the rod phase and the blue one to the matrix. Surface within a distance of $\lambda/2$ from the rod center is only depicted. b), c) and d): The function $w(s, t)$ and its reconstruction from the first N number of terms of the approximated series of Eq. (7.17) along three sample directions for various N .

method is demonstrated using one profile of the study, similar behaviors are observed in the case of all the other profiles. It must be highlighted that the finite reductions of the infinite system are considered in such a manner that the corresponding truncated series of Eq. (7.17) has a perfect square number of terms. Such a truncation along with the mapping Eq. (7.16) guarantees that the contributions from the terms of the series of

Eq. (7.3) are accommodated symmetrically with respect to the indices m and n . The approximated co-efficients when transformed to double index notation and substituted into the appropriately truncated series of Eq. (7.6) give an approximation to the steady state solute distribution of Eq. (7.6).

Thus, to borrow the terminology introduced in the last chapter, the ZOLPA solute distribution of rod growth is estimated by this point, albeit except for the plane-wave component.

7.2.3 Improved kinetics relation

The algebra for obtaining the ZOLPA plane wave coefficient and the accompanying $v - \lambda - \Delta T$ relation from the averaged Gibbs-Thomson conditions is the exact same as for the lamellar growth presented in section 6.19. Hence they are given by the same formulae of Eqs. (6.19) and (6.20) except for the obvious adjustments of the definitions of g_ν and ζ_1^ν in the following manner.

$$g_\nu = \frac{1}{\eta_\nu A_{\text{unit cell}}} \iint_\nu p(s, t) ds dt \quad \text{and} \quad (7.20)$$

$$\zeta_1^\nu = \frac{1}{\eta_\nu A_{\text{unit cell}}} \sum_{\substack{m=0, n=0 \\ (m, n) \neq (0, 0) \\ (m+n) \equiv 0 \pmod{2}}}^{\infty, \infty} \frac{A_{mn}}{\epsilon} \iint_\nu \cos(p_m) \cos(q_n) e^{-\kappa_{mn} p(s, t)} ds dt \quad (7.21)$$

where the region of integration is over all (s, t) corresponding to which solid phase ν is in contact with the liquid at the transformation front within a unit cell and $A_{\text{unit cell}}$ is the latter's area.

The terms $\langle \kappa \rangle_\alpha$ and $\langle \kappa \rangle_\beta$, the average curvatures of rod-liquid and matrix-liquid surfaces in a representative unit need some special attention: Jackson and Hunt have derived explicit expressions for these average curvatures which can be written as

$$\langle \kappa \rangle_\alpha = \frac{2\pi r_\alpha}{\eta_\alpha A_{\text{unit cell}}} \sin \theta_\alpha, \quad \langle \kappa \rangle_\beta = \frac{2\pi r_\alpha}{\eta_\beta A_{\text{unit cell}}} \sin \theta_\beta \quad (7.22)$$

with θ_α and θ_β denoting the acute angles made with the horizontal at the triple junction by the α and β surfaces, respectively. However, these expressions are valid only when the shapes of the rod-liquid and matrix-liquid interfaces are differentiable surfaces of revolution with the additional requirement that the matrix surface flattens out towards the boundaries of the representative unit. In the present case, the expression for $\langle \kappa \rangle_\alpha$ is accurate as the rods are cylinders making circularly symmetric smooth interfaces with the liquid. In contrast, the matrix phase β does not exhibit azimuthal symmetry, and hence the expression for $\langle \kappa \rangle_\beta$ is not entirely faithful. However, as the rods are circular, in the

close vicinity of the rods, the matrix is also circularly symmetric, which breaks down to a hexagonal symmetry as one goes away from them. For the current system, it is found that the breakdown is rather meagre; moreover, away from a rod, though the matrix surface is not completely planar within a single unit cell, it is not much curved either (refer to supplementary material). Hence, we make an approximation that it is a surface of revolution up to a distance of half the rod spacing where it flattens out smoothly and remains so until it approaches within $\lambda/2$ distance of a neighboring rod*. Therefore, we use the same expressions for $\langle \kappa \rangle_\alpha$ and $\langle \kappa \rangle_\beta$ as given in Eq. (7.22). As a result of which, the kinetics relations of the classical and the current extended JH theories become identical except for the square bracket term in the denominator, which, in keeping with the terminology of the last chapter, we refer to as geometric factor. Thus, a comparison of the kinetics predicted by both the theories essentially reduces to a comparison of the respective geometric factors. For the special case of planar solidification front, the geometric factor of the extended theory can be determined analytically: g_ν identically vanishes, and ζ_1^ν can be calculated from Eq. (7.12) and the calculations leading to it. The resulting expression reads as

$$\sum_{\substack{m=0, n=0 \\ (m,n) \neq (0,0) \\ (m+n) \equiv 0 \pmod{2}}}^{\infty, \infty} \frac{J_1^2(r_\alpha \kappa_{mn})}{\kappa_{mn}^3 (1 + \delta_{m0} + \delta_{n0})} \frac{16\pi(c^\beta - c^\alpha)}{\sin \theta} \left(1 + \frac{\eta_\alpha}{\eta_\beta}\right). \quad (7.23)$$

When $\theta = \pi/3$, we refer to the expression of Eq. (7.23) as $(G.F)_{\text{planar-hex}}$ as it corresponds to the geometric factor of the hexagonal symmetry respecting theory for the case of planar solid-liquid surface. The curved counterpart is named as $(G.F)_{\text{curved-hex}}$. The geometric factor of the classical theory for hexagonal arrangement of rods is already presented in this thesis in a different context and is the expression of Eq. (5.7). Note that while Bessel functions J_1 are present in both $(G.F)_{\text{classical}}$ and $(G.F)_{\text{planar-hex}}$, J_0 occur only in the former. A reasoning can be provided for this in the following manner: First of all, it must be noted that Bessel functions characterize circular symmetries. Next, a close inspection of the carried out analysis reveals that functions J_1 are the outcome of calculations pertaining to the rods, while functions J_0 correspond to the representative unit. Therefore, given that both the classical and extended theories consider circular rods whereas only the former employs circular representative unit, “more number” of ‘ J ’s occur in its expression. Also, the presence of two indices in $(G.F)_{\text{planar-hex}}$, but a single index in $(G.F)_{\text{classical}}$ can be traced back to the elimination of a dimension from the problem of determining solute distribution due to the implementation of circular symmetry in the classical theory.

*Implying that although the circular symmetry simplification is relaxed for the unit cell, it is still assumed for the surfaces.

To summarize the analysis carried out thus far in a single sentence, we have provided a prescription for solving the ZOLPA problem pertaining to the rod growth. At the same stage in the lamellar case, a recipe for predicting the self-consistent solidification front shapes is put forth. Implementing which was practical as it required only performing an integration (be it numerical), however, the counterpart procedure for the rod growth involves solving a highly non-linear boundary value problem in non-trivial geometries. Since this is a very formidable task, we stop our program of refining the JH theory of rod growth here.

Next, we proceed on to the concluding segment of the thesis where the comparisons between the simulated co-operative dynamics and the final JH predictions, i.e., after incorporating the improvements of the last two chapters, will be presented.

Part IV

Post-refinement comparisons

Chapter 8

Final comparisons and discussion

When the phase-field generated eutectic growth kinetics results are last compared with the JH theory predictions in chapter 5 and appendix E, the over-simplifying assumptions of the classical analysis were present in the latter. Since these are claimed to have been relaxed in the last two chapters, the new comparisons will now be looked at. Along with it, a comparison of the simulated growth front shapes with the converged profiles of the improved JH theory will also be carried out for the case of lamellar growth.

8.1 Lamellar growth

Figure 8.1 re-collects the lamellar growth v v.s. λ plots of Figs. 5.6, E.7, E.8 and 5.10 with the curvature-informed, self-consistent theory predictions of chapter 6 included in them. First of all, to dispose of the minor detail, the ZOLPA and the unapproximated analyses' results are observed to stay close to each other, the same as in section 6.4.2.1. No matter how small the improvement is, it still has to be acknowledged that the latter are without fail closer to the simulated results than the former. Another quick realization is that after incorporating the curvatures, the direction of the deviation between the computational and the theoretical results is reversed. That is, while the JH analysis kinetics curve stayed below the simulated one when the planar interface assumption is invoked, after relaxing it, it went above. However, for larger wavelengths—in fact not too big compared to the characteristic spacing—the deviation seems to die down and remain so thereafter. Considerable disagreement still exists for lamellar widths around and smaller than λ_{JH} , albeit it is unclear if it will continue all the way until v , or equivalently, the Péclet number becomes zero. In the case of Figs. 5.6 and 8.1a), where the triple junction angles are $\theta_\alpha = 50.1334^\circ$ and $\theta_\beta = 35.1079^\circ$, the relative error between the maximum speeds changed from 14.89% in the former to -4.15% in the latter. However, when the angles

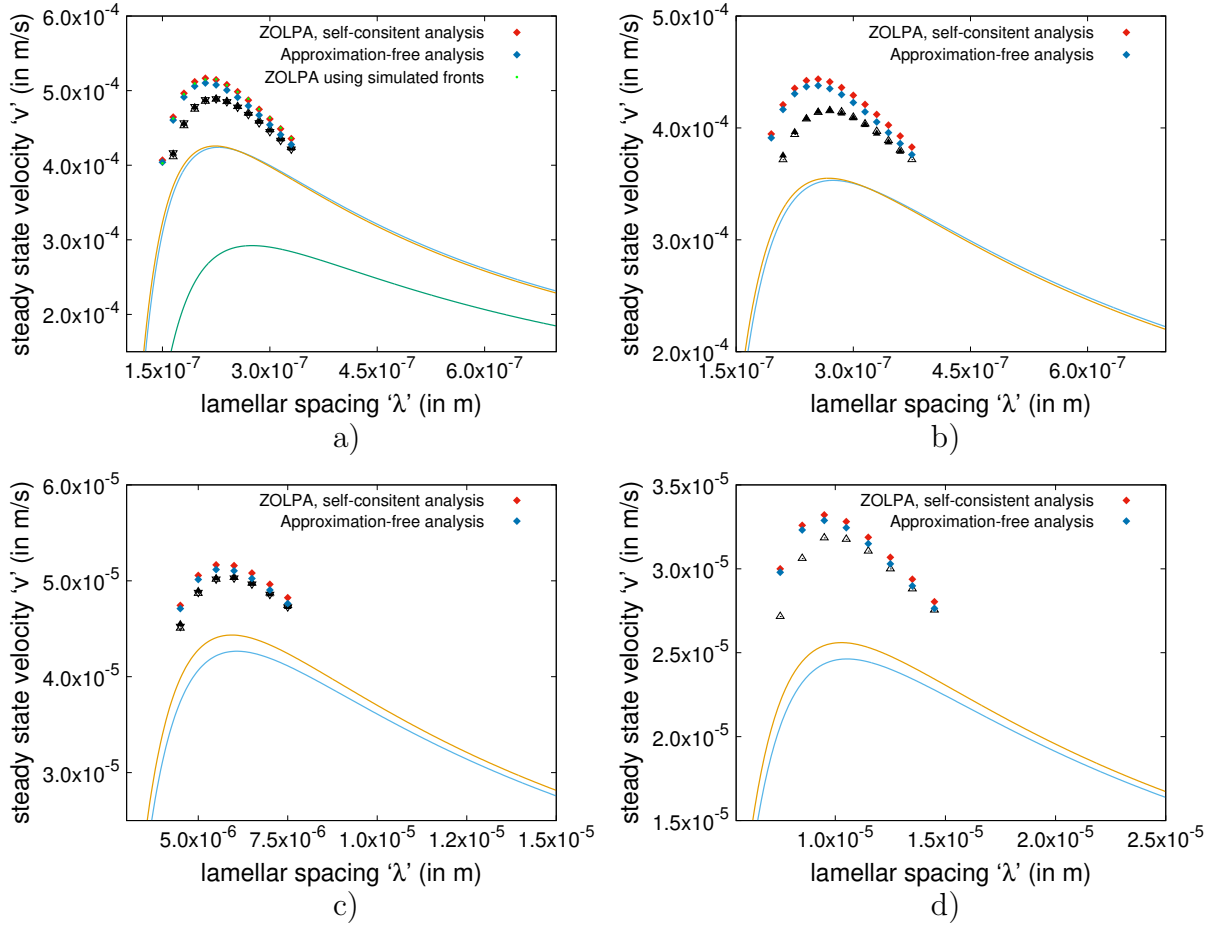


Figure 8.1: Figs. 5.6, E.7, E.8 and 5.10 replotted with the curvature-informed, self-consistent theory predictions of chapter 6 included in them. The subfigures a), b), c) and d) correspond to them in the same order.

are modified to $\theta_\alpha = 59.6492^\circ$ and $\theta_\beta = 49.8438^\circ$, a change from 17.00% to -5.13% is recorded extending from Fig. E.7 to Fig. 8.1b). Similarly, for the Al-AlCu₂ system, when the trijunction angles are 30° each for Fig. 8.1c) and E.8, the gap reduced from 13.43% to -1.69% , while when they are 60° each in Fig. 8.1d) and 5.10, the improvement seen is from 24.37% to -3.16% . In short, it can be safely concluded that the larger the angles at the tri-junctions, the higher is the deviation of the simulations from not only the classical JH analysis but also its ‘any-Peclet number and curvature-informed’ extension. Further, comparing Fig. 8.1a) with 8.1c) and 8.1b) with 8.1d) gives the indication that when the angles subtended by the two phases are dissimilar, the deviation is higher. Moreover, the phase-fractions of the *alpha-Aluminium* and the AlCu₂ phases in the considered eutectic solid are 0.4693 and 0.5307 respectively, hence, the higher the symmetry in the phase diagram and other thermo-physical properties of the constituting solids, the better is the level of agreement between the simulated growth kinetics and the approximation-free JH

analysis, at least for the characteristic spacing and above.

The problematic part, though, is the region to the left of λ_{JH} where higher deviations are clearly apparent, the reason for which is unclear at the moment. One might argue that there is, in fact, no serious issue here at all as it is seen in appendix E especially in Tables E.8 and E.10 that even higher errors could be expected at still higher resolutions depending on the size and the material properties of the system. In particular, in the light of the conclusion reached there that reducing the driving force holding everything else constant slows down the convergence, it can be inferred from Figs. E.3 and E.5 that reducing the grain width alone without changing anything else should also behave in the like manner*. Arguing thus, one might be tempted to conclude that “the larger deviations at smaller lamellar widths seen in the plots of Fig. 8.1 should not be considered so surprising and, in any case, are not final”. Essentially, the standpoint here is that the observed disagreement is a direct consequence of our current inability to go to still smaller interface widths due to computational cost constraints, overcoming which the triangles in the plots merge into the coloured diamonds. However, this may not be the right assessment as the convergence trends of the computational steady state speeds are not similar to those of pure grain evolution within the setup of Fig. 4.1, but are more nearer to those of planar alloy solidification: Note that in Table E.10—an exemplary case of the former—from a resolution of $1\times$ to $4\times$, the steady state speed increased by 6.54% or considering ‘the extent of interface width reduced’ as the parameter of actual relevance, it is above 10.63% for a thickness reduction of $4\times$. In contrast, in the second column of Table E.11, the former counterpart is 0.08% and the latter one is 0.1%. That is, a difference of an order exists in the recovered relative errors between the cases of pure grain growth and the alloy solidification. And, the observed pattern for the eutectic growth, as can be verified from Table E.12, is almost identical to the latter and (hence) no way close to the former. Therefore, it is unlikely that the gaps seen in the plots of Fig. 8.1 for low spacings are an artifact of larger interface widths.

Neither could they be an outcome of a limitation in the theoretical analysis: For one, no more approximations are left un-generalized in the JH extension presented in chapter 6. And secondly, the limit of convergence of the iterative scheme is practically achieved. One might say that the assignment of zero magnitude to the Péclet number for starting off the iterative procedure could be a reason, but it is observed that any other value in the typical range gives back only negligibly different results. Another argument could be that instead of assigning a value to the Péclet number in the first iteration, if it were to be left as an unknown to be determined, different results may be expected. If such were to be the truth, then it will not alter the low lamellar spacings region appreciably, but instead

*Which fact is also verified more explicitly through further simulations not reported in the thesis.

the higher one as the smaller widths are precisely the ones which correspond to the lower Péclet numbers: the typical Péclet number v.s. lamellar spacings plot in a JH theory is as depicted in Fig. 8.2. While, in principle, this may imply that substantial errors should in fact exist all through the curve and not just for smaller widths, it still does not refute the claim that the gap that is currently seen is not because of a limitation in the theoretical analysis. In the same vein, the usage of flat shape for the initial guess can also be held responsible. But, the fact of the matter is that none of this discussion even need be entertained as all these suggestions amount to changing the initial guess which might be helpful only when the problem has multiple solutions which we explicitly operate by under the assumption to not be the case. Note that the Jackson-Hunt problem is nothing more than finding a ' $p(x)$ ', a ' v ' and a ' $c(x, z)$ ' satisfying Eqs. (6.3a)- (6.3i). The form chosen in Eq. (6.6) already ensures that the requirements of Eqs. (6.3a) and (6.3d)-(6.3f) are fulfilled. Next, Eq. (6.3i) is explicitly ensured while reconstructing the profile shape using Eqs. (6.21) and (6.22). Further, that the conditions of Eqs. (6.3b) and (6.3c) are fulfilled is verified by the cross-checks of the kind depicted in Fig. 6.2. Finally, when the profile shape, the steady state speed and the solutal field obtained in the final iteration are substituted back into the right hand sides of Eqs. (6.3g) and (6.3h), the resultant left hand sides are seen to be deviant from the required constant by at most 0.025%[†]. In essence, if the JH problem were to have a unique solution, it is undoubtedly found to a very satisfactory level for all practical purposes.

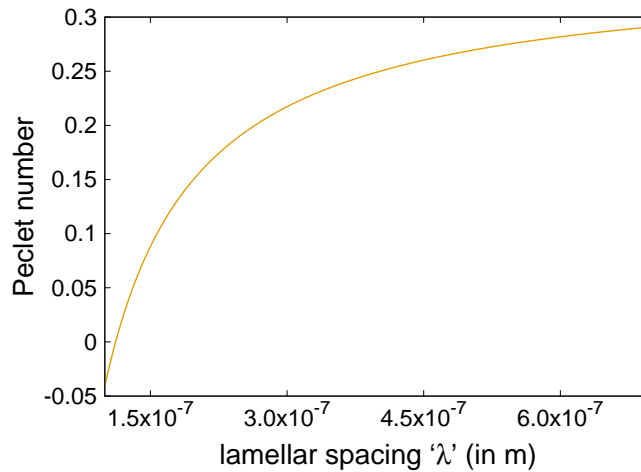


Figure 8.2: Typical Péclet number versus lamellar spacing trend to be expected at steady state in directional (lamellar) eutectic growth as predicted by the Jackson-Hunt analysis.

All of the above discussion goes to point that some detail is left unrefined in the

[†]Moreover this percentage is recovered for the largest lamellar spacing numerically studied in Fig. 8.1a), for the one on the other extreme it is even less at 0.01%, consistent with the low Péclet number approximation.

phase-field treatment of the problem or in appropriately connecting the sharp interface calculations to it. Given that the alloy solidification case not involving triple junctions and the three-grain evolution problem not involving an additional composition field separately gave quite satisfactory results, the only aspect that remains to be looked at more closely is the interaction of the chemical potential field with the triple junction. In particular, in the case of binary interfaces, up to three orders are worked out in the matched asymptotic analysis to come up with the right thin-interface limit corrections and anti-trapping current term prescriptions for establishing the appropriate kinetics laws. Whereas, for triple junctions, no such analysis is performed. Though the junction regions are extensively studied in the current thesis, all the analysis has been on the governing equations pertaining to the phase-indicator field but not the chemical potential field. In fact, the local analysis of appendix D up to the leading order can be easily expanded to include the triple point as well, and, the constancy of chemical potential—the same as for the binary interfaces—will indeed turn out to be the outcome. Whereas, nothing is readily evident about the remaining orders. Could it turn out that the $\tau(\phi)$ and the anti-trapping terms must be further modified to cater to the demands of the junction regions? That is, could it happen that the triple point needs its own thin-interface correction and experiences a chemical potential jump as a result of which would require its own anti-trapping current term? Note that the prime reason for having these currently is the demand for capturing the infinite kinetics of attachment of the binary interfaces, i.e., a particular form of a law is being chased after. However, we don't have a target in mind for how the kinetics law should look like for triple points in alloys. Even the pure grain growth version is not written down in its most reduced form but with integrals and limits involving phase-indicator field still appearing in them, in Eqs. 3.48 and 3.49. That the latter should together give $v_x = 0$ and v_y satisfying Eq. C.3 for the systems typified by Fig. 4.1 is claimed by observing the highly convincing presence of a steady state in the simulations but not the other way around (if a different relation were to arise, a steady state wouldn't be possible). Assuming a similar state of affairs for alloy triple points, i.e., assuming that the required condition—whatever it may be—is automatically fulfilled, the non-prescription of thin-interface correction will only mean that the rate of convergence is reduced. Similarly, if the chemical potential jump were to exist around the junction, since it can only happen due to the next order term, not correcting it will only delay the convergence but not change the limiting behavior. That means, the argument went full circle to connect back the gaps in the left side regions of the plots of Fig. 8.1 to the inability to reduce the interface width further. Of course, the preceding analysis is presented by having multi-well models at the back of mind whereas the actual calculations of the plots are carried out employing obstacle potential model. However, as already mentioned, a matching analysis is not possible for such model due to Gibbs-simplex projection at the junctions. Since

the latter has no direct contact with the chemical potential evolution equation and since it did not affect adversely in the simple grain growth case, one can expect that the same might hold in the eutectic solidification model as well. However, as the indirect influence is hard to fathom, this cannot be claimed with enough certainty.

This leaves us with making the right connections between the diffuse and the sharp interface treatments. Recall that only after the exact slope formula as recovered in the asymptotic limit problem of the phase-field model is utilized for the Jackson-Hunt calculations did the gaps reduce in chapter 5. In the similar manner, one might ask, if there is anything else that is different in the vanishing interface width limit of the employed phase-field model and the solved JH equations. The only assumption that is left which is repeatedly made in the asymptotic analysis is replacing any value in between $\tilde{\mu}^{(0)}$ and μ_{eq} , i.e., the zeroth order term in the local expansion of the chemical potential at a binary interface and the equilibrium value of the involving phase-pair, respectively, with the latter value (see appendix D or Ref. [23]). However, if that were to be such a far-fetched approximation, its effects would have already showed up in the planar alloy-solidification problem which is not the case.

Thus, to sum up, the origin of the deviation between the phase-field and the analytical results of the plots of Fig. 8.1 is very unclear at the moment. The only suggestion currently available is to re-do the studies on a completely symmetric toy-model system employing a multi-well formulation and continue therefrom to see the effects of various asymmetries and the switch to the obstacle potential implementation.

Next, we compare the simulated and the analytically predicted solidification front shapes. Fig. 8.3 collects the self-consistent profiles of the approximation-free JH theory and the simulated ones corresponding to the triangles of Fig. 8.1a) or 5.6. While for the NiZr side of the plots the convergence is self-evident, for the NiZr₂ phase, some of the plots do give the impression that the coloured profiles may converge to a different curve lying slightly above the dark one. This also tallies with our suspicion in section 5.4.1.2, namely, that θ_β seems to be converging to value slightly higher than the required value of 35.1079°. Of course, the deviation of the simulated junction angles by 1 or 2 degrees is not a very reliable indicator and can be easily overlooked, as, such a difference can very well be arising from the method adopted to measure them. For instance, the degree of the polynomial used for fitting the simulated profiles can easily affect the value to such an extent. Hence, it is important to carry out the entire interface shape comparisons which here reveal that the convergence behavior is not as orderly in the eutectic growth case as when the chemical potential field was absent.

We now move on to the comparisons for the rod-growth.

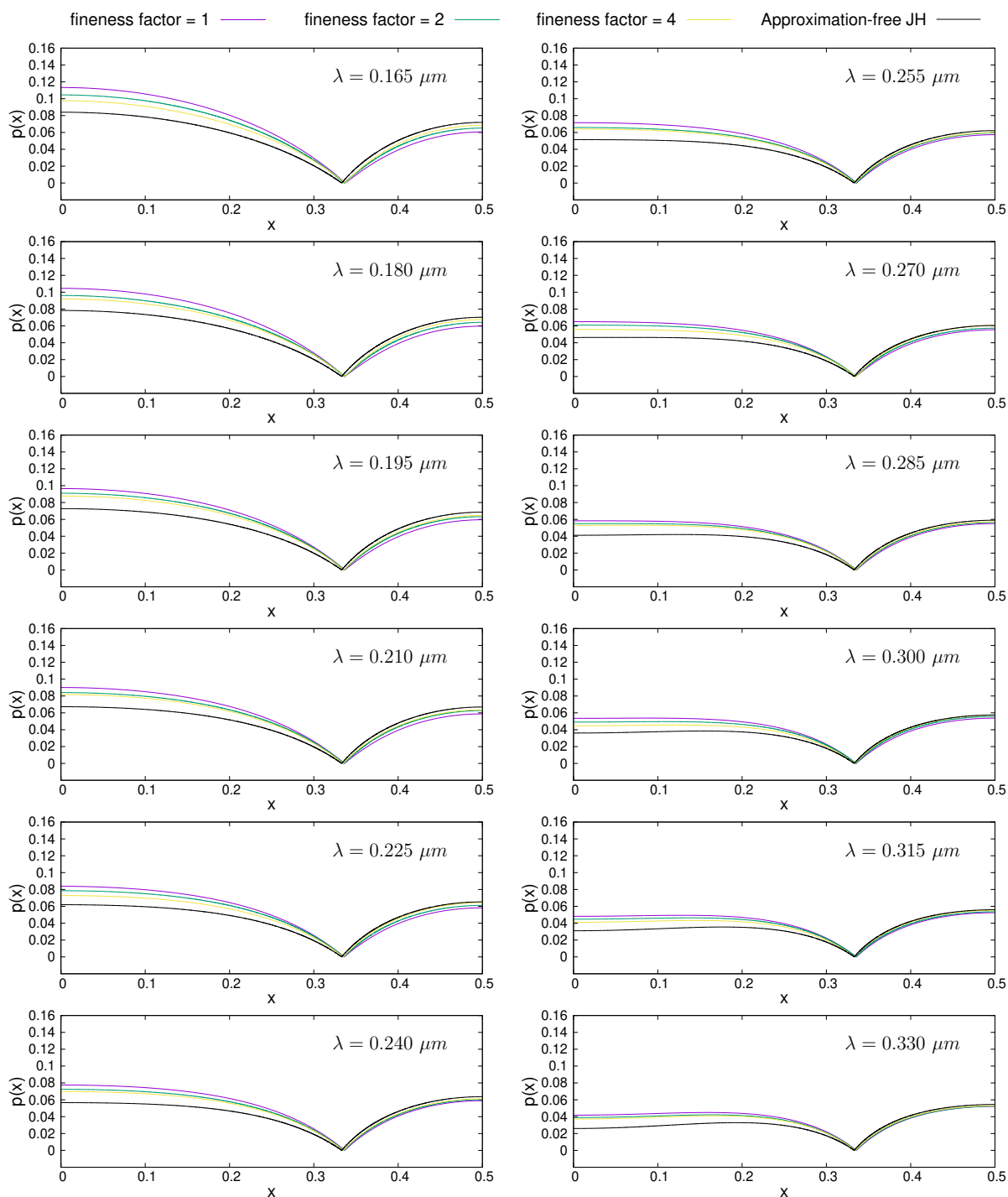


Figure 8.3: The steady state growth fronts recovered in the lamellar growth simulations of section 5.4.1.2 along with the respective converged profiles obtained through the iterative scheme of the extended JH analysis of section 6.4.1. The highest resolution front of the case $\lambda = 0.240 \mu\text{m}$, i.e., the yellow profile is precisely the one used for the convergence verification of Fig. 6.2.

8.2 Rod growth

Note that in our approach of relaxing the zeroth order and the low Péclet number approximations, re-prediction of solidification growth front shape in each iteration is indispensable. Since this is quite a formidable task for the case of rod growth, we confined ourselves in chapter 7 to merely the ZOLPA problem. However, the latter involves a pre-given profile shape which, in the case of stoichiometric systems, should in addition be consistent with the phase fractions which are pre-calculable. For the current comparisons, we first choose the shape as a planar front and next utilize the ones obtained from the simulations. It must be recalled that the former does not imply that it is the same as the classical theory calculation as the circular representative unit is replaced by an accurate one in the analysis of chapter 7. That is, first we compare the predictions of classical theory with those of the planar-hexagonal one and then with the latter's curved extension.

It was demonstrated in section 7.2.3 that a comparison of the classical, planar-hexagonal and the curved-hexagonal results is the same as comparing their respective geometric factors, the first two of which are given by Eqs. (5.7) and (7.23). Plugging the values corresponding to the NiZr-NiZr₂ system from Table 5.7 in these gave the following magnitudes:

$$GF_{\text{classical}} = 1.898446 \quad \text{and} \quad GF_{\text{planar-hex}} = 1.895185. \quad (8.1)$$

Note how small the difference between the two is, implying that the growth speeds predicted by the improved theory for planar case are almost the same as the classical ones. These are compared as functions of rod spacing in Fig. 8.5 where the graphs of Fig. 5.8 are reproduced. In short, it turns out that the circular representative unit approximation of the classical theory is indeed quite a good simplification, and hence, after all, the right symmetry incorporation does not improve the agreement between the computational and the theoretical ' v versus λ ' curves.

The outcome is different with the curvature incorporation, though. The scaled transformation fronts obtained in the higher resolution simulations of section 5.4.2 are fit to functions $a_{\text{rod}}(\sqrt{s^2 + t^2})^8 + b_{\text{rod}}(\sqrt{s^2 + t^2})^6 + c_{\text{rod}}(\sqrt{s^2 + t^2})^4 + d_{\text{rod}}(\sqrt{s^2 + t^2})^2 + e_{\text{rod}}$ for rods and—since the circular to hexagonal symmetry breakdown is rather meager— $a_{\text{matrix}}(\sqrt{s^2 + t^2} - 0.5)^8 + b_{\text{matrix}}(\sqrt{s^2 + t^2} - 0.5)^6 + c_{\text{matrix}}(\sqrt{s^2 + t^2} - 0.5)^4 + d_{\text{matrix}}(\sqrt{s^2 + t^2} - 0.5)^2 + e_{\text{matrix}}$ for matrix. These fits along with the originally simulated $\phi_\alpha = \phi_l = 0.5$ and the $\phi_\beta = \phi_l = 0.5$ surfaces are plotted in Fig. 8.4 (the same fitting was used for Fig. 7.3a) which is nothing but the $\lambda = 0.270 \mu\text{m}$ case of the figure). Thus, with the $p(s, t)$ for each simulated case at our disposal, the associated ' $(G.F)_{\text{curved-hex}}$'s are evaluated following the routine of section 7.2.2 and are tabulated in Table 8.1. The associated

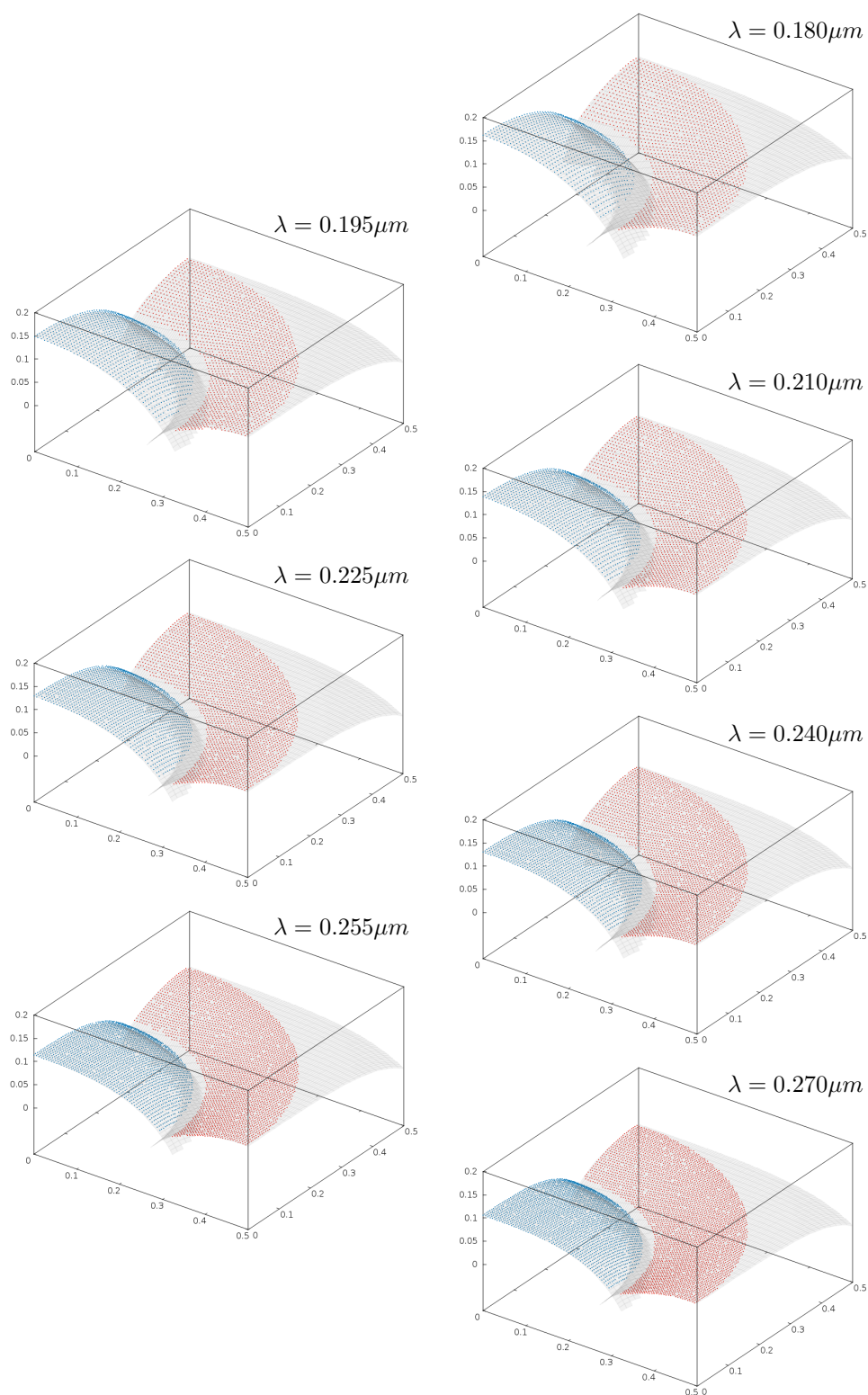


Figure 8.4: The solidification fronts of the rod growth simulations of section 5.4.2 and their fitting. The blue surfaces correspond to rod forming NiZr phase and the red ones to that of matrix forming NiZr_2 phase. The grey surfaces are the fits (whose forms are as given in the main text).

specific velocity numbers which are defined as the ratios of the velocities predicted by the curved-hexagonal theory to those by the planar-hexagonal one are also listed; the growth speeds are plotted in Fig. 8.5.

Table 8.1: Table showing the effect of curvature incorporation on the Jackson-Hunt analysis predicted growth kinetics for the investigated rod spacings and simulated surfaces of section 5.4.2.2.

Rod spacing ($\times 10^{-7}$ m)	$(G.F)_{\text{curved-hex}}$	specific velocity number
1.80	1.439072×10^{-2}	1.316950
1.95	1.458644×10^{-2}	1.299279
2.10	1.476743×10^{-2}	1.283355
2.25	1.494807×10^{-2}	1.267846
2.40	1.513830×10^{-2}	1.251914
2.55	1.532048×10^{-2}	1.237027
2.70	1.550581×10^{-2}	1.222242

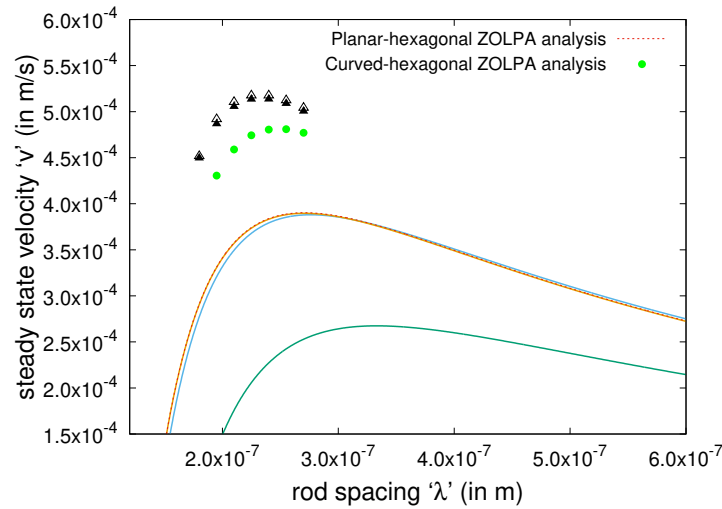


Figure 8.5: Fig. 5.8 replotted along with the predictions of the curvature-informed JH analysis of chapter 7.

An immediate difference that strikes is that unlike the lamellar case, the JH kinetics plot still stays below the simulated one even after curvature incorporation. More specifically, the deviation of the simulated maximum velocity from the analytically predicted value reduced from 31.570% to 6.769% after accounting for the curvedness of solidification front, but did not drop further into negative values as in the lamellar case. One may be tempted to conclude that this is because of the usage of simulated front shapes rather

than the self-consistent ones. However, this is very unlikely as carrying out the same analysis for the lamellar case, i.e., solving the ZOLPA problem by utilizing the growth fronts from the (highest resolution) simulations, yielded only negligibly different results as indicated by the green dots of Fig. 8.1a). That means, the differences in the profile shapes of the order seen for the depictions of Fig. 8.3, do not alter the outcome (predicted steady state speeds) appreciably. Assuming that even for the rod-growth the computed solidification fronts deviate from the self-consistent ones (if they are somehow estimated) by similar amounts, it can be concluded that the disagreement between the triangles and the green dots of Fig. 8.5 cannot be arising from the replacement of approximation-free treatment by the ZOLPA one. Similarly, the usage of azimuthal symmetry for the matrix surface instead of a strictly hexagonal one, although plays its part, can be considered to be insubstantial in the light of the good agreement seen between the extracted surfaces and their “isotropic fits” in Fig. 8.4.

Hence, same as in the lamellar case, the still lingering deviation between the predictions of the computational and the analytical treatments is unclear, and, at the most, the obstacle implementation may be suspected to be the culprit which has to be verified by re-doing the simulations with a well potential for a symmetric toy-model system.

Before moving on to the next section, we direct the attention of the reader to Ref. [92], where a huge disagreement, much higher than the 6 – 7% reported here, was recorded between the simulated rod-growth kinetics and the curved-hexagonal ZOLPA solution for the same material system. However, by the time of this study, none of the insights which are the fruits of the investigations of the current research were available. Hence, the precautionary measures proposed in chapters 3 through 7 are not followed in performing and comparing the theoretical and the analytical investigations of Ref. [92]. In particular, instead of the decisively better choice of harmonic form of inverse mobility interpolation, the arithmetic one is implemented. The solid-solid inverse mobility was a few hundred times larger than the solid-liquid ones and the resolution was also not high; in fact, it is exactly the same as the lower one considered in the current thesis. Hence, the speeds retrieved must be significantly off from the ones corresponding to the vanishing interface width limit. In the like manner, it should also mean and indeed is seen to be true that the angles recovered were not as per the Young’s law. Although the ones obtained in the simulation studies itself were used for the JH calculations, the slope formulae utilized were not as per the correct choice, i.e., Eq. (5.10). Further, because of using only 150 – 250 sample points while extracting the data from CALPHAD database through PANDAT, the error between the calculated liquidii slopes and the ones that should have actually been used is very large. All these factors together gave rise to the poor comparisons of Ref. [92]. In fact, it is these huge mismatches that stirred up an interest in looking at the details of this problem more closely which finally led to part II of the current thesis.

Part V
Summary and conclusion

Chapter 9

Summary and conclusion

The problem of cooperative growth in binary alloys lies at the transition point of pure grain growth and single phase solidification phenomena on one side, and, the multi-phase multi-component microstructural evolution on the other*. Particularly, the directional eutectic growth sub-case, being the simplest and supporting a steady state behavior, serves as an ideal benchmark case for validating the quantitative phase-field models of the latter. Though many diffuse-interface treatments of this problem exist, all of them leave something to be desired which have all been furnished in the current thesis.

For instance, it is well known that ensuring a separate control of bulk and interfacial properties is quite advantageous as it allows an easy prescription of thin-interface limit corrections. Although many models now-a-days accordingly avail this benefit, the so-called coarse-graining derivations among them still adopt the older argumentation of a) dissipation with regard to phase-indicator evolution and b) Fick's law connections for prescribing mass transport governing equations. The problem with this is that it is often criticized to be ad-hoc and not emerging from the thermodynamical first principles. Though not explicit, an algorithm has essentially been carved out for rectifying this by Wang *et al.* [28], however, attempts to re-cast the derivation as per their suggestions have never been carried out. Furthermore, it is shown in the present thesis that the current two-argument derivations of alloy growth models even fail to accomplish the decoupling when extended to non-isothermal processes. Hence, a fresh formulation is advanced in the present dissertation which invokes a simple initial set of hypothesis which itself has some thermodynamical promptings behind it along with the progression of the derivation. Also, it is demonstrated that the algorithm of Ref. [28], when explicitly interpreted to be invoking the same set of hypothesis, is immediately rendered generic. Thus, refining and unifying the model derivation is the first accomplishment of the thesis.

*Of course, when an enhanced surface diffusion is absent and convection in liquids can be ignored etc.

The notion of dynamical Young's law has been a topic of debate among experimentalists and theoreticians alike. Basically, the question is whether or not Young's law is fulfilled when the common meeting point of the three involved interfaces is in motion. Even in phase-field community, a common consensus does not exist. Some research works conclude that the mobilities of the interfaces have an effect on the angles subtended around a moving trijunction [52, 93, 94] while some other claim to have witnessed an influence of bulk driving forces. Performing an asymptotic analysis of the multi-phase-field model in its full detail will settle the issue. However, typically, the local analysis of the binary interfaces is performed after reducing the multi-phase-field equations to two-phase ones, and, the local analysis of the junction points is left unperformed. This is the next shortcoming that is removed in the current work. A full-fledged asymptotic analysis of the entire vector valued phase-indicator field is carried out and the outcome is the following. For the mobility, bulk energy and gradient energy dependencies on the interface width parameter typically chosen in the standard solidification models, the angles around a trijunction are always the same whether or not it is in motion. In fact, this has already been shown by Bronsard *et al.* [30]; however, their analysis which was specific for three-component phase-field variable is extended to any higher dimensional one here and for junctions of any order.

A question next arises: if Young's law should be satisfied irregardless of the junction's speed, then what explains the heretofore observed dependence on mobilities? The answer, unsurprisingly, happens to be the thickness of the interface (or the area of spread of the junction), reducing which the deviation decreases and the Young's law is eventually regained. However, the popularly adopted prescription for conducting the interface width reduction studies is shown in the current thesis to be inefficacious. The reason is identified and the remedy is proposed. Still, a thickness reduction of up to 25 times is seen to be required for the parameter sets studied implying a severe tax on the computational resources and time. The main source of this is identified to be the arithmetic form of inverse mobilities' interpolation replacing which by a harmonic one has produced satisfactory results without even requiring any interface width reduction. However, this is very problem specific in the sense that the instantaneous direction of motion of the trijunction has a huge say in what kind of mobility formulation will be cost-effective. Hence, a prescription which is universally superior is yet to be conceived. It has to be mentioned at this juncture that the arithmetic to harmonic type switch was also proposed previously in Ref. [93], however, it is independently figured out and proposed in the current thesis. Moreover, in Refs. [93, 94], it is thought that the effects produced by various interpolations are final, i.e., not interface width artifacts in any of the cases. Whereas, as mentioned, the asymptotic analysis reveals the actual truth to be otherwise.

Thus, with all the refinements furnished in the phase-field treatment of eutectic

growth, the focus is diverted towards relaxing the approximations invoked in its sharp-interface treatment, namely, the Jackson-Hunt analysis. It is well known that apart from the approximations related to the smallness of the Péclet number, the assumption of planar solidification front is a major limitation of this celebrated theory. The main problem with any other shape is that the Fourier series method cannot be readily executed for estimating the concentration fields as it will now require handling non-orthogonal basis functions. However, it is shown that choosing an appropriate set of test functions, a linear system of equations can be generated from the boundary condition pertaining to the curved front, solving which, the solution can be estimated to any desired level of accuracy. Also, an iterative scheme is devised for predicting the self-consistent growth-front shapes while simultaneously relieving the restriction to small growth speeds. This method of finding the solution is much cheaper and less complicated compared to the previously employed alternatives like the completely numerical approach of boundary-integral method or the electrical analogue technique. In the case of rod-growth, approximation affecting the proper accounting of rotational symmetry of the fiber distribution within the matrix is also relaxed, but the consequent improvement brought about was not as substantial as that by the curvature incorporation.

Thus, with the theoretical and computational methods refined, their predictions are next compared, however, it turned out that an *exact* overlap between the Jackson-Hunt problem and the asymptotic limit of the phase-field model demands choosing the liquidii slopes entering the former analysis in a very specific manner. Otherwise, the number of sample points specified for extracting the free-energy v.s. composition data from the CALPHAD databases through software packages like PANDAT may accentuate the mismatch between the recovered results.

The comparison of the results indeed revealed that the agreement is better post the above mentioned refinements. However, a deviation still exists between the computational and the analytical steady-state kinetics (v versus λ) curves for lamellar widths smaller than the characteristic one (λ_{JH}), and the disagreement is observed to increase as the spacings reduce. Likewise is the behavior of rod-growth except that the sign of the errors is opposite. The reason for such deviations is not entirely clear as of now. Of course, it would have been even more surprising had they been recovered with well potentials. In the current work, while the asymptotic analysis is performed on modeling equations employing multi-wells and their mapping onto the Jackson-Hunt problem is explicitly shown, the eutectic growth simulations are however not performed with them; instead, obstacle implementations were utilized. And the latter, unfortunately, cannot be mathematically analyzed in order to predict their limiting behavior due to some difficulties presented by the user interference. Hence, if at all the observed deviations can be ascribed to anything, as of now, it can only be to the usage of obstacle implementations.

Therefore, the conclusion is to re-perform the simulations first with a multi-well, and that too on a model system with complete symmetry among all the three phases, and then continue therefrom to introduce asymmetry and the switch to obstacle potential. Such a systematic study will help attribute the observed disagreement more decisively and accurately, and hence can potentially help eliminate it.

Part VI
Appendices

Appendix A

Appendices to chapter 2

A.1 Clarifications on the terminology

Even though the volumetric densities of extensive quantities are intensive, it is a common practice in the phase-field solidification community to continue calling them as extensive and reserve the latter word for their conjugate variables. Hence, in this terminology, quantities like entropy and energy densities or number densities are referred to as extensive quantities and temperature, chemical potentials etc are referred to as intensive thermodynamic variables. Further deviations from the standard terminology do exist as detailed below.

Consider the following fundamental relation for a homogeneous alloy composed of A and B atoms.

$$S = \frac{1}{T}E + \frac{P}{T}V - \frac{\mu_A}{T}N_A - \frac{\mu_B}{T}N_B \quad (\text{A.1})$$

where the various terms have the standard definitions. In particular, μ_A and μ_B are the chemical potentials of the A and B atoms in the alloy, respectively. Dividing the above equation with the volume of the system gives the relation in terms of per unit volume quantities:

$$\begin{aligned} \frac{S}{V} &= \frac{1}{T} \frac{E}{V} + \frac{P}{T} - \frac{\mu_A}{T} \frac{N_A}{V} - \frac{\mu_B}{T} \frac{N_B}{V} \\ \implies s &= \frac{1}{T}e + \frac{P}{T} - \frac{\mu_A}{T}\rho_A - \frac{\mu_B}{T}\rho_B \\ &= \frac{1}{T}e + \frac{P}{T} - \frac{(\mu_A - \mu_B)}{T}\rho_A - \frac{\mu_B}{T}(\rho_A + \rho_B) \\ \implies s &= \frac{1}{T}e + \frac{P}{T} - \frac{(\mu_A - \mu_B)}{T}\rho_A - \frac{\mu_B}{T}\rho \end{aligned} \quad (\text{A.2})$$

where ρ_A and ρ_B are the number densities of A and B species, respectively, and ρ is that of the A and B atoms considered together. Hence, $\rho_A = c\rho$ where c is the mole fraction

of A atoms. Re-arranging the terms of the above equation, we have

$$e - Ts - (\mu_A - \mu_B)c\rho = -P + \mu_B\rho. \quad (\text{A.3})$$

In regard to the above equation, the following nomenclature is employed: the term $\mu_A - \mu_B$ in Eq. (A.3) is referred to as the “chemical potential” and is denoted by μ . Even though the term chemical potential without any further qualifier referring to the species is not meaningful in case of multicomponent systems, using it to refer to the difference of μ_A and μ_B in case of binary alloys is a common practice in phase-field community. Similarly, we call the term $-P + \mu_B\rho$ as the “grand potential density” and denote it by ω even though the actual definition implies the quantity $e - Ts - \mu_A\rho_A - \mu_B\rho_B$.

A.2 Thermodynamic consistency and generality of the framework of Ref. [18] (and [23])

In this section, the thermodynamic consistency and the generality of the formulations presented in Refs. [18] and [23] are tested.

A.2.1 Thermodynamic consistency of the grand-potential model

To model isothermal rigid alloy solidification, Plapp’s approach considered the grand potential functional as the starting point. However, for thermodynamic consistency, it is mandatory that the local Helmholtz free energy production rate in the system has to be negative. Whether the formulation is consistent with this behavior or not is now tested. From the grand-potential functional of Ref. [18], using various relations utilized there, the free energy functional can be readily back-constructed which in the notation of the current thesis reads

$$F = \int \left(f_s(\mu)\mathbf{q}_s(\phi) + f_l(\mu)\mathbf{q}_l(\phi) + f_{\text{dw}}(\phi) + \frac{f_G}{2}(\nabla\phi)^2 \right) dV. \quad (\text{A.4})$$

Differentiating Eq. (A.4) with respect to time yields

$$\begin{aligned} \frac{dF}{dt} &= \int \left(\frac{\partial f_s}{\partial \mu}\mathbf{q}_s(\phi) + \frac{\partial f_l}{\partial \mu}\mathbf{q}_l(\phi) \right) \frac{\partial \mu}{\partial t} dV \\ &\quad + \int \left((f_s - f_l)\mathbf{q}'_s(\phi) + f'_{\text{dw}}(\phi) - f_G(\nabla^2\phi) \right) \frac{\partial \phi}{\partial t} dV + \text{boundary terms} \\ \implies \\ \frac{dF}{dt} &= \int \left(\frac{\partial f_s}{\partial \mu}\mathbf{q}_s(\phi) + \frac{\partial f_l}{\partial \mu}\mathbf{q}_l(\phi) \right) \frac{\partial \mu}{\partial t} dV + \int \mu\rho(c_s - c_l)\mathbf{q}'_s(\phi) \frac{\partial \phi}{\partial t} dV \\ &\quad + \int \left((\omega_s - \omega_l)\mathbf{q}'_s(\phi) + f'_{\text{dw}}(\phi) - f_G(\nabla^2\phi) \right) \frac{\partial \phi}{\partial t} dV + \text{boundary terms.} \end{aligned}$$

Since $\frac{\partial f_s}{\partial \mu} = \frac{\partial f_s}{\partial(\rho c_s)} \rho \frac{\partial c_s}{\partial \mu} = \mu \rho \frac{\partial c_s}{\partial \mu}$ and similarly for $\frac{\partial f_l}{\partial \mu}$, and since the interpolation retrieved for composition in the grand potential formulation is $c(\mu, \phi) = c_s(\mu) \mathbf{g}_s(\phi) + c_l(\mu) \mathbf{g}_l(\phi)$, the above equation reduces to

$$\begin{aligned} \frac{dF}{dt} = \int \mu \rho \frac{\partial c}{\partial t} dV + \int ((\omega_s - \omega_l) \mathbf{g}'_s(\phi) + f'_{\text{dw}}(\phi) - f_G(\nabla^2 \phi)) \frac{\partial \phi}{\partial t} dV \\ + \text{boundary terms.} \end{aligned} \quad (\text{A.5})$$

Given that the expressions for the phase and concentration evolutions are as in Eqs. (2.33) and (2.34), the integrands in the final volume integrals (i.e., after applying divergence theorem to the first integral) in the above equation are negative implying that the production rates due to internal changes in each subvolume are indeed thermodynamically consistent.

A.2.2 Thermodynamic consistency of the pure substance model

It will now be shown that the pure substance solidification model of Ref. [18] which is used to motivate the grand-potential formulation fails to fulfill the requirements of the thermodynamical laws.

We execute the same routine carried out in section A.2.1 for the pure substance case presented in Ref. [18], i.e., back construct the entropy functional and substitute the evolution equations in its time derivative and check if the local production rate is positive. The ϕ and $\nabla \phi$ dependent entropy density, $s_{\surd}(T, \phi, \nabla \phi)$, of Ref. [18] does not contain the intermediate states penalizing term, i.e, the double well, and it is formulated to be a local function of ϕ and T alone, i.e, no gradient terms occur in it. Therefore, the entropy functional reads

$$S = \int s_{\surd}(T, \phi, \nabla \phi) dV = \int s(T, \phi) dV = \int (s_s(T) \mathbf{g}_s(\phi) + s_l(T) \mathbf{g}_l(\phi)) dV$$

implying $\frac{dS}{dt} = \int \frac{\partial s}{\partial t} dV$. In Ref. [18], the integrand $\frac{\partial s}{\partial t}$ of this integral is related to the time derivative of energy density as

$$\frac{\partial s}{\partial t} = \frac{1}{T} \frac{\partial e_{\surd}}{\partial t} \quad (\text{A.6})$$

and the latter is chosen according to Fourier and energy conservation laws as $\partial e_{\surd} / \partial t = \nabla \cdot (\kappa(\phi, T) \nabla T)$. Substituting this in the time derivative of the entropy results in

$$\frac{dS}{dt} = \int \frac{\nabla \cdot (\kappa(\phi, T) \nabla T)}{T} dV = \int \frac{\kappa(\phi, T) (\nabla T)^2}{T^2} dV + \text{boundary terms}$$

indicating, contrary to what we claimed, that the local entropy production rate due to internal changes is indeed positive. However, there is an error in the above calculation

as a term is missing from Eq. (A.6). As a result, the energy conservation is not strictly satisfied and when the appropriate term is supplied, it adds an extra contribution to the above derivative which may potentially affect its positivity:

In Ref. [18], for modeling pure substance solidification, the ϕ and $\nabla\phi$ dependent free energy density is chosen as

$$\begin{aligned} f_{\sphericalangle}(T, \phi, \nabla\phi) &= f_s(T)\mathbf{g}_s(\phi) + f_l(T)\mathbf{g}_l(\phi) + f_{\text{dw}}(\phi) + \frac{f_G}{2}(\nabla\phi)^2 \\ &= (e_s(T) - Ts_s(T))\mathbf{g}_s(\phi) + (e_l(T) - Ts_l(T))\mathbf{g}_l(\phi) + f_{\text{dw}}(\phi) + \frac{f_G}{2}(\nabla\phi)^2 \\ \implies e_{\sphericalangle}(T, \phi, \nabla\phi) - Ts_{\sphericalangle}(T, \phi, \nabla\phi) &= \{e_s(T)\mathbf{g}_s(\phi) + e_l(T)\mathbf{g}_l(\phi)\} \\ &\quad - T\{s_s(T)\mathbf{g}_s(\phi) + s_l(T)\mathbf{g}_l(\phi)\} + f_{\text{dw}}(\phi) + \frac{f_G}{2}(\nabla\phi)^2. \end{aligned}$$

Given that the interpolation in entropy density is selected without the penalizing term, the ϕ and $\nabla\phi$ dependent energy density $e_{\sphericalangle}(T, \phi, \nabla\phi)$ turns out to be

$$e_{\sphericalangle}(T, \phi, \nabla\phi) = \{e_s(T)\mathbf{g}_s(\phi) + e_l(T)\mathbf{g}_l(\phi)\} + f_{\text{dw}}(\phi) + \frac{f_G}{2}(\nabla\phi)^2. \quad (\text{A.7})$$

Now, re-writing $e_s(T)$ and $e_l(T)$ in terms of entropy densities of the solid and liquid, respectively, instead of temperature by using $s_s(T)$ and $s_l(T)$, we have

$$e_{\sphericalangle} = e_s(s_s)\mathbf{g}_s(\phi) + e_l(s_l)\mathbf{g}_l(\phi) + f_{\text{dw}}(\phi) + \frac{f_G}{2}(\nabla\phi)^2 \quad (\text{A.8})$$

where the symbols e_s and e_l are retained for the energy densities even after re-expressing them in terms of respective entropies for simplicity of notation. The differential of e_{\sphericalangle} is therefore

$$\begin{aligned} de_{\sphericalangle} &= \frac{de_s}{ds_s}ds_s\mathbf{g}_s(\phi) + \frac{de_l}{ds_l}ds_l\mathbf{g}_l(\phi) + f'_{\text{dw}}(\phi)d\phi + f_G\nabla\phi \cdot d\nabla\phi \\ &= T_s(s_s)ds_s\mathbf{g}_s(\phi) + T_l(s_l)ds_l\mathbf{g}_l(\phi) + f'_{\text{dw}}(\phi)d\phi + f_G\nabla\phi \cdot d\nabla\phi \\ &= Tds_s\mathbf{g}_s(\phi) + Tds_l\mathbf{g}_l(\phi) + f'_{\text{dw}}(\phi)d\phi + f_G\nabla\phi \cdot d\nabla\phi \\ &= Tds + f'_{\text{dw}}(\phi)d\phi + f_G\nabla\phi \cdot d\nabla\phi \end{aligned}$$

where the second last equality followed because of the same logic as utilized in going from Eq. (2.9) to (2.10). Therefore, the completed relation of Eq. (A.6) is

$$\frac{\partial s}{\partial t} = \frac{1}{T} \frac{\partial e_{\sphericalangle}}{\partial t} - \frac{1}{T} f'_{\text{dw}}(\phi) \frac{\partial \phi}{\partial t} + f_G \nabla\phi \cdot \frac{\partial \nabla\phi}{\partial t}. \quad (\text{A.9})$$

Since Eq. (A.6) is used instead of Eq. (A.9) in writing down the temperature evolution equation, the energy is not conserved. Hence, in their present form, the governing

equations of the pure substance solidification model of Ref. [18] are not consistent with the laws of thermodynamics. When adjusted, i.e., when Eq. (A.9) is used to calculate $\frac{dS}{dt}$, it is unclear if there will ever be practical cases where this derivative ceases to be positive. The non-physical example of filling the entire domain with a constant undercooled temperature and a single value of ϕ appropriately close to zero can make this happen for short periods. To sum up, whether or not the equations rectified so as to respect the first law of thermodynamics fulfill the requirement of the second law for physical processes is inconclusive at the moment.

A.2.3 Generality of the framework

Even if it is assumed that the entropy production requirement is met in the case of physical processes, a problem still arises. This has to do with the fact that in order to satisfy the first law, the governing equation for T has to be extended to include the additional term of Eq. (A.9) which amounts to introducing a new source term arising due to the excess energies of the intermediate states. However, this produces undesirable contributions in the sharp interface limit problem of the model. The whole issue can be eliminated by getting rid of the double well term in the energy density. However, it then has to be accommodated in the entropy formula necessitating the inclusion of a temperature in the free energy excess thus coupling the interface and bulk properties. The upshot being, even if the thermodynamic consistency were to be assumed, the decoupling behavior is lost implying that the generic two-argument framework of Ref. [18] is not unified. That is, it works fine in all departments in one case, namely, isothermal alloy solidification but fails to do so in some other. This is further reinforced by the fact that the decoupling behavior is lost even when generalizing to the case of non-isothermal alloy solidification where a temperature and chemical potential dependent grand potential density is the starting point.

However, there is a simple workaround for this problem of reconciling bulk and interface properties decoupling with thermodynamic consistency in the two-argument derivation approaches. Upon a closer observation, it will become transparent that in both the cases considered above, the cause of the coupling is the temperature occurring as multiplied to the penalizing term. Hence, the problem can be avoided by using the functional of the same quantities but which are divided by the temperature. That is, instead of considering the free energy functional starting point for pure substance and grand potential for alloy solidification, these potentials divided by the temperature have to be considered and the excess has to be incorporated into the entropy density instead of energy density. We note that these functions can be realized as the Legendre transformations of the entropy and are referred to as the entropic thermodynamic potentials or the gener-

alized Massieu-Planck functions. Thus, for thermodynamic consistency, the Helmholtz free energy has to be replaced with Helmholtz free entropy or the Massieu potential and accordingly for the grand-potential.

A.3 Generality of the framework of Ref [28] (and [27])

Penrose and Fife [27] followed by Wang *et al.* [28] specifically set forth their derivation to overcome the ad-hocness of the two-argument approach and hence by design its progression is thermodynamically driven. However, the original derivation was only presented for the case of pure substance solidification; here, we test its generality by attempting to adapt it to the case of isothermal alloy solidification. One difficulty, though, is that Wang *et al.* did not state their algorithm in the most generic terms, hence, two possible ways of interpreting their derivation are possible, the details are as follows.

A.3.1 Adapting Wang *et al.*'s derivation: Method 1

For starting off the derivation the following logic is applied: since in the original Wang *et al.* derivation entropy functional and the energy field, i.e., a combination pertaining to maximum information is considered, for the case of alloy solidification, we consider concentration field and the following Helmholtz free energy functional in order to adopt their approach.

$$F = \int \left(f(c, \phi) + \frac{f_G}{2} (\nabla \phi)^2 \right) dV.$$

Differentiating with respect to time yields

$$\begin{aligned} \frac{dF}{dt} &= \int \left. \frac{\partial f(c, \phi)}{\partial c} \right|_{\phi} \frac{\partial c}{\partial t} dV + \int \left(\left. \frac{\partial f(c, \phi)}{\partial \phi} \right|_c - f_G \nabla^2 \phi \right) \frac{\partial \phi}{\partial t} dV + \text{boundary terms} \\ &= \int \mu(c, \phi) \rho \frac{\partial c}{\partial t} dV + \int \left(\left. \frac{\partial f(c, \phi)}{\partial \phi} \right|_c - f_G \nabla^2 \phi \right) \frac{\partial \phi}{\partial t} dV + \text{boundary terms.} \end{aligned} \quad (\text{A.10})$$

Next, the evolution equations are chosen as

$$\frac{\partial c}{\partial t} = \nabla \cdot (M_c \nabla \mu) \quad \text{and} \quad \frac{\partial \phi}{\partial t} = -M_{\phi} \left(\left. \frac{\partial f(c, \phi)}{\partial \phi} \right|_c - f_G \nabla^2 \phi \right) \quad (\text{A.11})$$

ensuring mass balance and negative free energy production due to internal changes. The steps so far are identical to the WBM [9] approach which was demonstrated to yield undesirable coupling of bulk and interface properties. However, a difference arises because of the way μ and $\frac{\partial f}{\partial \phi}$ are handled. In the WBM approach, $f(c)$ is interpolated as $f(c, \phi) =$

$f_s(c)\mathbf{g}_s(\phi) + f_l(c)\mathbf{g}_l(\phi) + f_{dw}(\phi)$ and μ is expressed in terms of c as $\mu(c, \phi) = \mu_s(c)\mathbf{g}_s(\phi) + \mu_l(c)\mathbf{g}_l(\phi)$ consistent with $f(c, \phi)$. However, in a Wang *et al.* kind of approach, no mention is made about the dependence of f or μ on c in Eq. (A.10) just yet, but is postponed to later.

In the next step of the original derivation, where entropy and the energy are the potential and the evolving variable field, respectively, a change of representation is made from $s = s(e, \phi)$ to $e = e(s, \phi)$ for handling the phase evolution equation. As a result, in the place where $\left.\frac{\partial f}{\partial \phi}\right|_c$ occurs in Eq. (A.11), $\left.\frac{1}{T}\frac{\partial e}{\partial \phi}\right|_s$ appears in the counterpart equation in Ref. [28]. However, instead of working with the entropy its conjugate variable T is preferred and instead of e its Legendre transformation with regard to s , i.e., f is considered and the identity $\frac{f}{T} = \frac{e}{T} - s$ is exploited to proceed forward. Following the same, we shift the focus from c to its conjugate variable μ and prefer the Legendre transformation of f with regard to c ; a change of representation is not needed as we are already working with a free energy. Hence, the appropriate identity to be considered is

$$\begin{aligned} \frac{\omega}{\mu} &= \frac{f}{\mu} - c & (\text{A.12}) \\ \implies d\left(\frac{\omega}{\mu}\right) &= -\frac{f}{\mu^2}d\mu + \frac{1}{\mu}df - dc \\ &= -\frac{f}{\mu^2}d\mu + \frac{1}{\mu}\left(\frac{\partial f}{\partial c}dc + \frac{\partial f}{\partial \phi}d\phi\right) - dc \\ &= -\frac{f}{\mu^2}d\mu + \frac{1}{\mu}\frac{\partial f}{\partial \phi}d\phi. \end{aligned}$$

This further implies that

$$\left.\frac{\partial(\omega/\mu)}{\partial \mu}\right|_{\phi} = -\frac{f}{\mu^2} \quad (\text{A.13})$$

$$\left.\frac{\partial \omega}{\partial \phi}\right|_{\mu} = \frac{\partial f}{\partial \phi}\bigg|_c. \quad (\text{A.14})$$

It is at this point that it is revealed that f was originally interpolated in terms of μ rather than c as

$$f(\mu, \phi) = f_s(\mu)\mathbf{g}_s(\phi) + f_l(\mu)\mathbf{g}_l(\phi) \quad (\text{A.15})$$

implying that the $f(c, \phi)$ in Eq. (A.10) is not of the form as in the WBM model [9]. Next, using this interpolation for f , Eq. (A.13) is integrated as

$$\omega(\mu, \phi) = \mu \left(- \int_{\mu_{\text{eq}}}^{\mu} \frac{f(\mu, \phi)}{\mu^2} d\mu + G(\phi) \right) \quad (\text{A.16})$$

where μ_{eq} is the equilibrium chemical potential and $G(\phi)$ is the integration “constant”. Using Eq. (A.15), the above becomes

$$\begin{aligned}\omega(\mu, \phi) &= -\mu \int_{\mu_{\text{eq}}}^{\mu} \frac{f_s(\mu, \phi)}{\mu^2} d\mu \mathbf{g}_s(\phi) - \mu \int_{\mu_{\text{eq}}}^{\mu} \frac{f_l(\mu, \phi)}{\mu^2} d\mu \mathbf{g}_l(\phi) + G(\phi) \\ &= \omega_s(\mu) \mathbf{g}_s(\phi) + \omega_l(\mu) \mathbf{g}_l(\phi) + \omega_{\text{eq}} + \mu G(\phi)\end{aligned}\quad (\text{A.17})$$

where ω_{eq} is the equilibrium grand potential and $G(\phi)$ is chosen as $G(\phi) = -\frac{\omega_{\text{eq}}}{\mu_{\text{eq}}} + \text{DW}(\phi)$ where $\text{DW}(\phi)$ is an intermediate states penalizing function, i.e., the double well. However, when Eq. (A.17) is used to obtain the phase evolution equation of Eq. (A.11) through Eq. (A.14), we see that the bulk and interface properties are explicitly coupled due to the occurrence of the chemical potential being multiplied to the double well term. Such a problem did not arise in the pure substance case for which the derivation was originally worked out because in that case, where T occurs in place of μ in the counterpart of Eq. (A.17), another T appears in the denominator in the phase evolution equation and they both cancel out. In contrast, such a neat cancellation does not occur in the alloy case. Further, Eq. (A.17) leads to the following interpolation in the composition

$$c(\mu) = c_s(\mu) \mathbf{g}_s(\phi) + c_l(\mu) \mathbf{g}_l(\phi) + \text{DW}(\phi),$$

i.e., the concentration of the intermediate states is not a simple interpolation of the bulk values but has an excess contribution. Therefore, an extra term arises in the chemical potential evolution equation leading to an undesirable addition to the recovered sharp interface limit problem.

To summarize, while in Plapp’s approach the isothermal alloy solidification was well modeled with all the ideal characteristics readily captured and the pure substance case yielding undesirable terms in the evolution equation of the intensive variable, the reverse happened here. Further, in both the cases, the failure can be traced back to the same reason, namely, the accommodation of double well in some other thermodynamic variable rather than in the entropy density. Before expanding on this further, a different way of adapting Wang *et al.*’s derivation for isothermal alloy solidification is presented.

A.3.2 Adapting Wang *et al.*’s derivation: Method 2

It will be presently shown that a step by step mimicking of the original derivation indeed leads to the right equations if an entropy functional starting point is leveraged. However, this requires treating the system as possessing only a single independent variable, namely, the composition. And, it has to be pretended as being characterized by a constant energy density which cannot be altered. This is similar to the modeling performed in section A.4.2 where the number density is treated as an absolute property of the body

inseparable from it and hence inaccessible to any manipulation. The appropriate entropy functional is

$$S = \int \left(s(c, \phi) - \frac{s_G}{2} (\nabla \phi)^2 \right) dV.$$

We point out that since the energy is modeled to be constant, that is, invariant upon solute redistribution and phase transitions, no heat evolution or absorption takes place and hence no interaction is necessary with a reservoir and thus only the system's entropy can be focused on for the calculation of the production rates. Differentiating the above with time yields

$$\begin{aligned} \frac{dS}{dt} &= \int \frac{\partial s(c, \phi)}{\partial c} \Big|_{\phi} \frac{\partial c}{\partial t} dV + \int \left(\frac{\partial s(c, \phi)}{\partial \phi} \Big|_c + s_G \nabla^2 \phi \right) \frac{\partial \phi}{\partial t} dV + \text{boundary terms.} \\ &= \int \frac{-\mu(c, \phi) \rho}{T} \frac{\partial c}{\partial t} dV + \int \left(\frac{\partial s(c, \phi)}{\partial \phi} \Big|_c + s_G \nabla^2 \phi \right) \frac{\partial \phi}{\partial t} dV + \text{boundary terms.} \end{aligned} \quad (\text{A.18})$$

Next, the evolution equations are chosen as

$$\frac{\partial c}{\partial t} = \nabla \cdot (M_c \nabla \mu) \quad \text{and} \quad \frac{\partial \phi}{\partial t} = M_{\phi} \left(\frac{\partial s(c, \phi)}{\partial \phi} \Big|_c + s_G \nabla^2 \phi \right)$$

ensuring mass balance and local positive entropy production. However, as mentioned before, in a Wang *et al.* kind of approach, no mention is made about the dependence of s or μ on c . Instead, a search is made for a function ζ which satisfies the following relation

$$\frac{\partial s}{\partial c} \Big|_{\phi} = \frac{\partial \zeta}{\partial \mu} \Big|_{\phi} \quad (\text{A.19})$$

Noting that a Legendre transformation of entropy with regard to composition can be made to identically satisfy this, ζ is chosen as

$$\zeta = s + \frac{\mu \rho}{T} c \quad (\text{A.20})$$

and can be verified to satisfy the required relation as

$$\begin{aligned} d\zeta &= \frac{\partial s}{\partial c} \Big|_{\phi} dc + \frac{\partial s}{\partial \phi} \Big|_c d\phi + \frac{\mu \rho}{T} dc + \frac{c \rho}{T} d\mu + c \mu d \left(\frac{\rho}{T} \right) \\ &= \frac{\partial s}{\partial c} \Big|_{\phi} dc + \frac{\partial s}{\partial \phi} \Big|_c d\phi + \frac{\mu \rho}{T} dc + \frac{c \rho}{T} d\mu \\ &= \frac{\partial s}{\partial \phi} \Big|_c d\phi + \frac{c \rho}{T} d\mu \end{aligned} \quad (\text{A.21})$$

where the second equality followed from the modeling of the system which ensures that ρ and T are constants. Thus, the generalized Massieu-Planck functions naturally enter into the formulation.

The next step of the Wang *et al.* model involves revealing the relationship between c and μ which is $c(\mu, \phi) = c_s(\mu)\mathbf{g}_s(\phi) + c_l(\mu)\mathbf{g}_l(\phi)$ and using it in conjunction with Eqs. (A.21) and (A.19) to find $\zeta(\mu, \phi)$ similar to the steps in going from Eq. (A.15) to Eq. (A.16). Thus the generalized Massieu-Planck function ζ is

$$\zeta(\mu, \phi) = \zeta_s(\mu)\mathbf{g}_s(\phi) + \zeta_l(\mu)\mathbf{g}_l(\phi) + \zeta_s(\mu_0)\mathbf{g}_s(\phi) + \zeta_l(\mu_0)\mathbf{g}_l(\phi) + G(\phi)$$

where μ_0 is some reference value considered for the lower limit of integration and $G(\phi)$, as before, is the integrating constant and has to be chosen such that $\zeta_s(\mu_0)\mathbf{g}_s(\phi) + \zeta_l(\mu_0)\mathbf{g}_l(\phi) + G(\phi) = -DW(\phi)$ where $DW(\phi)$ is a double well function (note that μ does not occur multiplied to the double well unlike in Eq. (A.17)). Thus the modeling equations are Eq. (2.34) for the concentration evolution and the following for the phase evolution.

$$\begin{aligned} \frac{\partial\phi}{\partial t} &= M_\phi \left([\zeta_s(\mu) - \zeta(\mu)] \mathbf{g}'_s(\phi) - DW(\phi) + s_G \nabla^2 \phi \right) \\ &= M_\phi \left(\left[-s_l - \frac{\mu\rho}{T} c_l - \left(-s_s - \frac{\mu\rho}{T} c_s \right) \right] \mathbf{g}'_s(\phi) - DW(\phi) + s_G \nabla^2 \phi \right) \\ &= M_\phi \left(\left[e - s_l - \frac{\mu\rho}{T} c_l - \left(e - s_s - \frac{\mu\rho}{T} c_s \right) \right] \mathbf{g}'_s(\phi) - DW(\phi) + s_G \nabla^2 \phi \right) \end{aligned}$$

where e is the unique energy density that characterizes the system. Since it is the same for all the phases, i.e., $0 \leq \phi \leq 1$, we have

$$\begin{aligned} \frac{\partial\phi}{\partial t} &= M_\phi \left(\left[e_l - s_l - \frac{\mu\rho}{T} c_l - \left(e_s - s_s - \frac{\mu\rho}{T} c_s \right) \right] \mathbf{g}'_s(\phi) - DW(\phi) + s_G \nabla^2 \phi \right) \\ &= M_\phi \left(\left(\frac{\omega_l}{T} - \frac{\omega_s}{T} \right) \mathbf{g}'_s(\phi) - DW(\phi) + s_G \nabla^2 \phi \right) \\ &= \widetilde{M}_\phi \left((\omega_l - \omega_s) \mathbf{g}'_s(\phi) - TDW(\phi) + f_G \nabla^2 \phi \right) \end{aligned}$$

where the T in the denominator is subsumed into M_ϕ in the last step and re-denoted as \widetilde{M}_ϕ . If $DW(\phi)$ is chosen as $s_{\text{dw}}(\phi)$, the resulting governing equation will be identical to Eq. (2.33) which is derived through the approach advanced in the current thesis and which is the same as that from Plapp's grand-potential formulation.

In summary, Wang *et al.*'s method of arriving at the governing equations fetched a decoupling behavior when starting from an entropy functional, but failed to do so with the free energy. To asses the reason, we make the system uniform in the both the cases, i.e., assume that the energy density is independent of ϕ in the free energy derivation of section A.3.1 as well. Then, it follows from Eq. (A.17) and the identity $\frac{\partial\omega}{\partial T} = -s$ that when starting from Helmholtz free energy functional, the entropy density is retrieved as being interpolated when expressed in terms of the intensive variable but without the excess term which is incorporated into the concentration; whereas in the entropy starting point it is accommodated in the former and not in the latter. Further, if the double well term were to be already incorporated in Eq. (A.15) and then integrated as in Eq.

(A.16) to give grand-potential by choosing the integration constant as identically zero, then the explicit coupling can be avoided and the resulting modeling equations merge with Eqs. (2.33) and (2.34). However, the combined effect of all this is to switch places of the double well term from concentration to entropy.

Hence, it can be concluded that the hypothesis (H_2) of our generic framework is a necessary requirement for the recovery of the modeling equations that exhibit all the ideal characteristics (i.e., give rise to the appropriate Stefan like problems in their asymptotic limit and facilitate a separate control of bulk and interfacial properties).

A.4 Further applications of the generic formulation

Some more applications of the generic formulation of section 2.3 are presented here.

A.4.1 Non-isothermal solidification in rigid alloy systems

It is not necessary to go through the entire routine of starting from a functional etc. The modeling equations of section 2.2 readily transfer to the current case by an appropriate re-mapping of various terms as shown below.

The fundamental relation in terms of per unit volume quantities for a binary alloy system is given in Eq. (A.2). If it is now considered that the alloy is rigid, i.e., the overall number density ρ is a constant in Eq. (A.2), we have that the entropy density s is a function of (e, c) satisfying

$$\left. \frac{\partial s}{\partial e} \right|_c = \frac{1}{T} \quad \text{and} \quad (\text{A.22})$$

$$\left. \frac{\partial s}{\partial(c\rho)} \right|_e = -\frac{\mu}{T} \quad (\text{A.23})$$

which can be readily seen to be an outcome of the form of the Eq. (A.1), i.e., the fact that S is first order homogeneous in E, V, N_A and N_B . Thus, due to the similarity of the forms of the equations (A.22) and (A.23) with those of (2.11) and (2.12), respectively, the same governing equations of section 2.2 with the changed meaning for various symbols model the solidification of incompressible binary alloys, the only difference being that wherever ρ occurs in section 2.2, it has to be replaced by $c\rho$. These will be listed here for the sake of completeness.

$$\frac{\partial \phi}{\partial t} = M_\phi \left[\frac{1}{T}(\omega_l - \omega_s)g'_s(\phi) - s'_{\text{dw}}(\phi) + s_G(\nabla^2 \phi) \right], \quad (\text{A.24})$$

$$\frac{\partial c}{\partial t} = \nabla \cdot (M_{c\rho}/\rho)\nabla(\mu/T), \quad (\text{A.25})$$

$$\begin{aligned} \frac{\partial T}{\partial t} &= \left. \frac{\partial e}{\partial T} \right|_{c,\phi}^{-1} \left(\nabla \cdot (M_T \nabla T) - \left. \frac{\partial e}{\partial c} \right|_{T,\phi} \frac{\partial c}{\partial t} - \left. \frac{\partial e}{\partial \phi} \right|_{T,c} \frac{\partial \phi}{\partial t} \right) \\ &\approx \left. \frac{\partial e}{\partial T} \right|_{c,\phi}^{-1} \left(\nabla \cdot (M_T \nabla T) - \left. \frac{\partial e}{\partial \phi} \right|_{T,c} \frac{\partial \phi}{\partial t} \right). \end{aligned} \quad (\text{A.26})$$

It has to be cautioned that apart from ensuring that each homogeneous phase is individually incompressible, Eqs. (A.24), (A.25) and (A.26) also assume that the invariant density is the same for all the bulk and intermediate states. Further, considering a single phase at constant temperature, the homogenization of composition fields is usually not accompanied by any heat release, therefore, the term $\left. \frac{\partial e}{\partial c} \right|_{T,\phi}$ in the temperature evolution equation can be safely considered to be identically zero leading to the simplification assumed in Eq. (A.26).

A.4.2 Solidification in incompressible pure systems

The constancy of the number density has to be treated as an absolute property of the body not accessible to manipulation. That is the systems have to be modeled as possessing only one independent thermodynamic variable. Thus, the fundamental relations are either entropy density expressed in terms of energy density or vice-versa. For homogeneous systems of such a kind, the fundamental Gibbs formula can be obtained as follows.

$$\begin{aligned} E(S, V, \rho V) &= T(S, V, \rho V)S - P(S, V, \rho V)V + \mu(S, V, \rho V)\rho V \\ \implies E(S, V) &= T(S, V)S - (P(S, V) - \mu(S, V)\rho)V =: T(S, V)S + f(S, V)V. \end{aligned} \quad (\text{A.27})$$

Since $E(S, V)$ of Eq. (A.27) is first order homogeneous in S and V , it follows that

$$Vdf = -SdT$$

and dividing Eq. (A.27) with V , this further leads to

$$ds = \frac{1}{T}de.$$

Incorporating the excess and gradient penalizing contributions in the entropy density as outlined in section 2.1 and implementing the routine presented there, the ϕ dependent version of the above equation works out to

$$ds = \frac{1}{T}de - \frac{1}{T}((f_s - f_l)\mathbf{g}'_s(\phi) + Ts'_{\text{dw}}(\phi))d\phi \quad (\text{A.28})$$

and the solidification modeling equations read

$$\frac{\partial \phi}{\partial t} = M_\phi \left[\frac{1}{T}(f_l - f_s)\mathbf{g}'_s(\phi) - s'_{\text{dw}}(\phi) + s_G(\nabla^2 \phi) \right] \quad \text{and} \quad (\text{A.29})$$

$$\frac{\partial T}{\partial t} = \left. \frac{\partial e}{\partial T} \right|_\phi^{-1} \left(\nabla \cdot (M_T \nabla T) - \left. \frac{\partial e}{\partial \phi} \right|_T \frac{\partial \phi}{\partial t} \right). \quad (\text{A.30})$$

Appendix B

Appendices to chapter 3

B.1 Existence, uniqueness and long time behavior

The analysis of existence and uniqueness related issues of the solutions of some of the differential equations encountered in chapter 3 which are left unanalyzed there are presented in the current section of this appendix.

B.1.1 Analysis of Eq. (3.8)

The existence of solution of Eq. (3.8) for long times and its uniqueness are assumed without explicit proofs in section. However, standard results in the theory of differential equations indeed guarantee this as argued underneath.

Consider an initial condition for the Eq. (3.8) satisfying

$$0 < \phi_0^{(0)} = \phi^{(0)}(\tau = 0) < 1/2$$

as shown in Fig B.1 for example. Also, consider an interval $I = (\phi_l^{(0)}, \phi_u^{(0)})$ around the initial value as depicted. From the first corollary to the Maximal Interval of Existence Theorem presented in Ref. [95], if $f_{\text{dw}}(\phi)$ is locally Lipschitz on the interval I , then the solution $\phi^{(0)}(\tau)$ either crosses either one of the end points of the interval in finite time or forever stays within it. Assuming the latter case, i.e., if the maximum interval of existence is infinite, then it means that for all $\tau \geq 0$, $\phi^{(0)}(\tau) > \phi_l^{(0)}$. Which further means, due to the double well shape and the chosen initial condition, $f'_{\text{dw}}(\phi^{(0)}(\tau)) > f'_{\text{dw}}(\phi_l^{(0)})$. Therefore,

$$\frac{\partial \phi^{(0)}}{\partial \tau} < -\gamma f'_{\text{dw}}(\phi_l^{(0)}) \quad \forall \tau \geq 0.$$

Hence, due to the Mean Value Theorem, on an interval $(0, \tau_u)$, there exists a τ_* satisfying $0 \leq \tau_* \leq \tau_u$ such that

$$\begin{aligned} \phi^{(0)}(\tau_u) &= \phi^{(0)}(0) + \frac{\partial \phi^{(0)}}{\partial \tau}(\tau_*)\tau_u \\ \implies \phi^{(0)}(\tau_u) &< \phi^{(0)}(0) - \gamma f'_{\text{dw}}(\phi_l^{(0)})\tau_u. \end{aligned}$$

Now, if τ_u is chosen as $\tau_u = \frac{1}{\gamma f'_{\text{dw}}(\phi_l^{(0)})} \left(\phi^{(0)}(0) - \frac{\phi_l^{(0)}}{2} \right)$, then it leads to $\phi^{(0)}(\tau_u) < \phi^{(0)}(\tau_u)/2$, contradicting the assumption that $\phi^{(0)}(\tau) > \phi_l^{(0)} \forall \tau \geq 0$. Hence, $\phi^{(0)}(\tau)$ leaves the interval in finite time. Furthermore, it does not leave by crossing the end point $\phi_u^{(0)}$ because it will then contradict Eq. (3.9). However, by enlarging the interval to include $\phi^{(0)} = 0$, the existence of solution for infinite times will be the picked behavior from the two alternatives of the corollary. This time, the crossing over of the lower end point does not happen, as it would mean the violation of Eq. (3.9) due to the Intermediate Value Theorem. In summary, the solution leaves any interval not containing $\phi^{(0)} = 0$ in finite time, but never leaves any interval containing it, thus implying that it converges to it as $\tau \rightarrow \infty$. The arguments for all the other initial conditions are similar. Finally, it may be unsettling to see the usage of results in the theory of ordinary differential equations for the analysis of Eq. (3.8) containing partial derivative. However, this isn't a big problem because the proven uniqueness for the ODE version of the initial value problem implies that the only way another variable can enter the solution is through the initial condition.

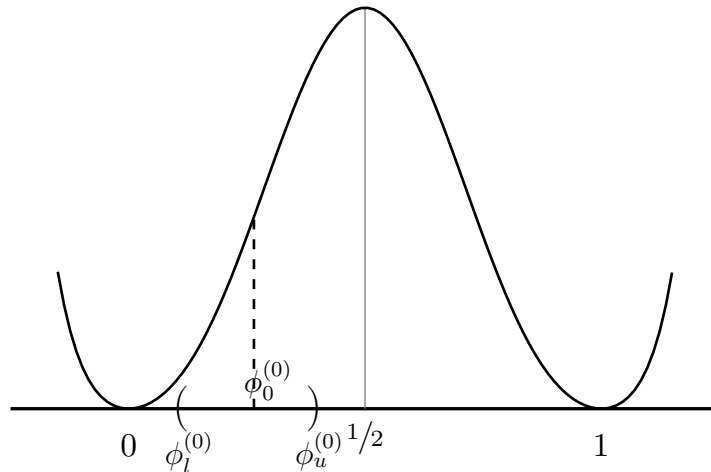


Figure B.1: A generic symmetric double well.

B.1.2 Analysis of Eq. (3.12)

The solutions of Eq. (3.12) will now be studied. For this, the differential equation is rewritten in terms of two dependent variables as follows

$$\frac{\partial \tilde{\phi}^{(0)}}{\partial \rho} = \tilde{\psi}^{(0)} =: f_1(\tilde{\phi}^{(0)}, \tilde{\psi}^{(0)}) \quad (\text{B.1})$$

and

$$\frac{\partial \tilde{\psi}^{(0)}}{\partial \rho} = f'_{\text{dw}}(\tilde{\phi}^{(0)}) =: f_2(\tilde{\phi}^{(0)}, \tilde{\psi}^{(0)}). \quad (\text{B.2})$$

This approach of handling a higher order differential equation by converting it to a system of first order equations is pretty standard in the theory of differential equations.

Now, considering a Euclidean norm for the \mathbb{R}^2 space in which $(\tilde{\phi}^{(0)}, \tilde{\psi}^{(0)})$ lives and also for it to which the latter is mapped to by $f = (f_1, f_2)$. It is easy to show that f is locally Lipschitz as follows.

For each $(a, b) \in \mathbb{R}^2$, consider a compact subset \mathcal{U} containing it. If $(\tilde{\phi}_1^{(0)}, \tilde{\psi}_1^{(0)})$ and $(\tilde{\phi}_2^{(0)}, \tilde{\psi}_2^{(0)})$ are two points of the subset, then

$$\begin{aligned} \frac{\|f(\tilde{\phi}_1^{(0)}, \tilde{\psi}_1^{(0)}) - f(\tilde{\phi}_2^{(0)}, \tilde{\psi}_2^{(0)})\|}{\|(\tilde{\phi}_1^{(0)}, \tilde{\psi}_1^{(0)}) - (\tilde{\phi}_2^{(0)}, \tilde{\psi}_2^{(0)})\|} &= \frac{\sqrt{(\tilde{\psi}_2^{(0)} - \tilde{\psi}_1^{(0)})^2 + (f'_{\text{dw}}(\tilde{\phi}_2^{(0)}) - f'_{\text{dw}}(\tilde{\phi}_1^{(0)}))^2}}{\sqrt{(\tilde{\psi}_2^{(0)} - \tilde{\psi}_1^{(0)})^2 + (\tilde{\phi}_2^{(0)} - \tilde{\phi}_1^{(0)})^2}} \\ &= \frac{\sqrt{(\tilde{\psi}_2^{(0)} - \tilde{\psi}_1^{(0)})^2 + (f''_{\text{dw}}(\tilde{\phi}_*^{(0)}))^2 (\tilde{\phi}_2^{(0)} - \tilde{\phi}_1^{(0)})^2}}{\sqrt{(\tilde{\psi}_2^{(0)} - \tilde{\psi}_1^{(0)})^2 + (\tilde{\phi}_2^{(0)} - \tilde{\phi}_1^{(0)})^2}} \\ &\text{for some } \tilde{\phi}_*^{(0)} \in (\tilde{\phi}_1^{(0)}, \tilde{\phi}_2^{(0)}) \text{ due to the Mean Value Theorem.} \\ &\leq \frac{\sqrt{(\tilde{\psi}_2^{(0)} - \tilde{\psi}_1^{(0)})^2 + M^2 (\tilde{\phi}_2^{(0)} - \tilde{\phi}_1^{(0)})^2}}{\sqrt{(\tilde{\psi}_2^{(0)} - \tilde{\psi}_1^{(0)})^2 + (\tilde{\phi}_2^{(0)} - \tilde{\phi}_1^{(0)})^2}} \\ &\quad \text{where } M = \max \{ |f''_{\text{dw}}(\tilde{\phi}^{(0)})| : (\tilde{\phi}^{(0)}, \tilde{\psi}^{(0)}) \in \mathcal{U} \} \\ &\leq \max\{1, M\}. \end{aligned}$$

Thus it is shown that f is locally Lipschitz. Therefore, from the second corollary to the Maximal Interval of Existence Theorem presented in Ref. [95], a solution exists to the system of equations Eqs. (B.1) and (B.2) for a given initial condition $(\tilde{\phi}^{(0)}(\rho_0), \tilde{\psi}^{(0)}(\rho_0))$ which either exists for all $\rho \in \mathbb{R}$ or grows unbounded as ρ approaches a finite value. Regardless, it is unique and this detail will be of huge relevance in proving that the solution of the boundary value problem of interest is identically $\tilde{\phi}^{(0)}(\rho) = 0$.

Claim: The only solution of Eq. (3.12) with boundary conditions at infinity given by $\tilde{\phi}^{(0)} \rightarrow 0$ as $\rho \rightarrow \pm\infty$ is $\tilde{\phi}^{(0)}(\rho) = 0$.

Proof:

Consider instead the following problem.

$$\left| \frac{\partial \tilde{\phi}^{(0)}}{\partial \rho} \right| = \sqrt{2} \sqrt{f_{\text{dw}}(\tilde{\phi}^{(0)})}, \quad (\text{B.3})$$

$$\tilde{\phi}^{(0)} \text{ is double differentiable and satisfies } \tilde{\phi}^{(0)} \rightarrow 0 \text{ as } \rho \rightarrow \pm\infty. \quad (\text{B.4})$$

This, and the original BVP are equivalent, in that, their solution sets coincide. First of all, since $\tilde{\phi}^{(0)}(\rho) = 0$ is a solution to both of them, their solutions sets are non empty. Further, a function $\tilde{\phi}^{(0)}$ is a solution of the original BVP if and only if it is a solution of the above. The “if” part can be proved by multiplying Eq. (3.12) with $\frac{\partial \tilde{\phi}^{(0)}}{\partial \rho}$ and integrating it from $-\infty$ to some ρ . The “only if” part can be proved by squaring Eq. (B.3) and noting that whenever $\frac{\partial \tilde{\phi}^{(0)}}{\partial \rho}$ is zero or non-zero on an interval of non-zero length, Eq. (3.12) has to be fulfilled, and furthermore, if it vanishes at isolated points, even then, Eq. (3.12) has to be fulfilled due to existence of the limits of $\frac{\partial^2 \tilde{\phi}^{(0)}}{\partial \rho^2}$ as the points are approached.

Now, a function satisfying $\frac{\partial \tilde{\phi}^{(0)}}{\partial \rho} > 0 \forall \rho \in \mathbb{R}$ cannot be a solution of Eqs. (B.3) and (B.4) because if it is and if it takes a positive value for some point, then the boundary condition at $+\infty$ cannot be satisfied. Similarly, if it assumes a negative value at some point, then the one at $-\infty$ cannot be fulfilled. If it is identically zero throughout, then the positivity of the derivative is violated. For similar reasons, $\frac{\partial \tilde{\phi}^{(0)}}{\partial \rho}$ cannot be negative for all ρ .

Hence, there should be at least one point where it is negative and one where it is positive, implying by Intermediate Value theorem that there exists a point ρ_0 such that $\frac{\partial \tilde{\phi}^{(0)}}{\partial \rho}(\rho_0) = 0$. However, this requires that at such a point, the value of $\tilde{\phi}^{(0)}$ should correspond to a zero of f_{dw} due to Eq. (B.3). Since the solution sets of the newly considered BVP and the original one of actual interest coincide, this means that any solution of the original BVP should necessarily fulfill $\tilde{\phi}^{(0)}(\rho_0) = \phi_{\text{zero}}$ and $\frac{\partial \tilde{\phi}^{(0)}}{\partial \rho}(\rho_0) = 0$ for some point ρ_0 where ϕ_{zero} is some zero of f_{dw} . However, this is equivalent to an initial value problem involving Eqs. (B.1) and (B.2) which is shown to possess unique solution. Since, $\tilde{\phi}^{(0)}(\rho) = \phi_{\text{zero}} \forall \rho \in \mathbb{R}$ is a candidate, it has to be the only solution. However, for the boundary conditions at infinity to be satisfied the said zero should necessarily be $\phi_{\text{zero}} = 0$. Hence, the solution of the original BVP is uniquely $\tilde{\phi}^{(0)}(\rho) = 0 \forall \rho \in \mathbb{R}$. Thus the claim is proved.

Next, the case of interface between stable phases is considered.

Claim: A solution of Eq. (3.12) for the boundary conditions $\tilde{\phi}^{(0)} \rightarrow 0$ as $\rho \rightarrow -\infty$ and

$\tilde{\phi}^{(0)} \rightarrow 1$ as $\rho \rightarrow \infty$ exists and is unique up to a translation and approaches the boundary conditions at an exponential rate.

Proof:

Consider instead the following problem:

- a) The differential equation given by Eq. (B.3) with $\tilde{\phi}^{(0)}$ being a double differentiable function.
- b) with the boundary conditions at infinity as in the present claim.

Once again, by the same logic as in the proof of the previous claim, both the BVPs have coinciding solution sets. However, now, there cannot be any point ρ_0 at which $\tilde{\phi}^{(0)}$ vanishes or it is unity: such a behavior immediately fixes the solution for the reasons mentioned in the previous proof which does not satisfy the boundary conditions at infinity. Therefore, it is recovered that if a solution exists it has to satisfy $0 < \tilde{\phi}^{(0)} < 1 \forall \rho$. This requires that $\frac{\partial \tilde{\phi}^{(0)}}{\partial \rho}$ is either positive or negative throughout. The latter cannot happen for the boundary conditions to be satisfied at the appropriate ends. Hence, if a solution exists, it has to satisfy the following.

$$\frac{\partial \tilde{\phi}^{(0)}}{\partial \rho} = \sqrt{2} \sqrt{f_{\text{dw}}(\tilde{\phi}^{(0)})}, \quad \frac{\partial \tilde{\phi}^{(0)}}{\partial \rho} > 0 \quad \text{and} \quad 0 < \tilde{\phi}^{(0)} < 1 \quad \forall \rho \in \mathbb{R}. \quad (\text{B.5})$$

We now shift our focus to yet another problem which is the following integral

$$\rho = k + \int_{0.5}^{\phi} \frac{d\phi}{\sqrt{2} \sqrt{f_{\text{dw}}(\phi)}}. \quad (\text{B.6})$$

where k is some constant. The upper limit in the integral can be taken as close to 0 or 1 as desired, the associated values of ρ can be estimated as follows

$$\begin{aligned} \rho - k &= \int_{0.5}^{\phi_i} \frac{d\phi}{\sqrt{2} \sqrt{f_{\text{dw}}(\phi)}} + \int_{\phi_i}^{\phi} \frac{d\phi}{\sqrt{2} \sqrt{f_{\text{dw}}(\phi)}} = \rho_* + \int_{\phi_i}^{\phi} \frac{d\phi}{\sqrt{2} \sqrt{f_{\text{dw}}(0) + f'_{\text{dw}}(0)\phi + f''_{\text{dw}}(\phi_*)\phi^2/2}} \\ &= \rho_* + \int_{\phi_i}^{\phi} \frac{d\phi}{\sqrt{f''_{\text{dw}}(\phi_*)\phi^2}} \leq \rho_* + \frac{1}{\sqrt{f''_{\text{dw},*}}} \int_{\phi_i}^{\phi} \frac{d\phi}{\phi} = \rho_* + \frac{1}{\sqrt{f''_{\text{dw},*}}} \ln \frac{\phi}{\phi_i}. \end{aligned} \quad (\text{B.7})$$

where ϕ_i is some intermediate value, $0 < \phi < \phi_i < 0.5$, such that $f''_{\text{dw}}(\phi_i) > 0$ and $f''_{\text{dw},*} = \max\{f''_{\text{dw}}(\phi) : \phi \in [0, \phi_i]\}$. Thus, as $\phi \rightarrow 0$, $\rho \rightarrow -\infty$ and similarly it can be shown that as $\phi \rightarrow 1$, $\rho \rightarrow \infty$. Further, since $\frac{d\rho}{d\phi}$ is positive for all $0 < \phi < 1$, $\rho(\phi)$ is a monotonically increasing function on $(-1, 1)$, and hence, so is $\rho - k$. Therefore, the latter is invertible;

specifically, Eq. (B.6) can be re-expressed as $\rho - k = I(\phi)$ where $I(\phi)$ is the integral in the equation which is invertible. Let its inverse function be $J : (-\infty, \infty) \rightarrow (0, 1)$. Hence the only solutions of the following problem are $\phi(\rho) = J(\rho - k)$ for some constant k .

$$\frac{d\phi}{d\rho} = \sqrt{2} \sqrt{f_{\text{dw}}(\phi)}, \quad \frac{d\phi}{d\rho} > 0 \quad \text{and} \quad 0 < \phi < 1.$$

And hence, these are the only solutions of Eq. (B.5) and thus, in turn, as the boundary conditions at infinity are also fulfilled, of the BVP of interest. Note that the dependence of the solution on any other variable is only through the dependence of k on it. Further, it is usually common to center the local coordinates on the $\phi = 1/2$ contour irrespective of the position along the interface s thus implying that the zeroth order contribution $\tilde{\phi}^{(0)}(s, \rho, t)$ is independent of s and t . The exponential rate of convergence of the solution to the far end boundary conditions can be realized from Eq. (B.7). Thus the claim is proved.

B.1.3 Analysis of Eqs. (3.26) and (3.27)

The existence of a minimizer of Eq. (3.26) is proved in Ref. [53] but for the case when γ is not restricted to the hyperplane. The same proof works for the current case as well, however, it is mandatory to show that the new metric is non-degenerate. That is, to show that $\left| \frac{d\gamma}{d\beta} \right|$, when γ lies entirely on the hyperplane, can be written as

$$\left| \frac{d\gamma}{d\beta} \right| = 2(\gamma_R)^T M \gamma_R$$

for some $(N-1) \times (N-1)$ invertible matrix M . Where, $(\gamma_R)^T$ is the row matrix corresponding to independent components of γ , i.e, w.l.o.g the first $N-1$ components $(\gamma_1, \gamma_2, \dots, \gamma_{N-1})$. γ_R is the transpose of $(\gamma_R)^T$.

The form of M is that the diagonal entries are all unity and all the off-diagonal ones are filled with $1/2$. The method of mathematical induction can be used to easily prove the invertibility of such a kind of matrix. Once this is done, the existence of a minimizer of the assumed form can be established using the technique presented in Ref. [53].

To prove the existence of the solution of Eq. (3.27) it will be assumed that the minimizing path connecting any two equilibrium phases does not pass through another such phase. Under this assumption, the following equation is studied.

$$\frac{d\rho}{d\beta} = \frac{|\gamma'_{\min}(\beta)|}{\sqrt{W(\gamma_{\min}(\beta))}}, \quad \rho(0) = 0.$$

Note that since the r.h.s is a continuous function on any bounded subset of $(-1, 1)$, $\rho(\beta)$ is defined on $(-1, 1)$ and is the integral of the r.h.s from 0 to β . Furthermore, since

the matrix $\left\{ \frac{\partial^2 W}{\partial \phi_\alpha \partial \phi_\beta} \right\}$ is assumed to be positive definite at the equilibrium points (second derivative test), due to a similar argumentation as used in Eq. (B.7), ρ approaches $\pm\infty$ as β approaches ± 1 at a logarithmic rate. This means, due to positivity of $\frac{d\rho}{d\beta}$, $\beta(\rho)$ exists and is unique and $\beta \rightarrow \pm 1$ at an exponential rate as $\rho \rightarrow \pm\infty$.

Finally, since the solution of Eq. (3.21) is $\tilde{\phi}^{(0)}(\rho) = \gamma_{\min}(\beta(\rho))$, it implies

$$\begin{aligned} \frac{\partial \tilde{\phi}_\alpha^{(0)}}{\partial \rho}(\rho) &= \gamma'_{\min}(\beta(\rho)) \frac{d\beta}{d\rho} \\ \implies \frac{\partial \tilde{\phi}_\alpha^{(0)}}{\partial \rho}(\rho) &\leq \left| \tilde{\phi}'^{(0)}(\rho) \right| \leq \max\{|\gamma'_{\min i}(\beta(\rho))| : i \in 1, 2, \dots, N\} \frac{d\beta}{d\rho}. \end{aligned}$$

That is, the inner solution attains the matching conditions at least at an exponential rate.

As for the assumption of ‘the minimizing path joining two equilibrium points not passing through any other such point’, the author of the thesis hasn’t been able to prove it. Hence, this detail is left unfurnished at the moment.

B.2 Derivations of the matching conditions

The conditions for matching the local solutions to those of the outer ones are derived in the current section by assuming a strong overlap hypothesis [96].

B.2.1 Single boundary layer variable

First, the case of single boundary layer variable is reviewed. To simplify things, only a single independent variable is assumed. Let a function $\phi(r; \epsilon)$, $r \in [0, 1]$ have a regular asymptotic expansion in the gauge set $\{\epsilon^0, \epsilon^1, \epsilon^2, \dots\}$ in the supremum norm in any interval of the form $[A, 1]$ with $A > 0$. When expressed in a stretched variable $\rho = r/\epsilon$, let the function be denoted by $\tilde{\phi}(\rho; \epsilon)$ and let it have a regular expansion within the same gauge set in any interval of the form $[0, A]$ where $A > 0$. Hence, by extension theorems [96], we have the following:

For some $\nu > 0$ and $\mu > 0$

$$\frac{\phi(r; \epsilon) - \phi^{(0)}(r)}{\epsilon} = \phi^{(1)}(r) + \mathcal{o}(1) \text{ uniformly in } r \in [\epsilon^\nu, 1] \quad \text{and} \quad (\text{B.8})$$

$$\frac{\tilde{\phi}(\rho; \epsilon) - \tilde{\phi}^{(0)}(\rho)}{\epsilon} = \tilde{\phi}^{(1)}(\rho) + \mathcal{o}(1) \text{ uniformly in } \rho \in \left[0, \frac{1}{\epsilon^\mu}\right]. \quad (\text{B.9})$$

We assume strong overlap of the extended domains of validity, that is, $\epsilon^\nu < \epsilon^{1-\mu}$. If μ were to be greater than unity, then the local expansion alone approximates the function in the

whole of the domain implying that the problem is not singular but regular, hence we take that $\mu < 1$. Eqs. (B.8) and (B.9) imply that if $\epsilon\phi^{(1)}(r) = \mathfrak{o}(1)$ uniformly in $r \in [\epsilon^\nu, 1]$ and $\epsilon\tilde{\phi}^{(1)}(\rho) = \mathfrak{o}(1)$ uniformly in $\rho \in [0, \frac{1}{\epsilon^\mu}]$ then

$$\phi(r; \epsilon) = \phi^{(0)}(r) + \mathfrak{o}(1) \text{ uniformly in } r \in [\epsilon^\nu, 1] \quad \text{and} \quad (\text{B.10})$$

$$\tilde{\phi}(\rho; \epsilon) = \tilde{\phi}^{(0)}(\rho) + \mathfrak{o}(1) \text{ uniformly in } \rho \in \left[0, \frac{1}{\epsilon^\mu}\right]. \quad (\text{B.11})$$

Re-expressing the first of the above statements in terms of ρ gives

$$\phi(\epsilon\rho; \epsilon) = \phi^{(0)}(\epsilon\rho) + \mathfrak{o}(1) \text{ uniformly in } \rho \in [\epsilon^{\nu-1}, \epsilon^{-1}].$$

Since $\tilde{\phi}(\rho; \epsilon)$ and $\phi(r; \epsilon)$ are the same quantity, for any $\rho \in [\epsilon^{\nu-1}, \epsilon^{-\mu}]$, we have

$$\begin{aligned} 0 &\leq \left| \tilde{\phi}^{(0)}(\rho) - \phi^{(0)}(\epsilon\rho) \right| = \left| \tilde{\phi}^{(0)}(\rho) - \tilde{\phi}(\rho; \epsilon) + \phi(r; \epsilon) - \phi^{(0)}(\epsilon\rho) \right| \\ &\leq \left| \tilde{\phi}^{(0)}(\rho) - \tilde{\phi}(\rho; \epsilon) \right| + \left| \phi(\epsilon\rho; \epsilon) - \phi^{(0)}(\epsilon\rho) \right| \\ &\leq \sup_{\rho \in [\epsilon^{\nu-1}, \epsilon^{-\mu}]} \left| \tilde{\phi}^{(0)}(\rho) - \tilde{\phi}(\rho; \epsilon) \right| + \sup_{\rho \in [\epsilon^{\nu-1}, \epsilon^{-\mu}]} \left| \phi(\epsilon\rho; \epsilon) - \phi^{(0)}(\epsilon\rho) \right|. \end{aligned}$$

In the limit of ϵ vanishing, because of Eqs. (B.10) and (B.11), we have

$$\lim_{\epsilon \rightarrow 0} \left(\tilde{\phi}^{(0)}(\rho) - \phi^{(0)}(\epsilon\rho) \right) = 0.$$

Since $\rho \in [\epsilon^{\nu-1}, \epsilon^{-\mu}]$ and $\mu < 1$, this implies

$$\boxed{\lim_{\rho \rightarrow \infty} \tilde{\phi}^{(0)}(\rho) = \lim_{r \rightarrow 0} \phi^{(0)}(r)}$$

if the limits exist. This is the matching condition for the zeroth order terms of the asymptotic expansion. Repeating the above calculations for the higher order corrections, that is, for Eqs. (B.8) and (B.9) we get

$$\lim_{\epsilon \rightarrow 0} \left(\tilde{\phi}^{(1)}(\rho) - \phi^{(1)}(\epsilon\rho) - \rho \left. \frac{\partial \phi^{(0)}}{\partial r} \right|_{0^+} - \epsilon \rho^2 \frac{1}{2} \left. \frac{\partial^2 \phi^{(0)}}{\partial r^2} \right|_{r^*} + \frac{\phi^{(0)}(0^+) - \tilde{\phi}^{(0)}(\rho)}{\epsilon} \right) = 0$$

where $r^* \in (0, \epsilon^{1-\mu})$, $\rho \in [\epsilon^{\nu-1}, \epsilon^{-\mu}]$ and $\lim_{r \rightarrow 0^+} \frac{\partial \phi^{(0)}}{\partial r}$ is assumed to exist. However, instead of this relation, the following gained fame to be the matching condition for the first order local correction.

$$\boxed{\tilde{\phi}^{(1)}(\rho) = \phi^{(1)}(0^+) + \rho \left. \frac{\partial \phi^{(0)}}{\partial r} \right|_{0^+} + \mathfrak{o}(1) \text{ as } \rho \rightarrow \infty.}$$

That is, either μ is assumed to be less than 0.5 or $\lim_{r \rightarrow 0} \frac{\partial^2 \phi^{(0)}}{\partial r^2}$ is assumed to vanish. Also, $\lim_{\epsilon \rightarrow 0} \left(\phi^{(0)}(0^+) - \tilde{\phi}^{(0)}(\epsilon^{-\mu}) \right)$ is assumed to approach zero faster than ϵ and $\lim_{r \rightarrow 0^+} \phi^{(1)}(r)$ is assumed to exist.

B.2.2 Two boundary layer variables

B.2.2.1 Some specific examples

Before beginning the derivation of the matching conditions, some examples of functions exhibiting a junction behavior are looked at. Our first example is the following.

$$\Phi(x, y; \epsilon) = e^{-x/\epsilon} + e^{-y/\epsilon} \quad \forall x \geq 0, y \geq 0. \quad (\text{B.12})$$

This function has the trivial function as the asymptotic approximation as $\epsilon \rightarrow 0$ when neither of x and y is zero. However, when one of them is zero and the other is not, the constant function 1 is the asymptotic approximation. As a result, traveling towards the x -axis along the dotted red line of Fig. B.2a) gives a limit of $\Phi(x, y; \epsilon) = 0$ as ϵ vanishes for any $y > 0$ but when y exactly equals zero, the limit is 1. Likewise is the behavior for any other vertical line except the y -axis and also any horizontal line except the x -axis. In other words, the function has a boundary layers along the positive x and y axes of the kind considered in section B.2.1. Furthermore, when $x = 0$ and $y = 0$, the value of the function is 2 as $\epsilon \rightarrow 0$. Hence, it exhibits a junction behavior at the origin.

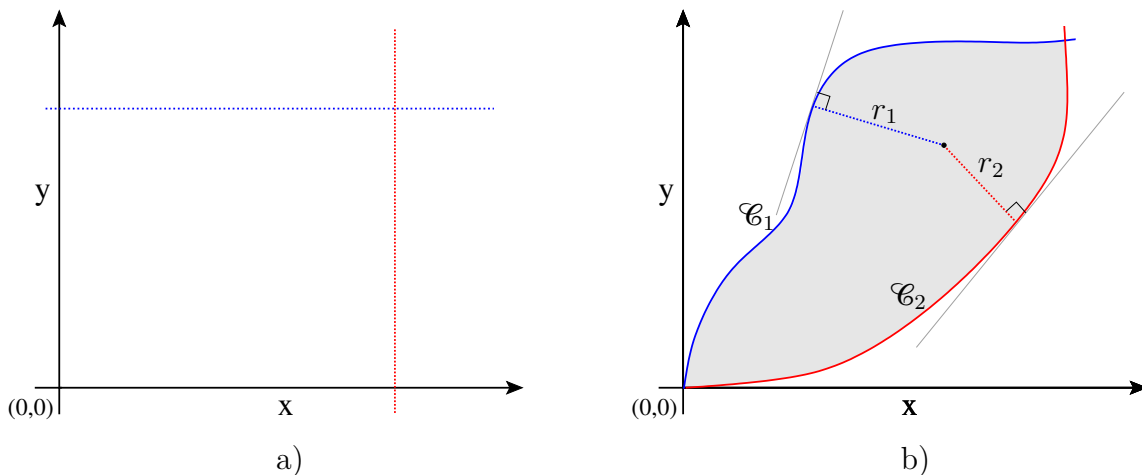


Figure B.2: Domains considered for some example functions exhibiting a junction behavior. Domain of a) corresponds to the simplest function Eq. (B.12), while that in b) is considered for the example in Eq. (B.13).

As a second example, traces of two curves \mathcal{C}_1 and \mathcal{C}_2 , both of which containing the origin, are considered in the first quadrant as shown in Fig. B.2b). Then, for all the points on the paths and in the intermediate region between them, the following function is defined.

$$\Phi(x, y; \epsilon) = e^{-r_1(x,y)/\epsilon} + e^{-r_2(x,y)/\epsilon}. \quad (\text{B.13})$$

where $r_1(x, y)$ is the distance of the point (x, y) from the trace of the first curve and $r_2(x, y)$ is from that of the second. It is easy to see, as before, that this function exhibits boundary layers of the kind considered in section B.2.1 along the paths except at origin where it shows a junction behavior. We now look at the asymptotic behavior of this function as ϵ vanishes. Particularly, the asymptotic expansions in the inner coordinates centered on the traces and on the junction point are connected with each other. The special case of the first trace coinciding with the y -axis and the second one with that of the graph of a function $f(x)$ is considered. That is, for the region depicted in Fig.B.3 and as extended to infinity, the function

$$\Phi(x, y; \epsilon) = e^{-x/\epsilon} + e^{-r(x,y)/\epsilon} \quad (\text{B.14})$$

is studied where, $r(x, y)$ is the distance of the point (x, y) from the graph of $f(x)$. Furthermore, let $f(x)$ be double differentiable with $f'(0) = 0$.

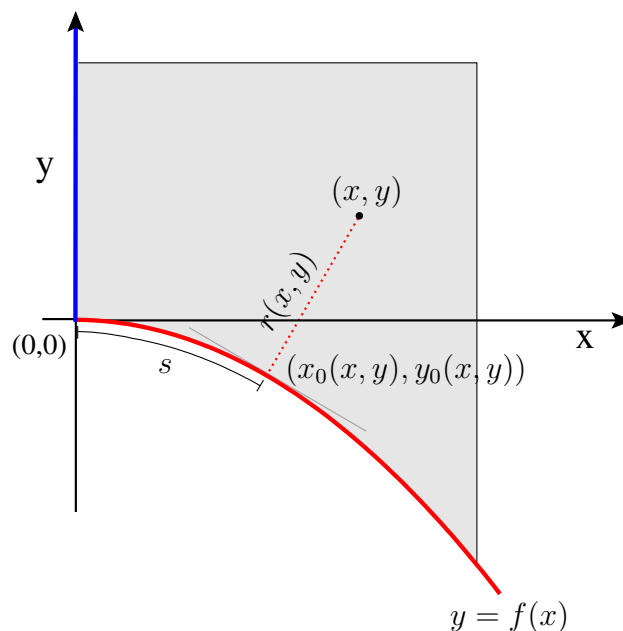


Figure B.3: Domain considered for the example function of Eq. (B.14).

Consider the natural co-ordinates associated with the graph of $f(x)$. Namely, the distance along the graph s and the distance normal to it r . The latter is stretched to give $\rho = r/\epsilon$. We make a further choice that the former is measured from the origin. For simplicity, let us assume that all the points of the region of interest have a unique representation in the local coordinate system (which is in fact true for the particular choice made in Fig. B.3). Then, in the inner coordinates, the function is

$$\tilde{\Phi}(s, \rho; \epsilon) = \Phi(x(s, \epsilon\rho), y(s, \epsilon\rho); \epsilon) = e^{-x(s, \epsilon\rho)/\epsilon} + e^{-\rho}.$$

Now, consider the regular asymptotic expansion of the above in the gauge set $\{\epsilon^0, \epsilon^1, \epsilon^2, \dots\}$ and in any neighborhood not containing $s = 0$, i.e., for instance, in “rectangles” of (s, ρ) of the form $[A, 1] \times [0, B] \forall A > 0$ and $B > 0$. Since $x(s, \epsilon\rho)$ is bounded below by a positive value as $\epsilon \rightarrow 0$ in these domains, the regular expansion in the considered gauge set has only one non-trivial term and that is the zeroth order contribution. Therefore, the asymptotic expansion of $\tilde{\Phi}(s, \rho; \epsilon)$ is identically

$$\begin{aligned}\tilde{\Phi}(s, \rho; \epsilon) &\sim \tilde{\Phi}^{(0)}(s, \rho) + \epsilon\tilde{\Phi}^{(1)}(s, \rho) + \epsilon^2\tilde{\Phi}^{(2)}(s, \rho) + \dots \\ &= e^{-\rho} + \epsilon 0 + \epsilon^2 0 + \dots.\end{aligned}$$

Next, we consider the inner expansion associated with the junction. Let the stretched coordinates centered at the junction be $\zeta = x/\epsilon$ and $\xi = y/\epsilon$. The function $\Phi(x, y; \epsilon)$ in these coordinates is

$$\hat{\Phi}(\zeta, \xi; \epsilon) := \Phi(\epsilon\zeta, \epsilon\xi; \epsilon) = e^{-\zeta} + e^{-r(\epsilon\zeta, \epsilon\xi)/\epsilon} \quad (\text{B.15})$$

whose domain of interest is $\{(\zeta, \xi) \in \mathbb{R} : \zeta \in [0, \infty) \text{ and } \xi \geq f(\epsilon\zeta)/\epsilon\}$. Now we consider the regular asymptotic expansion of the above in the gauge set $\{\epsilon^0, \epsilon^1, \epsilon^2, \dots\}$ in any neighborhood containing a segment of ξ -axis and particularly in rectangles of (ζ, ξ) of the form $[0, A] \times [B, C] \forall A > 0$ and $0 < B < C$. In these regions, the following is analyzed.

$$r(x, y) = \sqrt{(x - x_0(x, y))^2 + (y - y_0(x, y))^2} \quad (\text{B.16})$$

where $(x_0(x, y), y_0(x, y))$ is the nearest point of (x, y) on the graph of $f(x)$. Therefore, by definition, $y_0(x, y) = f(x_0(x, y))$ and

$$\begin{aligned}\frac{y - f(x_0)}{x - x_0} f'(x_0) &= -1 \\ \implies x_0 - x &= (y - f(x_0)) f'(x_0).\end{aligned} \quad (\text{B.17})$$

Hence, we have

$$\begin{aligned}\frac{r(\epsilon\zeta, \epsilon\xi)}{\epsilon} &= \frac{1}{\epsilon} \sqrt{\{\epsilon\zeta - x_0(\epsilon\zeta, \epsilon\xi)\}^2 + \{\epsilon\xi - f(x_0(\epsilon\zeta, \epsilon\xi))\}^2} \\ &= \frac{1}{\epsilon} \sqrt{[\{\epsilon\xi - f(x_0(\epsilon\zeta, \epsilon\xi))\} f'(x_0(\epsilon\zeta, \epsilon\xi))]^2 + \{\epsilon\xi - f(x_0(\epsilon\zeta, \epsilon\xi))\}^2} \\ &= \frac{\epsilon\xi - f(x_0(\epsilon\zeta, \epsilon\xi))}{\epsilon} \sqrt{1 + [f'(x_0(\epsilon\zeta, \epsilon\xi))]^2} \\ &= \frac{\epsilon\xi - \left\{ f(0) + f'(0)x_0(\epsilon\zeta, \epsilon\xi) + \frac{f''(x_*)}{2} x_0^2(\epsilon\zeta, \epsilon\xi) \right\}}{\epsilon} \sqrt{1 + [f'(x_0(\epsilon\zeta, \epsilon\xi))]^2} \\ &= \left\{ \xi - \frac{f''(x_*)}{2\epsilon} x_0^2(\epsilon\zeta, \epsilon\xi) \right\} \sqrt{1 + [f'(x_0(\epsilon\zeta, \epsilon\xi))]^2} \\ &= \left\{ \xi - \frac{f''(x_*)}{2\epsilon} x_0^2(\epsilon\zeta, \epsilon\xi) \right\} \left\{ 1 + \frac{f'(x_{**}) f''(x_{**})}{\sqrt{1 + [f''(x_{**})]^2}} x_0(\epsilon\zeta, \epsilon\xi) \right\}.\end{aligned} \quad (\text{B.18})$$

We now estimate the term $x_0(\epsilon\zeta, \epsilon\xi)$. Consider the Eq. (B.17) for $x = \epsilon\zeta$ and $y = \epsilon\xi$.

$$x_0 = \epsilon\zeta + (\epsilon\xi - f(x_0)) f'(x_0) \quad (\text{B.19})$$

$$= \epsilon\zeta + \left(\epsilon\xi - f(0) - f'(0)x_0 - \frac{f''(x^*)}{2}x_0^2 \right) (f'(0) + f''(x^{**})x_0)$$

$$= \epsilon\zeta + \left(\epsilon\xi - \frac{f''(x^*)}{2}x_0^2 \right) f''(x^{**})x_0$$

$$\implies \epsilon\zeta = (1 - \epsilon\xi f''(x^{**})) x_0 + \frac{f''(x^*)}{2} f''(x^{**}) x_0^3. \quad (\text{B.20})$$

Since $f(x)$ is double differentiable and $f'(0) = 0$, for some chosen constants $\zeta \geq 0$ and $\xi > 0$, $(\epsilon\zeta, \epsilon\xi)$ eventually ends up in the domain of interest, i.e., $\epsilon\xi \geq f(\epsilon\zeta)$ as $\epsilon \rightarrow 0$. Further, since every such point has a unique representation in the (s, ρ) coordinate system by assumption, it follows from Eq. (B.19) that the associated $x_0(\epsilon\zeta, \epsilon\xi) \rightarrow 0$. This means, from Eq. (B.20) we will have

$$\begin{aligned} \epsilon\zeta &\geq (1 - \epsilon\xi f''(x^{**})) x_0 \quad \text{and} \\ \epsilon\zeta &\leq \left(1 - \epsilon\xi f''(x^{**}) + \frac{f''(x^*)}{2} f''(x^{**}) \right) x_0 \end{aligned}$$

for small enough ϵ . That is

$$\frac{\epsilon\zeta}{\left(1 - \epsilon\xi f''(x^{**}) + \frac{f''(x^*)}{2} f''(x^{**}) \right)} \leq x_0 \leq \frac{\epsilon\zeta}{(1 - \epsilon\xi f''(x^{**}))}$$

for small enough ϵ . Or in other words, $x_0/\epsilon\zeta = \mathcal{O}(1)$ as $\epsilon \rightarrow 0$ due to the existence of $f''(0)$. From this, using limit laws, it follows from Eq. (B.20) that $\lim_{\epsilon \rightarrow 0} x_0/\epsilon = \zeta$. Therefore, Eq. (B.18) becomes

$$\begin{aligned} \frac{r(\epsilon\zeta, \epsilon\xi)}{\epsilon} &= \left\{ \xi - \epsilon \frac{f''(0)}{2} \zeta^2 \right\} \left\{ 1 + \frac{\mathfrak{o}(1) f''(0)}{\sqrt{1 + [f''(0)]^2}} \epsilon \zeta \right\} \quad \text{as } \epsilon \rightarrow 0 \\ \implies \frac{r(\epsilon\zeta, \epsilon\xi)}{\epsilon} &= \xi - \epsilon \frac{f''(0)}{2} \zeta^2 + \mathfrak{o}(\epsilon). \end{aligned}$$

Substituting this in Eq. (B.15) gives

$$\stackrel{\downarrow}{\Phi}(\zeta, \xi; \epsilon) = e^{-\zeta} + e^{-\xi} \left(1 + \epsilon \frac{f''(0)}{2} \zeta^2 + \mathfrak{o}(\epsilon) \right).$$

That is,

$$\begin{aligned} \stackrel{\downarrow}{\Phi}^{(0)}(\zeta, \xi) &= e^{-\zeta} + e^{-\xi} \quad \text{and} \\ \stackrel{\downarrow}{\Phi}^{(1)}(\zeta, \xi) &= e^{-\xi} \frac{f''(0)}{2} \zeta^2. \end{aligned}$$

Therefore, we have

$$\overset{\perp}{\Phi}^{(1)}(\zeta, \xi) = -\frac{\partial \tilde{\Phi}^{(0)}(s, \rho)}{\partial \rho}(0, \xi) \frac{f''(0)}{2} \zeta^2$$

implying that the matching conditions for relating the inner solution at the junction with the inner solution along a binary interface may very well have square dependence for the matching variable. This will now be derived explicitly for more generic functions exhibiting a junction behavior.

B.2.2.2 Matching relations for the generic case

Let $\phi(x, y; \epsilon)$ have local asymptotic regular approximation along a path whose natural and stretched coordinates are (s, ρ) . Let $s = 0$ correspond to the origin. Let the path correspond to the graph of a double differentiable function $f(x)$ with $f'(0) = 0$ for $s \in [0, 1]$. Let the gauge set be $\{0, \epsilon, \epsilon^2, \dots\}$ and the expansion be accurate upto order ϵ . That is, $\tilde{\phi}(s, \rho; \epsilon) = \tilde{\phi}^{(0)}(s, \rho) + \epsilon \tilde{\phi}^{(1)}(s, \rho) + \mathfrak{o}(\epsilon)$ uniformly in $(s, \rho) \in [A, 1] \times [-B, B] \forall A > 0, B > 0$. By extension theorem, we have

$$\tilde{\phi}(s, \rho; \epsilon) = \tilde{\phi}^{(0)}(s, \rho) + \epsilon \tilde{\phi}^{(1)}(s, \rho) + \mathfrak{o}(\epsilon) \text{ uniformly in } (s, \rho) \in [\epsilon^{\nu'}, 1] \times \left[-\frac{1}{\epsilon^{\nu'}}, \frac{1}{\epsilon^{\nu'}} \right]. \quad (\text{B.21})$$

For the sake of brevity, we denote the region $[\epsilon^{\nu'}, 1]$ by R_s and $\times \left[-\frac{1}{\epsilon^{\nu'}}, \frac{1}{\epsilon^{\nu'}} \right]$ by R_ρ . For the reason expounded in section B.2.1, we take that $\nu' < 1$. The domain of validity when considered in the outer co-ordinates is

$$\begin{aligned} x(s, \rho) &= x_0(s) + \hat{n}_x(s) \rho \epsilon = x_0(s) - \frac{f'(x_0(s))}{\sqrt{1 + f'(x_0(s))^2}} \rho \epsilon \quad \forall (s, \rho) \in R_s \times R_\rho \\ y(s, \rho) &= f(x_0(s)) + \hat{n}_y(s) \rho \epsilon = f(x_0(s)) + \frac{1}{\sqrt{1 + f'(x_0(s))^2}} \rho \epsilon \quad \forall (s, \rho) \in R_s \times R_\rho. \end{aligned} \quad (\text{B.22})$$

Since $\nu' < 1$, this means that for small enough ϵ , different (s, ρ) from the domain of validity corresponds to distinct spatial points. That is, there is no non-uniqueness in the representation of the points.

Next, let $\phi(x, y; \epsilon)$ exhibit a junction behaviour at $(0, 0)$. In the junction's local co-ordinates ($\zeta = \frac{x}{\epsilon}, \xi = \frac{y}{\epsilon}$), let it have an asymptotic expansion as follows

$$\begin{aligned} \overset{\perp}{\phi}(\zeta, \xi; \epsilon) &= \overset{\perp}{\phi}^{(0)}(\zeta, \xi) + \epsilon \overset{\perp}{\phi}^{(1)}(\zeta, \xi) + \mathfrak{o}(\epsilon) \text{ uniformly in} \\ &(\zeta, \xi) \in [0, C] \times [-D, D] \quad \forall C > 0 \text{ and } D > 0. \end{aligned} \quad (\text{B.23})$$

By extension theorem, we have

$$\begin{aligned} \overset{\frown}{\phi}(\zeta, \xi; \epsilon) &= \overset{\frown}{\phi}^{(0)}(\zeta, \xi) + \epsilon \overset{\frown}{\phi}^{(1)}(\zeta, \xi) + \mathfrak{o}(\epsilon) \quad \text{uniformly in} \\ (\zeta, \xi) &\in [0, \epsilon^\mu] \times \left[-\frac{1}{\epsilon^{\mu'}}, \frac{1}{\epsilon^\mu}\right]. \end{aligned} \quad (\text{B.24})$$

For a similar reason as in section B.2.1, let $\mu' < 1$.

We now re-express the domain of validity of the expansion of Eq. (B.21) in terms of the (ζ, ξ) co-ordinates system. However, of interest is not an exact prescription but an estimation of the “end points” up to the approximate powers of ϵ . Consider $x_0(s)$,

$$x_0(s) = x_0(0) + \left. \frac{dx_0}{ds} \right|_{s=0} s + \left. \frac{d^2x_0}{ds^2} \right|_{s_*} \frac{s^2}{2}. \quad (\text{B.25})$$

Since $x_0(s)$ is invertible and $x_0(0) = 0$, we have

$$\left. \frac{dx_0}{ds} \right|_{s=0} = \frac{1}{\left. \frac{ds}{dx_0} \right|_{x_0=0}} = \frac{1}{\sqrt{1 + f'(x_0(s))^2}} = \frac{1}{\sqrt{1 + f'(0)^2}} = 1, \quad (\text{B.26})$$

and

$$\frac{d^2x_0}{ds^2} = -\frac{f'(x_0(s_*))f''(x_0(s_*))}{1 + (f'(x_0(s_*)))^2} = -\frac{f'(x_*)f''(x_*)}{1 + (f'(x_*))^2}, \quad (\text{B.27})$$

where $x_* = x_0(s_*) \leq s_*$. Since $f'(x_0(s))$ and $f''(x_0(s))$ are bounded $\forall s \in [0, 1]$, this implies that when $s = \mathfrak{O}_s(\epsilon^\nu)$ then $x_0(s) = \mathfrak{O}_s(\epsilon^\nu)$. Therefore, for the domain of validity in Eq. (B.21), $x_0(s) \in [A\epsilon^\nu, A']$ for some positive constants A and A' . Similarly, the upper and lower bounds for $\hat{n}_x(s)\rho\epsilon$ for the domain considered for (s, ρ) in Eq. (B.21) can be estimated as

$$\begin{aligned} |\hat{n}_x(s)\rho\epsilon| &= \frac{\left| f'(x_0(s)) + f''(x_0(s)) \left. \frac{dx_0}{ds} \right|_{s_*} \right|}{\sqrt{1 + f'(x_0(s))^2}} \rho\epsilon = \frac{|f''(x_0(s))|}{\sqrt{1 + f'(x_0(s))^2} \sqrt{1 + f'(x_0(s_*))^2}} s\rho\epsilon \\ &\in \left[\mathfrak{O}_s(\epsilon^{\nu+1-\mu'}), \mathfrak{O}_s(\epsilon^{1-\mu'}) \right] \quad \text{when } (s, \rho) \in R_\nu. \end{aligned} \quad (\text{B.28})$$

Therefore, $x(s, \rho) \in [B\epsilon^\nu, B']$ for some positive B and B' which implies $\zeta \in [B\epsilon^{\nu-1}, B'\epsilon^{-1}]$ for the domain of the local approximation of Eq. (B.21). We carry out similar analysis for $y(s, \rho)$:

$$\begin{aligned} y(s, \rho) &= f(0) + f'(0)x_0(s) + f''(x_*) \frac{x_0^2(s)}{2} + \frac{1}{\sqrt{1 + f'(x_0(s))^2}} \rho\epsilon \\ &= \frac{1}{2} \left(s + \left. \frac{d^2x_0}{ds^2} \right|_{s_{**}} \frac{s^2}{2} \right)^2 + \frac{1}{\sqrt{1 + f'(x_0(s))^2}} \rho\epsilon \\ &= \mathfrak{O}_s(\epsilon^{2\nu}) + \mathfrak{O}_s(\epsilon^{1-\nu'}) \quad \text{when } s = \mathfrak{O}_s(\epsilon^\nu) \quad \text{and } \rho = \mathfrak{O}_s(1/\epsilon^{\nu'}). \end{aligned} \quad (\text{B.29})$$

Hence, $\xi \in [-C\epsilon^{-\max(1-2\nu, \nu')}, C\epsilon^{-\max(1-2\nu, \nu')}]$ for some $C > 0$ for the domain of the local approximation of Eq. (B.21). As a consequence, Eq. (B.21) can be re-expressed as follows

$$\begin{aligned} \tilde{\phi}(s(\epsilon\zeta, \epsilon\xi), \rho(\epsilon\zeta, \epsilon\xi); \epsilon) &= \tilde{\phi}^{(0)}(s(\epsilon\zeta, \epsilon\xi), \rho(\epsilon\zeta, \epsilon\xi)) + \epsilon\tilde{\phi}^{(1)}(s(\epsilon\zeta, \epsilon\xi), \rho(\epsilon\zeta, \epsilon\xi)) + \mathfrak{o}(\epsilon) \\ &\text{uniformly in } (\zeta, \xi) \in [B\epsilon^{\nu-1}, B'\epsilon^{-1}] \times [-C\epsilon^{-\max(1-2\nu, \nu')}, C\epsilon^{-\max(1-2\nu, \nu')}] . \end{aligned} \quad (\text{B.30})$$

We next proceed by assuming a strong overlap, i.e., $\epsilon^{\nu-1} < \epsilon^\mu$. Furthermore, if $\lim_{\epsilon \rightarrow 0} \epsilon \|\tilde{\phi}^{(1)}(s, \rho)\|_{L^\infty(R_s \times R_\rho)} = 0$ and $\lim_{\epsilon \rightarrow 0} \epsilon \|\overset{\perp}{\phi}^{(1)}(\zeta, \xi)\|_{L^\infty([0, \epsilon^{-\mu}] \times [-1/\epsilon^{\mu'}, 1/\epsilon^{\mu'}])} = 0$ then

$$\begin{aligned} \tilde{\phi}(s(\epsilon\zeta, \epsilon\xi), \rho(\epsilon\zeta, \epsilon\xi); \epsilon) &= \tilde{\phi}^{(0)}(s(\epsilon\zeta, \epsilon\xi), \rho(\epsilon\zeta, \epsilon\xi)) + \mathfrak{o}(1) \quad \text{uniformly in} \\ &(\zeta, \xi) \in [B\epsilon^{\nu-1}, B'\epsilon^{-1}] \times [-C\epsilon^{-\max(1-2\nu, \nu')}, C\epsilon^{-\max(1-2\nu, \nu')}] \end{aligned} \quad (\text{B.31})$$

and

$$\overset{\perp}{\phi}(\zeta, \xi) = \overset{\perp}{\phi}^{(0)}(\zeta, \xi) + \mathfrak{o}(1) \quad \text{uniformly in } (\zeta, \xi) \in [0, \epsilon^{-\mu}] \times [-\frac{1}{\epsilon^{\mu'}}, \frac{1}{\epsilon^{\mu'}}]. \quad (\text{B.32})$$

We define $R_\zeta = [B\epsilon^{\nu-1}, \epsilon^{-\mu}]$ and $R_\xi = [-D\epsilon^{-\min\{\mu', \max\{1-2\nu, \nu'\}\}}, D\epsilon^{-\min\{\mu', \max\{1-2\nu, \nu'\}\}}]$ in the following. Now consider

$$\left| \overset{\perp}{\phi}^{(0)}(\zeta, \xi) - \tilde{\phi}^{(0)}(s(\epsilon\zeta, \epsilon\xi), \rho(\epsilon\zeta, \epsilon\xi)) \right| \quad \text{for any } (\zeta, \xi) \in R_\zeta \times R_\xi. \quad (\text{B.33})$$

One can write

$$\begin{aligned} &\left| \overset{\perp}{\phi}^{(0)}(\zeta, \xi) - \tilde{\phi}^{(0)}(s(\epsilon\zeta, \epsilon\xi), \rho(\epsilon\zeta, \epsilon\xi)) \right| \leq \left| \overset{\perp}{\phi}^{(0)}(\zeta, \xi) - \overset{\perp}{\phi}(\zeta, \xi; \epsilon) \right| \\ &\quad + \left| \tilde{\phi}^{(0)}(s(\epsilon\zeta, \epsilon\xi), \rho(\epsilon\zeta, \epsilon\xi)) - \tilde{\phi}(s(\epsilon\zeta, \epsilon\xi), \rho(\epsilon\zeta, \epsilon\xi); \epsilon) \right| \\ &\leq \sup_{\zeta \in R_\zeta, \xi \in R_\xi} \left\{ \left| \overset{\perp}{\phi}^{(0)}(\zeta, \xi) - \overset{\perp}{\phi}(\zeta, \xi; \epsilon) \right| + \left| \tilde{\phi}^{(0)}(s(\epsilon\zeta, \epsilon\xi), \rho(\epsilon\zeta, \epsilon\xi)) - \tilde{\phi}(s(\epsilon\zeta, \epsilon\xi), \rho(\epsilon\zeta, \epsilon\xi); \epsilon) \right| \right\} \\ &\leq \sup_{\zeta \in [0, \epsilon^{-\mu}], \xi \in [-1/\epsilon^{\mu'}, 1/\epsilon^{\mu'}]} \left| \overset{\perp}{\phi}^{(0)}(\zeta, \xi) - \overset{\perp}{\phi}(\zeta, \xi; \epsilon) \right| \\ &\quad + \sup_{\substack{\zeta \in [B\epsilon^{\nu-1}, B'\epsilon^{-1}] \\ \xi \in [-C\epsilon^{-\max(1-2\nu, \nu')}, C\epsilon^{-\max(1-2\nu, \nu')}]}} \left| \tilde{\phi}^{(0)}(s(\epsilon\zeta, \epsilon\xi), \rho(\epsilon\zeta, \epsilon\xi)) - \tilde{\phi}(s(\epsilon\zeta, \epsilon\xi), \rho(\epsilon\zeta, \epsilon\xi); \epsilon) \right|. \end{aligned} \quad (\text{B.34})$$

In the limit $\epsilon \rightarrow 0$, due to Eqs. (B.31) and (B.32), we have

$$\lim_{\epsilon \rightarrow 0} \left(\overset{\perp}{\phi}^{(0)}(\zeta, \xi) - \tilde{\phi}^{(0)}(s(\epsilon\zeta, \epsilon\xi), \rho(\epsilon\zeta, \epsilon\xi)) \right) = 0 \quad \forall (\zeta, \xi) \in R_\zeta \times R_\xi \quad (\text{B.35})$$

or,

$$\lim_{\epsilon \rightarrow 0} \overset{\lambda(0)}{\phi}(\zeta, \xi) = \lim_{\epsilon \rightarrow 0} \tilde{\phi}^{(0)}(s(\epsilon\zeta, \epsilon\xi), \rho(\epsilon\zeta, \epsilon\xi)), \quad (\text{B.36})$$

if the limits exist. Note that due to the domain of concern for (ζ, ξ) being the way it is, as $\epsilon \rightarrow 0$, ζ grows arbitrarily large. Therefore, Eq. (B.36) becomes

$$\lim_{\zeta \rightarrow \infty} \overset{\lambda(0)}{\phi}(\zeta, \xi) = \lim_{\epsilon \rightarrow 0} \tilde{\phi}^{(0)}(s(\epsilon\zeta), \rho(\epsilon\zeta, \epsilon\xi)). \quad (\text{B.37})$$

Let us now estimate the behavior of $s(\epsilon\zeta, \epsilon\xi)$ and $\rho(\epsilon\zeta, \epsilon\xi)$ as $\epsilon \rightarrow 0$. We re-write them as

$$\begin{aligned} s(\epsilon\zeta, \epsilon\xi) &= s(0, \epsilon\xi) + \left. \frac{\partial s}{\partial x} \right|_{(*, \epsilon\xi)} \epsilon\zeta \\ &= s(0, \epsilon\xi) + \left. \frac{ds}{dx_0} \right|_{x_0(*, \epsilon\xi)} \left. \frac{\partial x_0}{\partial x} \right|_{(*, \epsilon\xi)} \epsilon\zeta = 0 + \sqrt{1 + f'(x_0(*, \epsilon\xi))^2} \left. \frac{\partial x_0}{\partial x} \right|_{(*, \epsilon\xi)} \epsilon\zeta \end{aligned} \quad (\text{B.38})$$

and

$$\begin{aligned} \rho(\epsilon\zeta, \epsilon\xi) &= \rho(0, \epsilon\xi) + \left. \frac{\partial \rho}{\partial x} \right|_{(0, \epsilon\xi)} \epsilon\zeta + \left. \frac{\partial^2 \rho}{\partial x^2} \right|_{(*, \epsilon\xi)} \frac{\epsilon^2 \zeta^2}{2} \\ &= \xi + \left. \frac{\partial r}{\partial x} \right|_{(0, \epsilon\xi)} \zeta + \left. \frac{\partial^2 r}{\partial x^2} \right|_{(*, \epsilon\xi)} \frac{\epsilon \zeta^2}{2} \end{aligned} \quad (\text{B.39})$$

where $x_0(\epsilon\zeta, \epsilon\xi)$ is the solution of Eq. (B.19) and $r(x, y)$ is given by Eq. (B.16). Since it is established that each $(\epsilon\zeta, \epsilon\xi)$ for the domain concerned for (ζ, ξ) has a unique representation in the (s, ρ) co-ordinate system for small enough ϵ , $x_0(*, \epsilon\xi) \rightarrow 0$ as $\epsilon \rightarrow 0$. Further, differentiating Eq. (B.17), we have,

$$\begin{aligned} \frac{\partial x_0}{\partial x} - y f''(x_0) \frac{\partial x_0}{\partial x} - f'(x_0)^2 \frac{\partial x_0}{\partial x} - f(x_0) f''(x_0) \frac{\partial x_0}{\partial x} &= 1 \\ \implies \left. \frac{\partial x_0}{\partial x} \right|_{(*, \epsilon\xi)} &= \frac{1}{(1 - \epsilon\xi f''(x_0) - (f'(x_0))^2 \frac{\partial x_0}{\partial x} - f(x_0) f''(x_0))} \\ \implies \left. \frac{\partial x_0}{\partial x} \right|_{(*, \epsilon\xi)} &\rightarrow 1 \text{ as } \epsilon \rightarrow 0. \end{aligned} \quad (\text{B.40})$$

Similarly, from Eq. (B.16), we have for $\frac{\partial r}{\partial x}$

$$\begin{aligned} \frac{\partial r}{\partial x} &= \frac{x - x_0}{\sqrt{(x - x_0)^2 + (y - f(x_0))^2}} \\ &= -\frac{f'(x_0)}{\sqrt{1 + (f'(x_0))^2}} \\ \implies \left. \frac{\partial r}{\partial x} \right|_{(0, \epsilon\xi)} &= 0. \end{aligned} \quad (\text{B.41})$$

For $\frac{\partial^2 r}{\partial x^2}$, we have

$$\begin{aligned} \frac{\partial^2 r}{\partial x^2} &= -\frac{\sqrt{1+(f'(x_0))^2}f''(x_0)\frac{\partial x_0}{\partial x} - \frac{(f'(x_0)^2)f''(x_0)}{\sqrt{1+(f'(x_0))^2}}\frac{\partial x_0}{\partial x}}{1+(f'(x_0))^2} \\ &= -\kappa(x_0)\frac{1}{(1-\epsilon\xi f''(x_0) - (f'(x_0))^2\frac{\partial x_0}{\partial x} - f(x_0)f''(x_0))}. \\ \implies \frac{\partial^2 r}{\partial x^2}\Big|_{(*, \epsilon\xi)} &\rightarrow -\kappa(0) \text{ as } \epsilon \rightarrow 0. \end{aligned} \quad (\text{B.42})$$

where $\kappa(x_0)$ is the curvature of the function $f(x)$ at x_0 and is defined as $\kappa(x) = \frac{f''(x)}{(\sqrt{1+(f'(x))^2})^3}$. That is, with the sign convention that concave upwards has positive curvature.

Eqs. (B.38), (B.39), (B.40), (B.41) and (B.42) indicate that $s(\epsilon\zeta, \epsilon\xi) \rightarrow 0$ and $\rho(\epsilon\zeta, \epsilon\xi) \rightarrow \xi$ as $\epsilon \rightarrow 0$ for $(\zeta, \xi) \in R_\zeta \times R_\xi$ under the assumption that $1 > 2\min\{\mu', \max\{1-2\nu, \nu'\}\}$. Which implies that Eq. (B.37) modifies as

$$\boxed{\lim_{\zeta \rightarrow \infty} \overset{\perp}{\phi}(\zeta, \xi) = \lim_{s \rightarrow 0} \tilde{\phi}^{(0)}(s, \xi)} \quad (\text{B.43})$$

This is the matching relation for the zeroth order term of the local expansion corresponding to the junction point. We repeat the above analysis for Eqs. (B.24) and (B.30) to obtain the matching condition for the first order correction:

Consider

$$\left| \overset{\perp}{\phi}^{(1)}(\zeta, \xi) + \frac{1}{\epsilon} \overset{\perp}{\phi}^{(0)}(\zeta, \xi) - \tilde{\phi}^{(1)}(s(\epsilon\zeta, \epsilon\xi) - \frac{1}{\epsilon} \tilde{\phi}^{(0)}(s(\epsilon\zeta, \epsilon\xi))) \right| \quad (\text{B.44})$$

for any $(\zeta, \xi) \in R_\zeta \times R_\xi$

$$\implies \lim_{\epsilon \rightarrow 0} \left(\overset{\perp}{\phi}^{(1)}(\zeta, \xi) - \tilde{\phi}^{(1)}(s(\epsilon\zeta, \epsilon\xi), \rho(\epsilon\zeta, \epsilon\xi)) - \frac{1}{\epsilon} \left[\tilde{\phi}^{(0)} \left(0 + \frac{\partial s}{\partial x}\Big|_{(*, \epsilon\xi)} \epsilon\zeta, \xi + 0 + \frac{\partial^2 r}{\partial x^2}\Big|_{(*, \epsilon\xi)} \frac{\epsilon\zeta^2}{2} \right) - \overset{\perp}{\phi}^{(0)}(\zeta, \xi) \right] \right) = 0$$

$$\implies \lim_{\epsilon \rightarrow 0} \left(\overset{\perp}{\phi}^{(1)}(\zeta, \xi) - \tilde{\phi}^{(1)}(s(\epsilon\zeta, \epsilon\xi), \rho(\epsilon\zeta, \epsilon\xi)) - \frac{1}{\epsilon} \left[\tilde{\phi}^{(0)}(0, \xi) + \frac{\partial \tilde{\phi}^{(0)}}{\partial s}\Big|_{(*, *)} \frac{\partial s}{\partial x}\Big|_{(*, \epsilon\xi)} \epsilon\zeta + \frac{\partial \tilde{\phi}^{(0)}}{\partial \rho}\Big|_{(*, *)} \frac{\partial^2 r}{\partial x^2}\Big|_{(*, \epsilon\xi)} \frac{\epsilon\zeta^2}{2} - \overset{\perp}{\phi}^{(0)}(\zeta, \xi) \right] \right) = 0$$

$$\implies \boxed{\overset{\perp}{\phi}^{(1)}(\zeta, \xi) = \lim_{s \rightarrow 0} \left(\overset{\perp}{\phi}^{(1)}(s, \xi) + \zeta \frac{\partial \tilde{\phi}^{(0)}}{\partial s}(s, \xi) - \frac{\kappa(0)}{2} \zeta^2 \frac{\partial \tilde{\phi}^{(0)}}{\partial \rho}(s, \xi) \right) + \mathcal{O}(1) \text{ as } \zeta \rightarrow \infty} \quad (\text{B.45})$$

assuming that the limit exists and that $\lim_{\epsilon \rightarrow 0} \overset{\perp}{\phi}^{(0)}(\epsilon^{-\mu}, \xi)$ approaches $\tilde{\phi}^{(0)}(0, \xi)$ faster than ϵ .

B.3 Analysis of the explicit solution of Eq. (3.32) for W^{FP} multi-well

The Eqs. (3.32) written down explicitly for the multi-well W^{FP} read

$$\begin{aligned}
\frac{\partial^2 \hat{\phi}_1^{(0)}}{\partial \zeta^2} + \frac{\partial^2 \hat{\phi}_1^{(0)}}{\partial \xi^2} &= 4a \hat{\phi}_1^{(0)} \left(\hat{\phi}_1^{(0)} - 0.5 \right) \left(\hat{\phi}_1^{(0)} - 1 \right) - \frac{4a}{3} \sum_{\alpha=1}^3 \hat{\phi}_\alpha^{(0)} \left(\hat{\phi}_\alpha^{(0)} - 0.5 \right) \left(\hat{\phi}_\alpha^{(0)} - 1 \right) \\
\frac{\partial^2 \hat{\phi}_2^{(0)}}{\partial \zeta^2} + \frac{\partial^2 \hat{\phi}_2^{(0)}}{\partial \xi^2} &= 4a \hat{\phi}_2^{(0)} \left(\hat{\phi}_2^{(0)} - 0.5 \right) \left(\hat{\phi}_2^{(0)} - 1 \right) - \frac{4a}{3} \sum_{\alpha=1}^3 \hat{\phi}_\alpha^{(0)} \left(\hat{\phi}_\alpha^{(0)} - 0.5 \right) \left(\hat{\phi}_\alpha^{(0)} - 1 \right) \\
\frac{\partial^2 \hat{\phi}_3^{(0)}}{\partial \zeta^2} + \frac{\partial^2 \hat{\phi}_3^{(0)}}{\partial \xi^2} &= 4a \hat{\phi}_3^{(0)} \left(\hat{\phi}_3^{(0)} - 0.5 \right) \left(\hat{\phi}_3^{(0)} - 1 \right) - \frac{4a}{3} \sum_{\alpha=1}^3 \hat{\phi}_\alpha^{(0)} \left(\hat{\phi}_\alpha^{(0)} - 0.5 \right) \left(\hat{\phi}_\alpha^{(0)} - 1 \right)
\end{aligned} \tag{B.46}$$

when it is kept in mind that the solution space is restricted to functions satisfying the summation rule property, i.e., $\hat{\phi}_1^{(0)}(\zeta, \xi) + \hat{\phi}_2^{(0)}(\zeta, \xi) + \hat{\phi}_3^{(0)}(\zeta, \xi) = 1 \forall (\zeta, \xi) \in \mathbb{R}^2$.

Bollada et.al proposed a possible multi-phase-field profile around a triple junction by generalizing the “tanh solution” of the 1D problem. Using it, they studied what gradient energy will be associated with a spatial point that corresponds to a particular phase field value, for various choices of the gradient energy forms. However, it is unclear from their manuscript if they explicitly verified whether the proposed profile does actually solve the equilibrium equations for any of the combinations of the potential wells and the gradient energy forms considered. It will now be tested if the postulated profile, which is reproduced in Eq. (B.47), is the solution of the above equations, Eq. (B.46).

B.3.1 Verification of the exactness

The equilibrium phase-field profile around a triple junction hypothesized by Bollada *et al.* is considered as a potential candidate for the solution of Eq. (B.46). That is,

$$\begin{aligned}
\hat{\phi}_1^{(0)} &= \frac{1}{1 + e^{(\zeta n_{12}^\zeta + \xi n_{12}^\xi)} + e^{(\zeta n_{13}^\zeta + \xi n_{13}^\xi)}} \\
\hat{\phi}_2^{(0)} &= \frac{1}{1 + e^{(\zeta n_{21}^\zeta + \xi n_{21}^\xi)} + e^{(\zeta n_{23}^\zeta + \xi n_{23}^\xi)}} \\
\hat{\phi}_3^{(0)} &= \frac{1}{1 + e^{(\zeta n_{31}^\zeta + \xi n_{31}^\xi)} + e^{(\zeta n_{32}^\zeta + \xi n_{32}^\xi)}}
\end{aligned} \tag{B.47}$$

where n_{ij}^ζ and n_{ij}^ξ are the ζ and ξ components of a vector \mathbf{n}_{ij} which is (i) normal to the interface between phases ϕ_i and ϕ_j , (ii) at the triple junction and (iii) pointing

toward phase ϕ_j (and hence away from phase ϕ_i). Further, the vectors \mathbf{n}_{ij} should satisfy $\mathbf{n}_{12} + \mathbf{n}_{23} + \mathbf{n}_{31} = 0$. This last property makes sure that the component functions $\hat{\phi}_\alpha^{(0)}$ satisfy the summation rule which can be quickly shown by re-expressing Eq. (B.47) in the following manner by using the property.

$$\begin{aligned}\hat{\phi}_1^{(0)} &= \frac{1}{1 + e^{(\zeta n_{12}^\zeta + \xi n_{12}^\xi)} + e^{(\zeta n_{13}^\zeta + \xi n_{13}^\xi)}} \\ \hat{\phi}_2^{(0)} &= \frac{1}{1 + e^{-(\zeta n_{12}^\zeta + \xi n_{12}^\xi)} + e^{(\zeta n_{23}^\zeta + \xi n_{23}^\xi)}} = \frac{e^{(\zeta n_{12}^\zeta + \xi n_{12}^\xi)}}{1 + e^{(\zeta n_{12}^\zeta + \xi n_{12}^\xi)} + e^{(\zeta n_{13}^\zeta + \xi n_{13}^\xi)}} \\ \hat{\phi}_3^{(0)} &= \frac{1}{1 + e^{-(\zeta n_{13}^\zeta + \xi n_{13}^\xi)} + e^{(\zeta n_{32}^\zeta + \xi n_{32}^\xi)}} = \frac{e^{(\zeta n_{13}^\zeta + \xi n_{13}^\xi)}}{1 + e^{(\zeta n_{12}^\zeta + \xi n_{12}^\xi)} + e^{(\zeta n_{13}^\zeta + \xi n_{13}^\xi)}}.\end{aligned}\tag{B.48}$$

Expressed in this form, the summation property is easy to verify.

Substituting Eq. (B.48) in Eq. (B.46) and verifying if the latter is satisfied for some constant ‘a’ could be a very cumbersome and lengthy calculation. To minimize this, we make the following observations. First, due to the nature of the equations in Eq. (B.46), if $(\hat{\phi}_1^{(0)}, \hat{\phi}_2^{(0)}, \hat{\phi}_3^{(0)})$ is a solution, then a rotation of it about the origin is also a solution. Thus, without loss of generality, one of the interfaces can be oriented along the ζ axis; specifically, we choose the phase above the positive axis as ϕ_1 , therefore, \mathbf{n}_{12} is $-\hat{\zeta}$. Secondly, Eq. (B.48) may or may not solve Eq. (B.46) for any given three vectors \mathbf{n}_{12} , \mathbf{n}_{23} and \mathbf{n}_{31} satisfying $\mathbf{n}_{12} + \mathbf{n}_{23} + \mathbf{n}_{31} = 0$. However, we are only interested in vectors that are 120-120-120 degrees apart, as that is what the demand of the asymptotic analysis is in the present problem of interest (equal interfacial energies). Hence, it will be enough to test the case of \mathbf{n}_{12} , \mathbf{n}_{23} and \mathbf{n}_{31} being unit vectors. In fact, this is exactly the recommendation of Bollada et.al when the interfacial energies are all equal. Thus, as \mathbf{n}_{12} is fixed as $-\hat{\zeta}$, \mathbf{n}_{23} and \mathbf{n}_{31} readily get determined and the test solution becomes

$$\begin{aligned}\hat{\phi}_1^{(0)} &= \frac{1}{1 + e^{-\xi} + e^{-\frac{\sqrt{3}}{2}\zeta - \frac{1}{2}\xi}} \\ \hat{\phi}_2^{(0)} &= \frac{e^{-\xi}}{1 + e^{-\xi} + e^{-\frac{\sqrt{3}}{2}\zeta - \frac{1}{2}\xi}} \\ \hat{\phi}_3^{(0)} &= \frac{e^{-\frac{\sqrt{3}}{2}\zeta - \frac{1}{2}\xi}}{1 + e^{-\xi} + e^{-\frac{\sqrt{3}}{2}\zeta - \frac{1}{2}\xi}}.\end{aligned}\tag{B.49}$$

Note that the r.h.s of the last equation of Eq. (B.46) is the same as the sum of the r.h.s of the first two equations but with a negative sign irrespective of what $\hat{\phi}_1^{(0)}$, $\hat{\phi}_2^{(0)}$ and $\hat{\phi}_3^{(0)}$ are. Further, when these latter are chosen to satisfy the summation rule, the left hand sides of Eq. (B.46), as well, behave identically, i.e., add up to zero. Therefore, it follows that it suffices to check the validity of only the first two equations. These latter can be

rewritten further as follows to facilitate a reduction of number of algebra steps.

$$\begin{aligned}\frac{\partial^2 \hat{\phi}_1^{(0)}}{\partial \zeta^2} + \frac{\partial^2 \hat{\phi}_1^{(0)}}{\partial \xi^2} &= 4a \hat{\phi}_1^{(0)} \begin{pmatrix} \hat{\phi}_1^{(0)} & -0.5 \end{pmatrix} \begin{pmatrix} \hat{\phi}_1^{(0)} & -1 \end{pmatrix} - 4a \hat{\phi}_1^{(0)} \hat{\phi}_2^{(0)} \hat{\phi}_3^{(0)} \\ \frac{\partial^2 \hat{\phi}_2^{(0)}}{\partial \zeta^2} + \frac{\partial^2 \hat{\phi}_2^{(0)}}{\partial \xi^2} &= 4a \hat{\phi}_2^{(0)} \begin{pmatrix} \hat{\phi}_2^{(0)} & -0.5 \end{pmatrix} \begin{pmatrix} \hat{\phi}_2^{(0)} & -1 \end{pmatrix} - 4a \hat{\phi}_1^{(0)} \hat{\phi}_2^{(0)} \hat{\phi}_3^{(0)} .\end{aligned}$$

Substituting Eq.(B.49) in the above equations shows that the latter are satisfied for $a = 0.5$. Thus, Eq. (B.47) with unit vectors \mathbf{n}_{12} , \mathbf{n}_{23} and \mathbf{n}_{31} satisfying $\mathbf{n}_{12} + \mathbf{n}_{23} + \mathbf{n}_{31} = 0$ is the exact solution of the leading order junction equations for the Folch-Plapp multi-well with $a = 0.5$.

Next, various properties of this solution are studied. Some of the main results in sections treating generic multi-wells are derived by assuming that these properties are exhibited by the latter's solutions as well.

B.3.2 Exponential “decay”

It will now be shown that approaching infinity along lines parallel to the interfacial directions recovers the consequent limiting values of $(\hat{\phi}_1^{(0)}, \hat{\phi}_2^{(0)}, \hat{\phi}_3^{(0)})$ at an exponential rate. First, let us consider the particular case of Eq. (B.49), i.e., when one of the interfaces is along the positive ζ -axis. Now, let us approach infinity always staying at a distance of δ from the latter. That is, we travel along the ray $\vec{r}(\rho) = (0, \delta) + \rho \times (1, 0)$ as $\rho \rightarrow \infty$. The result is

$$\lim_{\rho \rightarrow \infty} \hat{\phi}_1^{(0)}(\rho, \delta) = \left(\frac{1}{1 + e^{-\delta} + 0}, \frac{e^{-\delta}}{1 + e^{-\delta} + 0}, \frac{0}{1 + e^{-\delta} + 0} \right) = \left(\frac{1}{1 + e^{-\delta}}, \frac{e^{-\delta}}{1 + e^{-\delta}}, 0 \right).$$

To find the rate at which this “value” is converged to, we subtract $\hat{\phi}_1^{(0)}(\rho, \delta)$ from the limiting value. Particularly, considering the first component, we have

$$\frac{1}{1 + e^{-\delta}} - \hat{\phi}_1^{(0)}(\rho, \delta) = \left| \frac{1}{1 + e^{-\delta}} - \hat{\phi}_1^{(0)}(\rho, \delta) \right| = \frac{e^{-\frac{\sqrt{3}}{2}\rho - \frac{1}{2}\delta}}{(1 + e^{-\delta})(1 + e^{-\delta} + e^{-\frac{\sqrt{3}}{2}\rho - \frac{1}{2}\delta})} < e^{-\frac{\sqrt{3}}{2}\rho - \frac{1}{2}\delta}.$$

That is, the first component exponentially attains its limiting value as $\rho \rightarrow \infty$; similar calculations reveal the same for the others as well.

The above is for that interface lying along ζ -axis, the like nature of the others can be argued without re-performing the calculations: Rotating the solution $\hat{\phi}_1^{(0)}(\zeta, \xi)$ by 120° and 270° , the other interfaces will align along the ζ -axis. Furthermore, the resultant components will be permutations of the current ones. Since, the functional forms remain unchanged, the convergence behavior carries over.

B.3.3 Behavior of integrals of the kind given in Eqs. (3.44) and (3.45)

B.3.3.1 Bounds for the integral containing only ξ derivatives

It will now be shown that for the Bollada et.al solution, the integral $\int_{-\sigma}^{\sigma} \frac{\partial \phi_{\alpha}^{(0)}}{\partial \xi} \frac{\partial \phi_{\alpha}^{(0)}}{\partial \xi} d\xi$ is bounded above by a constant and below by a positive function independent of ζ . This fact is used in establishing the boundedness of the second limit on the l.h.s of Eq. (3.44).

First, let us consider $\int_{-\infty}^{\infty} \frac{\partial \phi_1^{(0)}}{\partial \xi} \frac{\partial \phi_1^{(0)}}{\partial \xi} d\xi$. Plugging Eq. (B.49) into it gives

$$\begin{aligned} \int_{-\infty}^{\infty} \frac{\partial \phi_1^{(0)}}{\partial \xi} \frac{\partial \phi_1^{(0)}}{\partial \xi} d\xi &= \int_{-\infty}^{\infty} \frac{\left(-e^{-\xi} - \frac{1}{2}e^{-\frac{\sqrt{3}}{2}\zeta - \frac{1}{2}\xi}\right) \left(-e^{-\xi} - \frac{1}{2}e^{-\frac{\sqrt{3}}{2}\zeta - \frac{1}{2}\xi}\right)}{\left(1 + e^{-\xi} + e^{-\frac{\sqrt{3}}{2}\zeta - \frac{1}{2}\xi}\right)^4} d\xi \\ &= \int_{-\infty}^{\infty} \frac{\left(-e^{-\xi} - \frac{1}{2}e^{-\frac{\sqrt{3}}{2}\zeta - \frac{1}{2}\xi}\right) \left(-e^{-\xi} - e^{-\frac{\sqrt{3}}{2}\zeta - \frac{1}{2}\xi} + \frac{1}{2}e^{-\frac{\sqrt{3}}{2}\zeta - \frac{1}{2}\xi}\right)}{\left(1 + e^{-\xi} + e^{-\frac{\sqrt{3}}{2}\zeta - \frac{1}{2}\xi}\right)^4} d\xi \\ &= - \int_{-\infty}^{\infty} \frac{\left(-e^{-\xi} - \frac{1}{2}e^{-\frac{\sqrt{3}}{2}\zeta - \frac{1}{2}\xi}\right) \left(e^{-\xi} + e^{-\frac{\sqrt{3}}{2}\zeta - \frac{1}{2}\xi}\right)}{\left(1 + e^{-\xi} + e^{-\frac{\sqrt{3}}{2}\zeta - \frac{1}{2}\xi}\right)^4} d\xi \\ &\quad + \frac{1}{2} \int_{-\infty}^{\infty} \frac{\left(2e^{-\xi} + e^{-\frac{\sqrt{3}}{2}\zeta - \frac{1}{2}\xi}\right) e^{-\frac{\sqrt{3}}{2}\zeta - \frac{1}{2}\xi} (-1/2)}{\left(1 + e^{-\xi} + e^{-\frac{\sqrt{3}}{2}\zeta - \frac{1}{2}\xi}\right)^4} d\xi \end{aligned}$$

To evaluate the first integral, let x stand for the denominator, then the integral is equivalent to

$$\int_{\infty}^1 \frac{x-1}{x^4} dx = -\frac{1}{6}.$$

Similarly, letting $x = e^{-\frac{\sqrt{3}}{2}\zeta - \frac{1}{2}\xi}$, the second integral modifies to $\int_{\infty}^1 \frac{x(2a^2x+1)}{(1+a^2x^2+x)^4} dx$

where $a = e^{-\frac{\sqrt{3}}{2}\zeta}$. Integrating the latter by parts simplifies it to

$$\begin{aligned} \int_{\infty}^1 \frac{x(2a^2x+1)}{(1+a^2x^2+x)^4} dx &= \left[x \int \frac{(2a^2x+1)}{(1+a^2x^2+x)^4} dx \right]_{\infty}^0 - \int_{\infty}^0 \left(\int \frac{(2a^2x+1)}{(1+a^2x^2+x)^4} dx \right) dx \\ &= -\frac{1}{3} \left[\frac{x}{(1+a^2x^2+x)^3} dx \right]_{\infty}^0 + \frac{1}{3} \int_{\infty}^0 \frac{dx}{(1+a^2x^2+x)^3}. \end{aligned}$$

In summary,

$$\int_{-\infty}^{\infty} \frac{\partial \overset{\lambda(0)}{\phi}_1}{\partial \xi} \frac{\partial \overset{\lambda(0)}{\phi}_1}{\partial \xi} d\xi = \frac{1}{6} - \frac{1}{6} \int_0^{\infty} \frac{dx}{(1+a^2x^2+x)^3} \leq \frac{1}{6}.$$

Therefore, $\int_{-\infty}^{\infty} \frac{\partial \overset{\lambda(0)}{\phi}_1}{\partial \xi} \frac{\partial \overset{\lambda(0)}{\phi}_1}{\partial \xi} d\xi$ is bounded above. Further, since $\overset{\lambda(0)}{\phi}_2(\zeta, \xi) = \overset{\lambda(0)}{\phi}_2(\zeta, -\xi)$, the integral of the second component equals that of the first and hence is bounded. Moreover, since $\overset{\lambda(0)}{\phi}_1 + \overset{\lambda(0)}{\phi}_2 + \overset{\lambda(0)}{\phi}_3 = 1 \forall (\zeta, \xi) \in \mathbb{R}^2$,

$$\begin{aligned} \frac{\partial \overset{\lambda(0)}{\phi}_3}{\partial \xi} \frac{\partial \overset{\lambda(0)}{\phi}_3}{\partial \xi} &= \left(\frac{\partial \overset{\lambda(0)}{\phi}_1}{\partial \xi} + \frac{\partial \overset{\lambda(0)}{\phi}_2}{\partial \xi} \right)^2 \\ &\leq 2 \left(\frac{\partial \overset{\lambda(0)}{\phi}_1}{\partial \xi} \frac{\partial \overset{\lambda(0)}{\phi}_1}{\partial \xi} + \frac{\partial \overset{\lambda(0)}{\phi}_2}{\partial \xi} \frac{\partial \overset{\lambda(0)}{\phi}_2}{\partial \xi} \right). \quad (\because \text{AM} \geq \text{GM}) \end{aligned}$$

Hence, the integral of the third component as well, and thus $I(\zeta, \sigma)$ is bounded above for all positive ζ . To show that it is greater than a monotonically increasing positive function of σ for all positive ζ , we proceed as follows

$$\begin{aligned} \int_{-\sigma}^{\sigma} \frac{\partial \overset{\lambda(0)}{\phi}_\alpha}{\partial \xi} \frac{\partial \overset{\lambda(0)}{\phi}_\alpha}{\partial \xi} d\xi &\geq \int_{-\sigma}^{\sigma} \frac{\partial \overset{\lambda(0)}{\phi}_1}{\partial \xi} \frac{\partial \overset{\lambda(0)}{\phi}_1}{\partial \xi} d\xi \geq \int_0^{\sigma} \frac{\partial \overset{\lambda(0)}{\phi}_1}{\partial \xi} \frac{\partial \overset{\lambda(0)}{\phi}_1}{\partial \xi} d\xi \\ &= \int_0^{\sigma} \frac{\left(e^{-\xi} + \frac{1}{2} e^{-\frac{\sqrt{3}}{2}\zeta - \frac{1}{2}\xi} \right)^2}{\left(1 + e^{-\xi} + e^{-\frac{\sqrt{3}}{2}\zeta - \frac{1}{2}\xi} \right)^4} d\xi \\ &\geq \int_0^{\sigma} \frac{(e^{-\xi} + 0)^2}{(1+1+1)^4} d\xi \\ &= \frac{1}{81} \int_0^{\sigma} e^{-2\xi} d\xi \\ &= (1 - e^{-2\sigma})/162. \end{aligned}$$

B.3.3.2 Bounds for the integral containing only ζ derivatives

Now it is the turn of $\int_{-\sigma}^{\sigma} \int_{-\sigma}^{\sigma} \frac{\partial \overset{\lambda(0)}{\phi}_\alpha}{\partial \zeta} \frac{\partial \overset{\lambda(0)}{\phi}_\alpha}{\partial \zeta} d\xi d\zeta$ to be shown to be of the sharp order of σ as the latter grows arbitrarily large.

We first establish the upper “bound”. For the component $\phi_1^{(0)}$, we have

$$\begin{aligned}
\int_{-\sigma}^{\sigma} \int_{-\sigma}^{\sigma} \frac{\partial \phi_1^{(0)}}{\partial \zeta} \frac{\partial \phi_1^{(0)}}{\partial \zeta} d\zeta d\xi &\leq \int_{-\sigma}^{\sigma} \int_{-\infty}^{\infty} \frac{\partial \phi_1^{(0)}}{\partial \zeta} \frac{\partial \phi_1^{(0)}}{\partial \zeta} d\zeta d\xi \\
&= \frac{3}{4} \int_{-\sigma}^{\sigma} \int_{-\infty}^{\infty} \frac{\left(e^{-\frac{\sqrt{3}}{2}\zeta - \frac{1}{2}\xi}\right)^2}{\left(1 + e^{-\xi} + e^{-\frac{\sqrt{3}}{2}\zeta - \frac{1}{2}\xi}\right)^4} d\zeta d\xi \\
&\leq \frac{3}{4} \int_{-\sigma}^{\sigma} \int_{-\infty}^{\infty} \frac{\left(e^{-\frac{\sqrt{3}}{2}\zeta - \frac{1}{2}\xi}\right) \left(1 + e^{-\xi} + e^{-\frac{\sqrt{3}}{2}\zeta - \frac{1}{2}\xi}\right)}{\left(1 + e^{-\xi} + e^{-\frac{\sqrt{3}}{2}\zeta - \frac{1}{2}\xi}\right)^4} d\zeta d\xi \\
&= \frac{3}{4} \int_{-\sigma}^{\sigma} \int_{-\infty}^{\infty} \frac{e^{-\frac{\sqrt{3}}{2}\zeta - \frac{1}{2}\xi}}{\left(1 + e^{-\xi} + e^{-\frac{\sqrt{3}}{2}\zeta - \frac{1}{2}\xi}\right)^4} d\zeta d\xi
\end{aligned} \tag{B.50}$$

Letting $x = 1 + e^{-\xi} + e^{-\frac{\sqrt{3}}{2}\zeta - \frac{1}{2}\xi}$, we have through integration by substitution

$$\int_{-\sigma}^{\sigma} \int_{-\sigma}^{\sigma} \frac{\partial \phi_1^{(0)}}{\partial \zeta} \frac{\partial \phi_1^{(0)}}{\partial \zeta} d\zeta d\xi \leq \frac{3\sqrt{3}}{4} \int_{-\sigma}^{\sigma} \frac{1}{(1 + e^{-\xi})^2} d\xi. \tag{B.51}$$

Similar calculations give

$$\int_{-\sigma}^{\sigma} \int_{-\sigma}^{\sigma} \frac{\partial \phi_2^{(0)}}{\partial \zeta} \frac{\partial \phi_2^{(0)}}{\partial \zeta} d\zeta d\xi \leq \frac{3\sqrt{3}}{4} \int_{-\sigma}^{\sigma} \frac{1}{(1 + e^{\xi})^2} d\xi. \tag{B.52}$$

Adding Eqs. (B.51) and (B.52) gives

$$\begin{aligned}
\int_{-\sigma}^{\sigma} \int_{-\sigma}^{\sigma} \left(\frac{\partial \phi_1^{(0)}}{\partial \zeta} \frac{\partial \phi_1^{(0)}}{\partial \zeta} + \frac{\partial \phi_2^{(0)}}{\partial \zeta} \frac{\partial \phi_2^{(0)}}{\partial \zeta} \right) d\zeta d\xi &\leq \frac{3\sqrt{3}}{4} \int_{-\sigma}^{\sigma} \frac{1 + e^{2\xi}}{1 + e^{2\xi} + 2e^{\xi}} d\xi \\
&\leq \frac{3\sqrt{3}}{4} \int_{-\sigma}^{\sigma} d\xi \\
&= \frac{3\sqrt{3}}{4} 2\sigma.
\end{aligned} \tag{B.53}$$

Since $\phi_1^{(0)} + \phi_2^{(0)} + \phi_3^{(0)} = 1 \forall (\zeta, \xi) \in \mathbb{R}^2$, it follows that $\frac{1}{\sigma} \int_{-\sigma}^{\sigma} \int_{-\sigma}^{\sigma} \frac{\partial \phi_{\alpha}^{(0)}}{\partial \zeta} \frac{\partial \phi_{\alpha}^{(0)}}{\partial \zeta} d\zeta d\xi$ is bounded above for all $\sigma > 0$ and hence in the limit $\sigma \rightarrow \infty$.

To show the lower bound, we proceed as follows.

$$\begin{aligned}
\int_{-\sigma}^{\sigma} \int_{-\sigma}^{\sigma} \frac{\partial \overset{\wedge}{\phi}_{\alpha}^{(0)}}{\partial \zeta} \frac{\partial \overset{\wedge}{\phi}_{\alpha}^{(0)}}{\partial \zeta} d\zeta d\xi &\geq \int_{-\sigma}^{\sigma} \int_{-\sigma}^{\sigma} \frac{\partial \overset{\wedge}{\phi}_3^{(0)}}{\partial \zeta} \frac{\partial \overset{\wedge}{\phi}_3^{(0)}}{\partial \zeta} d\zeta d\xi \geq \int_{-\sigma}^0 \int_{-\sigma}^0 \frac{\partial \overset{\wedge}{\phi}_3^{(0)}}{\partial \zeta} \frac{\partial \overset{\wedge}{\phi}_3^{(0)}}{\partial \zeta} d\zeta d\xi \\
&= \frac{3}{4} \int_{-\sigma}^0 \int_{-\sigma}^0 \frac{\left(e^{\frac{\sqrt{3}}{2}\zeta} \left(e^{-\frac{1}{2}\xi} + e^{\frac{1}{2}\xi} \right) \right)^2}{\left(1 + e^{\frac{\sqrt{3}}{2}\zeta} \left(e^{-\frac{1}{2}\xi} + e^{\frac{1}{2}\xi} \right) \right)^4} d\zeta d\xi \\
&\geq \frac{3}{4} \int_{-\sigma}^0 \int_{-\sigma}^0 \frac{\left(e^{\frac{\sqrt{3}}{2}\zeta - \frac{1}{2}\xi} \right)^2}{\left(2 + e^{\frac{\sqrt{3}}{2}\zeta - \frac{1}{2}\xi} \right)^4} d\zeta d\xi \\
&\geq \frac{3}{4} \iint_{\Delta_{\sigma}} \frac{\left(e^{\frac{\sqrt{3}}{2}\zeta - \frac{1}{2}\xi} \right)^2}{\left(2 + e^{\frac{\sqrt{3}}{2}\zeta - \frac{1}{2}\xi} \right)^4} d\zeta d\xi =: I_{\Delta_{\sigma}}
\end{aligned} \tag{B.54}$$

where Δ_{σ} is the shaded region of Fig. B.4.

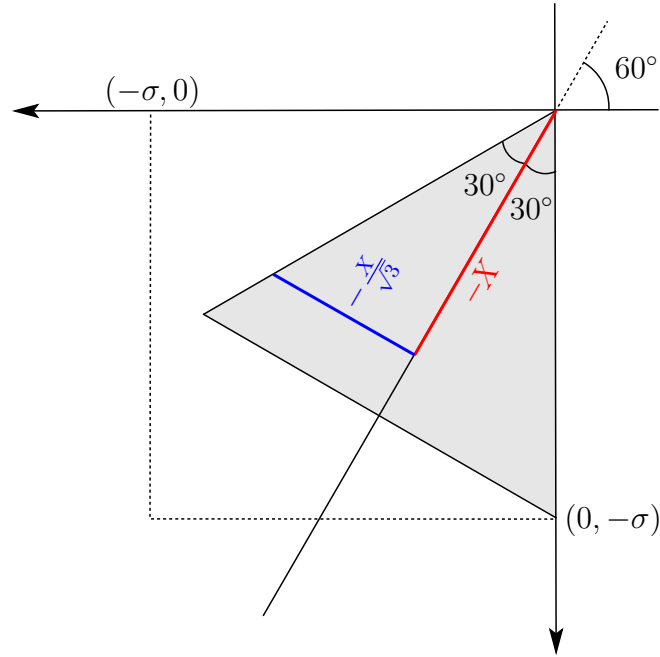


Figure B.4: A subregion of the domain of intergration of the integral on the l.h.s of Eq. (B.54).

Now let us make the following substitution

$$\begin{aligned}
X &= \frac{1}{2}\zeta + \frac{\sqrt{3}}{2}\xi \\
Y &= -\frac{\sqrt{3}}{2}\zeta + \frac{1}{2}\xi.
\end{aligned} \tag{B.55}$$

Note that this is nothing but the rotation of the axis by 60° in the counterclockwise direction. Therefore, the integral $I_{\Delta\sigma}$ becomes

$$I_{\Delta\sigma} = -\frac{3}{4} \int_0^{-\frac{\sigma\sqrt{3}}{2} - \frac{X}{\sqrt{3}}} \int_{\frac{X}{\sqrt{3}}} \frac{(e^{-Y})^2}{(2 + e^{-Y})^4} dY dX. \quad (\text{B.56})$$

Making the transformation $X \rightarrow -X$ gives

$$\begin{aligned} I_{\Delta\sigma} &= -\frac{3}{4} \int_0^{\frac{\sigma\sqrt{3}}{2} - \frac{X}{\sqrt{3}}} \int_{-\frac{X}{\sqrt{3}}} \frac{(e^{-Y})^2}{(2 + e^{-Y})^4} dY (-dX) \\ &= \frac{3}{4} \int_0^{\frac{\sigma\sqrt{3}}{2} - \frac{X}{\sqrt{3}}} \int_{-\frac{X}{\sqrt{3}}} \frac{(e^{-Y})^2}{(2 + e^{-Y})^4} dY dX \\ &\geq \frac{3}{4} \int_0^{\frac{\sigma\sqrt{3}}{2} - \frac{X}{\sqrt{3}}} \int_0^{\frac{X}{\sqrt{3}}} \frac{(e^{-Y})^2}{(2 + e^{-Y})^4} dY dX \\ &\geq \frac{3}{4} \int_0^{\frac{\sigma\sqrt{3}}{2} - \frac{X}{\sqrt{3}}} \int_0^{\frac{X}{\sqrt{3}}} \frac{(e^{-Y})^2}{3^4} dY dX \\ &= \frac{3}{4} \frac{1}{3^4} \int_0^{\frac{\sigma\sqrt{3}}{2} - \frac{X}{\sqrt{3}}} \left(-\frac{1}{2} e^{-2Y} \Big|_0^{\frac{X}{\sqrt{3}}} \right) dX \\ &= \frac{1}{6^3} \int_0^{\frac{\sigma\sqrt{3}}{2}} \left(1 - e^{-\frac{2X}{\sqrt{3}}} \right) dX = \frac{\sigma\sqrt{3}}{2 \cdot 6^3} - \left(-\frac{\sqrt{3}}{2 \cdot 6^3} e^{-\frac{2X}{\sqrt{3}}} \Big|_0^{\frac{\sigma\sqrt{3}}{2}} \right) \\ &= \frac{\sigma\sqrt{3}}{2 \cdot 6^3} + \frac{\sqrt{3}}{2 \cdot 6^3} (e^{-\frac{\sigma}{2}} - 1). \end{aligned} \quad (\text{B.57})$$

Equation (B.57) indicates that $\frac{1}{\sigma} \int_{-\sigma}^{\sigma} \int_{-\sigma}^{\sigma} \frac{\partial \phi_\alpha^{\lambda(0)}}{\partial \zeta} \frac{\partial \phi_\alpha^{\lambda(0)}}{\partial \zeta} d\zeta d\xi$ is bounded below by a positive constant as $\sigma \rightarrow \infty$.

B.3.3.3 Analysis of the integral containing both ζ and ξ derivatives

Next, it will be shown that for the Bollada et.al solution, the integration of $\frac{\partial \phi_\alpha^{\lambda(0)}}{\partial \xi} \frac{\partial \phi_\alpha^{\lambda(0)}}{\partial \zeta}$ over the whole of \mathbb{R}^2 vanishes. The details are as follows.

The expressions of the concerned terms are given by

$$\frac{\partial \overset{\lambda}{\phi}_1^{(0)}}{\partial \xi} \frac{\partial \overset{\lambda}{\phi}_1^{(0)}}{\partial \zeta} = \frac{\sqrt{3} \left(2e^{-\xi} + e^{-\frac{\sqrt{3}}{2}\zeta - \frac{1}{2}\xi} \right) \left(e^{-\frac{\sqrt{3}}{2}\zeta - \frac{1}{2}\xi} \right)}{4 \left(1 + e^{-\xi} + e^{-\frac{\sqrt{3}}{2}\zeta - \frac{1}{2}\xi} \right)^4} \quad (\text{B.58a})$$

$$\frac{\partial \overset{\lambda}{\phi}_2^{(0)}}{\partial \xi} \frac{\partial \overset{\lambda}{\phi}_2^{(0)}}{\partial \zeta} = -\frac{\sqrt{3} \left(2e^{\xi} + e^{-\frac{\sqrt{3}}{2}\zeta + \frac{1}{2}\xi} \right) \left(e^{-\frac{\sqrt{3}}{2}\zeta + \frac{1}{2}\xi} \right)}{4 \left(1 + e^{\xi} + e^{-\frac{\sqrt{3}}{2}\zeta + \frac{1}{2}\xi} \right)^4} \quad (\text{B.58b})$$

$$\frac{\partial \overset{\lambda}{\phi}_3^{(0)}}{\partial \xi} \frac{\partial \overset{\lambda}{\phi}_3^{(0)}}{\partial \zeta} = -\frac{\sqrt{3} \left(e^{\sqrt{3}\zeta - \xi} - e^{\sqrt{3}\zeta + \xi} \right)}{4 \left(1 + e^{\frac{\sqrt{3}}{2}\zeta - \frac{1}{2}\xi} + e^{\frac{\sqrt{3}}{2}\zeta + \frac{1}{2}\xi} \right)^4}. \quad (\text{B.58c})$$

First, we show that the integration over the first two terms of Eq. (B.3.3.3) vanishes:

$$\begin{aligned} & \int_{-\infty}^{\infty} \int_{-\infty}^{\infty} \left(\frac{\partial \overset{\lambda}{\phi}_1^{(0)}}{\partial \xi} \frac{\partial \overset{\lambda}{\phi}_1^{(0)}}{\partial \zeta} + \frac{\partial \overset{\lambda}{\phi}_2^{(0)}}{\partial \xi} \frac{\partial \overset{\lambda}{\phi}_2^{(0)}}{\partial \zeta} \right) d\xi d\zeta \\ &= \frac{\sqrt{3}}{4} \int_{-\infty}^{\infty} \int_{-\infty}^{\infty} \left[\frac{\left(2e^{-\xi} + e^{-\frac{\sqrt{3}}{2}\zeta - \frac{1}{2}\xi} \right) \left(e^{-\frac{\sqrt{3}}{2}\zeta - \frac{1}{2}\xi} \right)}{\left(1 + e^{-\xi} + e^{-\frac{\sqrt{3}}{2}\zeta - \frac{1}{2}\xi} \right)^4} - \frac{\left(2e^{\xi} + e^{-\frac{\sqrt{3}}{2}\zeta + \frac{1}{2}\xi} \right) \left(e^{-\frac{\sqrt{3}}{2}\zeta + \frac{1}{2}\xi} \right)}{\left(1 + e^{\xi} + e^{-\frac{\sqrt{3}}{2}\zeta + \frac{1}{2}\xi} \right)^4} \right] d\xi d\zeta \\ &= \frac{\sqrt{3}}{4} \int_{-\infty}^{\infty} \int_{-\infty}^{\infty} \left[\frac{\left(2e^{-\xi} + e^{-\frac{\sqrt{3}}{2}\zeta - \frac{1}{2}\xi} \right) \left(e^{-\frac{\sqrt{3}}{2}\zeta - \frac{1}{2}\xi} \right)}{\left(1 + e^{-\xi} + e^{-\frac{\sqrt{3}}{2}\zeta - \frac{1}{2}\xi} \right)^4} - \frac{\left(2e^{-\xi} + e^{-\frac{\sqrt{3}}{2}\zeta - \frac{1}{2}\xi} \right) \left(e^{-\frac{\sqrt{3}}{2}\zeta - \frac{1}{2}\xi} \right)}{\left(1 + e^{-\xi} + e^{-\frac{\sqrt{3}}{2}\zeta - \frac{1}{2}\xi} \right)^4} \right] d\xi d\zeta \\ &= 0 \end{aligned} \quad (\text{B.59})$$

where a change of variable $\xi \rightarrow -\xi$ is made in the second summand of the integrand on the r.h.s in going from first equality to the second. As for the term in Eq. (B.58c), we note that it is an odd function of ξ for any given ζ . Hence, its integration over any symmetric interval is identically equal to zero, i.e.,

$$\int_{-a}^a \frac{\partial \overset{\lambda}{\phi}_3^{(0)}}{\partial \xi} \frac{\partial \overset{\lambda}{\phi}_3^{(0)}}{\partial \zeta} d\xi = 0. \quad (\text{B.60})$$

Using eq. (B.59) and Eq. (B.60), we have

$$\int_{-\infty}^{\infty} \int_{-\infty}^{\infty} \left(\frac{\partial \overset{\lambda}{\phi}_1^{(0)}}{\partial \xi} \frac{\partial \overset{\lambda}{\phi}_1^{(0)}}{\partial \zeta} + \frac{\partial \overset{\lambda}{\phi}_2^{(0)}}{\partial \xi} \frac{\partial \overset{\lambda}{\phi}_2^{(0)}}{\partial \zeta} + \frac{\partial \overset{\lambda}{\phi}_3^{(0)}}{\partial \xi} \frac{\partial \overset{\lambda}{\phi}_3^{(0)}}{\partial \zeta} \right) d\xi d\zeta = 0. \quad (\text{B.61})$$

Appendix C

Analysis of some relevant sharp interface problems

C.1 Sharp interface treatment of three grain evolution within the setup of Fig. 4.1

The growth front's shape and speed at steady state are to be determined given its mobility τ , energy γ and driving force Δf .

The law governing the interfacial evolution is

$$\tau v_n = \Delta f - \gamma \kappa \quad (\text{C.1})$$

where v_n is the normal velocity and the same sign convention, as in the local analysis of binary interfaces, is used for curvature κ .

Since there is a mirror symmetry in the system about the $\phi_2 - \phi_3$ interface, only the right side grain's evolution is explicitly worked on. Let us position the coordinate system such that the origin coincides with the triple point. Since the interface profile is assumed to be always expressible as graph of a function, various points on it can be identified using just the abscissa x . Therefore, Eq. (C.1) re-written highlighting this would read

$$\tau v_n(x) = \Delta f - \gamma \kappa(x) \quad \forall \quad 0 < x \leq l$$

where l is the width of the growing grain ϕ_3 . Since the front moves upwards without changing its shape, it can be readily shown that this equation reduces to

$$\frac{\tau v}{\sqrt{1 + \left(\frac{dy}{dx}\right)^2}} = \Delta f - \gamma \kappa(x) \quad \forall \quad 0 < x \leq l \quad (\text{C.2})$$

where v is the steady state speed.

We now extend the domain of validity of this equation to the origin as well. That is, the triple junction's instantaneous velocity is assumed to be as per $v_x = 0$ and

$$\tau v_y \cos \theta_1 = \Delta f + \gamma \kappa_{0,1} \quad (\text{C.3})$$

in the current sharp interface analysis. Where θ_1 is the angle made by the $\phi_1 - \phi_3$ interface with the horizontal and note the usage of the convention introduced in chapter 3, for numbering the interfaces and denoting their curvatures at the junction point.

That means, the problem statement is to find a $y(x)$ and a v satisfying

$$\frac{-\frac{d^2 y}{dx^2}}{\left(\sqrt{1 + \left(\frac{dy}{dx}\right)^2}\right)^3} + \frac{\tau}{\gamma} \frac{v}{\sqrt{1 + \left(\frac{dy}{dx}\right)^2}} - \frac{\Delta f}{\gamma} = 0 \quad (\text{C.4})$$

in the interval $[0, l]$ subject to the boundary conditions

$$\begin{aligned} \frac{dy}{dx}(x=0) &= \tan \theta_1 \quad \text{and} \\ \frac{dy}{dx}(x=l) &= 0. \end{aligned}$$

The second of the above conditions is realized in the phase-field simulations of chapter 4 due to implementation of no-flux boundary conditions in the lateral directions [30].

The solution is obtained in the following manner: Substituting $m = dy/dx$ in Eq. (C.4) yields

$$\frac{-\frac{dm}{dx}}{(1+m^2)^{3/2}} + \frac{a}{(1+m^2)^{1/2}} - b = 0 \quad (\text{C.5})$$

where a and b are used to denote $\tau v/\gamma$ and $\Delta f/\gamma$, respectively. If $\theta(x)$ is the angle made by the interface with the horizontal at x , then by definition, $m = \tan \theta$. This would imply

$$\frac{dm}{dx} = \sec^2 \theta \frac{d\theta}{dx} \quad (\text{C.6})$$

Substituting Eq. (C.6) in Eq. (C.5) leads to

$$-\frac{\sec^2 \theta}{(\sec^2 \theta)^{3/2}} \frac{d\theta}{dx} + \frac{a}{(\sec^2 \theta)^{1/2}} - b = 0 \quad (\text{C.7})$$

$$\implies -\cos \theta \frac{d\theta}{dx} + a \cos \theta - b = 0 \quad (\text{C.8})$$

$$\implies \frac{a \cos \theta}{(a \cos \theta - b)} \frac{d\theta}{dx} = a \quad (\text{C.9})$$

$$\implies \frac{d\theta}{dx} + \frac{b}{(a \cos \theta - b)} \frac{d\theta}{dx} = a \quad (\text{C.10})$$

Substituting $\cos \theta = \frac{(1 - \tan^2 \frac{\theta}{2})}{(1 + \tan^2 \frac{\theta}{2})}$ and rearranging yields

$$\frac{d\theta}{dx} + \frac{b \sec^2 \frac{\theta}{2} \frac{d\theta}{dx}}{(a - b - (a + b) \tan^2 \frac{\theta}{2})} = a \quad (\text{C.11})$$

Let $\tan \frac{\theta}{2} = p$ for the second summand on the l.h.s. This transforms Eq. (C.11) to

$$\frac{d\theta}{dx} - \frac{2b}{b+a} \frac{dp/dx}{\left\{ p^2 + \left(\sqrt{\frac{b-a}{b+a}} \right)^2 \right\}} = a \quad (\text{C.12})$$

Integrating Eq. (C.12) gives

$$\theta - \frac{2b}{b+a} \sqrt{\frac{b+a}{b-a}} \tan^{-1} \left(\sqrt{\frac{b+a}{b-a}} \tan \frac{\theta}{2} \right) = a(x + c) \quad (\text{C.13})$$

where c is the integration constant which can be easily shown to equal $-l$ by considering the equation for $x = l$ and using the corresponding boundary condition. Thus, the angle made by the interface with the horizontal at every x is given by

$$\theta - \frac{2}{\sqrt{1 - \left(\frac{a}{b}\right)^2}} \tan^{-1} \left(\sqrt{\frac{1 + \frac{a}{b}}{1 - \frac{a}{b}}} \tan \frac{\theta}{2} \right) = \frac{a}{b} b(x - l). \quad (\text{C.14})$$

Note that the unknown v is in a/b and it can be determined by considering the above equation for $x = 0$. Expressing a/b in closed form from the above may not be possible, however, using numerical techniques, it can be determined for any given θ_1 upto desired level of accuracy. The free online Wolfram Mathematica tool is used to evaluate a/b for all the problems considered in the current thesis. Once it is available, the interface profile $y(x)$ can be obtained from $\theta(x)$ using numerical integration. The same route is taken in obtaining the profiles presented in chapters 4 and 5, and appendix E.

C.2 Sharp interface treatment of isothermal planar alloy solidification

Let a binary solid be in contact with its melt in a rectangular domain forming a planar interface and an effectively 1D system. That is, no variation in direction parallel to the interface. Let the concentration in the liquid at a distance X_l from the interface be always maintained at a constant value c_l^e . Further, let it be assumed that it is somehow ensured that the derivative of the concentration in the solid at a distance X_s from the interface vanishes. Finally, let it be supposed that as a consequence of the above impositions

and the thermo-physical properties of the system, the composition fields in the solid and liquid evolve in such a manner that the former grows at the expense of the latter with constant speed v . The governing equations for this dynamics in a moving frame whose origin coincides with the interface are as follows.

$$D_s \frac{\partial^2 c_s}{\partial x^2} + v \frac{\partial c_s}{\partial x} = 0 \quad \forall x < 0 \quad (\text{C.15a})$$

$$D_l \frac{\partial^2 c_l}{\partial x^2} + v \frac{\partial c_l}{\partial x} = 0 \quad \forall x > 0 \quad (\text{C.15b})$$

$$\frac{\partial c_s}{\partial x}(x = -X_s) = 0 \quad (\text{C.15c})$$

$$D_l \frac{\partial c_l}{\partial x}(x = 0) - D_s \frac{\partial c_s}{\partial x}(x = 0) = v(c_s(x = 0) - c_l(x = 0)) \quad (\text{C.15d})$$

$$\mu_s(x = 0) = \mu_l(x = 0) \quad (\text{C.15e})$$

$$\omega_s(x = 0) - \omega_l(x = 0) = -\beta v \quad (\text{C.15f})$$

$$c_l(x = X_l) = c_l^e \quad (\text{C.15g})$$

where D_s , μ_s and ω_s are the diffusivity, chemical potential and grand potential of the solid phase, and $c_s(x)$ is the composition field in the growing solid. The other quantities are similarly defined and correspond to the melt phase. An interfacial property also enters the equations, namely β , which is the kinetic co-efficient.

The goal is to find a $c_s(x)$, $c_l(x)$ and a v satisfying Eq. (C.15) given all the other quantities.

Solution:

The most generic solutions of Eq. (C.15a) and (C.15b) are

$$c_s = -\frac{M_s D_s}{v} \exp\left\{-\frac{v}{D_s} x\right\} + K_s \quad (\text{C.16})$$

and

$$c_l = -\frac{M_l D_l}{v} \exp\left\{-\frac{v}{D_l} x\right\} + K_l, \quad (\text{C.17})$$

respectively. Substituting the former in Eq. (C.15c) leads to

$$M_s = 0 \quad \text{implying} \quad c_s = K_s. \quad (\text{C.18})$$

From Eqs. (C.15d) and (C.18), we have

$$D_l \left(-\frac{M_l D_l}{v}\right) \left(-\frac{v}{D_l}\right) - D_s \times 0 = v \left\{K_s - \left(K_l - \frac{M_l D_l}{v}\right)\right\}$$

which gives

$$K_s = K_l =: K \quad (\text{C.19})$$

Now, let us assume parabolic forms for the free energies of the solid and the liquid phases, particularly in the form $f_s = A_s(c - c_s^{\min})^2 + E_s$ and $f_l = A_l(c - c_l^{\min})^2 + E_l$. As a result, Eq. (C.15e) gives

$$\begin{aligned} 2A_s(K - c_s^{\min}) &= 2A_l \left(K - \frac{M_l D_l}{v} - c_l^{\min} \right) \\ \implies -\frac{M_l D_l}{v} &= (c_l^{\min} - c_s^{\min}) + \left(\frac{A_s}{A_l} - 1 \right) (K - c_s^{\min}). \end{aligned}$$

Making use of this, we so far have

$$c_s = K \quad (\text{C.20})$$

and

$$c_l = \left\{ (c_l^{\min} - c_s^{\min}) + \left(\frac{A_s}{A_l} - 1 \right) (K - c_s^{\min}) \right\} \exp \left(-\frac{v}{D_l} x \right) + K. \quad (\text{C.21})$$

That is, c_s and c_l are determined except for the unknowns K and v . Substituting Eqs. (C.20) and (C.21) in Eq. (C.15f) gives, upon some manipulation,

$$\left(\frac{A_s}{A_l} - 1 \right) A_s (K - c_s^{\min})^2 + 2A_s (K - c_s^{\min}) (c_l^{\min} - c_s^{\min}) + \beta v - (E_l - E_s) = 0. \quad (\text{C.22})$$

Similarly, from Eqs. (C.15g) and (C.21), we will have

$$c_l^e = \left\{ (c_l^{\min} - c_s^{\min}) + \left(\frac{A_s}{A_l} - 1 \right) (K - c_s^{\min}) \right\} \exp \left(-\frac{v}{D_l} X_l \right) + K. \quad (\text{C.23})$$

Thus we have two equations, Eqs. (C.22) and (C.23), to determine the two unknowns K and v . The existence and uniqueness of the steady state solutions reduces to the solvability of this problem in real values. For instance, in systems with $A_s = A_l$ and $E_s = E_l$, for the infinite domain version of the problem, i.e., with Eq. (C.15g) replaced by $\lim_{x \rightarrow \infty} c_l(x) = c_l^e$, on the one hand, when $\beta \neq 0$, no solutions exist if the far-field composition is chosen between the equilibrium values, i.e., c_s^{\min} and c_l^{\min} . And on the other, when $\beta = 0$, no solutions exist except when $c_l^e = c_s^{\min}$, and for the latter, there are infinitely many as every $v \geq 0$ happens to be a solution. However, this is not the case for the finite domain version where solutions always exist for all non-negative β when c_l^e lies between c_s^{\min} and c_l^{\min} , no matter how big X_l is. Also, if the latter is made arbitrarily large in the constructed solution, then v would tend to vanish and again the freedom of choosing c_l^e in a range is lost.

Appendix D

Asymptotic analysis of multiphase binary alloy solidification model

The derivation pertaining to the matched asymptotic analysis of the chemical potential evolution equation in a multi-phase-field setting is not very different compared to the scalar case which is presented many a times in the literature. Hence, the recovered behavior and laws are directly presented without showing the intermediate steps. Furthermore, the timescale of actual interest, i.e., $\tau = t$ is only considered.

D.1 Asymptotic analysis of Eqs. (2.43) and (2.44)

D.1.1 Outer analysis

The leading order requirement for the phase-field variable is

$$\frac{\partial W(\phi)}{\partial \phi_\beta}(\phi^{(0)}) - \frac{1}{N} \sum_{\alpha=1}^N \frac{\partial W(\phi)}{\partial \phi_\alpha}(\phi^{(0)}) = 0 \quad (\text{D.1})$$

and the implication is that at the leading order, bulks corresponding to the critical points of the restricted multi-well are formed.

The leading order requirement for the chemical potential is the same as Eq. (2.44) except with μ and ϕ replaced by $\mu^{(0)}$ and $\phi^{(0)}$, respectively. This implies that in the outer region that is occupied by the bulk of the α^{th} phase, the standard diffusion equation is retrieved at the leading order, i.e.,

$$\frac{\partial c_\alpha(\mu^{(0)})}{\partial t} = \nabla \cdot (D_\alpha \nabla c_\alpha(\mu^{(0)})).$$

Note that there is no summation convention on the right hand side of the above equation.

D.1.2 Local analysis of binary interfaces

D.1.2.1 Leading order local analysis of binary interfaces

The leading order requirement for the phase-field variable is the same as in section 3.3.3.1, i.e., Eq. (3.21). Integrating the latter goes on to establish that the bulks (which correspond to one or the other critical point) are in such a way the corresponding multi-well values are all the same. Hence, the implication is that the bulks only correspond to the local minima of the restricted multi-well assuming that the initial filling is appropriate to this. Further, the path traced on the Gibbs-simplex by the interface between two equilibrium phases minimizes the weighted distance, Eq. (3.26).

The leading order requirement for the chemical potential is

$$\frac{\partial}{\partial \rho} \left\{ \left(\sum_{\alpha=1}^N D_{\alpha} \frac{dc_{\alpha}}{d\mu}(\tilde{\mu}^{(0)}) \mathfrak{h}_{\alpha}(\tilde{\phi}^{(0)}) \right) \frac{\partial \tilde{\mu}^{(0)}}{\partial \rho} \right\} = 0$$

and the implication is

$$\tilde{\mu}^{(0)}(\rho) = \text{constant.}$$

Further, because of matching conditions, $\mu^{(0)}|_{-} = \tilde{\mu}^{(0)} = \mu^{(0)}|_{+}$.

D.1.2.2 Next-to-leading order local analysis of binary interfaces

One of the requirements at this order is the same as Eq. (3.28) except that f_{α} is replaced by $\omega_{\alpha}(\tilde{\mu}^{(0)})$. Since $\tilde{\mu}^{(0)}$ turned out to be independent of ρ , the retrieved law is the same as Eq. (3.30), again, with f_{α} replaced by $\omega_{\alpha}(\tilde{\mu}^{(0)})$.

Pertaining to the chemical potential evolution equation, the requirement is

$$\frac{\partial}{\partial \rho} \left\{ \left(\sum_{\alpha=1}^N D_{\alpha} \frac{dc_{\alpha}}{d\mu}(\tilde{\mu}^{(0)}) \mathfrak{h}_{\alpha}(\tilde{\phi}^{(0)}) \right) \frac{\partial \tilde{\mu}^{(1)}}{\partial \rho} \right\} + v^{(0)} \left(c_{\alpha}(\tilde{\mu}^{(0)}) \frac{\partial \mathfrak{g}_{\alpha}(\tilde{\phi}^{(0)})}{\partial \rho} \right) = 0 \quad (\text{D.2})$$

where the Einstein's summation convention is utilized for the second summand. The recovered law is

$$\begin{aligned} \sum_{\alpha=1}^N D_{\alpha} \frac{\partial c_{\alpha}(\mu^{(0)})}{\partial r} \Big|_{+} \mathfrak{h}_{\alpha}(\phi^{(0)}|_{+}) - \sum_{\alpha=1}^N D_{\alpha} \frac{\partial c_{\alpha}(\mu^{(0)})}{\partial r} \Big|_{-} \mathfrak{h}_{\alpha}(\phi^{(0)}|_{-}) \\ = v^{(0)} \left(c_{\alpha}(\tilde{\mu}^{(0)}) \mathfrak{g}_{\alpha}(\phi^{(0)}|_{-}) - c_{\alpha}(\tilde{\mu}^{(0)}) \mathfrak{g}_{\alpha}(\phi^{(0)}|_{+}) \right). \end{aligned}$$

From here on, we restrict ourselves to multi-wells that give rise to binary interfaces free of third phases at zeroth order. Further, let them be chosen such that the integral

$\int_{-\infty}^{\infty} \frac{\partial \tilde{\phi}_\beta^{(0)}}{\partial \rho} \frac{\partial \tilde{\phi}_\beta^{(0)}}{\partial \rho} d\rho$ is unity. Then, for an interface between the s^{th} and the l^{th} phases, the requirements are

$$(\tau_{sl}v^{(0)} + \gamma\kappa^{(0)}) = \omega_l(\tilde{\mu}_{\text{int}}^{(0)}) - \omega_s(\tilde{\mu}_{\text{int}}^{(0)}) \quad \text{and} \quad (\text{D.3})$$

$$D_s \left. \frac{\partial c_s(\mu^{(0)})}{\partial r} \right|_{r=0^-} - D_l \left. \frac{\partial c_l(\mu^{(0)})}{\partial r} \right|_{r=0^+} = v^{(0)} \left(c_l(\tilde{\mu}_{\text{int}}^{(0)}) - c_s(\tilde{\mu}_{\text{int}}^{(0)}) \right) \quad (\text{D.4})$$

under the assumption that the positive direction of r points to the ϕ_l phase, and, where, for better emphasis, the constant $\tilde{\mu}^{(0)}$ is replaced by $\tilde{\mu}_{\text{int}}^{(0)}$, the chemical potential at the given s -coordinate of the interface in question.

The Gibbs-Thomson condition Eq. (D.3) is usually re-expressed in terms of the equilibrium chemical potential μ_{eq} between the two involving phases as

$$\begin{aligned} (\tau_{sl}v^{(0)} + \gamma\kappa^{(0)}) &= \omega_l(\mu_{\text{eq}}) + \omega'_l(\mu^*)(\tilde{\mu}_{\text{int}}^{(0)} - \mu_{\text{eq}}) - \omega_s(\mu_{\text{eq}}) - \omega'_s(\mu^{**})(\tilde{\mu}_{\text{int}}^{(0)} - \mu_{\text{eq}}) \\ &= - (c_l(\mu^*) - c_s(\mu^{**})) (\tilde{\mu}_{\text{int}}^{(0)} - \mu_{\text{eq}}) \\ &\approx - (c_l(\mu_{\text{eq}}) - c_s(\mu_{\text{eq}})) (\tilde{\mu}_{\text{int}}^{(0)} - \mu_{\text{eq}}) \end{aligned} \quad (\text{D.5})$$

where μ^* and μ^{**} lie in the interval whose end points are $\tilde{\mu}_{\text{int}}^{(0)}$ and μ_{eq} .

Often, sharp interface models of many solidification processes, including the Jackson-Hunt analysis, adopt the special choice of infinite kinetics of attachment or, equivalently, the case of vanishing kinetic coefficient. Also, as the diffusivity in the (undercooled) melt phase of a substance is a few orders higher than that in the solid phase at the same temperature, typically, the latter is approximated to vanish. We now accommodate these two aspects into the phase-field model. The former is done by performing a thin-interface analysis, i.e., by carrying on with the asymptotic analysis at the next order. We proceed accordingly, but before that, $\tilde{\mu}^{(1)}$ is expressed explicitly for the $\phi_s - \phi_l$ interface from Eq. (D.2) as

$$\tilde{\mu}^{(1)} = \tilde{\mu}^{(1)}(0) + \int_0^\rho \frac{v^{(0)} \left\{ c_s(\tilde{\mu}^{(0)}) \left(1 - \mathbf{g}_s(\tilde{\phi}^{(0)}) \right) - c_l(\tilde{\mu}^{(0)}) \mathbf{g}_l(\tilde{\phi}^{(0)}) \right\}}{D_l \frac{dc_l}{d\mu}(\tilde{\mu}^{(0)}) \mathbf{h}_l(\tilde{\phi}^{(0)})} d\rho \quad (\text{D.6})$$

where it is tacitly assumed that the considered s^{th} and l^{th} components of the phase-field variable characterize solid and liquid phases, respectively and hence D_s is chosen to vanish.

D.1.2.3 Next order local analysis of binary interfaces

It is not necessary to analyze the differential equation for the chemical potential at this order, only that of the phase-field suffices which for the case of the interface between the

ϕ_s and ϕ_l phases considered above happens to be

$$\begin{aligned}
& -(\tau_{sl}v^{(0)} + \gamma\kappa^{(0)}) \frac{\partial \tilde{\phi}_\beta^{(1)}}{\partial \rho} - (\tau_{sl}v^{(1)} + \gamma\kappa^{(1)}) \frac{\partial \tilde{\phi}_\beta^{(0)}}{\partial \rho} - \tau^{(1)}(\tilde{\phi}^{(0)}, \tilde{\phi}^{(1)})v^{(0)} \frac{\partial \tilde{\phi}_\beta^{(0)}}{\partial \rho} \\
& = -\omega'_\alpha(\tilde{\mu}^{(0)})\tilde{\mu}^{(1)} \frac{\partial \mathbf{g}_\alpha(\phi)}{\partial \phi_\beta}(\tilde{\phi}^{(0)}) - \omega_\alpha(\tilde{\mu}^{(0)}) \frac{\partial^2 \mathbf{g}_\alpha(\phi)}{\partial \phi_\gamma \partial \phi_\beta}(\tilde{\phi}^{(0)})\tilde{\phi}_\gamma^{(1)} \\
& \quad - \frac{\gamma}{2} \frac{\partial^3 W(\phi)}{\partial \phi_\gamma \partial \phi_\alpha \partial \phi_\beta}(\tilde{\phi}^{(0)})\tilde{\phi}_\alpha^{(1)}\tilde{\phi}_\gamma^{(1)} - \gamma \frac{\partial^2 W(\phi)}{\phi_\alpha \partial \phi_\beta}(\tilde{\phi}^{(0)})\tilde{\phi}_\alpha^{(2)} \\
& \quad + \gamma \frac{\partial^2 \tilde{\phi}_\beta^{(2)}}{\partial \rho^2} + \gamma(\kappa^{(0)})^2 \rho \frac{\partial \tilde{\phi}_\beta^{(0)}}{\partial \rho} - \tilde{\lambda}^{(2)}.
\end{aligned}$$

where $\tilde{\lambda}^{(2)} = \sum_{i=1}^N -\frac{\delta R}{\delta \phi_\beta}^{(2)}$ with $-\frac{\delta R}{\delta \phi_\beta}^{(2)}$ standing for the r.h.s of the above equation excluding $\tilde{\lambda}^{(2)}$. Like in section 4.3.1.1, from the above, we can have

$$\begin{aligned}
& 2(\tau_{sl}v^{(0)} + \gamma\kappa^{(0)}) \int_{-\infty}^{\infty} \frac{\partial \tilde{\phi}_\beta^{(1)}}{\partial \rho} \frac{\partial \tilde{\phi}_\beta^{(0)}}{\partial \rho} d\rho + (\tau_{sl}v^{(1)} + \gamma\kappa^{(1)}) \int_{-\infty}^{\infty} \frac{\partial \tilde{\phi}_\beta^{(0)}}{\partial \rho} \frac{\partial \tilde{\phi}_\beta^{(0)}}{\partial \rho} d\rho \\
& + v^{(0)} \int_{-\infty}^{\infty} \tau^{(1)}(\tilde{\phi}^{(0)}, \tilde{\phi}^{(1)}) \frac{\partial \tilde{\phi}_\beta^{(0)}}{\partial \rho} \frac{\partial \tilde{\phi}_\beta^{(0)}}{\partial \rho} d\rho \\
& = \int_{-\infty}^{\infty} \omega'_\alpha(\tilde{\mu}^{(0)})\tilde{\mu}^{(1)} \frac{\partial \mathbf{g}_\alpha(\phi)}{\partial \phi_\beta}(\tilde{\phi}^{(0)}) \frac{\partial \tilde{\phi}_\beta^{(0)}}{\partial \rho} d\rho
\end{aligned}$$

\Rightarrow

$$\begin{aligned}
& 2(\tau_{sl}v^{(0)} + \gamma\kappa^{(0)}) \int_{-\infty}^{\infty} \frac{\partial \tilde{\phi}_\beta^{(1)}}{\partial \rho} \frac{\partial \tilde{\phi}_\beta^{(0)}}{\partial \rho} d\rho + (\tau_{sl}v^{(1)} + \gamma\kappa^{(1)}) + v^{(0)} \int_{-\infty}^{\infty} \tau^{(1)}(\tilde{\phi}^{(0)}, \tilde{\phi}^{(1)}) \frac{\partial \tilde{\phi}_\beta^{(0)}}{\partial \rho} \frac{\partial \tilde{\phi}_\beta^{(0)}}{\partial \rho} d\rho \\
& = \int_{-\infty}^{\infty} \omega'_\alpha(\tilde{\mu}^{(0)})\tilde{\mu}^{(1)} \frac{\partial \mathbf{g}_\alpha(\tilde{\phi}^{(0)})}{\partial \rho} d\rho = - \int_{-\infty}^{\infty} c_\alpha(\tilde{\mu}^{(0)})\tilde{\mu}^{(1)} \frac{\partial \mathbf{g}_\alpha(\tilde{\phi}^{(0)})}{\partial \rho} d\rho \quad (\text{D.7})
\end{aligned}$$

The first integral on the l.h.s of the above equation vanishes due to each component of $\frac{\partial \tilde{\phi}^{(1)}}{\partial \rho}$ being an odd function when certain assumptions are made in regard to the multi-well and the bulk energy interpolating functions. Note that we are already working with multi-wells which have the property that among all the paths connecting a given two minima, the one along the edge of the Gibbs-hyper-simplex minimizes the integral in Eq. (3.21). That is, wells with the property that third phases are absent at zeroth order on binary interfaces. In fact, it is owing to this property that for the current case of interface between the s^{th} and the l^{th} phases, the corresponding inverse mobility τ_{sl} directly entered the above equation; otherwise, the entire function $\tau(\tilde{\phi}^{(0)})$ must have occurred in its place. Since this property is already invoked, due to the nature of Eqs. (3.22) and (3.28), what remains to be assumed for the identical vanishment of the first integral is the following:

the well and its second partial derivatives, and the first partial derivatives of all the bulk energy interpolating functions when restricted to any edge of the Gibb-hyper-simplex should be symmetric around the edge center. Note that both the Folch-Plapp triple-well and the Toth's multi-well satisfy this condition in addition to ensuring the absence of third phases (of course, with a necessary implementation of the Lagrange multiplier formulation in the former case). On confining to such kind of multi-wells and bulk energy density interpolants, Eq. (D.7) reduces to

$$(\tau_{sl}v^{(1)} + \gamma\kappa^{(1)}) + v^{(0)} \int_{-\infty}^{\infty} \tau^{(1)}(\tilde{\phi}^{(0)}, \tilde{\phi}^{(1)}) \frac{\partial \tilde{\phi}_{\beta}^{(0)}}{\partial \rho} \frac{\partial \tilde{\phi}_{\beta}^{(0)}}{\partial \rho} d\rho = - \int_{-\infty}^{\infty} c_{\alpha}(\tilde{\mu}^{(0)}) \tilde{\mu}^{(1)} \frac{\partial \mathbf{g}_{\alpha}(\tilde{\phi}^{(0)})}{\partial \rho} d\rho \quad (\text{D.8})$$

Let us now assume that the interpolation functions further satisfy some additional conditions viz. Eq. (4.7d) and the following: when only two components ϕ_{α} and ϕ_{β} of the phase-field variable are non-zero and add up to unity, then the corresponding interpolants $\mathbf{g}_{\alpha}(\phi)$ and $\mathbf{g}_{\beta}(\phi)$ as well add up to unity. Then, Eqs. (D.6) and (D.8) modify to

$$\begin{aligned} \tilde{\mu}^{(1)} &= \tilde{\mu}_{\text{int}}^{(1)} + \int_0^{\rho} \frac{v^{(0)} (c_s(\tilde{\mu}^{(0)}) - c_l(\tilde{\mu}^{(0)})) \mathbf{g}_l(\tilde{\phi}^{(0)})}{D_l \frac{dc_l}{d\mu}(\tilde{\mu}^{(0)}) \mathfrak{h}_l(\tilde{\phi}^{(0)})} d\rho \\ &\approx \tilde{\mu}_{\text{int}}^{(1)} + \int_0^{\rho} \frac{v^{(0)} (c_s(\mu_{\text{eq}}) - c_l(\mu_{\text{eq}})) \mathbf{g}_l(\tilde{\phi}^{(0)})}{D_l \frac{dc_l}{d\mu}(\tilde{\mu}^{(0)}) \mathfrak{h}_l(\tilde{\phi}^{(0)})} d\rho \end{aligned} \quad (\text{D.9})$$

and

$$\begin{aligned} (\tau_{sl}v^{(1)} + \gamma\kappa^{(1)}) + v^{(0)} \int_{-\infty}^{\infty} \tau^{(1)}(\tilde{\phi}^{(0)}, \tilde{\phi}^{(1)}) \frac{\partial \tilde{\phi}_{\beta}^{(0)}}{\partial \rho} \frac{\partial \tilde{\phi}_{\beta}^{(0)}}{\partial \rho} d\rho \\ = - \int_{-\infty}^{\infty} (c_l(\tilde{\mu}^{(0)}) - c_s(\tilde{\mu}^{(0)})) \tilde{\mu}^{(1)} \frac{\partial \mathbf{g}_l(\tilde{\phi}^{(0)})}{\partial \rho} d\rho \\ \approx - (c_l(\mu_{\text{eq}}) - c_s(\mu_{\text{eq}})) \int_{-\infty}^{\infty} \tilde{\mu}^{(1)} \frac{\partial \mathbf{g}_l(\tilde{\phi}^{(0)})}{\partial \rho} d\rho, \end{aligned} \quad (\text{D.10})$$

respectively, where $\tilde{\mu}^{(1)}(0)$ is re-denoted by $\tilde{\mu}_{\text{int}}^{(1)}$. Combining Eqs. (D.5), (D.9) and (D.10) gives

$$-(c_l(\mu_{\text{eq}}) - c_s(\mu_{\text{eq}})) \left(\tilde{\mu}_{\text{int}}^{(0)} + \epsilon \tilde{\mu}_{\text{int}}^{(1)} - \mu_{\text{eq}} \right) = \tau_{sl}^T (v^{(0)} + \epsilon v^{(1)}) + \gamma (\kappa^{(0)} + \epsilon \kappa^{(1)}) + \mathcal{O}(\epsilon^2) \quad (\text{D.11})$$

where

$$\begin{aligned} \tau_{sl}^T = & \tau_{sl} + \epsilon \int_{-\infty}^{\infty} \tau^{(1)}(\tilde{\phi}^{(0)}, \tilde{\phi}^{(1)}) \frac{\partial \tilde{\phi}_{\beta}^{(0)}}{\partial \rho} \frac{\partial \tilde{\phi}_{\beta}^{(0)}}{\partial \rho} d\rho \\ & - \epsilon \frac{(c_l(\mu_{\text{eq}}) - c_s(\mu_{\text{eq}}))^2}{D_l \frac{\partial c_l}{\partial \mu}(\tilde{\mu}^{(0)})} \int_{-\infty}^{\infty} \left(\int_0^{\rho} \frac{\mathbf{q}_l(\tilde{\phi}^{(0)})}{\hbar_l(\tilde{\phi}^{(0)})} d\rho \right) \frac{\partial \mathbf{q}_l(\tilde{\phi}^{(0)})}{\partial \rho} d\rho. \end{aligned} \quad (\text{D.12})$$

Hence, the thin-interface correction to retrieve Gibbs-Thomson law upto first order can be prescribed from the above equation. Where, the superscript T can be interpreted to stand for ‘theoretical’ implying that the actual kinetic coefficient value of the material system should be chosen for τ_{sl}^T while the corresponding value to be used in the simulations is τ_{sl} .

The first integral on the r.h.s of Eq (D.12) does not arise in a scalar phase-field model and is only specific to a multi-phase one. That means, in multi-phase-field models, the thin-interface correction has an additional term. Note however, if it is taken care that the third phases do not arise even at the first order, i.e, in $\tilde{\phi}^{(1)}$, then for the arithmetic and harmonic τ -formulations, this term identically vanishes. Hence, if Toth’s multi-well is used without Lagrange implementation, the thin-interface correction is the same as the one obtained in a scalar phase-field model if the interpolation functions satisfy the minimum requirements of Eqs. (4.7a)-(4.7d) along with ‘ $\phi_{\alpha} + \phi_{\beta} = 1 \implies \mathbf{q}_{\alpha} + \mathbf{q}_{\beta} = 1$ ’. However, if Folch-Plapp triple well is used in conjunction with the Lagrange multiplier implementation, to have this, the interpolation functions have to be chosen necessarily as per the second row of Table 2.1 or should include Eq. (4.7e) as well.

Finally, it is worth mentioning that although Eq. (D.11) is a perfectly valid relation to utilize for the purpose of prescribing the thin-interface limit correction, the following is typically preferred over it.

$$- (c_l(\mu_{\text{eq}}) - c_s(\mu_{\text{eq}})) \left(\mu_{\text{int}}^{(0)} + \epsilon \mu_{\text{int}}^{(1)} - \mu_{\text{eq}} \right) = \tau_{sl}^T (v^{(0)} + \epsilon v^{(1)}) + \gamma (\kappa^{(0)} + \epsilon \kappa^{(1)}) + \mathcal{O}(\epsilon^2) \quad (\text{D.13})$$

where $\mu_{\text{int}}^{(0)}$ and $\mu_{\text{int}}^{(1)}$ are defined as $\mu_{\text{int}}^{(0)} := \lim_{r \rightarrow 0} \mu^{(0)}(r, s, t)$ and $\mu_{\text{int}}^{(1)} := \lim_{r \rightarrow 0} \mu^{(1)}(r, s, t)$. That is, instead of the $\rho = 0$ values of the local chemical potential, the inner limits of the outer expansion are preferred. The corresponding modification to the thin-interface correction, Eq. (D.12), can be easily put forth by noting that from the matching conditions, we have the following

$$\mu^{(1)}(r \rightarrow 0^{\pm}) = \lim_{\rho \rightarrow \pm\infty} \left(\tilde{\mu}_{\text{int}}^{(1)} - \rho \lim_{\rho \rightarrow \pm\infty} \frac{\partial \tilde{\mu}_{\text{int}}^{(1)}}{\partial \rho} \right). \quad (\text{D.14})$$

Clubbing Eqs. (D.9) and (D.14) leads to

$$\mu^{(1)}(r \rightarrow 0^\pm) = \tilde{\mu}_{\text{int}}^{(1)} + \int_0^{\pm\infty} (\mathfrak{p}(\rho) - \mathfrak{p}(\rho \rightarrow \pm\infty)) d\rho \quad (\text{D.15})$$

where $\mathfrak{p}(\rho)$ is used to denote the integrand of Eq. (D.9). Substituting Eq. (D.15) in Eq. (D.11), the second variant of the thin interface limit correction, Eq. (D.12), is obtained which is as follows.

$$\begin{aligned} \tau_{sl}^T = \tau_{sl} + \epsilon \frac{(c_l(\mu_{\text{eq}}) - c_s(\mu_{\text{eq}}))^2}{D_l \frac{\partial c_l}{\partial \mu}(\tilde{\mu}^{(0)})} \int_0^{\pm\infty} \left(\frac{\mathfrak{g}_l(\tilde{\phi}^{(0)})}{\mathfrak{h}_l(\tilde{\phi}^{(0)})} - \lim_{\rho \rightarrow \pm\infty} \frac{\mathfrak{g}_l(\tilde{\phi}^{(0)})}{\mathfrak{h}_l(\tilde{\phi}^{(0)})} \right) d\rho \\ - \epsilon \frac{(c_l(\mu_{\text{eq}}) - c_s(\mu_{\text{eq}}))^2}{D_l \frac{\partial c_l}{\partial \mu}(\tilde{\mu}^{(0)})} \int_{-\infty}^{\infty} \left(\int_0^{\rho} \frac{\mathfrak{g}_l(\tilde{\phi}^{(0)})}{\mathfrak{h}_l(\tilde{\phi}^{(0)})} d\rho \right) \frac{\partial \mathfrak{g}_l(\tilde{\phi}^{(0)})}{\partial \rho} d\rho \end{aligned} \quad (\text{D.16})$$

where the first integral of Eq. (D.12) is not carried over by assuming that the interpolation functions and the well are appropriately chosen (as discussed above) for it to vanish.

However, there is an issue that needs to be resolved in regard to Eq. (D.16). Usually, the $r \rightarrow 0^+$ and the $r \rightarrow 0^-$ limits of $\mu^{(1)}(r, s, t)$ do not coincide which gives rise to an artifact solute trapping behavior. To counteract this, what is called an anti-trapping current term is introduced into the chemical potential evolution equation. Mostly, only the scalar or the three-phase multi-phase-field models have been considered for presenting this term. However, the counterpart arguments for the generic multi-phase-field formulations can be easily constructed if absence of third phases at zeroth order is invoked. Before providing the details, we address an alternative idea that may arise in the minds of the readers in which the usage of any new terms in the evolution equations can be obviated altogether. Which is, if $\mathfrak{g}_l(\phi)$ and $\mathfrak{h}_l(\phi)$ are chosen identical to each other, then the integrand of the first integral of Eq. (D.16) vanishes or, in other words, the problem of $\lim_{r \rightarrow 0^+} \mu^{(1)}(r, s, t)$ and $\lim_{r \rightarrow 0^-} \mu^{(1)}(r, s, t)$ being unequal can be eliminated. This is a good enough suggestion, but the problem is that even the second integral vanishes in such a case. While this is even more welcome as it means that Gibbs-Thomson condition can be recovered to first order in ϵ without having to adjust the interfacial mobilities, it will defeat the purpose of providing prescriptions for being able to simulate the infinite kinetics case. Thus, the anti-trapping current method is the only solution that is currently available. Its form in the current multi-phase-field model when chosen in the following manner will avoid the artifact solute trapping and should be added into the curly brackets term of Eq. (2.44)

$$\mathbf{J}_{\text{at}} = - \sum_{\alpha=1}^N \epsilon c_\alpha(\mu) s_\alpha(\phi) \frac{\partial \phi_\alpha}{\partial t} \frac{\nabla \phi_\alpha}{|\nabla \phi_\alpha|}.$$

where $s_\alpha(\phi)$ is such that when the zeroth order (local) phase-field profile is substituted for its argument, it should satisfy

$$s_\alpha(\tilde{\phi}^{(0)}) = - \frac{\left[1 - \mathbf{g}_\alpha(\tilde{\phi}^{(0)})\right] \mathbf{h}_\alpha(\tilde{\phi}^{(0)})}{\frac{\partial \tilde{\phi}_\alpha^{(0)}}{\partial \rho}}.$$

However, it is mandatory to choose $\mathbf{g}_\alpha(\phi)$ and $\mathbf{h}_\alpha(\phi)$ to be identical to each other for this purpose and also such that ' $\phi_\alpha + \phi_\beta = 1 \implies \mathbf{g}_\alpha + \mathbf{g}_\beta = 1$ '. We point out that if the interpolation functions are chosen in the uncoupled form and particularly as $\mathbf{g}_\alpha(\phi) = \mathbf{g}_S(\phi_\alpha) = \phi_\alpha^2(3 - 2\phi_\alpha)$ or $\phi_\alpha^3(10 - 15\phi_\alpha + 6\phi_\alpha^2)$, then the latter is fulfilled. Thus, the final thin-interface limit prescription for τ_{sl} for a surface with vanishing kinetic coefficient separating a diffusionless solid from melt is

$$\begin{aligned} \tau_{sl} = & -\epsilon \frac{(c_l(\mu_{\text{eq}}) - c_s(\mu_{\text{eq}}))^2}{D_l \frac{\partial c_l}{\partial \mu}(\tilde{\mu}^{(0)})} \int_0^{-\infty} \mathbf{g}_l(\tilde{\phi}^{(0)}) d\rho \\ & + \epsilon \frac{(c_l(\mu_{\text{eq}}) - c_s(\mu_{\text{eq}}))^2}{D_l \frac{\partial c_l}{\partial \mu}(\tilde{\mu}^{(0)})} \int_{-\infty}^{\infty} \left(\int_0^\rho \mathbf{g}_l(\tilde{\phi}^{(0)}) d\rho \right) \frac{\partial \mathbf{g}_l(\tilde{\phi}^{(0)})}{\partial \rho} d\rho. \end{aligned} \quad (\text{D.17})$$

Appendix E

Appendices to chapter 5

E.1 Three grain evolution

Some more parameter sets, in addition to those presented in chapter 5, are considered for the three grain evolution within the setup of Fig. 4.1 and the recovered simulation results are compiled here. The main aspect that is tested is, what happens to the behavior when the steady state speeds are reduced? Note that the data chosen in section 5.3 is such that the obtained steady state speeds are around 0.075. And it was seen that the converged profiles did not quite agree well with the theoretical ones. Whereas, as can be seen from Figs. E.1, E.2 and E.3, when the steady state speeds are reduced roughly by 30 – 40 times, improved agreement is found. The difference is especially striking in the case of low angle, i.e., from Fig. 5.3 to E.2. On the other hand, the rate of convergence of the steady state speeds seems to be reducing for the larger angle case as can be noted by comparing Tables 5.6 and E.6. Currently, for lowering the growth velocities, the bulk driving forces and the average curvatures are reduced. That is, the essential difference between, say, Table 5.3 and E.3 is the reduction in the bulk energy of the ϕ_1 phase and a raise in the grain size $N_x \times \Delta x$. If this is further carried forward, as in Table E.7, it is indeed seen that the convergence of the growth speed is lowered even when the angle is small as indicated by Table E.8. In fact, if the f_1 alone were to be reduced without altering $N_x \times \Delta x$, then the errors at the same interface thickness are even higher as reported for the large angle case in Table E.10, and as was also observed for the small angle one which is not reported here. Thus, it can be concluded that the reduction of driving force and the increase of grain width have opposite effects on the convergence rate of the steady state speeds, and the enhancement seen in Table E.4 is due the latter dominating the former.

Table E.1: A parameter set employed for simulating the three grain evolution in the setup of Fig. 4.1 using obstacle potential.

f_1	f_2	f_3	γ	τ_{12}	τ_{13}	τ_{23}	N_x	N_y	Δx	Δt	ϵ
0.018	0.0	0.0	1.0	1.0	1.0	1000.0	64	32	1.0	$0.1(\Delta x)^2$	$4.0\sqrt{\Delta x}$
$\{g_\alpha(\phi)\}$			$W(\phi)$				$\tau(\phi)$				
$\{\phi_\alpha^3(10 - 15\phi_\alpha + 6\phi_\alpha^2)\}$			$W_{\text{obs}}(\phi)$ with $a = 16/\pi^2$, $a_{12} = a_{13} = 1.0$ and $a_{23} = 1.0$				$\tau_{\text{H}}(\phi) = \frac{\sum_{\alpha<\beta} \phi_\alpha \phi_\beta}{\sum_{\alpha<\beta} \frac{1}{\tau_{\alpha\beta}} \phi_\alpha \phi_\beta}$				

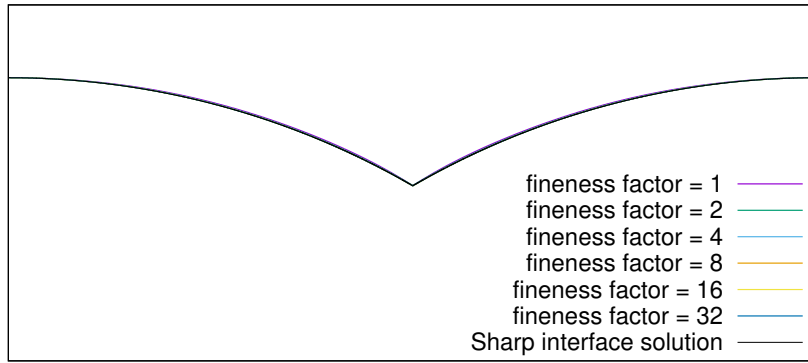


Figure E.1: Steady-state growth fronts obtained in the three grain evolution simulations within the setup of Fig. 4.1 for the parameter set of Table. E.1.

Table E.2: Steady state speeds recovered for the growth fronts of Fig. E.1.

Fineness factor	Recovered angle at the triple junction	Recovered steady state speed (rel. error)
1	33.42894°	0.002217382 (10.66%)
2	31.17339°	0.002323780 (6.38%)
4	30.71436°	0.002364658 (4.73%)
8	30.52105°	0.002406066 (3.06%)
16	30.39902°	0.002425666 (2.27%)
32	30.09731°	0.002441726 (1.63%)
Sharp interface solution	30.0°	0.002482081

Table E.3: A parameter set employed for simulating the three grain evolution within the setup of Fig. 4.1 using obstacle potential.

f_1	f_2	f_3	γ	τ_{12}	τ_{13}	τ_{23}	N_x	N_y	Δx	Δt	ϵ
0.01	0.0	0.0	1.0	1.0	1.0	1000.0	64	32	1.0	$0.1(\Delta x)^2$	$4.0\sqrt{\Delta x}$
$\{g_\alpha(\phi)\}$			$W(\phi)$				$\tau(\phi)$				
$\{\phi_\alpha^3(10 - 15\phi_\alpha + 6\phi_\alpha^2)\}$			$W_{\text{obs}}(\phi)$ with $a = 16/\pi^2$, $a_{12} = a_{13} = 1.0$ and $a_{23} = 0.5$				$\tau_{\text{H}}(\phi) = \frac{\sum_{\alpha<\beta} \phi_\alpha \phi_\beta}{\sum_{\alpha<\beta} \frac{1}{\tau_{\alpha\beta}} \phi_\alpha \phi_\beta}$				

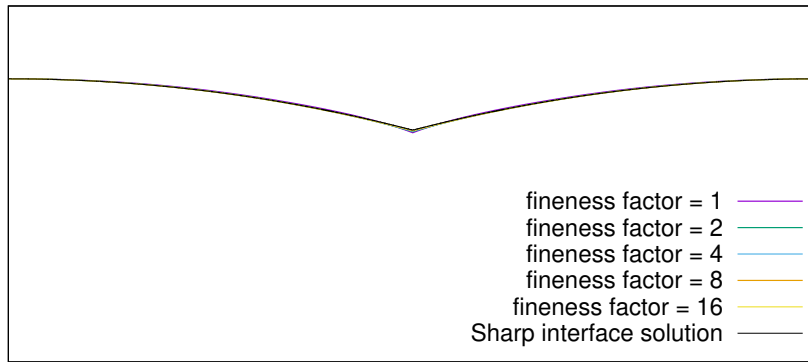


Figure E.2: Steady-state growth fronts obtained in the three grain evolution simulations within the setup of Fig. 4.1 for the parameter set of Table. E.3.

Table E.4: Steady state speeds recovered for the growth fronts of Fig. E.2.

Fineness factor	Recovered angle at the triple junction	Recovered steady state speed (rel. error)
1	20.95266°	0.001857443 (15.98%)
2	17.03339°	0.001992341 (9.88%)
4	16.07695°	0.002046328 (7.43%)
8	15.06462°	0.002095833 (5.20%)
16	14.76645°	0.002128014 (3.74%)
Sharp interface solution	14.47751°	0.002210693

Table E.5: A parameter set employed for simulating the three grain evolution within the setup of Fig. 4.1 using obstacle potential.

f_1	f_2	f_3	γ	τ_{12}	τ_{13}	τ_{23}	N_x	N_y	Δx	Δt	ϵ
0.018	0.0	0.0	1.0	1.0	1.0	1000.0	64	64	1.0	$0.1(\Delta x)^2$	$4.0\sqrt{\Delta x}$
$\{g_\alpha(\phi)\}$			$W(\phi)$				$\tau(\phi)$				
$\{\phi_\alpha^3(10 - 15\phi_\alpha + 6\phi_\alpha^2)\}$			$W_{\text{obs}}(\phi)$ with $a = 16/\pi^2$, $a_{12} = a_{13} = 0.6$ and $a_{23} = 1.0$				$\tau_{\text{H}}(\phi) = \frac{\sum_{\alpha<\beta} \phi_\alpha \phi_\beta}{\sum_{\alpha<\beta} \frac{1}{\tau_{\alpha\beta}} \phi_\alpha \phi_\beta}$				

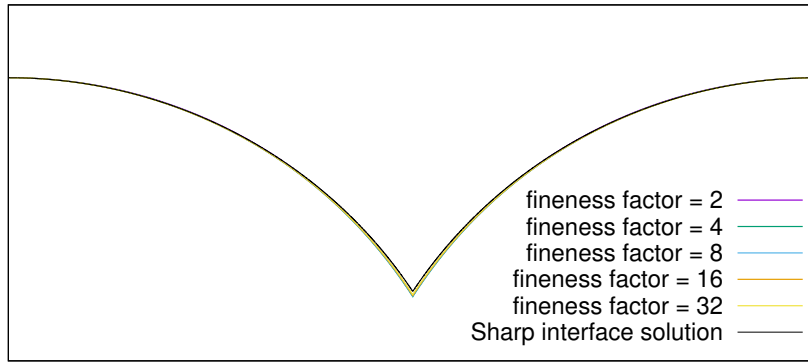


Figure E.3: Steady-state growth fronts obtained in the three grain evolution simulations within the setup of Fig. 4.1 for the parameter set of Table. E.5.

Table E.6: Steady state speeds recovered for the growth fronts of Fig. E.3.

Fineness factor	Recovered angle at the triple junction	Recovered steady state speed (rel. error)
1	54.84003°	0.002446928 (10.34%)
2	56.49607°	0.002428584 (11.02%)
4	57.04364°	0.002447236 (10.33%)
8	57.11612°	0.002490291 (8.76%)
16	57.04425°	0.002538486 (6.99%)
32	56.91713°	0.002583488 (5.34%)
Sharp interface solution	56.44269°	0.002729245

Table E.7: A parameter set employed for simulating the three grain evolution within the setup of Fig. 4.1 using obstacle potential.

f_1	f_2	f_3	γ	τ_{12}	τ_{13}	τ_{23}	N_x	N_y	Δx	Δt	ϵ
0.00625	0.0	0.0	1.0	1.0	1.0	1000.0	128	32	1.0	$0.1(\Delta x)^2$	$4.0\sqrt{\Delta x}$
$\{g_\alpha(\phi)\}$			$W(\phi)$				$\tau(\phi)$				
$\{\phi_\alpha^3(10 - 15\phi_\alpha + 6\phi_\alpha^2)\}$			$W_{\text{obs}}(\phi)$ with $a = 16/\pi^2$, $a_{12} = a_{13} = 1.0$ and $a_{23} = 0.5$				$\tau_{\text{H}}(\phi) = \frac{\sum_{\alpha < \beta} \phi_\alpha \phi_\beta}{\sum_{\alpha < \beta} \frac{1}{\tau_{\alpha\beta}} \phi_\alpha \phi_\beta}$				

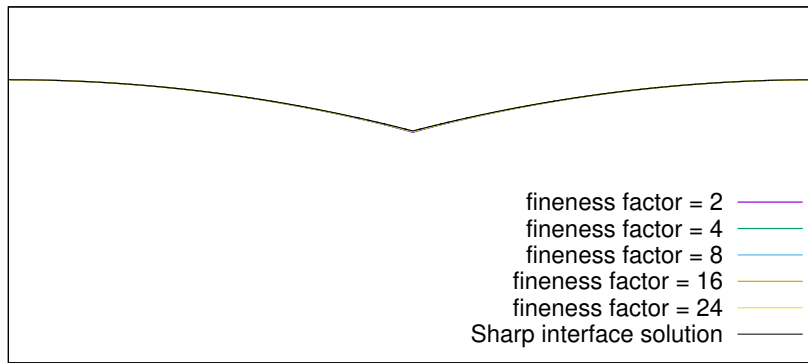


Figure E.4: Steady-state growth fronts obtained in the three grain evolution simulations within the setup of Fig. 4.1 for the parameter set of Table. E.7.

Table E.8: Steady state speeds recovered for the growth fronts of Fig. E.4.

Fineness factor	Recovered angle at the triple junction	Recovered steady state speed (rel. error)
1	20.95266°	0.002006801 (15.27%)
2	16.24719°	0.002108675 (10.97%)
4	15.67747°	0.002139397 (9.67%)
8	14.95330°	0.002169372 (8.41%)
16	14.82446°	0.002185306 (7.74%)
24	14.70746°	0.002194382 (7.35%)
Sharp interface solution	14.47751°	0.002368531

Table E.9: A parameter set employed for simulating the three grain evolution within the setup of Fig. 4.1 using obstacle potential..

f_1	f_2	f_3	γ	τ_{12}	τ_{13}	τ_{23}	N_x	N_y	Δx	Δt	ϵ
0.03348	0.0	0.0	1.0	1.0	1.0	1000.0	64	64	0.5	$0.1(\Delta x)^2$	$4.0(\Delta x)^{0.6}$
$\{g_\alpha(\phi)\}$			$W(\phi)$				$\tau(\phi)$				
$\{\phi_\alpha^3(10 - 15\phi_\alpha + 6\phi_\alpha^2)\}$			$W_{\text{obs}}(\phi)$ with $a = 16/\pi^2$, $a_{12} = a_{13} = 0.6$ and $a_{23} = 1.0$				$\tau_{\text{H}}(\phi) = \frac{\sum_{\alpha < \beta} \phi_\alpha \phi_\beta}{\sum_{\alpha < \beta} \frac{1}{\tau_{\alpha\beta}} \phi_\alpha \phi_\beta}$				

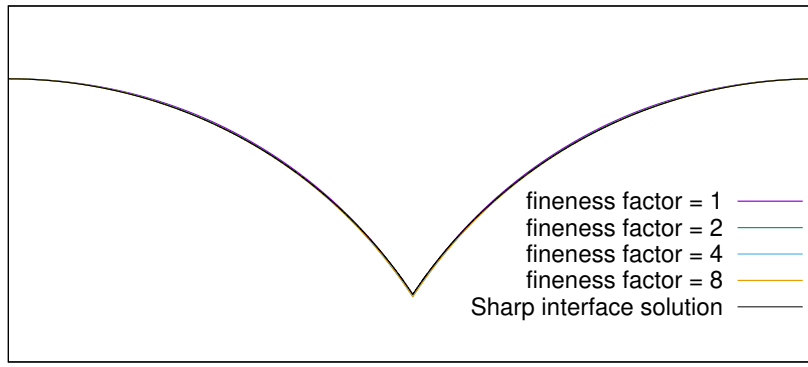


Figure E.5: Steady-state growth fronts obtained in the three grain evolution simulations within the setup of Fig. 4.1 for the parameter set of Table. E.9.

Table E.10: Steady state speeds recovered for the growth fronts of Fig. E.5.

Fineness factor	Recovered angle at the triple junction	Recovered steady state speed (rel. error)
1	57.17629°	0.002089984 (18.58%)
2	56.41203°	0.002136347 (16.77%)
4	56.42978°	0.002226663 (13.25%)
8	56.45840°	0.002312287 (9.918%)
16	—————	0.002384786 (7.094%)
Sharp interface solution	56.44269°	0.002566881

E.2 Single phase planar solidification

The planar solidification of NiZr alloy under isothermal conditions within the setup of Fig. E.6 is simulated using the modeling equations and the thermo-physical data of section 5.4. The recovered steady state speeds at various resolutions and ϵ v.s. $(\Delta x)^p$ prescriptions are tabulated in Table. E.11 for different Dirichlet data. In addition, the limiting sharp interface problem, viz. Eq. (C.15)* is solved and the predicted result is also listed in the table. It can be seen that the computational speeds are pretty close to the actual value even at lower resolutions or larger interface widths indicating that the implemented thin-interface correction and the anti-trapping current terms are quite efficacious and satisfactory. The beginning of the failure of $\epsilon \propto \Delta x$ simulations can also be perceived.

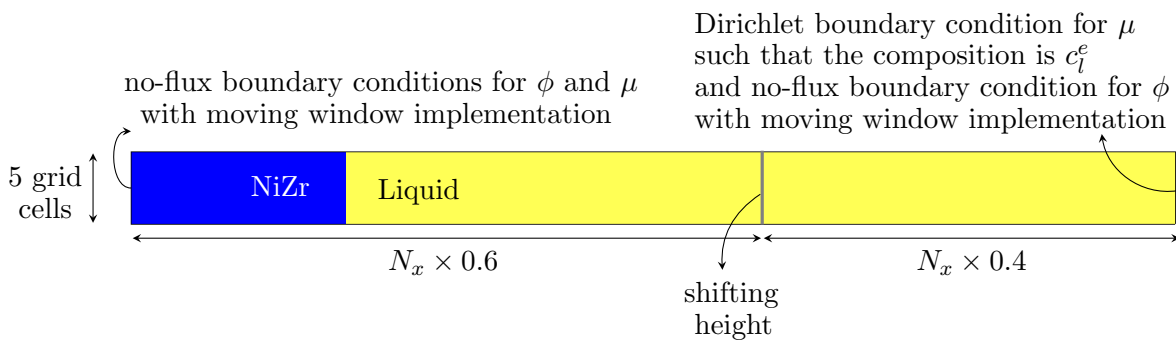


Figure E.6: Setup used for the NiZr planar solidification simulations.

*Of course, the NiZr solid is considered to have zero diffusivity; nevertheless, the end result is still the same, i.e., the one given by Eqs. (C.20)- (C.23).

Table E.11: Steady state planar solidification speeds of NiZr solid simulated within the setup of Fig. E.6 for various Dirichlet data c_l^e , $\epsilon \propto (\Delta x)^p$ choices and resolutions. The physical units of the speeds are $m s^{-1}$. At the base resolution, the N_x chosen is 100 grid cells.

Fineness factor	$c_l^e = 0.6115$		$c_l^e = 0.5615$	$c_l^e = 0.5115$
	$\epsilon = 5.0\sqrt{30\Delta x}$	$\epsilon = 5.0 \times \Delta x$	$\epsilon = 5.0\sqrt{30\Delta x}$	$\epsilon = 5.0\sqrt{30\Delta x}$
1	1.6823000×10^{-5}	1.682521510^{-5}	0.000292238	Unstable
2	1.6835056×10^{-5}	1.682606110^{-5}	0.000291660	Unstable
4	1.6837767×10^{-5}	1.679527410^{-5}	0.000291545	0.00108174
8	1.6839701×10^{-5}	1.661643310^{-5}	0.000291521	0.00108005
16	1.6840045×10^{-5}	1.573880710^{-5}	—————	0.00107971
Sharp interface solution	1.6858417×10^{-5}		0.0002915456	0.00107972

E.3 Cooperative growth

Table E.12: The magnitudes of the simulated speeds of Fig. 5.6.

Lamellar spacing (in μm)	Recovered steady state speed (in $\times 10^{-4} m/s$)		
	Resolution =1	Resolution =2	Resolution =4
0.150	3.4191	3.4693	3.4622
0.165	4.1133	4.1548	4.1670
0.180	4.5291	4.5564	4.5692
0.195	4.7503	4.7781	4.7875
0.210	4.8575	4.8711	4.8788
0.225	4.8848	4.8896	4.8914
0.240	4.8524	4.8530	4.8522
0.255	4.7865	4.7817	4.7793
0.270	4.6989	4.6879	4.6817
0.285	4.5928	4.5807	4.5702
0.300	4.4782	4.4654	4.4528
0.315	4.3602	4.3435	4.3349
0.330	4.2383	4.2223	4.2169

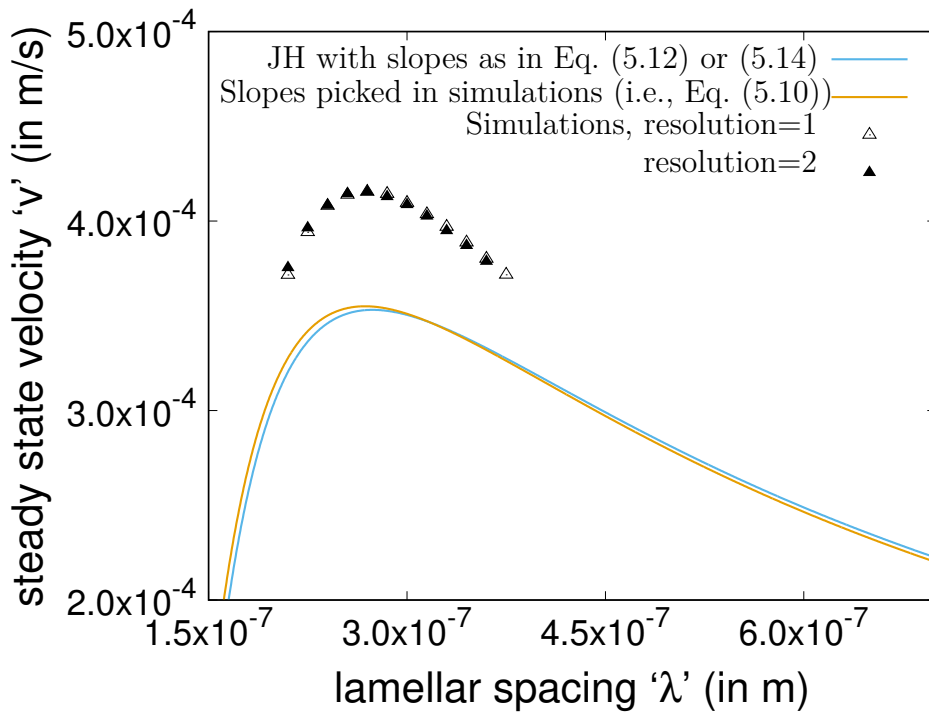


Figure E.7: Studies of Fig. 5.6 reperformed but by increasing the solid-solid interfacial energy to $\sigma_{\alpha\beta} = 0.6 \text{ Jm}^{-2}$.

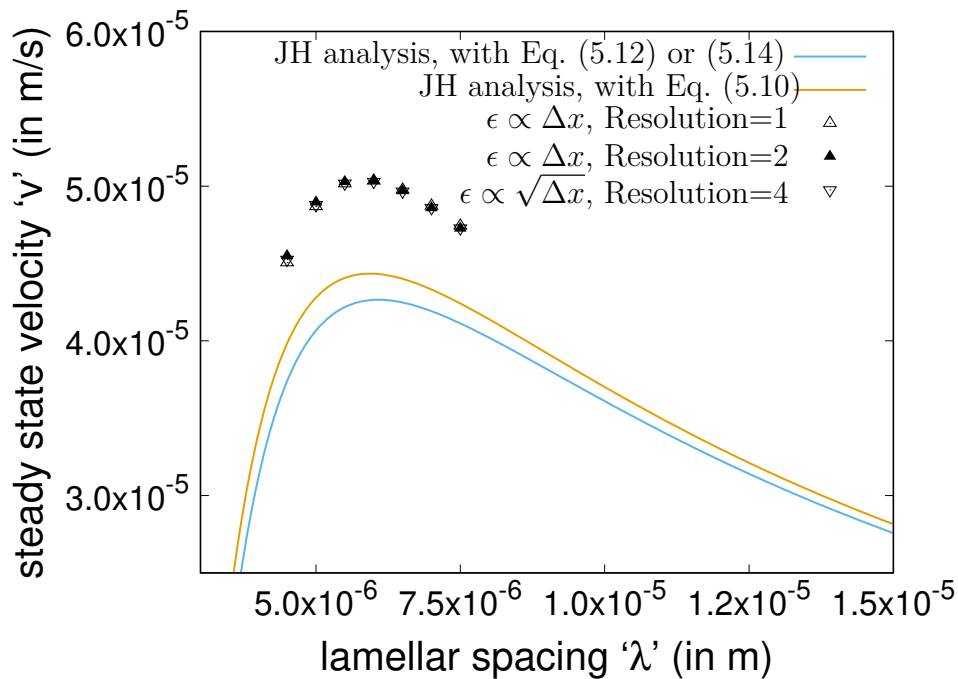


Figure E.8: Studies of Fig. 5.10 reperformed but by decreasing the solid-solid interfacial energy such that the angles made by the surfaces with the horizontal are reduced by half. Simulation results at higher resolutions are also presented with the ϵ v.s. $(\Delta x)^p$ relationship varied as indicated. The base resolution corresponds to $\Delta x = 1$, hence, the interface width is reduced by half in both the higher resolution cases.

Appendix F

Appendices to chapter 6

F.1 Order and error estimates for the solutions of the ZOLPA problem in stoichiometric systems

F.1.1 Error in estimating the concentration field

First, some order estimates on the unapproximated solute distribution are derived which will be useful both in showing that the zeroth order approximation is rightly implemented and in proving that the approximated solute distribution is accurate upto first order in Péclet number.

The approach we adopt is as follows. The BVP of interest is considered in its weak form. The existence and regularity of the solutions of the latter are investigated. In estimating the regularity of the solutions, bounds on them in certain norms are obtained in terms of the norms of the known functions of Eqs. (6.3b) and (6.3c). Since the latter functions all contain the parameter ϵ , the “size” of the solutions are related to the magnitude of the Péclet number. All the essential results to execute this program are already available in the literature related to the theory of partial differential equations. The only obstruction is that they pertain to the cases of bounded domains. However, since the domain Ω_∞ that concerns us is very simple, by using almost trivial modifications, the results can be adapted. Particularly speaking, we cover the domain using a countable number of bounded sub-regions and hence in each of them the existing results apply directly. As a consequence, the “size” of the solution in each sub-region is related to ϵ and some other positive constants which depend only on the dimensions, i.e, shapes and sizes, of the sub-region. Now, if care is taken such that the number of these constants is finite, then the norm of the solution in the whole domain can be bounded by the size of the known functions and the maximum of these constants.

First, the existence of weak solutions of Eq. (6.3a) is proved. We begin by multiplying Eq. (6.3a) with some function $\tilde{c}(x, z)$ and integrating the resultant in Ω_∞ :

$$\begin{aligned}
& \int_{\Omega_\infty} (\nabla^2 c) \tilde{c} dV + \epsilon \int_{\Omega_\infty} \frac{\partial c}{\partial z} \tilde{c} dV = 0 \\
\implies & - \int_{\Omega_\infty} \nabla c \cdot \nabla \tilde{c} dV + \int_{\partial\Omega_\infty} \tilde{c} \nabla c \cdot \vec{n} ds + \epsilon \int_{\Omega_\infty} \frac{\partial c}{\partial z} \tilde{c} dV = 0 \\
& \implies \int_{\Omega_\infty} \nabla c \cdot \nabla \tilde{c} dV - \epsilon \int_{\Omega_\infty} \frac{\partial c}{\partial z} \tilde{c} dV = \int_{\partial\Omega_\infty} \tilde{c} \nabla c \cdot \vec{n} ds \\
\implies & a(c, \tilde{c}) := \int_{\Omega_\infty} \nabla c \cdot \nabla \tilde{c} dV - \epsilon \int_{\Omega_\infty} \frac{\partial c}{\partial z} \tilde{c} dV - \epsilon \int_{\partial\Omega} \tilde{c} c dx = -\epsilon \int_{\partial\Omega} \tilde{c} (c_\infty - c^\nu(x)) dx \quad (\text{F.1})
\end{aligned}$$

Next, we consider the Sobolev space $H^1(\Omega_\infty)$. We look at one of its subspaces defined as the closure of $C_*^\infty(\Omega_\infty) \cap H^1(\Omega_\infty)$ in $H^1(\Omega_\infty)$ and denote it with $H_*^1(\Omega_\infty)$ where

$$C_*^\infty(\Omega_\infty) = \left\{ u \in C^\infty(\Omega_\infty) : \text{condition (a) is satisfied} \right\}$$

with the definition of condition (a) written as

$$(\text{a}) \int_{\substack{-1/2 \\ z=z^*}}^{1/2} u dx = \int_{\substack{-1/2 \\ z=z^*}}^{1/2} \frac{\partial u}{\partial z} dx = 0 \quad \forall z^* \geq \max \left\{ p(x) : x \in \left[-\frac{1}{2}, \frac{1}{2} \right] \right\}.$$

Now, we show that a $c(x, z)$ exists in $H_*^1(\Omega_\infty)$ such that Eq. (F.1) is satisfied for all $\tilde{c}(x, z) \in H_*^1(\Omega_\infty)$ with the derivatives of $c(x, z)$ and $\tilde{c}(x, z)$ chosen in the weak sense. For this, the Lax-Milgram theorem is appealed to. However, this requires showing that the bilinear operator $a(\cdot, \cdot)$ on the l.h.s of Eq. (F.1) is coercive and the linear form on the r.h.s is continuous. The calculations are as follows.

Consider $u \in C_*^\infty(\Omega_\infty) \cap H^1(\Omega_\infty)$.

$$\begin{aligned}
a(u, u) &= \int_{\Omega_\infty} |\nabla u|^2 dV - \epsilon \int_{\Omega_\infty} \frac{\partial u}{\partial z} u dV - \epsilon \int_{\partial\Omega} u^2 dx \\
&= \int_{\Omega_\infty} |\nabla u|^2 dV - \epsilon \int_{\Omega_\infty} \frac{\partial u}{\partial z} u dV + \epsilon \int_{\partial\Omega} u^2 \vec{n} \cdot \hat{z} ds = \int_{\Omega_\infty} |\nabla u|^2 dV + \epsilon \int_{\Omega_\infty} \frac{\partial u}{\partial z} u dV \\
&\geq \int_{\Omega_\infty} |\nabla u|^2 dV - \epsilon \sqrt{\int_{\Omega_\infty} \left(\frac{\partial u}{\partial z} \right)^2 dV} \int_{\Omega_\infty} u^2 dV \\
&\geq \int_{\Omega_\infty} |\nabla u|^2 dV - \epsilon \sqrt{\int_{\Omega_\infty} |\nabla u|^2 dV} \int_{\Omega_\infty} u^2 dV
\end{aligned}$$

In section F.2.1, it is shown that for functions u satisfying condition (a), the following Poincare inequality is valid.

$$\int_{\Omega_\infty} u^2 dV \leq Y \int_{\Omega_\infty} |\nabla u|^2 dV \quad (\text{F.2})$$

where $Y = \max \{2, 24z_{\max}^2\}$ with $z_{\max} = \max \{p(x) : x \in [-1/2, 1/2]\}$. Therefore,

$$\begin{aligned} a(u, u) &\geq (1 - \sqrt{\epsilon}Y) \int_{\Omega_\infty} |\nabla u|^2 dV \\ \implies a(u, u) &\geq \min \left\{ \frac{1 - \sqrt{\epsilon}Y}{2}, \frac{1 - \sqrt{\epsilon}Y}{2Y} \right\} \|u\|_{H^1(\Omega_\infty)}^2. \end{aligned} \quad (\text{F.3})$$

Thus, for small enough ϵ , the bilinear form $a(\cdot, \cdot)$ is coercive in $H_*^1(\Omega_\infty)$.

Now, consider $u \in H^1(\Omega_\infty)$

$$\begin{aligned} \left| -\epsilon \int_{\partial\Omega} u(c_\infty - c^\nu(x)) dx \right| &= \epsilon \left| \int_{-1/2}^{1/2} (c_\infty - c^\nu(x)) u(x, p(x)) dx \right| \\ &\leq \epsilon \| (c_\infty - c^\nu(x)) \|_{L^2[-\frac{1}{2}, \frac{1}{2}]} \| u(x, p(x)) \|_{L^2[-\frac{1}{2}, \frac{1}{2}]} \\ &\leq \epsilon \| (c_\infty - c^\nu(x)) \|_{L^2[-\frac{1}{2}, \frac{1}{2}]} \| u(x, p(x)) \| \| u \|_{L^2(\partial\Omega)} \\ &\leq \epsilon \| (c_\infty - c^\nu(x)) \|_{L^2[-\frac{1}{2}, \frac{1}{2}]} \| u(x, p(x)) \| \| u \|_{L^2(\partial\Omega_\infty)} \\ &\leq \epsilon \| (c_\infty - c^\nu(x)) \|_{L^2[-\frac{1}{2}, \frac{1}{2}]} \| u(x, p(x)) C_* \| \| u \|_{H^1(\Omega_\infty)}^2 \end{aligned}$$

where the last step follows from appendix F.2.2.

As all the hypotheses of the Lax-Milgram theorem are met, a unique weak solution $c_*(x, z)$ to Eq. (F.1) exists in the space $H_*^1(\Omega_\infty)$ with the bound

$$\|c_*(x, z)\|_{H^1(\Omega_\infty)}^2 \leq m\epsilon$$

for some constant m . Following a treatment similar to that of section 3.1 of [97] and using the analysis of appendix F.2.2, one can show that in each of the cylindrical pairs, $(Z(P_k, r_k), \varphi_k)$, $k \in \mathbb{Z} \cup A$, the following condition is satisfied.

$$\|c_*(x, z)\|_{C^{0,\delta}(\Omega_\infty \cap Z(P_k, r_k))} \leq m\epsilon (\| (c_\infty - c^\nu(x)) \|_{L^2[-\frac{1}{2}, \frac{1}{2}]}) \quad \text{where } \delta \in (0, 1) \quad (\text{F.4})$$

where m is some constant. Further, the lengths of the cylinders $Z(P_k, r_k)$ and $Z(P_{-k}, r_{-k})$ for some $k \in \mathbb{Z} \setminus \{0\}$ can be extended so that they overlap. By carrying out such a length increment for all the cylinders on vertical boundaries, we achieve a covering of the entire domain, Ω_∞ , consisting of cylindrical pairs. As all but finitely many of the cylinders in

the covering are of the same dimensions, the associated constants ‘ m ’ of Eq. (F.4) that are distinct are only finitely many. Hence, we have the following result:

$$|c_*(x, z)| < m\epsilon \quad \forall (x, z) \in \overline{\Omega}_\infty. \quad (\text{F.5})$$

Note that the above is true of a solution belonging to the space of functions that satisfy condition (a). Further, this exact condition is also true of the solution of the BVP Eqs. (6.3a)-(6.3f) except for the plane-wave term. Thus, it is established that the Fourier series of Eq. (6.6) except the plane wave term is of the order of ϵ and indeed the zeroth order approximation is rightly implemented.

Similar derivation shows that the difference between the solution of the ZOLPA problem and that of the unapproximated problem, except for their plane wave terms, is of the order of ϵ^2 . That is, if $c_{*,U}(x, z)$ and $c_{*,ZOLPA}(x, z)$ are the solutal fields of Eqs. (6.6) and (6.8) minus the respective plane wave terms, then

$$|c_{*,U}(x, z) - c_{*,ZOLPA}| < m\epsilon \quad \forall (x, z) \in \overline{\Omega}_\infty \quad (\text{F.6})$$

for some constant m .

We next provide some error estimates for the steady state growth speed.

F.1.2 Error in the estimation of the growth speed

Using the above result, Eq. (F.6), we next show that the relative error in the estimated steady state speed (Eq. (6.19)) is of the order of ϵ . Consider the generalized Gibbs-Thomson relations, Eqs. (6.3g) and (6.3h). The concentration entering into these equations should be the one that is obtained without invoking the zeroth and low Péclet number assumptions, i.e., $c(x, z)$ of Eq. (6.6). Instead, we have used the one of Eq. (6.8). The associated error can be evaluated as follows:

$$\begin{aligned} \langle \Delta T \rangle_\alpha &= -m^\alpha \langle c_\infty + c_U - c_E \rangle_\alpha + \Gamma_\alpha \langle \kappa \rangle_\alpha \\ \implies \Delta T &= -m^\alpha \langle c_\infty + a_{0,U} e^{-\epsilon p(x)} + c_{*,U} - c_E \rangle_\alpha + \Gamma_\alpha \langle \kappa \rangle_\alpha \\ &= -m^\alpha b_0 - m^\alpha a_{0,U} \zeta_0^\alpha - m^\alpha \langle c_{*,U} \rangle_\alpha + \Gamma_\alpha \langle \kappa \rangle_\alpha \\ &= -m^\alpha b_0 - m^\alpha a_{0,U} \zeta_0^\alpha - m^\alpha \langle c_{*,U} - c_{*,ZOLPA} + c_{*,ZOLPA} \rangle_\alpha + \Gamma_\alpha \langle \kappa \rangle_\alpha \\ &= -m^\alpha b_0 - m^\alpha a_{0,U} \zeta_0^\alpha - m^\alpha \langle c_{*,ZOLPA} \rangle_\alpha + \Gamma_\alpha \langle \kappa \rangle_\alpha - m^\alpha \langle c_{*,U} - c_{*,ZOLPA} \rangle_\alpha \\ &= -m^\alpha b_0 - m^\alpha a_{0,U} \zeta_0^\alpha - m^\alpha \epsilon \zeta_1^\alpha + \Gamma_\alpha \langle \kappa \rangle_\alpha + \mathcal{O}(\epsilon^2) \end{aligned} \quad (\text{F.7})$$

where, $a_{0,U}$ is the plane wave component of the unapproximated problem; $c_{*,U}$ is the solution of the unapproximated problem excluding the zeroth order term and $c_{*,ZOLPA}$ is

its ZOLPA counterpart. Similar to Eq. (F.7), for the averaging over the β phase, we have

$$\begin{aligned}\Delta T &= -m^\beta b_0 - m^\beta a_{0,U} \zeta_0^\beta - m^\beta \epsilon \zeta_1^\beta + \Gamma_\beta \langle \kappa \rangle_\beta - m^\beta \langle c_{*,U} - c_{*,ZOLPA} \rangle_\beta \\ &= -m^\beta b_0 - m^\beta a_{0,U} \zeta_0^\beta - m^\beta \epsilon \zeta_1^\beta + \Gamma_\beta \langle \kappa \rangle_\beta + \mathcal{O}(\epsilon^2).\end{aligned}\quad (\text{F.8})$$

Eliminating $a_{0,U}$ from Eqs. (F.7) and (F.8) gives

$$v_{\text{actual}} = v_{\text{approx}} - m^\alpha m^\beta \frac{(\zeta_0^\alpha \langle c_{*,U} - c_{*,ZOLPA} \rangle_\beta - \zeta_0^\beta \langle c_{*,U} - c_{*,ZOLPA} \rangle_\alpha)}{\frac{\lambda}{D} \left(\frac{-m^\alpha m^\beta}{m^\beta - m^\alpha} \right) (\text{G.F})_{\text{ZOLPA}}}\quad (\text{F.9})$$

$$\implies \left| 1 - \frac{v_{\text{approx}}}{v_{\text{actual}}} \right| = \left| \frac{(\zeta_0^\alpha \langle c_{*,U} - c_{*,ZOLPA} \rangle_\beta - \zeta_0^\beta \langle c_{*,U} - c_{*,ZOLPA} \rangle_\alpha)}{\frac{\lambda v_{\text{actual}}}{D} \left(\frac{1}{m^\beta - m^\alpha} \right) (\text{G.F})_{\text{ZOLPA}}} \right| = \mathcal{O}(\epsilon)\quad (\text{F.10})$$

where, v_{approx} is the expression given by Eq. (6.17) and $(\text{G.F})_{\text{ZOLPA}}$ is the square bracket term in the denominator of Eq.(6.19). Thus, the relative error in velocity is of the order of Péclet number and independent of the shape of the solid-liquid interface.

F.2 Some relevant inequalities

F.2.1 Poincare inequality for functions in $H_*^1(\Omega_\infty)$

We now establish a Poincare kind inequality for functions in $H_*^1(\Omega_\infty)$. For this, it is convenient to split the domain into two regions; one, the infinite ‘‘rectangular’’ box, defined as $\Omega_{\text{box}} = \Omega_\infty \setminus \Omega_{2z_{\text{max}}}$ where $z_{\text{max}} = \max \{p(x) : x \in [-\frac{1}{2}, \frac{1}{2}]\}$ and the other, the remaining region.

Now consider the following fact: $\forall u(x, z) \in C_*^\infty(\Omega_\infty) \cap H^1(\Omega_\infty)$, in the region Ω_{box} , for any given z , we have condition (a), particularly, $\int_{-1/2}^{1/2} u dx = 0$. Given the continuity of u , this implies that for every z there exists an x^* such that $u(x^*, z) = 0$. From this it follows that

$$\begin{aligned}u(x, z) - u(x^*, z) &= \int_{x^*}^x \frac{\partial u}{\partial x}(\xi, z) d\xi \\ \implies u(x, z) &= \int_{x^*}^x \frac{\partial u}{\partial x}(\xi, z) d\xi \\ \implies u^2(x, z) &\leq \int_{-1/2}^{1/2} \left(\frac{\partial u}{\partial x}(\xi, z) \right)^2 d\xi\end{aligned}$$

(Cauchy-Schwarz inequality)

$$\begin{aligned}
&\implies \int_{-1/2}^{1/2} u^2(x, z) dx \leq \int_{-1/2}^{1/2} \left(\frac{\partial u}{\partial x}(\xi, z) \right)^2 d\xi \\
&\implies \int_{2z_{\max}}^{z^*} \int_{-1/2}^{1/2} u^2(x, z) dx dy \leq \int_{2z_{\max}}^{z^*} \int_{-1/2}^{1/2} \left(\frac{\partial u}{\partial x}(\xi, z) \right)^2 d\xi dz \\
&\implies \int_{\Omega_{\text{box}}} u^2 dV \leq \int_{\Omega_{\text{box}}} \left(\frac{\partial u}{\partial x} \right)^2 dV \tag{F.11}
\end{aligned}$$

Now consider the following fact in Ω_∞ . $\forall u \in C_*^\infty(\Omega_\infty) \cap H^1(\Omega_\infty)$,

$$\begin{aligned}
u(x_1, z_1) &= u(x_1, z_2) + \int_{z_2}^{z_1} \frac{\partial u}{\partial z}(x_1, \zeta) d\zeta \\
\implies u^2(x_1, z_1) &\leq 2u^2(x_1, z_2) + 2z_2 \int_{p(x_1)}^{z_2} \left(\frac{\partial u}{\partial z}(x_1, \zeta) \right)^2 d\zeta \\
\implies \int_{p(x_1)}^{2z_{\max}} u^2(x_1, z_1) dz_1 &\leq 4y_{\max} u^2(x_1, z_2) + 4z_{\max} z_2 \int_{p(x_1)}^{z_2} \left(\frac{\partial u}{\partial z}(x_1, \zeta) \right)^2 d\zeta
\end{aligned}$$

Integrating w.r.t z_2 from $2z_{\max}$ to $10z_{\max}$

$$\begin{aligned}
\int_{p(x_1)}^{2z_{\max}} u^2(x_1, z_1) dz_1 &\leq \frac{1}{2} \int_{2z_{\max}}^{10z_{\max}} u^2(x_1, z_2) dz_2 + 24z_{\max}^2 \int_{p(x_1)}^{10z_{\max}} \left(\frac{\partial u}{\partial z}(x_1, \zeta) \right)^2 d\zeta \\
\implies \int_{\Omega_{2z_{\max}}} u^2 dV &\leq \frac{1}{2} \int_{\Omega_{10z_{\max}} \setminus \Omega_{2z_{\max}}} u^2 dV + 24z_{\max}^2 \int_{\Omega_\infty} \left(\frac{\partial u}{\partial z} \right)^2 dV \tag{F.12}
\end{aligned}$$

Thus, from Eqs. (F.11) and (F.12), $\forall u \in C_*^\infty(\Omega_\infty) \cap H^1(\Omega_\infty)$ and hence $\forall u \in H_*^1(\Omega_\infty)$, we have the following Poincare inequality:

$$\frac{1}{2} \int_{\Omega_\infty} u^2 dV \leq \max\{1, 24y_{\max}^2\} \int_{\Omega_\infty} (\nabla u)^2 dV. \tag{F.13}$$

F.2.2 Trace theorem for $H_*^1(\Omega_\infty)$

Claim: The trace operator $\gamma|_{\partial\Omega_\infty}$ — defined for all $C^\infty(\overline{\Omega_\infty})$ as $\gamma|_{\partial\Omega_\infty} u(x) = u(x)$, $x \in \partial\Omega_\infty$ — is a bounded linear operator from $H^1(\Omega_\infty)$ to $H^{1/2}(\partial\Omega_\infty)$.

Note that the domains we are considering are Lipschitz domains, and one can find a

countable number of cylinder co-ordinate pairs $(Z(P_k, r_k), \varphi_k)$, $k \in \mathbb{Z} \cup A$ (see Definition 1 of [98]) to cover the boundary $\partial\Omega_\infty$, where \mathbb{Z} is the set of integers and A is a finite set. In this paper, we have chosen the ‘‘cylinders’’ on the vertical boundaries and the corresponding co-ordinate systems (x, s) as shown in Fig. F.1; the cylinders with negative index are on the left boundary and the ones with positive index are on the right boundary. Furthermore, the indices from the set A and the index 0 are used

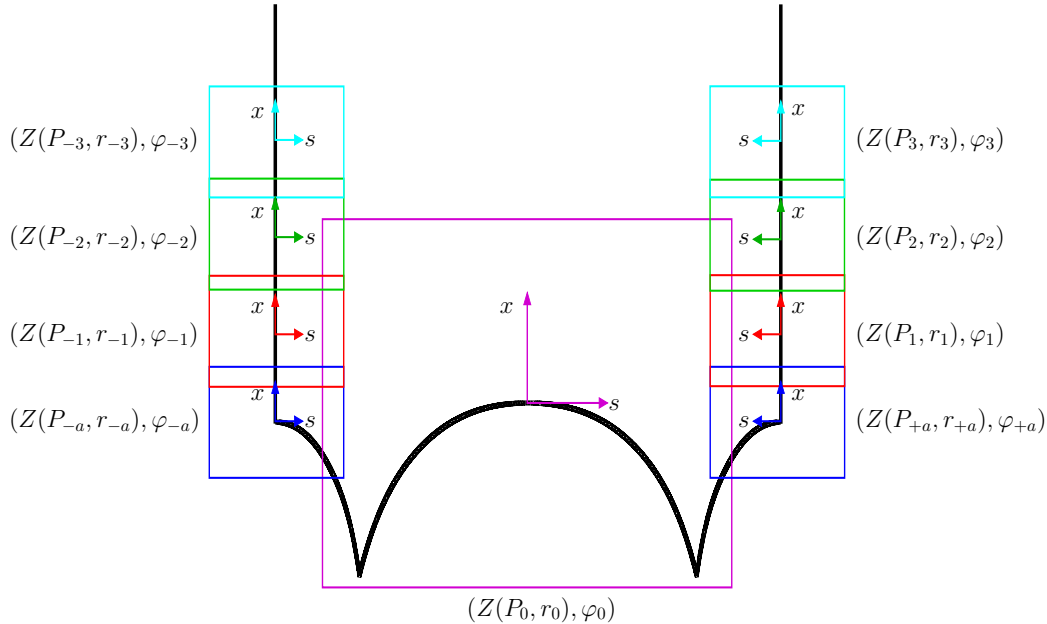


Figure F.1: A covering of the boundary with cylindrical co-ordinate pairs.

for the cylinders on the remaining boundary. The associated functions ‘ φ_k ’s are defined in the obvious way as $\varphi_k(x) = 0 \forall k \in \mathbb{Z} \setminus \{0\}$. The exact way in which the other cylinder co-ordinate pairs are chosen is irrelevant for the rest of the discussion as long as the general requirements are fulfilled; nevertheless, we give one such example for the profile considered in the Fig. F.1. We choose the set A to be $\{-a, +a\}$; the orientation of the corresponding cylinders and the associated co-ordinate systems are as displayed in the diagram. The corresponding functions are: $\varphi_0(x) = p(0) - p(x)$, $\varphi_{\pm a}(x) = 0$ for $x \geq 0$, $= p^{-1}(p(-1/2) + x) + 1/2$ for $x < 0$ (note that for the profile considered, its restriction to $(-1/2, -\eta_\beta/2)$ is invertible).

The claim follows from an argument similar to the proof of Theorem 1 of [98] (pg.nos: 599,600) as follows. Let $\{\phi_k\}_{k \in \mathbb{Z} \cup A}$ be the unit decomposition of $\partial\Omega_\infty$. i.e., let them satisfy the following two conditions.

- (i) $\text{supp}(\phi_k) \subset Z(P_k, r_k)$, $k \in \mathbb{Z} \cup A$.
- (ii) $\sum_{k \in \mathbb{Z} \cup A} \phi_k(x) = 1$, $x \in \partial\Omega$.

Then, for any $u \in H^1(\Omega_\infty)$, we have

$$\phi_k u \in H^1(\Omega_\infty \cap Z(P_k, r_k)) \quad \forall \quad k \in \mathbb{Z} \cup A.$$

Now consider

$$\begin{aligned} \|\gamma|_{\partial\Omega_\infty} u\|_{H^{1/2}(\partial\Omega_\infty)} &= \lim_{m \rightarrow \infty} \left\| \sum_{k=-m}^m \phi_k u + \sum_{k \in A} \phi_k u \right\|_{H^{1/2}(\partial\Omega_\infty)} \\ &\leq \lim_{m \rightarrow \infty} \sum_{k=-m}^m \|\phi_k u\|_{H^{1/2}(\partial(\Omega_\infty \cap Z(P_k, r_k)))} \\ &\quad + \sum_{k \in A} \|\phi_k u\|_{H^{1/2}(\partial(\Omega_\infty \cap Z(P_k, r_k)))} \\ &\leq \lim_{m \rightarrow \infty} \sum_{k=-m}^m C \|\phi_k u\|_{H^1(\Omega_\infty \cap Z(P_k, r_k))} \\ &\quad + \sum_{k \in A} C_k \|\phi_k u\|_{H^1(\Omega_\infty \cap Z(P_k, r_k))} \\ &\leq C_* \|u\|_{H^1(\Omega_\infty)}. \end{aligned}$$

Note that the same constant C appears for all the cylinders on the vertical boundaries. This follows from the fact that these constants are dependent only on the shape and size of the cylinder, and the cylinders on the vertical boundaries are all of same dimensions.

List of Figures

3.1	The evolution of an initially set profile in the lower timescales $\tau = t/\epsilon^2$ and $\tau = t/\epsilon$. The (red) curve in a) corresponds to the initial filling; the green profile in b) is its state by the “end” of timescale $\tau = t/\epsilon^2$; and the blue one of c) corresponds to that by the end of $\tau = t/\epsilon$ scale. The red and green curves are replotted in later timescales for easy reference. . . .	33
3.2	Schematic showing the shrinkage of a) an extended region corresponding to $\phi = 1/2$ to b) a spike, as per the prediction of the asymptotic analysis in the $\tau = t/\epsilon$ timescale.	35
3.3	Evolution of an initially set phase-field profile in timescales $\tau = t/\epsilon^2$, t/ϵ and t as per the predictions of the current section. The initial filling is shown in a). Profiles towards the end of times scales $\tau = t/\epsilon^2$ and t/ϵ are shown in b) and c), respectively. A late stage in $\tau = t$ scale where the $\phi = 0$ circle almost shrank down is shown in d).	36
3.4	Gibbs triangle showing the regions R1, R2 and R3 which are characterized by their relation to the stable phases (vertices), and the lines T1, T2 and T3 which are the only choices that are available for the saddle points (the metastable phases) to lie on. A trail ABC passing through the critical point at the centroid is also shown.	39
3.5	Plot of the restriction of the three phase, symmetric classical well $W^C = \phi_1^2\phi_2^2 + \phi_2^2\phi_3^2 + \phi_3^2\phi_1^2$ to the Gibbs triangle; a) as a surface graph over the triangle and b) as a heat map.	39
3.6	Plot of the restriction of the Folch-Plapp well $W^{FP} = \phi_1^2(1 - \phi_1)^2 + \phi_2^2(1 - \phi_2)^2 + \phi_3^2(1 - \phi_3)^2$ to the Gibbs triangle; a) as a surface graph over the triangle and b) as a heat map.	40

- 3.7 Various stages and possibilities for the evolution of an initial profile filled as per the trail ABC of Fig. 3.4. Profile towards the end of the timescale $\tau = t/\epsilon^2$ is schematically shown in a) while b) and c) are two possibilities for its further evolution. In b) the third component survived whereas it disintegrated completely in c) as highlighted by the insets. 41
- 3.8 Schematic of a perturbation in which the non-zero components ϕ_1 and ϕ_2 (i.e., the components characterizing the stable phases $(1, 0, 0)$ and $(0, 1, 0)$, respectively) split midway giving rise to $(1/2, 1/2, 0)$ phase. This transition is unstable in the current, $\tau = t/\epsilon$, timescale and reverts back immediately. 43
- 3.9 Schematic of a perturbation in which the non-zero components ϕ_1 and ϕ_2 (characterizing the stable phases $(1, 0, 0)$ and $(0, 0, 1)$, respectively) move apart giving rise to $(0, 0, 0)$ phase. Depending on the choice of the model, this perturbation may sustain but never grows in the current timescale of $\tau = t/\epsilon$ 44
- 3.10 Schematic showing the shrinkage of a) an extended region of the $(1/2, 1/2, 0)$ phase resulting in the formation of b) spikes in the profiles of the components ϕ_1 and ϕ_2 as per the prediction of the asymptotic analysis pertaining to the $\tau = t/\epsilon$ timescale. 45
- 3.11 An initial filling corresponding to the trail ABC of Fig. 3.4, but with an extended region corresponding to point B, i.e., phase $(1/3, 1/3, 1/3)$ 46
- 3.12 Figure showing $M = 5$ interfaces meeting to form a junction. $x - y$ is the laboratory coordinate frame corresponding to the outer co-ordinates and $\zeta - \xi$ is the local frame. The interfaces are numbered with reference to the ζ -axis by starting there and moving in the counter clockwise direction. The local coordinate system rotated so as to align the ζ -axis with the tangent of an interface and suffixed with the number assigned to the latter is also shown exemplarily for the second interface. 51
- 3.13 Some example ray-diagram constructions; a) corresponds to the interfacial configuration of Fig. 3.12 while b) gives an instance of a ray diagram of a special kind (please refer to the main text). 51
- 3.14 Figure showing the polygonal constructions for the ray diagrams of Fig. 3.13; a) corresponds to Fig. 3.13a) while b) to Fig. 3.13b). 52
- 3.15 Setup considered for demonstrating the accuracy of the asymptotic laws Eqs. (3.44) and (3.45) in predicting the instantaneous motion of a junction. 64

4.1	A simulation setup used for the study of three phase growth. The growth direction is as depicted by the arrows and accordingly is the implementation of the shifting window.	66
4.2	Steady state growth fronts realized in the simulations performed with the parameter set of Table 4.1 within the setup of Fig. 4.1 for various values of τ_{23} . Also depicted is the sharp interface theory predicted profile in black. 66	66
4.3	Initial filling and material parameter set used in the study of 1D two phase evolution problem through the multi-phase-field model with $N=3$	77
4.4	Steady state vector phase-field profile simulated using the classical multi-well form $W^C = 36[\phi_1^2\phi_2^2 + \phi_2^2\phi_3^2 + \phi_3^2\phi_1^2]$ from an initial set up and parameter set of Fig. 4.3. The presence of third phase is highlighted by zooming in appropriately.	78
4.5	Steady state vector phase-field profile simulated using the Folch-Plapp multi-well form $W^{FP} = 18[\phi_1^2(1 - \phi_1)^2 + \phi_2^2(1 - \phi_2)^2 + \phi_3^2(1 - \phi_3)^2]$ from an initial set up and parameter set of Fig. 4.3. The presence of third phase is highlighted by zooming in on the appropriate part.	79
4.6	Sustenance of third phase at lower interface widths in simulations employing classical multi-well $W^C = 36[\phi_1^2\phi_2^2 + \phi_2^2\phi_3^2 + \phi_3^2\phi_1^2]$	79
4.7	Decay of third phase as interface width is reduced in simulations employing Folch-Plapp multi-well $W^{FP} = 18[\phi_1^2(1 - \phi_1)^2 + \phi_2^2(1 - \phi_2)^2 + \phi_3^2(1 - \phi_3)^2]$. 80	80
4.8	Convergence of the steady state speed as the interface width is reduced in simulations employing the classical well $W^C = 36[\phi_1^2\phi_2^2 + \phi_2^2\phi_3^2 + \phi_3^2\phi_1^2]$. The value approached is different from the desired result of 0.1 due to the presence of the third phases at zeroth order.	81
4.9	Convergence of the steady state speed as the interface width is reduced in simulations employing the Folch-Plapp well $W^{FP} = 18[\phi_1^2(1 - \phi_1)^2 + \phi_2^2(1 - \phi_2)^2 + \phi_3^2(1 - \phi_3)^2]$. The value approached is the same as the desired result of 0.1 due to the absence of third phases at the zeroth order.	81
4.10	Effect of ghost phase mobility on the recovered planar growth kinetics for the Foch-Plapp well with Lagrange implementation and for the Toth well with and without Lagrange implementation. The highest resolution that is studied in Figs. 4.6–4.9 is used for this investigation. The targeted value is 0.1. Lines are drawn connecting the points for easy reference.	82

4.11	Plot of the restriction of the three phase Toth's well (i.e, W^T of Eq.(4.9) for $N = 3$) to the Gibbs triangle; a) as a surface graph over the triangle and b) as a heat map.	85
4.12	Simulated results at various grid discretizations obtained using Toth's well in the absence of Lagrange multiplier implementation. The zoomed in figure on the top shows the sum of all the components $\phi_1 + \phi_2 + \phi_3$ and the one on the bottom shows the absence of springing up of the ghost phase.	86
4.13	Simulated results at various grid finenesses obtained using Toth's well and a Lagrange multiplier implementation. The zoomed in figure on the top shows the sum of all the components $\phi_1 + \phi_2 + \phi_3$ and the one on the bottom shows the rise of the ghost phase and its progressive suppression at higher resolutions similar to that found in the case of Folch-Plapp well in Fig. 4.7.	87
4.14	The $\tau_{23} = 100$ case of Fig. 4.2 re-studied at various degrees of grid fineness using Toth's multi-well $W^T = 36 \left(\frac{\phi_1^4 + \phi_2^4 + \phi_3^4}{4} + \frac{\phi_1^2 \phi_2^2 + \phi_2^2 \phi_3^2 + \phi_3^2 \phi_1^2}{2} - \frac{\phi_1^3 + \phi_2^3 + \phi_3^3}{3} - \frac{1}{12} \right)$ and by turning off the Lagrange multiplier implementation. The prescription of $\epsilon = 5.0 \times \Delta x$ is utilized for the simulations with the resolution of Table 4.1 corresponding to fineness factor = 2.	88
4.15	Simulation results at various degrees of fineness of the grid obtained by varying ϵ as $\epsilon = 4.5 \times \Delta x$. The values of Table 4.10 are chosen for the base resolution.	90
4.16	Simulation results at various degrees of fineness of the grid obtained by varying ϵ as $\epsilon = 4.5 \times (\Delta x)^{0.6}$. The values of Table 4.10 correspond to the base resolution.	90
4.17	Schematic of the steady state profile of the three grain growth within the setup of Fig. 4.1, with triple junction region and regions well removed from it highlighted.	91
4.18	Simulations of Fig. 4.14 re-performed with inverse mobility interpolation chosen in a harmonic fashion as in Eq. (4.10).	92
4.19	Simulations of Fig. 4.18 re-performed by instead varying ϵ as $\epsilon = 5.0 \times (\Delta x)^{0.6}$	93
4.20	A simulation setup used for the study of three phase growth. The growth direction is as depicted by the arrow and accordingly is the implementation of the shifting window.	98

4.21	A sequence of simulation images illustrating the general growth tendency of the three phase system indicated in Fig. 4.20	99
4.22	Simulated $\phi_2 = 0.5$ contours indicating the slow convergence of the arithmetic and Steinbach formulations compared to the harmonic τ -interpolation for the setup of Fig. 4.20 and the base resolution parameter set listed in Table 4.18.	99
5.1	Plot of the restriction of the obstacle potential form $W_{\text{obs}} = \phi_1\phi_2 + \phi_2\phi_3 + \phi_3\phi_1$ to the Gibbs triangle; a) as a surface graph over the triangle and b) as a heat map.	104
5.2	Steady-state growth fronts obtained in the three grain evolution simulations in the setup of Fig. 4.1 for the parameter set of Table. 5.1.	108
5.3	Steady-state growth fronts obtained in the three grain evolution simulations within the setup of Fig. 4.1 for the parameter set of Table. 5.3. . .	109
5.4	Steady-state growth fronts obtained in the three grain evolution simulations within the setup of Fig. 4.1 for the parameter set of Table. 5.5. . .	110
5.5	The setup used for the simulation of cooperative lamellar growth of NiZr and NiZr ₂ solids.	114
5.6	NiZr-NiZr ₂ lamellar growth kinetics predicted by the JH relation for various choices of the slopes prescription, and their comparison with the simulation results at various interface widths.	116
5.7	Setup applied for the simulation of hexagonally arranged rods.	118
5.8	Comparison of NiZr-NiZr ₂ rod growth kinetics predicted by the JH relation for various choices of the slopes formula with those of the simulations pertaining to various interface widths.	120
5.9	NiZr-NiZr ₂ lamellar JH results (i.e., from Eq. (5.5)) for various slopes m_α and m_β . The dark curve corresponds to the classical analysis, i.e., with the precise slopes at the eutectic point chosen from the phase diagram and hence is the same as the green curve of Fig. 5.6. The others correspond to the slopes from various rows of Table 5.11.	124
5.10	Comparison of Al-AlCu ₂ lamellar growth kinetics predicted by the JH relation Eq. (5.5) when the slopes and Gibbs-Thomson coefficients are approximated as in Ref. [73] (i.e., Eqs. (5.12) and (5.13)) and when chosen as the ones picked in simulations(i.e., Eqs. (5.10) and (5.11)) with those of the computational results.	126

6.1	Schematic of one representative unit of the lamellar eutectic undergoing a directional growth under isothermal conditions. The zoomed in part shows a control volume over a small region of the solidification front.	131
6.2	a): Typical shape of the function $W(x)$ of Eq. (6.9) (labelled ‘Actual’ in the figure), and its reconstruction from the series on the l.h.s truncated up to N terms for various N . The profile shape $p(x)$ used for the calculations is borrowed from the simulations of section 5.4.1.2 and is presented in b).	137
6.3	Specific velocity number—defined as the ratio between the steady-state velocity predicted by the curvature informed theory to that by the classical JH analysis—calculated for the self-consistently obtained profiles and plotted as function of lamellar widths. Both the cases of ZOLPA and the complete solution are presented.	145
6.4	Comparison of growth kinetics predicted by the classical and the extended JH analyses.	145
6.5	Higher order contribution to the interfacial solute distribution $c_*(x, p(x))$ divided by the Péclet number for the converged interfaces of Table 6.2 compared with their flat interface counterparts.	146
7.1	Hexagonal lattice showing three different unit cells and the circular representative unit considered in the classical JH theory.	152
7.2	Schematic of a) a unit cell of a generic lattice with the co-ordinate axis (x, y, z) and b) a primitive unit cell of equal sides with the (x, y, z) and the (s, t, z) co-ordinate axes. The z -axis is normal to the plane of the paper.	153
7.3	a): One of the solidification surfaces obtained in the simulations of section 5.4.2. The red mesh corresponds to the rod phase and the blue one to the matrix. Surface within a distance of $\lambda/2$ from the rod center is only depicted. b), c) and d): The function $w(s, t)$ and its reconstruction from the first N number of terms of the approximated series of Eq. (7.17) along three sample directions for various N	158
8.1	Figs. 5.6, E.7, E.8 and 5.10 replotted with the curvature-informed, self-consistent theory predictions of chapter 6 included in them. The subfigures a), b), c) and d) correspond to them in the same order.	164
8.2	Typical Péclet number versus lamellar spacing trend to be expected at steady state in directional (lamellar) eutectic growth as predicted by the Jackson-Hunt analysis.	166

8.3	The steady state growth fronts recovered in the lamellar growth simulations of section 5.4.1.2 along with the respective converged profiles obtained through the iterative scheme of the extended JH analysis of section 6.4.1. The highest resolution front of the case $\lambda = 0.240\mu m$, i.e., the yellow profile is precisely the one used for the convergence verification of Fig. 6.2.	169
8.4	The solidification fronts of the rod growth simulations of section 5.4.2 and their fitting. The blue surfaces correspond to rod forming NiZr phase and the red ones to that of matrix forming NiZr ₂ phase. The grey surfaces are the fits (whose forms are as given in the main text).	171
8.5	Fig. 5.8 replotted along with the predictions of the curvature-informed JH analysis of chapter 7.	172
B.1	A generic symmetric double well.	193
B.2	Domains considered for some example functions exhibiting a junction behavior. Domain of a) corresponds to the simplest function Eq. (B.12), while that in b) is considered for the example in Eq. (B.13).	200
B.3	Domain considered for the example function of Eq. (B.14).	201
B.4	A subregion of the domain of intergration of the integral on the l.h.s of Eq. (B.54).	215
E.1	Steady-state growth fronts obtained in the three grain evolution simulations within the setup of Fig. 4.1 for the parameter set of Table. E.1.	232
E.2	Steady-state growth fronts obtained in the three grain evolution simulations within the setup of Fig. 4.1 for the parameter set of Table. E.3.	233
E.3	Steady-state growth fronts obtained in the three grain evolution simulations within the setup of Fig. 4.1 for the parameter set of Table. E.5.	234
E.4	Steady-state growth fronts obtained in the three grain evolution simulations within the setup of Fig. 4.1 for the parameter set of Table. E.7.	235
E.5	Steady-state growth fronts obtained in the three grain evolution simulations within the setup of Fig. 4.1 for the parameter set of Table. E.9.	236
E.6	Setup used for the NiZr planar solidification simulations.	237
E.7	Studies of Fig. 5.6 reperformed but by increasing the solid-solid interfacial energy to $\sigma_{\alpha\beta} = 0.6\text{Jm}^{-2}$	239

-
- E.8 Studies of Fig. 5.10 reperformed but by decreasing the solid-solid interfacial energy such that the angles made by the surfaces with the horizontal are reduced by half. Simulation results at higher resolutions are also presented with the ϵ v.s. $(\Delta x)^p$ relationship varied as indicated. The base resolution corresponds to $\Delta x = 1$, hence, the interface width is reduced by half in both the higher resolution cases. 239
- F.1 A covering of the boundary with cylindrical co-ordinate pairs. 246

List of Tables

2.1	Examples of some of the standard choices of interpolating and multi-well forms which are repeatedly employed in the thesis.	27
4.1	Table showing a parameter set used in the study of three phase growth within the setup of Fig. 4.1. N_x and N_y are the number of grid points in the x and y directions, respectively.	66
4.2	Steady state growth speeds realized in the simulations performed with the parameter set of Table 4.1 within the setup of Fig. 4.1 for various values of τ_{23} . Also listed is the sharp interface theory predicted growth speed. .	67
4.3	Effect of reducing the interface width by choosing ϵ proportional to Δx on the simulated growth speeds for three different proportionality constants. The expected speed is 0.1 units.	69
4.4	Speeds recovered in simulations as interface width is reduced whilst choosing $\epsilon = 6.0 \times \Delta x$ for three different values of the driving force specifier Δf viz. 0.1, 0.01 and 0.001. The expected speeds are 0.1, 0.01 and 0.001, respectively.	73
4.5	Simulated steady state speeds as interface width is reduced by choosing $\epsilon = 4.0 \times \Delta x$ for various values of interfacial energy specifier γ . The expected speed is 0.1.	74
4.6	Study of Table 4.3 repeated instead by choosing ϵ proportional to $\sqrt{\Delta x}$ for the same proportionality constants.	74
4.7	Study of Table 4.4 reperformed instead with $\epsilon = 6.0 \times \sqrt{\Delta x}$	75
4.8	Study of Table 4.5 reperformed instead with $\epsilon = 4.0 \times \sqrt{\Delta x}$	75
4.9	Steady state angles and speeds recovered for the growth fronts of Fig. 4.14.	89
4.10	A parameter set designed to prove that the jump behavior of Fig. 4.14 is due to the $\epsilon \propto \Delta x$ selection.	89

4.11	Steady state speeds recovered for the growth fronts of a) Fig. 4.15 and b) Fig. 4.16.	90
4.12	Steady state angles and speeds recovered for the growth fronts of Fig. 4.18.	92
4.13	Steady state angles and speeds recovered for the growth fronts of Fig. 4.19.	93
4.14	Simulations performed with the parameter set used for Fig. 4.19 but with three different mobility formulations and a modification of the inverse mobility values as $\tau_{12} = \tau_{13} = 100$ and $\tau_{23} = 1$. That is, the growth front is made less mobile and the mobility of the interface between the two grains on the bottom is enhanced.	95
4.15	Steady state angles and speeds recovered for the growth fronts of Table 4.14.	95
4.16	Simulations of Table 4.14 reperformed but with 10 times larger driving force, i.e, with $f_1 = 2.0$, $f_2 = 0.0$ and $f_3 = 0.0$	96
4.17	Steady state angles and speeds recovered for the growth fronts of Table 4.16.	96
4.18	Table showing a parameter set used for the study of three phase evolution within the setup of Fig. 4.20.	98
5.1	A parameter set employed for simulating the three grain evolution in the setup of Fig. 4.1 using obstacle potential.	108
5.2	Steady state speeds recovered for the growth fronts of Fig. 5.2.	108
5.3	A parameter set employed for simulating the three grain evolution within the setup of Fig. 4.1 using obstacle potential.. . . .	109
5.4	Steady state speeds recovered for the growth fronts of Fig. 5.3.	109
5.5	A parameter set employed for simulating the three grain evolution within the setup of Fig. 4.1 using obstacle potential.. . . .	110
5.6	Steady state speeds recovered for the growth fronts of Fig. 5.4.	110
5.7	Thermo-physical parameters of the NiZr-NiZr ₂ system corresponding to near eutectic temperatures. Symbols α , β and l are used to mark the NiZr, NiZr ₂ and melt phases, respectively. f is the fineness factor.	112
5.8	Triple junction angles subtended by the NiZr-liquid and NiZr ₂ -liquid interfaces that are recovered in the simulations as interface width is reduced whilst choosing $\epsilon \propto \Delta x$. The angles are measured with respect to the horizontal (i.e., axis perpendicular to the growth direction). Symbols α , β and l mark the NiZr, NiZr ₂ and melt phases, respectively.	115

5.9	Triple “junction” angles subtended by the NiZr-liquid and NiZr ₂ -liquid surfaces recovered in the rod growth simulations as interface width is reduced whilst choosing $\epsilon \propto \Delta x$. The angles are measured with respect to the plane perpendicular to the growth direction. Symbols α , β and l mark the NiZr, NiZr ₂ and melt phases, respectively.	119
5.10	CALPHAD data of the constituting solids of NiZr-NiZr ₂ eutectic system corresponding to an undercooling of 5.9K, as extracted using the software package PANDAT.	123
5.11	The NiZr and NiZr ₂ CALPHAD data extracted by the PANDAT software when the number of sample points are changed by fixing the Zr mole fraction range as ‘0.48 to 0.68’. Also listed are the liquidii slopes estimated from Eq. (5.10) by utilizing the common tangents made with the melt data.	125
6.1	Thermo-physical parameters of the NiZr-NiZr ₂ system corresponding to near eutectic temperatures. Symbols α , β and l mark the NiZr, NiZr ₂ and melt phases, respectively.	142
6.2	Reconstructed profiles at various iterations tabulated along with the corresponding Péclet numbers and specific velocities for different spacings.	143
6.3	Reconstructed profile shapes at characteristic lamellar spacings (λ_{JH}) for various off-eutectic cases. Also listed are the geometry and kinetics related data of the converged profiles and the respective classical geometric factors.	147
8.1	Table showing the effect of curvature incorporation on the Jackson-Hunt analysis predicted growth kinetics for the investigated rod spacings and simulated surfaces of section 5.4.2.2.	172
E.1	A parameter set employed for simulating the three grain evolution in the setup of Fig. 4.1 using obstacle potential.	232
E.2	Steady state speeds recovered for the growth fronts of Fig. E.1.	232
E.3	A parameter set employed for simulating the three grain evolution within the setup of Fig. 4.1 using obstacle potential.	233
E.4	Steady state speeds recovered for the growth fronts of Fig. E.2.	233
E.5	A parameter set employed for simulating the three grain evolution within the setup of Fig. 4.1 using obstacle potential.	234
E.6	Steady state speeds recovered for the growth fronts of Fig. E.3.	234

E.7	A parameter set employed for simulating the three grain evolution within the setup of Fig. 4.1 using obstacle potential.	235
E.8	Steady state speeds recovered for the growth fronts of Fig. E.4.	235
E.9	A parameter set employed for simulating the three grain evolution within the setup of Fig. 4.1 using obstacle potential..	236
E.10	Steady state speeds recovered for the growth fronts of Fig. E.5.	236
E.11	Steady state planar solidification speeds of NiZr solid simulated within the setup of Fig. E.6 for various Dirichlet data c_l^e , $\epsilon \propto (\Delta x)^p$ choices and resolutions. The physical units of the speeds are m s^{-1} . At the base resolution, the N_x chosen is 100 grid cells.	238
E.12	The magnitudes of the simulated speeds of Fig. 5.6.	238

Bibliography

- [1] J. W. Cahn and J. E. Hilliard. Free energy of a nonuniform system. I. interfacial free energy. *The Journal of chemical physics*, 28(2):258–267, 1958.
- [2] J. W. Cahn. Free energy of a nonuniform system. II. thermodynamic basis. *The Journal of chemical physics*, 30(5):1121–1124, 1959.
- [3] G. J. Fix. Phase field methods for free boundary problems. *Carnegie–Mellon University, Pittsburgh, Pennsylvania*, 1982.
- [4] J. B. Collins and H. Levine. Diffuse interface model of diffusion-limited crystal growth. *Physical Review B*, 31(9):6119, 1985.
- [5] J. Langer. Models of pattern formation in first-order phase transitions. In *Directions in Condensed Matter Physics: Memorial Volume in Honor of Shang-Keng Ma*, pages 165–186. World Scientific, 1986.
- [6] G. Caginalp. An analysis of a phase field model of a free boundary. *Archive for Rational Mechanics and Analysis*, 92(3):205–245, 1986.
- [7] G. Caginalp. Stefan and hele-shaw type models as asymptotic limits of the phase-field equations. *Physical Review A*, 39(11):5887, 1989.
- [8] R. Kobayashi. Modeling and numerical simulations of dendritic crystal growth. *Physica D: Nonlinear Phenomena*, 63(3-4):410–423, 1993.
- [9] A. A. Wheeler, W. J. Boettinger, and G. B. McFadden. Phase-field model for isothermal phase transitions in binary alloys. *Physical Review A*, 45(10):7424, 1992.
- [10] A. A. Wheeler, B. T. Murray, and R. J. Schaefer. Computation of dendrites using a phase field model. *Physica D: Nonlinear Phenomena*, 66(1-2):243–262, 1993.
- [11] S.-L. Wang and R. F. Sekerka. Algorithms for phase field computation of the dendritic operating state at large supercoolings. *Journal of Computational Physics*, 127(1):110–117, 1996.

-
- [12] S.-L. Wang and R. F. Sekerka. Computation of the dendritic operating state at large supercoolings by the phase field model. *Physical Review E*, 53(4):3760, 1996.
- [13] A. Karma and W.-J. Rappel. Quantitative phase-field modeling of dendritic growth in two and three dimensions. *Physical Review E*, 57(4):4323, 1998.
- [14] R. F. Almgren. Second-order phase field asymptotics for unequal conductivities. *SIAM Journal on Applied Mathematics*, 59(6):2086–2107, 1999.
- [15] A. Karma. Phase-field formulation for quantitative modeling of alloy solidification. *Physical Review Letters*, 87(11):115701, 2001.
- [16] B. Echebarria, R. Folch, A. Karma, and M. Plapp. Quantitative phase-field model of alloy solidification. *Physical Review E*, 70(6):061604, 2004.
- [17] S. G. Kim, W. T. Kim, and T. Suzuki. Phase-field model for binary alloys. *Physical Review E*, 60(6):7186, 1999.
- [18] M. Plapp. Unified derivation of phase-field models for alloy solidification from a grand-potential functional. *Physical Review E*, 84(3):031601, 2011.
- [19] I. Steinbach, F. Pezzolla, B. Nestler, M. Seeßelberg, R. Prieler, G. J. Schmitz, and J. L. Rezende. A phase field concept for multiphase systems. *Physica D: Nonlinear Phenomena*, 94(3):135–147, 1996.
- [20] H. Garcke, B. Nestler, and B. Stoth. A multiphase field concept: numerical simulations of moving phase boundaries and multiple junctions. *SIAM Journal on Applied Mathematics*, 60(1):295–315, 1999.
- [21] B. Nestler, H. Garcke, and B. Stinner. Multicomponent alloy solidification: phase-field modeling and simulations. *Physical Review E*, 71(4):041609, 2005.
- [22] R. Folch and M. Plapp. Quantitative phase-field modeling of two-phase growth. *Physical Review E*, 72(1):011602, 2005.
- [23] A. Choudhury and B. Nestler. Grand-potential formulation for multicomponent phase transformations combined with thin-interface asymptotics of the double-obstacle potential. *Physical Review E*, 85(2):021602, 2012.
- [24] J. Eiken, B. Böttger, and I. Steinbach. Multiphase-field approach for multicomponent alloys with extrapolation scheme for numerical application. *Physical Review E*, 73(6):066122, 2006.
- [25] M. Ohno and K. Matsuura. Quantitative phase-field modeling for dilute alloy solidification involving diffusion in the solid. *Physical Review E*, 79(3):031603, 2009.

- [26] M. Ohno, T. Takaki, and Y. Shibuta. Variational formulation of a quantitative phase-field model for nonisothermal solidification in a multicomponent alloy. *Physical Review E*, 96(3):033311, 2017.
- [27] O. Penrose and P. C. Fife. Thermodynamically consistent models of phase-field type for the kinetic of phase transitions. *Physica D: Nonlinear Phenomena*, 43(1):44–62, 1990.
- [28] S.-L. Wang, R. Sekerka, A. Wheeler, B. Murray, S. Coriell, R. Braun, and G. McFadden. Thermodynamically-consistent phase-field models for solidification. *Physica D: Nonlinear Phenomena*, 69(1-2):189–200, 1993.
- [29] K. Jackson and J. Hunt. Lamellar and rod eutectic growth. *AIME Met. Soc. Trans.*, 236:1129–1142, 1966.
- [30] L. Bronsard and F. Reitich. On three-phase boundary motion and the singular limit of a vector-valued ginzburg-landau equation. *Archive for Rational Mechanics and Analysis*, 124(4):355–379, 1993.
- [31] A. A. Wheeler, G. McFadden, and W. Boettinger. Phase-field model for solidification of a eutectic alloy. *Proceedings of the Royal Society of London. Series A: Mathematical, Physical and Engineering Sciences*, 452(1946):495–525, 1996.
- [32] J. Hötzer, M. Jainta, P. Steinmetz, B. Nestler, A. Dennstedt, A. Genau, M. Bauer, H. Köstler, and U. Rude. Large scale phase-field simulations of directional ternary eutectic solidification. *Acta Materialia*, 93:194–204, 2015.
- [33] H. Johannes, K. Michael, S. Philipp, and N. Britta. Applications of the phase-field method for the solidification of microstructures in multi-component systems. *Journal of the Indian Institute of Science*, 96(3):235–256, 2016.
- [34] J. Hötzer, P. Steinmetz, A. Dennstedt, A. Genau, M. Kellner, I. Sargin, and B. Nestler. Influence of growth velocity variations on the pattern formation during the directional solidification of ternary eutectic al-ag-cu. *Acta Materialia*, 136:335–346, 2017.
- [35] P. Steinmetz, M. Kellner, J. Hötzer, A. Dennstedt, and B. Nestler. Phase-field study of the pattern formation in al-ag-cu under the influence of the melt concentration. *Computational Materials Science*, 121:6–13, 2016.
- [36] K. D. Noubary, M. Kellner, P. Steinmetz, J. Hoetzer, and B. Nestler. Phase-field study on the effects of process and material parameters on the tilt angle during directional solidification of ternary eutectics. *Computational Materials Science*, 138:403–411, 2017.

- [37] A. Choudhury, M. Plapp, and B. Nestler. Theoretical and numerical study of lamellar eutectic three-phase growth in ternary alloys. *Physical Review E*, 83(5):051608, 2011.
- [38] M. Plapp, S. Bottin-Rousseau, G. Faivre, and S. Akamatsu. Eutectic solidification patterns: Interest of microgravity environment. *Comptes Rendus Mécanique*, 345(1):56–65, 2017.
- [39] M. Plapp. Three-dimensional phase-field simulations of directional solidification. *Journal of crystal growth*, 303(1):49–57, 2007.
- [40] A. Parisi, M. Plapp, S. Akamatsu, S. Bottin-Rousseau, M. Perrut, and G. Faivre. Three-dimensional phase-field simulations of eutectic solidification and comparison to in situ experimental observations. *TMS (The Minerals, Metals & Materials Society)*, 2005.
- [41] A. Parisi and M. Plapp. Stability of lamellar eutectic growth. *Acta Materialia*, 56(6):1348–1357, 2008.
- [42] M. Plapp and A. Karma. Eutectic colony formation: A phase-field study. *Physical Review E*, 66(6):061608, 2002.
- [43] A. Lahiri, C. Tiwary, K. Chattopadhyay, and A. Choudhury. Eutectic colony formation in systems with interfacial energy anisotropy: A phase field study. *Computational Materials Science*, 130:109–120, 2017.
- [44] T. Pusztai, L. Rátkai, A. Szállás, and L. Gránásy. Spiraling eutectic dendrites. *Physical Review E*, 87(3):032401, 2013.
- [45] J. Hötzer, P. Steinmetz, M. Jainta, S. Schulz, M. Kellner, B. Nestler, A. Genau, A. Dennstedt, M. Bauer, H. Köstler, et al. Phase-field simulations of spiral growth during directional ternary eutectic solidification. *Acta Mater.*, 106:249–259, 2016.
- [46] L. Rátkai, A. Szállás, T. Pusztai, T. Mohri, and L. Gránásy. Ternary eutectic dendrites: Pattern formation and scaling properties. *The Journal of chemical physics*, 142(15):154501, 2015.
- [47] P. Steinmetz, J. Hötzer, M. Kellner, A. Dennstedt, and B. Nestler. Large-scale phase-field simulations of ternary eutectic microstructure evolution. *Computational Materials Science*, 117:205–214, 2016.
- [48] M. Kellner, I. Sprenger, P. Steinmetz, J. Hötzer, B. Nestler, and M. Heilmaier. Phase-field simulation of the microstructure evolution in the eutectic NiAl-34Cr system. *Computational Materials Science*, 128:379–387, 2017.

- [49] Y. Lu, D. Jia, T. Hu, Z. Chen, and L. Zhang. Phase-field study the effects of elastic strain energy on the occupation probability of cr atom in Ni–Al–Cr alloy. *Superlattices and Microstructures*, 66:105–111, 2014.
- [50] K. Wu, Y. Chang, and Y. Wang. Simulating interdiffusion microstructures in Ni–Al–Cr diffusion couples: a phase field approach coupled with calphad database. *Scripta materialia*, 50(8):1145–1150, 2004.
- [51] H. B. Callen. *Thermodynamics and an Introduction to Thermostatistics*. John Wiley & Sons Inc., Singapore, 1985.
- [52] S. Ghosh, A. Karma, M. Plapp, S. Akamatsu, S. Bottin-Rousseau, and G. Faivre. Influence of morphological instability on grain boundary trajectory during directional solidification. *Acta Materialia*, 175:214–221, 2019.
- [53] P. Sternberg. Vector-valued local minimizers of nonconvex variational problems. *Rocky Mountain J. Math.*, 21(2):799–807, 06 1991.
- [54] P. Bollada, P. Jimack, and A. Mullis. Multiphase field modelling of alloy solidification. *Computational Materials Science*, 171:109085, 2020.
- [55] L.-Q. Chen and W. Yang. Computer simulation of the domain dynamics of a quenched system with a large number of nonconserved order parameters: The grain-growth kinetics. *Phys. Rev. B*, 50:15752–15756, Dec 1994.
- [56] D. Fan and L.-Q. Chen. Computer simulation of grain growth using a continuum field model. *Acta Materialia*, 45(2):611–622, 1997.
- [57] A. Kazaryan, Y. Wang, S. Dregia, and B. R. Patton. Grain growth in systems with anisotropic boundary mobility: Analytical model and computer simulation. *Physical Review B*, 63(18):184102, 2001.
- [58] N. Moelans, B. Blanpain, and P. Wollants. Quantitative analysis of grain boundary properties in a generalized phase field model for grain growth in anisotropic systems. *Phys. Rev. B*, 78:024113, Jul 2008.
- [59] N. Ofori-Opoku and N. Provatas. A quantitative multi-phase field model of polycrystalline alloy solidification. *Acta Materialia*, 58(6):2155–2164, 2010.
- [60] C. Y and Y. X. Projection onto a simplex. *arXiv:1101.6081*, pages 1–7, 2011.
- [61] D. A. Cogswell and W. C. Carter. Thermodynamic phase-field model for microstructure with multiple components and phases: The possibility of metastable phases. *Physical Review E*, 83(6):061602, 2011.

- [62] R. Tavakoli. On the coupled continuous knapsack problems: projection onto the volume constrained gibbs n-simplex. *Optimization Letters*, 10(1):137–158, 2016.
- [63] P. W. Hoffrogge, A. Mukherjee, E. Nani, P. K. Amos, F. Wang, D. Schneider, and B. Nestler. Multiphase-field model for surface diffusion and attachment kinetics in the grand-potential framework. *Physical Review E*, 103(3):033307, 2021.
- [64] T. Voigtmann, A. Meyer, D. Holland-Moritz, S. Stüber, T. Hansen, and T. Unruh. Atomic diffusion mechanisms in a binary metallic melt. *EPL (Europhys. Lett.)*, 82(6):66001, 2008.
- [65] K. Hashimoto and T. Abe. NiZr. Calphad database, Particle Simulation and Thermodynamics Group, National Institute for Materials Science, 2 2007.
- [66] G. Ghosh. Thermodynamics and kinetics of stable and metastable phases in the Ni–Zr system. *Jour. Mater. Res.*, 9(3):598–616, 1994.
- [67] A. Zaitsev, N. Zaitseva, E. K. Shakhpazov, and A. Kodentsov. Thermodynamic properties and phase equilibria in the Nickel–Zirconium system. the liquid to amorphous state transition. *PCCP*, 4(24):6047–6058, 2002.
- [68] G. Shao. Prediction of amorphous phase stability in metallic alloys. *J. Appl. Phys.*, 88(7):4443–4445, 2000.
- [69] T. Abe, H. Onodera, M. Shimono, and M. Ode. Thermodynamic modeling of the undercooled liquid in the Ni-Zr system. *Mater. Trans.*, 46(12):2838–2843, 2005.
- [70] S. Liu, J. Lee, and R. Trivedi. Dynamic effects in the lamellar–rod eutectic transition. *Acta Mater.*, 59(8):3102–3115, 2011.
- [71] A. Parisi and M. Plapp. Defects and multistability in eutectic solidification patterns. *EPL (Europhysics Letters)*, 90(2):26010, 2010.
- [72] A. Vondrous, M. Selzer, J. Hötzer, and B. Nestler. Parallel computing for phase-field models. *Int. J. High Perform. C.*, page 1094342013490972, 2013.
- [73] K. Ankit, A. Choudhury, C. Qin, S. Schulz, M. McDaniel, and B. Nestler. Theoretical and numerical study of lamellar eutectoid growth influenced by volume diffusion. *Acta Mater.*, 61(11):4245–4253, 2013.
- [74] O. Senninger and P. W. Voorhees. Eutectic growth in two-phase multicomponent alloys. *Acta Mater.*, 116:308–320, 2016.
- [75] W. Kurz. Eutectic growth before and after Jackson & Hunt 1966. In *Proceedings of the John Hunt International Symposium, London*, pages 1–15, 2011.

- [76] A. Hultgren. *Journal of the Iron and Steel Institute*, 114:421–422, 1926.
- [77] E. Scheil. Kristallisationsgeschwindigkeit, dargestellt an beispiel des perlits. *Z. Metallkunde*, 37:123–131, 1946.
- [78] W. Brandt. Solution of the diffusion equation applicable to the edgewise growth of pearlite. *Journal of Applied Physics*, 16(3):139–146, 1945.
- [79] C. Zener. Kinetics of the decomposition of austenite. *Trans. Aime*, 167:550–595, 1946.
- [80] M. Hillert. The role of interfacial energy during solid state phase transformations. *Jernkontorets Ann.*, 141:757–789, 1957.
- [81] W. Tiller. Polyphase solidification. *Liquid Metals and Solidification*, ASM, Cleveland, Ohio, pages 276–318, 1958.
- [82] L. Donaghey and W. Tiller. On the diffusion of solute during the eutectoid and eutectic transformations, part I. *Mater. Sci. Eng.*, 3(4):231–239, 1968.
- [83] R. Trivedi, P. Magnin, and W. Kurz. Theory of eutectic growth under rapid solidification conditions. *Acta Metall.*, 35(4):971–980, 1987.
- [84] A. Ludwig and S. Leibbrandt. Generalised Jackson–Hunt model for eutectic solidification at low and large pecelet numbers and any binary eutectic phase diagram. *Mater. Sci. Eng., A*, 375:540–546, 2004.
- [85] L. Zheng, D. Larson Jr., and H. Zhang. Revised form of Jackson–Hunt theory: application to directional solidification of MnBi/Bi eutectics. *J. Cryst. Growth*, 209(1):110–121, 2000.
- [86] T. Himemiya and T. Umeda. Three-phase planar eutectic growth models for a ternary eutectic system. *Mater. Trans., JIM*, 40(7):665–674, 1999.
- [87] A. Catalina, P. Voorhees, R. Huff, and A. Genau. A model for eutectic growth in multicomponent alloys. In *IOP Conference Series: Materials Science and Engineering*, volume 84, page 012085. IOP Publishing, Bristol, United Kingdom, 2015.
- [88] A. Lahiri and A. Choudhury. Revisiting Jackson-Hunt calculations: Unified theoretical analysis for generic multi-phase growth in a multi-component system. *Acta Mater.*, 133:316 – 332, 2017.
- [89] R. Series, J. Hunt, and K. Jackson. The use of an electric analogue to solve the lamellar eutectic diffusion problem. *Journal of Crystal Growth*, 40(2):221–233, 1977.

-
- [90] E. Nani, B. Nestler, and K. Ankit. Analyzing the cooperative growth of intermetallic phases with a curved solidification front. *Acta Materialia*, 159:135–149, 2018.
- [91] E. Nani and B. Nestler. Extension of Jackson-Hunt analysis for curved solid-liquid interfaces. *Journal of Crystal Growth*, 512:230–240, 2019.
- [92] S. N. Enugala, M. Kellner, R. Kobold, J. Hötzer, M. Kolbe, B. Nestler, and D. Herlach. Theoretical and numerical investigations of rod growth of an Ni-Zr eutectic alloy. *Journal of Materials Science*, 54(19):12605–12622, 2019.
- [93] F. Wendler, A. Okamoto, and P. Blum. Phase-field modeling of epitaxial growth of polycrystalline quartz veins in hydrothermal experiments. *Geofluids*, 16(2):211–230, 2016.
- [94] N. Prajapati, A. Abad Gonzalez, M. Selzer, B. Nestler, B. Busch, and C. Hilgers. Quartz cementation in polycrystalline sandstone: Insights from phase-field simulations. *Journal of Geophysical Research: Solid Earth*, 125(2):e2019JB019137, 2020.
- [95] C. P. Grant. Theory of ordinary differential equations. *Lecture notes. Brigham Young University, Provo, USA*, 2014.
- [96] W. Eckhaus. *Asymptotic analysis of singular perturbations*. Elsevier, 2011.
- [97] R. Nittka. *Elliptic and parabolic problems with Robin boundary conditions on Lipschitz domains*. PhD thesis, Universität Ulm, 2010.
- [98] Z. Ding. A proof of the trace theorem of Sobolev spaces on Lipschitz domains. *Proceedings of the American Mathematical Society*, 124(2):591–600, 1996.